Demonstration of Quantum-Enhanced LIDAR robust against classical jamming

Mateusz Piotr Mrozowski

Abstract

This thesis systematically addresses two main objectives. The first part focuses on the creation of a high-brightness source of heralded single photons, essential for the development of an advanced LIDAR system. The second part is dedicated to the experimental development of a quantum-enhanced LIDAR, employing coincidence detection to effectively discriminate between signal photons and background level.

In the initial sections, the focus is placed on the development of an Optical Frequency Comb Generator (OFCG) designed to produce high-efficiency, microsecond pulses optimised for photon generation through the Four Wave Mixing process. A new numerical model is introduced and utilised for the optimal design and refinement of the OFCG. The theoretical predictions of the model are validated by experimental realisations and comprehensive characterisation, confirming the anticipated efficiency and performance of the OFCG.

The latter part of the thesis transitions to the development and assessment of the quantum-enhanced LIDAR. This system integrates a continuously pumped photon pair source with a simplified detection mechanism. It proves effective in operational environments characterised by a significant imbalance between signal and background level, with the presence of noise levels exceeding million counts per second while the returning signal was on the level of single counts per second. Target discrimination was successfully performed even with extremely low target reflectivity down to -52 dB. The LIDAR's performance is thoroughly evaluated using a log-likelihood analysis framework, demonstrating robustness against various forms of classical jamming. It is capable of performing rangefinding measurement limited by the timing jitter of silicon-based room-temperature Single Photon Avalanche Detectors (SPADs).

Demonstration of Quantum-Enhanced LIDAR robust against classical jamming

Mateusz Piotr Mrozowski

A thesis submitted in partial fulfilment
of the requirements for the degree of
Doctor of Philosophy

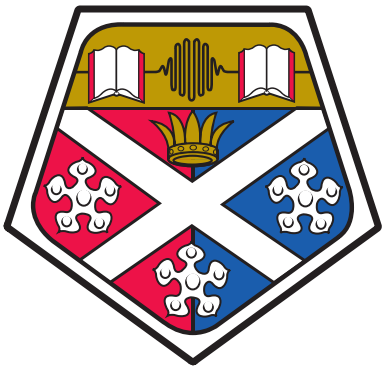

Department of Physics
University of Strathclyde

October 4, 2024

Contents

List of Figures

Declaration

I confirm that no part of the material offered has previously been submitted by myself for a degree in this or any other University. Where material has been generated through joint work, the work of others has been indicated.

Mateusz Piotr Mrozowski
Glasgow, October 4, 2024

Acknowledgements

When I began my PhD, I was not sure I would reach the point of writing this section, expressing my gratitude to those who made this achievement possible.

First and foremost, I want to thank Jonathan Pritchard, my primary supervisor. His expertise, generosity, and kindness have been invaluable. Jonathan's unwavering patience and support not only refined my skills as a scientist but also provided friendship when research challenges seemed overwhelming.

I also extend my thanks to John Jeffers, my secondary supervisor. His relaxed approach and keen insights provided balance during our research meetings.

Richard Murchie deserves special recognition. Sharing the PhD journey with him made the tough times easier to bear and the successes even sweeter. Our brainstorming sessions, filled with both challenges and victories, have been crucial.

I am deeply grateful to my brother Marcin, my lifelong ally. Every obstacle and every celebration has been shared with him. His steadfast support, especially during the long, daunting nights, has been my anchor.

To my brother.

Table of Symbols and Acronyms

Symbols

c	speed of light in vacuum
δ	modulation depth
F	optical finesse
κ	phase mismatch
λ	wavelength
ν_c	characteristic mode
ω_m	modulation frequency
τ_p	Full Width at Half Maximum pulse width
$\chi^{(2)}$	second order non-linear susceptibility
$\chi^{(3)}$	third order non-linear susceptibility

Acronyms

APD	Avalanche Photodiode
AR	Anti-Reflective
CW	Continuous Wave
EOM	Electro-Optical Modulator
FSR	Free Spectral Range
FSWM	Spontaneous Four Wave Mixing
FWHM	Full Width at Half Maximum
GVD	Group Velocity Dispersion
HR	High-Reflective
JSA	Joint Spectral Amplitude
JSI	Joint Spectral Intensity
LIDAR	Light Detection and Ranging
LLV	Log Likelihood Value
NPBS	Non-Polarising Beam Splitter
OFCG	Optical Frequency Comb Generator
PBS	Polarising Beam Splitter
PDH	Pound-Drever-Hall
ppKTP	periodically poled Potassium Titanyl Phosphate
QPM	Quasi Phase-Matching
ROC	Radius of Curvature
SBR	Signal-to-Background Ratio
SFWM	Spontaneous Four Wave Mixing
SPAD	Single Photon Avalanche Diode
SPDC	Spontaneous Parametric Down Conversion
TCSPC	Time Correlated Single Photon Counting
TT	Time Tagger

Part I

Introduction

Chapter 1

Introduction

The art and science of target detection and rangefinding are as ancient as human curiosity and strategic ingenuity. Over the centuries, a journey from rudimentary attempts to modern technological innovations has been marked by the constant evolution of tools and methodologies. In ancient times, civilisations deployed basic instruments like astrolabes and quadrants for celestial navigation and observations. The evolution of these tools was not just a technological advancement but a strategic enhancement in naval warfare, where estimating the enemy's distance was often the game-changer.

The inception of RADAR (Radio Detection and Ranging) in the 20th century marked a monumental leap in this domain [1]. As illustrated in Fig. 1.1, RADAR systems, capitalising on time-of-flight measurements, offered unprecedented accuracy in determining distances. The equation

$$r = \frac{\Delta t \cdot c}{2}, \tag{1.1}$$

describes this principle, where r is the distance to the target, Δt is the time it takes for the electromagnetic wave to travel to the target and back, and c is the speed of light. The factor of 2 accounts for the round-trip journey of the wave. Furthermore, RADARs are also capable of detecting the velocity of

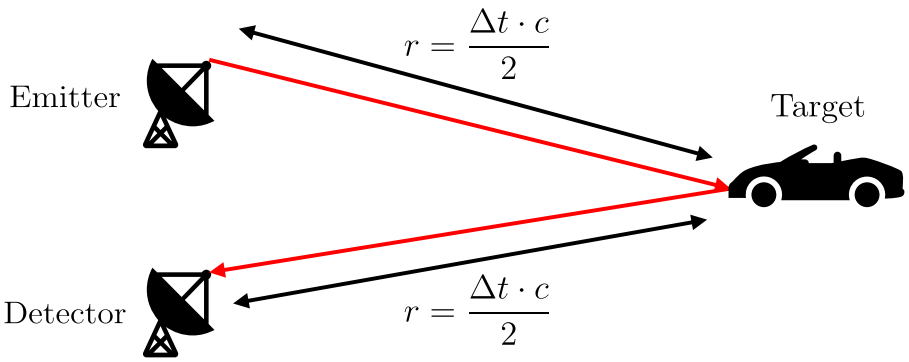

Figure 1.1: Diagram depicting the principle of the time-of-flight measurement. An emitter sends an electro-magnetic wave towards a target which reflects a portion of the signal. The returning signal is detected by a detector. The distance r between the measurement devices and the target can be estimated by measuring the time between sending and receiving the signal Δt.

moving targets by utilising the Doppler shift of the returned signal [2]. This technology became instrumental in World War II and equally significant in civilian applications, including weather forecasting.

Despite RADAR's contributions, its usage of long wavelengths of electromagnetic waves had inherent limitations, especially when it came to detailed observations at shorter ranges. These waves are prone to significant diffraction effects, which can compromise the precision of target detection.

In contrast, LIDAR (Light Detection and Ranging) emerged with the promise of excelling in short-range detailed observations, thanks to its utilisation of shorter optical wavelengths. The use of laser beams in LIDAR offers greater precision and detail, making it particularly advantageous for close-proximity target detection and rangefinding.

However, LIDAR is not without its limitations. Over very long distances, the laser light from LIDAR systems can be absorbed or scattered by atmospheric particles, such as dust, moisture, and gases. This attenuation of the

signal, combined with the need for high-resolution and high-sensitivity detectors that face challenges with low photon return rates at extended ranges, means that LIDAR is less effective over extremely long distances compared to RADAR.

Despite these challenges, the potential and versatility of LIDAR in various applications can not be understated. The following sections provide an in-depth examination of LIDAR's principles, technologies, and its pivotal role in modern remote sensing.

1.1 Introduction to LIDAR

LIDAR has firmly established itself as a linchpin technology in the arena of precise target detection and rangefinding, with its footprint expanding across diverse applications including ground surveys, sea-level monitoring, and as a cornerstone for the navigational prowess of autonomous vehicles [3–7].

The operational essence of LIDAR is encapsulated in the emission of short optical pulses, their journey to the target, and the reflection back to the source [8]. The precision in measuring the time lapse of this round trip provides crucial data for determining the target's presence and exact distance.

However, challenges arise in classical LIDAR applications, especially when operating at long distances or with low reflectivity targets. When performing measurements outdoors, there is an inherent risk that a bystander might inadvertently receive an eye strike from the emitted optical pulses. To mitigate this risk and ensure the safety of all individuals in the vicinity, the adoption of eye-safe operational standards becomes imperative. These standards, while prioritising safety, necessitate the use of less intense emitted optical pulses, leading to an extremely weak return signal. Given these circumstances, it becomes increasingly difficult for classical LIDAR systems to distinguish useful return photons from the background level. This limitation not only affects

the accuracy but also renders the systems vulnerable to jamming and other intentional interference.

One significant advancement that aimed to address these challenges is the introduction of Single-Photon Avalanche Diodes (SPADs) [9]. Celebrated for their ability to register avalanche events upon the detection of a lone photon, SPADs have become indispensable in LIDAR applications where weak-signal detection is of utmost importance [10, 11].

Complementing the evolution of SPADs, the advent of single-photon sources represents another pivotal progression. These sources, primarily based on spontaneous parametric down-conversion (SPDC) and spontaneous four-wave mixing (SFWM), have shown exceptional promise in enhancing the efficiency and brightness crucial for LIDAR applications [12–16]. The fundamental processes within these sources involve the destruction and creation of photons within non-linear crystals, resulting in the generation of 'idler' and 'signal' photon pairs. This mechanism enables accurate distance measurements through analysing the time delay between these paired detections [14].

Despite the low-light operations, SPDC sources have demonstrated effectiveness in rangefinding over extended distances [13, 15]. Embracing this single-photon regime signifies a transformative era for LIDAR, offering unmatched sensitivity and overcoming challenges that were once insurmountable due to environmental and technical constraints.

This evolution in LIDAR technology, marked by its immersion into the quantum realm, elevates it from a mere technological instrument to a strategic asset. Its unique attributes encompass enhanced situational awareness, superior operational security, and unparalleled data accuracy.

In the following sections, we will delve into the intricate relationship between photon detectors, quantum phenomena, and the operational principles that define the current state of the LIDAR field. This exploration will provide insights into its current capabilities and address future advancements.

1.1.1 Quantum Illumination

Quantum illumination, as first presented by Lloyd in 2008, is rooted in the theoretical application of quantum correlations to exponentially enhance the signal-to-background ratio in target detection and discrimination [17]. Although quantum states are inherently vulnerable to loss and background perturbation, the exquisite sensitivity arising from the entanglement of photon pairs offers a remarkable advantage over classical approaches.

In the quantum illumination paradigm, an entangled pair of photons is prepared, where the idler photon is kept locally, and the signal photon is sent to probe a target immersed in substantial background level. The reflected signal is subsequently combined with the locally retained idler in a joint quantum measurement. The correlations between the idler and signal photons enable the differentiation of the signal photon from the pervasive background, thereby enhancing the signal-to-background ratio.

Lloyd's foundational work demonstrated the possibility of transcending the capabilities of classical systems by leveraging the potent effects of entanglement [17]. Further explorations, particularly the Gaussian state analysis, have postulated a 6 dB cap on the quantum advantage, contingent upon an as-yet unidentified optimal measurement [18, 19]. Existing measurement protocols, albeit promising, have realized up to a 3 dB advantage [20, 21]. The aspiration to harness the full quantum advantage has been primarily hindered by the implicit technical challenge of necessitating phase-sensitive detection from a target at an unknown distance. This requirement demands a stability level below $\lambda/2$, introducing complexities in implementation [22, 23].

Empirical forays into quantum illumination have yielded phase-sensitive detection demonstrations in-fibre, albeit with detector-incurred background [21]. These initial endeavours have recently been extrapolated into the microwave domain, heralding a new frontier that aligns with contemporary radar technologies [24–26].

The ensuing discussion is set to introduce a simplified, yet effective, detection scheme. Moving away from the complexity of entanglement, this approach capitalises on the temporal correlation between photon pairs, offering a pragmatic solution for background rejection while preserving the essence of quantum-enhanced sensitivity [27].

1.1.2 Quantum-Enhanced LIDAR

In the preceding section, the intriguing prospects of enhancing LIDAR detection capabilities through quantum illumination, specifically via entanglement, were explored. However, practical implementation of this method is laden with challenges, warranting the exploration of alternative, simpler yet effective, strategies.

One such pragmatic approach on the non-classical temporal correlations characteristic of photon pairs born from spontaneous parametric processes like SPDC and SFWM, irrespective of whether pulsed or continuous sources are employed [28]. The underlying principle is straightforward yet powerful. Given that these photon pairs are conceived almost simultaneously, the detection of the idler photon effectively heralds the presence of its signal counterpart. This temporal alignment is crucial for eliminating uncorrelated background photons. Detection events are recorded only when correlated signal-idler pairs are identified, a technique referred to as coincidence detection.

This technique, though less complex, has proven its mettle in experimental arenas. Enhanced signal-to-background ratios, an essential metric for the fidelity of detection, have been consistently observed [14, 15, 29, 30]. Moreover, this method exhibits an inherent resilience against classical interference [14, 16]. Rangefinding, a cornerstone application of LIDAR, has also been successfully demonstrated employing this approach [13, 15, 31].

A notable advancement in this domain is the integration of dispersion compensating fibres. By dispersing background across multiple time-bins while preserving the temporal correlation intrinsic to photon pairs, a remarkable 43 dB enhancement in SBR has been achieved, even amidst background levels thrice that of the signal [32]. Furthermore, the advent of detector multiplexing is broadening the horizons of LIDAR technology [33]. This innovation facilitates multi-mode rangefinding and empowers LIDAR systems to operate covertly, deploying light that is both spectrally and statistically camouflaged against the background [31].

Such covert operations, which hinge on manipulating the statistical properties of light, are underlined by the understanding of the second-order correlation function. This function, discussed in detail in Section 1.1.3, serves as a quantitative tool to discern the temporal coherence of varied light sources, enabling differentiation between thermal, coherent, and non-classical light sources. With a grasp on these coherence properties, LIDAR systems can ensure their operations remain discreet and virtually undetectable in certain scenarios.

It is crucial to distinguish between the roles of non-classical and quantum correlations in our approach. While the background suppression in our system achieves an improvement greater than 40 dB (as shown in Chapter 6), it is important to note that this improvement is largely attributed to strong photon number correlations, which are distinctly non-classical and arise from the SPDC process. These correlations are more robust than those achievable with classical light, thereby providing a heralding gain significantly beyond what classical correlations can offer. The potential addition of phase-sensitive measurements (the quantum illumination protocol described in the previous section), could further enhance this advantage by an estimated 3 to 6 dB, pushing the boundaries of what is currently achieved.

In the domain of quantum-enhanced LIDAR, exploiting entanglement of-

fers theoretical advantages, notably in terms of accuracy and signal-to-background ratio enhancement. However, this approach is beset with practical challenges, making its real-world application complex. In contrast, the utilisation of temporal correlations between photon pairs emerges as a more practicable alternative. While perhaps not reaching the theoretical peak performance of entanglement, temporal correlations provide a significant, tangible improvement in LIDAR operations [14–16]. This method is considerably easier to implement in practical settings, sidestepping many of the difficulties associated with entanglement. Thus, in the balance of theoretical perfection and practical feasibility, leveraging temporal correlations stands out as a robust, efficient solution for advancing LIDAR technology.

1.1.2.1 Coincidence Detection

Coincidence detection emerges as a pivotal technique in the sphere of quantum-enhanced LIDAR, particularly due to its efficacy in amplifying the signal-to-background ratio amidst a backdrop of ambient background and potential interference. It hinges on the principle of exploiting the intrinsic temporal correlations between photon pairs generated through spontaneous parametric processes like SPDC and SFWM.

In the operational schema of coincidence detection, shown in Fig. 1.2, two detectors are typically employed - one dedicated to the idler photon and another to the signal photon. Owing to the near-simultaneous generation of these photon pairs, the detection of an idler photon signals the immediate anticipation of its corresponding signal photon [29]. The idler photon, serving as a herald, triggers the monitoring window wherein the signal photon is expected. The probability of background photons infiltrating this narrowed temporal window is drastically reduced, leading to a purified and enhanced signal.

This quantum-enhanced sensitivity can be understood by considering a LI-

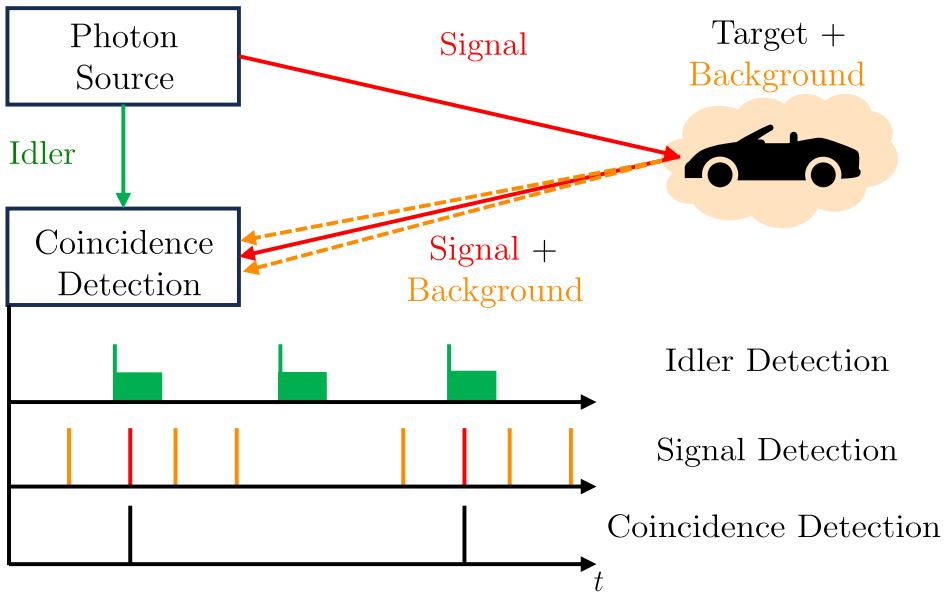

Figure 1.2: Diagram illustrating coincidence detection principle: A photon pair source emits near-simultaneous pairs of signal (red) and idler (green) photons. The idler photons are detected locally, while signal photons are sent out to probe a target against a strong background. Reflected signal photons and background level are detected upon return. Coincidence detection between idler and signal detectors is initiated by an idler click, followed by a search for signal clicks within a precise, few-nanoseconds window, depicted as a green bar post-idler detection. This window is timed to match the signal's round-trip travel to the target and back, ensuring only temporally correlated signal clicks are counted as coincidence events.

DAR system that sends one photon every second while there are 10,000 background photons present in the one second time window. In such a scenario, the probability of successfully distinguishing the signal photon from a background photon is very low, at approximately 1/10,001 or 0.01%. However, by utilising non-classical correlations and employing an idler-conditioned detection method, as described above, and selecting a coincidence window of 1 nanosecond, the probability that one of the 10,000 background photons will be detected within this window is reduced to 0.001%. This approach effectively suppresses the background level using non-classical correlated photon pairs generated in processes such as SFWM and SPDC, and in this simple

example would lead to an improvement in sensitivity by approximately 40 dB.

The effectiveness of coincidence detection is not merely theoretical but finds empirical validation. Experimental setups employing this technique have consistently demonstrated elevated levels of detection accuracy, even in scenarios characterised by substantial background level [30].

1.1.3 Second-Order Correlation Function

The second-order correlation function $g^{(2)}(\tau)$ is a vital statistical tool used to characterise the correlation between photons arriving at two different times, providing insights into the temporal coherence properties of light. Using classical formalism the second-order coherence can be expressed

$$g^{(2)}(\tau) = \frac{\langle I(t)I(t+\tau)\rangle}{\langle I(t)\rangle^2}, \tag{1.2}$$

where $I(t)$ is the light intensity at time t, τ is the time delay and $\langle . \rangle$ denotes a time average much longer than the coherence time of . The second-order correlation function is instrumental in distinguishing between different types of light based on their temporal coherence properties.

This function enables characterisation of light into three different regimes dependent upon the value of $g^{(2)}(0)$ as shown in Fig. 1.3. For a coherent source, such as light from a laser, $g^{(2)}(0) = 1$ [34], meaning the arrival times of photons at the detector is entirely random. When $g^{(2)}(0) > 1$, photons are more likely to arrive together leading to the term bunched or super-Poissonian light. This is the case for thermal light which typically can be modelled as a chaotic, with an intensity that fluctuates around a mean value $\langle I \rangle$. The numerator of Eq. 1.2 will then exaggerate higher intensity values over lower ones, hence $\langle I(t)^2\rangle / \langle I(t)\rangle^2 > 1$ [35]. Finally, $g^{(2)}(0) < 1$ is known as sub-Poissonian or anti-bunched as photons are more likely to arrive individually,

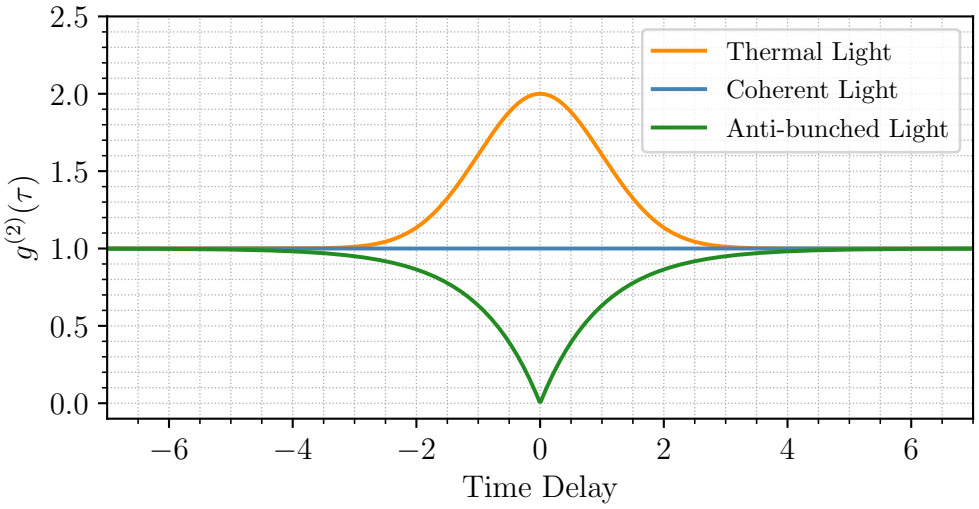

Figure 1.3: Second-order coherence function for thermal, coherent, and anti-bunched light. The distinct $g^{(2)}(0)$ values serve as identifiers for each light type.

with $g^{(2)}(0) = 0$ indicating an ideal single photon source.

Thus, recording a second order correlation function becomes another possibility to distinguish between a classical LIDAR and background light. In practice, distinguishing between the coherent light from a classical LIDAR system and the thermal background light involves measuring the $g^{(2)}(0)$ value. While theoretically feasible, practical challenges arise due to the subtle intensity fluctuations of thermal light, necessitating highly sensitive detectors. It is important to note that the decay time of $g^{(2)}$ is governed by the inverse bandwidth, which could be as short as a few femtoseconds. This requires femtosecond-level resolution from the detectors. Ambient background further complicates signal isolation, and the weak signal strength of thermal light requires a full quantum mechanical treatment of the sensing problem [36]. Practical implementation is also hindered by the complexity of necessary equipment, such as Hanbury Brown and Twiss setups, and the demand for precise calibration and stability. Despite these challenges, advancements in detection technology and signal processing are gradually enhancing the practicality of such measurements [37].

For a single-mode light source the second-order coherence can be expressed using quantum mechanical formalism as [38]

$$g^{(2)}(\tau) = \frac{\langle \hat{a}^\dagger(t)\hat{a}^\dagger(t+\tau)\hat{a}(t)\hat{a}(t+\tau)\rangle}{\langle \hat{a}^\dagger(t)\hat{a}(t)\rangle^2}, \tag{1.3}$$

where the operators $\hat{a}$ and $\hat{a}^\dagger$ are known as annihilation and creation operators, respectively. Their physical meaning can be understood as removing or adding a single photon. For example, the action of annihilation operator on a number state $|n\rangle$, which is a state that contains precisely n photons (also known as a Fock state), is [38]

$$\hat{a}|n\rangle = \sqrt{n}|n-1\rangle, \tag{1.4}$$

for number states where $n \neq 0$. The term $\sqrt{n}$ is normalisation factor.

1.1.3.1 Idler-conditioned second order coherence function

The idler-conditioned second-order correlation function $g_c^{(2)}(\tau)$ is a statistical tool used to verify the emission of single photons from a light source emitting single photon pairs such as SPDC and SFWM. This technique leverages the correlation between the idler and signal photons generated by a single-photon source. By splitting the signal beam and measuring coincidences between the idler photon detector and two signal photon detectors, one can confirm the presence of single photons.

The idler-conditioned second-order correlation function $g_c^{(2)}(\tau)$ is defined as [39]

$$g_c^{(2)}(\tau) = \frac{P_{IS_1S_2}}{P_{IS_1}P_{IS_2}} \tag{1.5}$$

where $P_{IS_1S_2}$ is the probability of obtaining a threefold coincidence between the idler (I), signal 1 (S_1), and signal 2 (S_2) detectors. The P_{IS_1} and P_{IS_2}

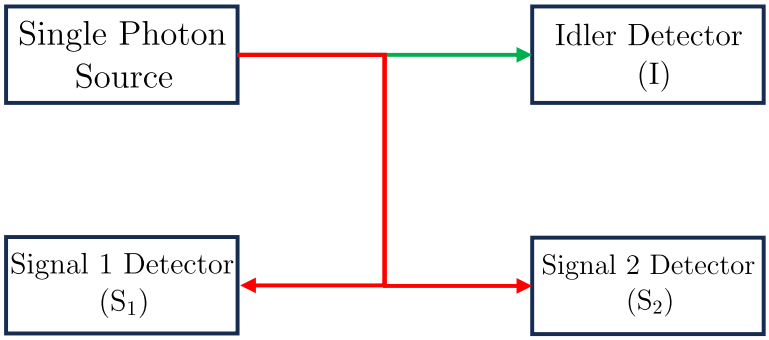

Figure 1.4: Experimental setup for measuring the idler-conditioned second-order correlation function. The single-photon source emits photon pairs, signal (in red) and idler (in green). The idler is directed to the idler detector (I), and the signal photon is split evenly between the Signal 1 detector (S_1) and the Signal 2 detector (S_2).

are the probabilities of twofold coincidences between the idler and signal 1/2 detectors.

For a true single-photon source, it is impossible for all three detectors to click simultaneously (assuming the detectors involved in measurements are perfect). This is because if the idler and one of the signal detectors (either signal 1 or signal 2) detect a photon, there should be no photon left to be detected by the other signal detector. Therefore, the absence of simultaneous clicks among the three detectors is a strong indication that the source is indeed emitting single photons.

The experimental setup for measuring the idler-conditioned second-order correlation function is based on the Hanbury-Brown-Twiss configuration [39]. This setup, shown in Fig 1.4, will be used to characterise our single photon source in Chapter 5.

In summary, the second-order correlation function, $g^{(2)}(\tau)$, serves as a powerful tool for discerning the temporal coherence properties of different light sources. Its ability to differentiate between thermal, coherent, and anti-bunched light is crucial, especially in contexts where these distinctions have practical implications. As we transition to more advanced LIDAR applica-

tions in the following sections, the insights derived from this function will play a pivotal role in understanding the intricacies of covert operations and the challenges they present.

1.2 Covert Target Detection

With the foundational understanding of the second-order correlation function and the insights it offers, we now delve into the advanced realm of LIDAR operations, especially in scenarios where stealth and secrecy are of utmost importance.

The evolution of LIDAR technology into the single-photon regime has unlocked unprecedented capabilities for covert operations, a development of paramount significance in military and security applications. The ability to generate and detect individual photons ensures minimal energy emission, thus reducing the detectability of the LIDAR systems while maintaining their rangefinding and imaging efficacy [14, 16].

However, despite the advancements, potential adversaries equipped with sophisticated detection technologies can identify LIDAR operations through several mechanisms:

1. **Spectral Signature:** Typical LIDAR operation introduces a distinct spectral signature in the ambient light environment. The emission of focused laser beams, though minimal, can be detected due to the sharp spike they create in the light spectrum. This spectral signature can be camouflaged by deploying tunable lasers and spectral broadening techniques, thereby diffusing the sharp spectral peaks into a more randomised and natural-looking emission pattern [31].

2. **Pulsed Operation Mode:** In pulsed operation mode, the LIDAR system can potentially be detected through its characteristic pulse rep-

etition rate. Analysing the temporal distribution of photons in the environment can unveil the presence of a LIDAR system if an unintended rhythmic emission pattern is detected [24].

3. **Coherence:** The second-order coherence function, introduced in previous Section, provides another avenue for detection. By distinguishing the coherent laser light, which is a hallmark of LIDAR systems, from the chaotic and highly bunched emissions of thermal light sources, the operation of LIDAR can be potentially unveiled.

Considering these detection mechanisms, designing quantum-enhanced LIDAR systems for covert operations necessitates meticulous strategising to mitigate these vulnerabilities. By modulating the spectral emission patterns, manipulating pulse repetition rates, and obfuscating the coherence of emitted light, our objective is to make the LIDAR operations indistinguishable from the ambient light and electromagnetic noise.

Subsequent sections will elucidate our proposed methods for obscuring the LIDAR's spectral signature through operation in the single-photon regime, reducing the spectral spike associated with laser emissions. We will present two strategies: one involving continuous mode operation and another exploiting pulsed mode with a high repetition rate (∼GHz) and minimal photon generation probability.

1.2.1 Spectral Signature

Understanding the spectral signature of a LIDAR system in the context of its operational environment is pivotal for evaluating its covert capabilities. The background light, particularly in daytime operations, is dominated by the solar spectrum, which adheres to Planck's law for black-body radiation.

Figure 1.5 illustrates the solar spectrum. In this radiant expanse, the emissions from a LIDAR operating in the single photon regime are practically

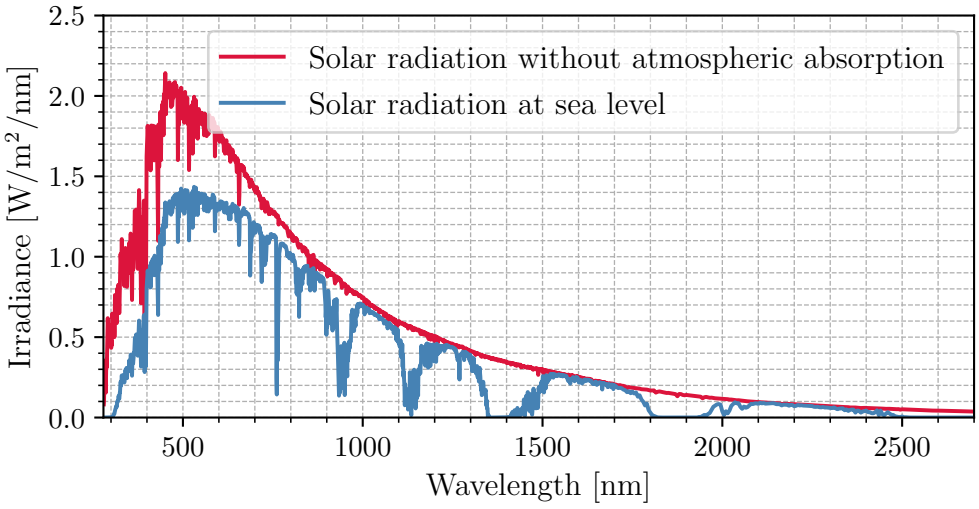

Figure 1.5: The solar radiation spectrum for direct light, comparing conditions at the top of the Earth's atmosphere (depicted in red) and at sea level (depicted in blue) [40].

indiscernible, thus enhancing its covert attributes.

Single photon sources emit light at an extraordinarily dim level, especially when compared to conventional light sources used in rangefinding systems. With photon-pair rates typically in ∼MHz mW^{-1} [41, 42] and even reaching GHz mW^{-1} regime for optimised sources [43], the resulting power levels range from hundreds of femtowatts to tens of picowatts, depending on the pump power.

This interplay between the dim emissions of single-photon sources and the overwhelming brightness of the solar spectrum effectively camouflages the LIDAR emissions. The increase in the ambient light power due to quantum-enhanced LIDAR operation is indistinguishable, thus affording a level of operational secrecy that is unattainable with more potent light sources.

1.2.2 Time-like Signature

Traditional LIDAR systems often utilise pulsed sources, operating at repetition rates within the MHz regime. Though effective, these systems are

identifiable by scrutinising the background spectrum for periodic increases in radiance, a vulnerability that can compromise covert operations.

We propose two strategies to mitigate this issue, enhancing the stealth characteristics of LIDAR systems. The first involves the deployment of Continuous Wave (CW) illumination, eliminating the time-like signature inherent to pulsed sources. Classically, LIDAR systems are restricted from CW operation due to the necessity for a time-stamp to initiate the time-of-flight measurement. However, by integrating single-photon sources based on SPDC, the heralding of the idler photon can serve as a unique time-stamp, initiating the measurement process and enabling accurate rangefinding within the CW regime.

The second strategy employs a weak pulsed source in the GHz repetition rate regime to pump the SFWM process. Given the low probability of photon-pair generation per pulse, a majority of emitted pulses contain no photons, with only a sparse few containing signal photons. This random, intermittent emission of photon-pairs effectively obscures the time-like signature.

Additionally, utilising an attenuated weak coherent pulsed source [44], potentially with randomised emission times driven by a quantum random number generator, offers an alternative approach to further enhance LIDAR system stealth. This method can further obscure the periodicity inherent to pulsed sources, complicating detection efforts.

These advancements, while instrumental in mitigating detection via time-like signatures, necessitate innovative pulse generation techniques to ensure effectiveness and efficiency. In the forthcoming section, we will delve into the intricacies of generating a GHz train of pulses utilising Optical Frequency Comb Generation (OFCG), a technology instrumental in achieving the desired pulse characteristics and operational stealth for a quantum-enhanced LIDAR systems.

1.2.2.1 Optical Frequency Comb Generation

The evolution of optical frequency comb technology has been marked by significant milestones, underpinning various applications from sensing and metrology to the realisation of scalable quantum systems [45–48]. In the historical context, mode-locked laser systems were predominant sources of pulsed light for the quantum experiments. These devices, characterised by their size, high power, and substantial cost, produce temporal pulses with widths ranging from a few femtoseconds to hundreds of picoseconds and operating at repetition rates of approximately 1 to 100 MHz [49, 50].

Transitioning from these traditional systems, the OFCG offers a more compact and adaptable method for generating pulsed light. Figure 1.6 provides an illustrative diagram of the OFCG setup. The advent of the OFCG presented a breakthrough, allowing for effectively converting a CW pump into a mode-locked pulse train and achieving repetition rates up to 20 GHz [51–54]. Despite its low output efficiency due to impedance mismatches during light coupling, the OFCG's adaptability to various pump wavelengths and dynamic pulse width adjustability have positioned it as a pivotal innovation in the field [51, 55, 56].

To address the low output efficiency, the integration of a coupled cavity design in OFCG has been proposed as a solution [57]. This design not only promises improved efficiency but also expanded operational capabilities for the OFCG, positioning it as a viable tool for advanced LIDAR systems.

In the Chapters 3 and 4, a thorough investigation into the coupled cavity OFCG will be conducted. Chapter 3 is dedicated to the modelling and theoretical analysis of this enhanced OFCG design, while Chapter 4 will present the experimental realization and evaluation of its performance. These explorations aim to articulate the potential of coupled cavity OFCG in augmenting the operational efficiency and covert capabilities of quantum-enhanced LIDAR systems, shedding light on its prospective contributions to the field.

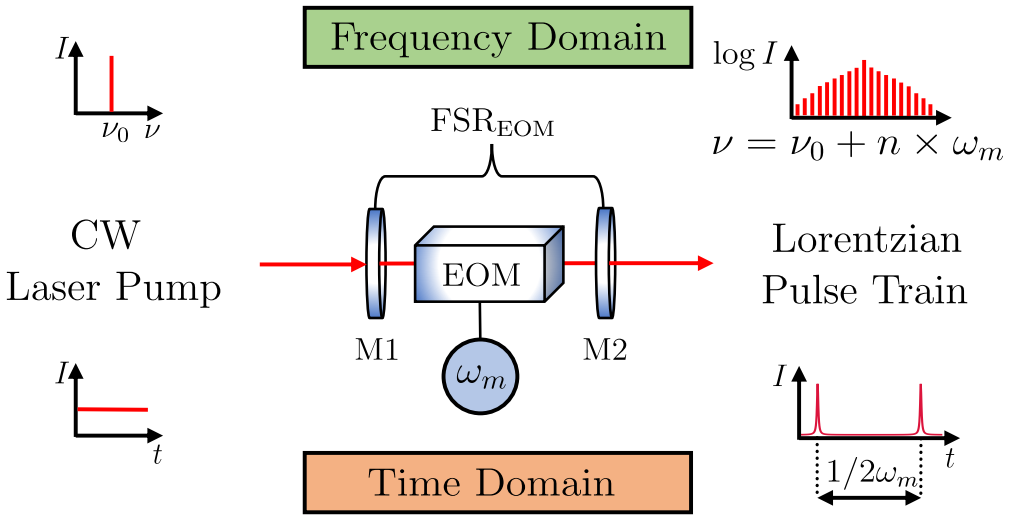

Figure 1.6: Diagram illustrating the OFCG setup formed from a CW pump laser injected into an optical cavity containing the EOM. The light passing through an EOM undergoes phase modulation, which causes creation of sidebands about the central frequency of the input light separated by the frequency ω_m. The EOM is placed in an optical cavity consisting of mirrors M1 & M2. The free spectral range $\mathrm{FSR}_{\mathrm{EOM}}$ is chosen to be an integer multiple of a modulation frequency of an EOM ω_m. This configuration efficiently transforms the input CW signal into a frequency comb, facilitating the generation of short temporal pulses with a repetition rate of $2\omega_m$.

1.3 Summary of Thesis and Publication List

The structure of this thesis is systematically divided into specific parts, each highlighting a central theme of the research undertaken during the Ph.D. The first Part of this thesis is primarily introductory, setting the stage for the more intricate details that follow.

Part II of the thesis is centred on the development and characterisation of the OFCG. Here, the emphasis is laid on its foundational theory, the modelling aspects, and the eventual experimental realisation.

Part III delves into the demonstrations of quantum-enhanced LIDAR using a CW Source. This section concentrates on the integration of heralded photon source and its application in quantum-enhanced LIDAR experiments.

With the overarching themes laid out, we proceed to a detailed breakdown of the contents of each Chapter:

- **Chapter 2**: Delivers an in-depth theoretical backdrop, focusing on non-linear optics, and the primary methods for generating non-classical light, namely SPDC and SFWM. The Chapter also introduces electro-optical modulation and the intra-cavity EOM OFCG.
- **Chapter 3**: Explores the modelling dynamics of single and coupled cavity OFCG, with emphasis on designing an optimised OFCG for high-power pulse generation.
- **Chapter 4**: Chronicles the experimental journey of realising the coupled cavity OFCG, discussing its limitations and showcasing the characterisation results.
- **Chapter 5**: Unveils the creation and characterisation of the heralded photon source based on the SPDC Type-II process, setting the stage for its application in quantum LIDAR.
- **Chapter 6**: Provides an account of quantum-enhanced LIDAR's experimental demonstration. It details improvements in the signal-to-background ratio, the application of a loglikelihood analysis framework, and introduces a comprehensive experimental setup with realistic imaging optics.
- **Chapter 7**: Concludes the thesis, summarising the pivotal findings and reflecting on potential future trajectories in quantum-enhanced rangefinding and coupled-cavity OFCG.

1.3.1 Publication list

The following publications have been produced during the course of this Ph.D. project:

1. M. P. Mrozowski, J. Jeffers, and J. D. Pritchard, *A practical compact source of heralded single photons for a simple detection LIDAR*, SPIE **11835** (2021). Available at doi:10.1117/12.2597218.

   Relation to Thesis: This paper serves as the foundation of Chapter 3.

   My Contribution: As the first author, I was responsible for developing the numerical model, designing the simulations, and drafting the manuscript.

2. M. P. Mrozowski, J. Jeffers, and J. D. Pritchard, *High-efficiency coupled-cavity optical frequency comb generation*, Opt. Continuum **2**, 894-901 (2023). Available at doi:10.1364/OPTCON.481563.

   Relation to Thesis: This paper serves as the foundation of Chapter 4.

   My Contribution: I conducted the experiments, analysed the resulting data, and was the principal author of the manuscript.

3. R. J. Murchie, M. P. Mrozowski, J. D. Pritchard, and J. Jeffers, *Towards Simple-detection Quantum Illumination LIDAR*, STO-SET-311/RSY (2023).

   Relation to Thesis: This paper is not directly used in the thesis.

   My Contribution: I authored the section on the heralded photon source, conducted the experimental work, and provided the experimental data.

4. M. P. Mrozowski, R. J. Murchie, J. Jeffers, and J. D. Pritchard, *Demonstration of quantum-enhanced rangefinding robust against classical jamming*, Opt. Express **32**, 2916-2928 (2024). Available at doi:10.1117/12.2597218.

   Relation to Thesis: This paper serves as the foundation of Chapter 6.

   Contributions: M.M. and J.P. devised the experiment; M.M. con-

ducted the experiment; R.M. and J.J. developed the underpinning theoretical framework; J.P., R.M., and M.M. performed the analysis of the data. All authors contributed to the discussion of results and the preparation of the manuscript.

Chapter 2

Background Theory of Non-linear Optics

2.1 Introduction

The field of non-linear optics considers processes where the optical properties of a material have a non-linear response in electric field amplitude, originating with the observation of the Kerr effect in the early 19$^{\text{th}}$ century [58, 59]. However, the practical application of these effects was limited due to the absence of intense light sources. The advent of lasers in the 1960s revolutionised the field of non-linear optics by providing researchers with coherent and high-intensity light sources, enabling deeper exploration of the non-linear phenomena exhibited by materials under intense optical fields.

These advancements in non-linear optics not only expanded our understanding of light-matter interactions but also played a crucial role in enabling the generation of single photons for quantum information experiments [60]. For the purpose of this thesis the following non-linear effects capable of generating non-classical light will be introduced, these are Spontaneous Four-Wave Mixing (SFWM) [61–63] and Spontaneous Parametric

Down-Conversion (SPDC) [64–67].

In addition to the concepts of SFWM and SPDC, this Chapter will outline the theory of Electro-Optic Modulation (EOM). Electro-Optic Modulation involves the manipulation of a laser's frequency spectrum using electrical signals. EOM-enabled optical frequency comb generation (OFCG) is a powerful technique that enables the generation of comb-like spectra within the frequency domain, leading to the production of short temporal pulses in the temporal domain. This aspect of EOM will play a crucial role in achieving the objectives of this thesis by providing a method for precise and versatile optical pulse generation [53–57]. This capability is particularly important as it enables the generation of optical pulses at arbitrary wavelengths.

This Chapter provides a comprehensive background on non-linear optics, focusing on key topics such as electro-optic modulation, spontaneous parametric down-conversion, and spontaneous four-wave mixing. The insights gained from these discussions will be applied in the subsequent Chapters, specifically Chapters 3 & 4 for EOM and OFCG pulse generation, and Chapters 5 & 6 for SPDC.

2.2 Concepts from Non-linear Optics

To describe an optical non-linearity, we can consider the dependence of the dipole moment per unit volume, or polarisation $P(t)$, of a material system on the electric field amplitude $E(t)$ of an applied optical field. In linear optics, the induced polarisation is directly proportional to the electric field strength, described by the relationship $P(t) = \chi^{(1)}E(t)$, where $\chi^{(1)}$ is the linear susceptibility. However, in non-linear optics, the polarisation can be described as a power series in the field strength

$$P(t) = \chi^{(1)}E(t) + \chi^{(2)}E^2(t) + \chi^{(3)}E^3(t) + \ldots, \tag{2.1}$$

here, $\chi^{(2)}$ and $\chi^{(3)}$ represent the second- and third-order non-linear optical susceptibilities, respectively. These coefficients quantify the non-linear response of the material to the applied optical field. Equation 2.1 uses tensor notation to describe the anisotropic medium. The susceptibility $\chi^{(n)}$ is a tensor of the $n+1$ rank. The magnitude of these tensors rapidly decreases with increasing rank ($\chi^{(1)} : \chi^{(2)} : \chi^{(3)} \sim 1 : 1^{-12} : 1^{-24}$) [68]. This reduction in magnitude means that as the order of non-linear interaction increases, the optical power required to observe the process increases drastically. Therefore, higher order non-linear processes, like $\chi^{(3)}$ often necessitate the use of pulsed light [69].

The even-order non-linear processes require materials that lack inversion symmetry within their crystal structure [68]. In centrosymmetric crystals, which have a centre of inversion, polarisation vectors at pairs of points related by inversion are equal in magnitude but opposite in sign, leading to a net zero overall contribution. To observe even-order non-linear processes, non-centrosymmetric crystals are essential.

2.3 Electro-optic modulation

Electro-optic modulation is a technique enabling the manipulation and control of light using an electrical signal. This modulation scheme involves altering the properties of light, such as its intensity, phase, or polarisation, to encode and transmit information or perform various light manipulation tasks. This technique finds its use in laser stabilisation [70–72], synchronisation of atomic clocks [73] and as a frequency reference [74].

Frequency conversion arises from the modulation of the refractive index of the medium, along one or more axes, proportional to an externally applied electric field at a given optical frequency. This modulation alters the optical path of the light modes propagating through the medium, producing

sidebands equidistantly spaced in the frequency domain, with the spacing set by the modulation frequency. This phenomenon is known as the Pockels effect or the linear electro-optic effect. The relationship between the index of refraction and the applied electric field is described as [75]

$$\vec{n}(\vec{E}) = \vec{n}_0 + \frac{\chi^{(2)}}{2\vec{n}_o\epsilon_o}\vec{E}, \tag{2.2}$$

where $\vec{n}$ is the vector of the resulting refractive index in a birefringent material, emphasising directionality. $\vec{n}_0$ represents the refractive index vector in the absence of an applied electric field, underlining the direction-dependent nature of refractive indices in such materials. $\chi^{(2)}$ is the second order electric susceptibility tensor of the medium, ϵ_o is vacuum permittivity, and $\vec{E}$ is the applied electric field vector. The Pockels effect can be utilised to modulate an electric field propagating through an appropriate non-centrosymmetric crystal [75].

For our application (OFCG for wavelength agnostic pulse generation), we apply a modulation voltage $V\sin(\omega_m t)$ across the non-linear crystal. This introduces an internal electric field

$$E_m = A\sin\omega_m t, \tag{2.3}$$

where A is the peak amplitude, and ω_m is the modulation frequency. This internal electric field, E_m, modulates the refractive index of the medium but only along a specific axis. The electric field component of the optical field after passing through the modulator, aligned with this axis, is given by

$$E_{out} = \mathcal{E}_{in}\exp\{[i\,(\nu_0 t + \delta\sin\omega_m t)]\}, \tag{2.4}$$

where E_{out} is the amplitude of the optical electric field, ν_0 is that field's

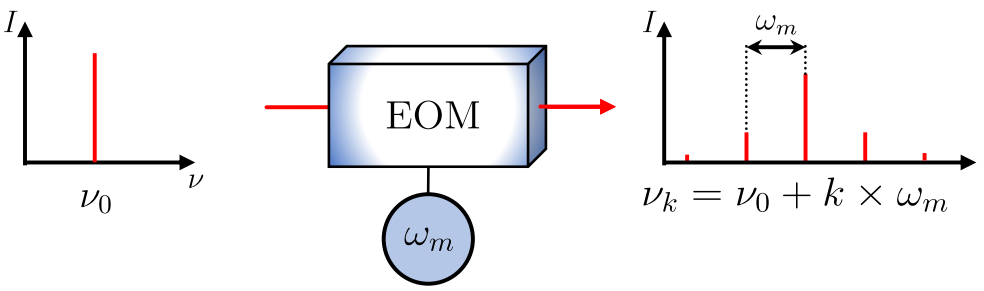

Figure 2.1: Single frequency light propagates through an EOM modulated with frequency ω_m. This process results in transferring energy from the central mode ν_0 into sidebands separated by the frequency ω_m

frequency, and δ is the modulation depth determined from

$$\delta = \frac{\pi V}{V_\pi}, \tag{2.5}$$

where V is the maximum voltage, and V_π is the half-wave voltage for the EOM crystal. The latter is a parameter depending on $\chi^{(2)}$ of the material and the waveguide structure of the modulator.

The applied electric field modulates the phase of the optical field, transferring energy from the central frequency into sidebands at $\pm k\omega_m$. This phenomenon is illustrated in Fig. 2.1, where a single frequency light undergoes a phase modulation. The resulting spectrum produced by the EOM can be expanded by using Bessel function identities [76]

$$E_{out} = \mathcal{E}_{in}\left[\sum_{k=0}^{\infty} J_k(\delta)\exp\{ik\omega_m t\} + \sum_{k=1}^{\infty}(-1)^k J_k(\delta)\exp\{-ik\omega_m t\}\right]\exp\{i\nu_0 t\}, \tag{2.6}$$

where $J_i(j)$ is the Bessel's function of the first kind of order i, and k represents sideband order, with $k = 0$ being the central frequency mode. In the frequency domain, the relation between the frequencies of modes k and $k+1$

is given by

$$\nu_{k+1} - \nu_k = \omega_m. \tag{2.7}$$

The result shown in this section will be used in Chapters 3 & 4 as a basis for the behaviour of the crystal used in the OFCG.

2.4 Generation of photon pairs

Non-classically correlated photon pairs are fundamental resources in quantum information science and technology, finding applications in quantum communications, computations, sensing, and investigations into the fundamental rules of quantum mechanics [77–79]. In this section, we will explore two distinct methods for generating photon pairs, SPDC and SFWM. The primary motivation of our research is to employ these photon pairs in a quantum-enhanced LIDAR scheme, where one of the generated photons (called the idler) heralds the presence of the other photon (the signal). Both SPDC and SFWM processes occur spontaneously. This spontaneity is advantageous for LIDAR as the probabilistic generation means the photon statistics in the signal mode appear as a thermal source to an observer without access to the idler photon counts [80, 81]. Additionally, this inherent randomness aligns with our application, where photons need to be generated at unpredictable intervals. To make the quantum-enhanced LIDAR practical, we aim to use silicon-based single photon avalanche detectors (SPADs). These devices have a high quantum efficiency, typically over 40% at wavelengths used in this work, and always more than 10% throughout the visible to near-infrared spectrum due to the silicon band-gap properties [82]. Thus, our focus remains on methods capable of generating photons in the wavelength range of 400 to 1000 nm.

The generation of non-classically correlated photon pairs through SPDC and SFWM relies on two different non-linear processes, namely second-order

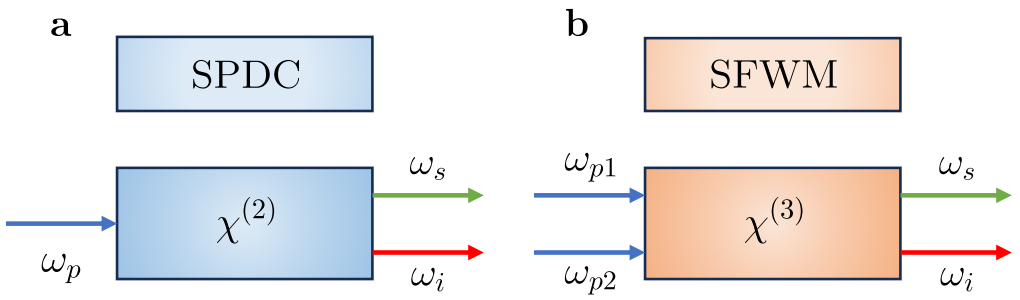

Figure 2.2: **a** Process of SPDC, here a pump photon ω_p interacts with the non-linear medium exhibiting second-order non-linearity to generate pair of signal ω_s and idler ω_i photon pair. **b** Process of SFWM, where two pump photons ω_{p1} & ω_{p2} interact with a third-order non-linear medium to generate a photon pair.

($\chi^{(2)}$) and third order ($\chi^{(3)}$) respectively, as shown in Fig. 2.2. SPDC is a $\chi^{(2)}$ non-linear process which involves a higher-frequency pump (ω_p) photon giving rise to two lower-frequency photons (ω_s and ω_i) - Fig. 2.2**a**. This process can occur in non-linear materials which lack the inversion symmetry, such as Lithium Triborate (LBO) [83], Beta Barium Borate (BBO) [84], Lithium Niobate (LN) [85], periodically poled Potassium Titanyl Phosphate (ppKTP) [86] and periodically poled Lithium Niobate (ppLN) [87]. Depending on the properties of the non-linear material, SPDC is classified into three categories.

- Type-0, where the pump, signal, and idler have the same polarisation.
- Type-I, where the pump has orthogonal polarisation to the signal and idler pair.
- Type-II, where signal and idler photons have orthogonal polarisation.

In SFWM - Fig. 2.2**b**, two pump photons (ω_{p1} and ω_{p2}) interact within a non-linear medium to create signal and idler photons. Experimental demonstrations of SFWM often use a degenerate pump, where instead of utilising two distinct pump frequencies (as shown in Fig. 2.2**b**), a single strong pump

frequency is employed. This approach is motivated by the experimental simplicity of using a single laser. From discussions in Section 2.2, we know that the $\chi^{(3)}$ processes require significantly more power than $\chi^{(2)}$ processes. Because of this, pulsed light sources are often used to generate photons in the process of SFWM [88]. Alternatively, CW pumped microring cavities can be used to achieve SFWM [89]. SFWM can occur in various media, such as atomic ensembles [90, 91], single-mode birefringent fibers [92, 93], photonic crystal fibres [94, 95] and silicon-on-insulator waveguides [96, 97]. Photon pairs generated in waveguides have well-defined spatial modes, allowing for the highly efficient integration into optical fibre networks used in quantum-key distribution [98] and quantum networks [99].

The state generated in the processes of SFWM and SPDC can be expressed in the Fock basis as [100]

$$\frac{1}{\sqrt{1+\bar{n}}}\sum_{n=0}^{\infty}\left(\frac{\bar{n}}{1+\bar{n}}\right)^{\frac{n}{2}}|n,n\rangle, \tag{2.8}$$

where $|n,n\rangle$ denotes the state with n photons in each of the two modes. Specifically, $|n_{\mathrm{S}},n_{\mathrm{I}}\rangle$ represents the number of photons in the signal (n_{S}) and idler (n_{I}) modes, respectively. Each of the modes individually has mean photon number $\bar{n}=\sinh^2 r$ with r as the squeezing amplitude which depends on the nonlinearity of the crystal and the intensity of the pump light. Due to weak nonlinearities, typically the parameter $r << 1$ and hence the probability of generating states with more than one signal & idler photons is small. Research in this thesis focuses on the low intensity regime of the pump where the probability of generating multi-photon states can be neglected.

Both the SPDC and SFWM processes abide by fundamental conservation laws of energy and momentum. In SPDC, the total energy of the signal and idler photons combined must equal the energy of the pump photon. Similarly, in SFWM, the sum of the energies of the two pump photons must be equal to the energies of the signal and idler photons. Furthermore, the total

momentum of the signal and idler photons must balance with the momentum of the pump photons in both processes.

In mathematical terms, the conservation laws of SPDC process can be expressed as

$$\omega_p = \omega_s + \omega_i, \tag{2.9a}$$

$$\vec{k}_p = \vec{k}_s + \vec{k}_i, \tag{2.9b}$$

where $\vec{k}_{p,s,i}$ are the wave vectors of the pump, signal and idler photons, respectively. Similarly, these laws for the SFWM process can be expressed as

$$\omega_{p_1} + \omega_{p_2} = \omega_s + \omega_i \tag{2.10a}$$

$$\vec{k}_{p_1} + \vec{k}_{p_2} = \vec{k}_s + \vec{k}_i \tag{2.10b}$$

To satisfy the momentum conservation phase matching is required. Phase matching ensures that the interacting waves involved in the non-linear process propagate with the same phase velocities, allowing for constructive interference [101].

2.4.1 Phase matching

For many non-linear optical processes, such as harmonic generation, it is essential to minimise the wave-vector mismatch in order to maximise the efficiency of non-linear interaction. The wave-vector mismatch, denoted by $\vec{\kappa}$, represents the difference between the wave vectors of the interacting waves

$$\vec{\kappa} = \sum_i \vec{k}_i. \tag{2.11}$$

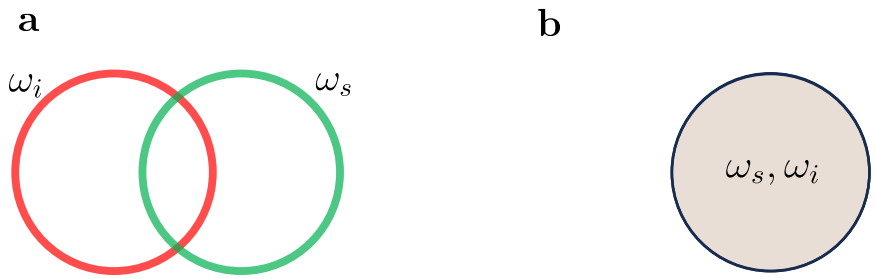

Figure 2.3: **a** Non-collinear output of an SPDC process, where the signal (ω_s) and idler (ω_i) photons are emitted from the non-linear crystal as two cones. **b** Collinear output of the SPDC process, where signal and idler beams are concentric and overlapped.

Minimising this mismatch is achieved by adjusting the propagation direction and polarisation properties of the waves [68, 101], as well as manipulation of the properties of the non-linear medium [102].

Certain techniques can be employed to achieve phase-matching. In the case of birefringent non-linear materials, phase-matching can be achieved by ensuring that the interacting waves possess a suitable combination of ordinary and extraordinary polarisation. This technique utilises the inherent birefringence of the material to compensate for the wave-vector mismatch.

2.5 Type-II Spontaneous Parametric Down Conversion in periodically-poled crystals

Spontaneous parametric down-conversion (SPDC) is a second-order ($\chi^{(2)}$) non-linear process, resulting in the generation of entangled photon pairs. In type-II SPDC, the pump photon (ω_p) interacts with a non-linear crystal, and two daughter photons, signal (ω_s) and idler (ω_i) are produced.

To conduct experiments in Chapter 5 and 6, we have selected a periodically-polled KTP crystal (ppKTP) and a pump wavelength of 405 nm. The choice

of the ppKTP crystal was motivated by its capability to facilitate the generation of wavelength-degenerate photon pairs through collinear Type-II SPDC. Notably, photon pairs generated through this process possess orthogonal polarisation states, rendering them easily separable by use of polarising beam splitter and ideal for performing coincidence measurements. The benefit of generating photon pairs that are degenerate in wavelength is that SPAD detectors used in the experiments described in Chapters 5 and 6 will have the same efficiency of detecting both signal and idler photons. Moreover, the crystal's collinear output permits straightforward fibre coupling into detectors, simplifying our experimental setup significantly. Figure 2.3 shows the difference between the collinear and non-collinear outputs of the SPDC process. As for the pump wavelength, we chose 405 nm to generate degenerate photon pairs at wavelengths suitable (810 nm) for detection using the silicon-based SPADs. This specific wavelength was selected due to the availability and cost efficiency of 405 nm laser diodes. These diodes are an industry standard, widely used in Blu-ray disc technology, making them a cost-effective choice for our experimental setup.

To describe the SPDC phenomenon mathematically, we consider the principles of energy conservation and momentum conservation [103], shown in Fig. 2.4. Energy conservation law can be expressed with Eq. 2.9a and the momentum conservation equation for SPDC can be written as

$$\vec{k}_p = \vec{k}_s + \vec{k}_i + \kappa, \tag{2.12}$$

where $\vec{k}_p$ is the wave vector of the pump photon, $\vec{k}_s$ and $\vec{k}_i$ are the wave vectors of the signal and idler photons, and κ is the phase mismatch.

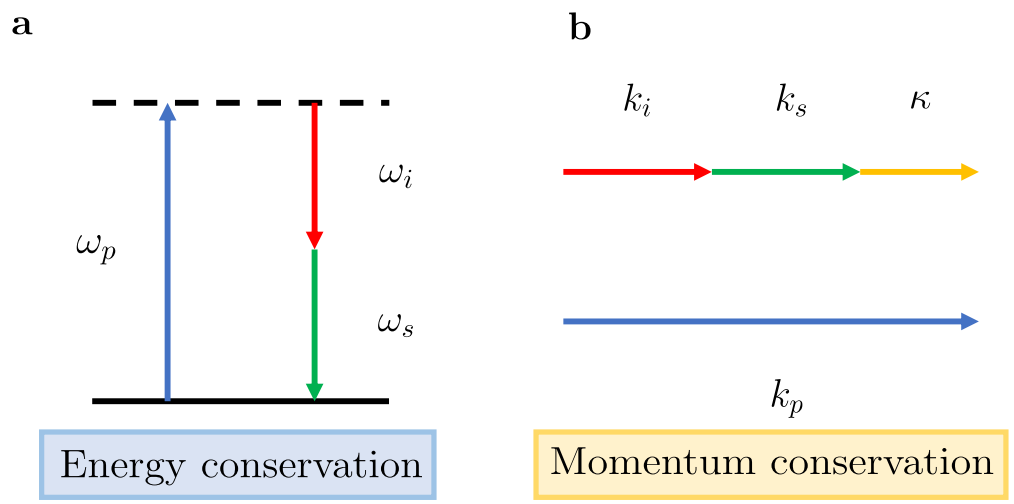

Figure 2.4: Diagram depicting the principles of **a** energy conservation (Eq. 2.9a), where the energy of the pump photon (ω_p) is equal to the combined energies of the signal (ω_s) and idler photons (ω_i), and **b** momentum conservation (Eq 2.9b) where momentum of the pump photon (k_p) is equal to the combined wave vectors of idler photon (k_i) and signal photon (k_s) and phase mismatch $\kappa = \frac{2\pi}{\Lambda}$ where Λ is the poling period of the non-linear crystal (See Section 2.5.1). Here the wave vectors are aligned in the same direction. Thus, their magnitudes can be added as scalars, simplifying the conservation of momentum equation.

2.5.1 Quasi Phase-Matching

From section 2.4.1 we know that for non-linear processes to be observed efficiently, the sum of wave vectors and phase mismatch needs to equal 0. This problem can be solved by either adjusting the wave vectors of the pump, signal and idler to counteract the influence of κ or by tailoring the material so that the κ allows for the Eq. 2.12 to be fulfilled. The latter can be achieved by utilising the technique known as Quasi-Phase-Matching (QPM) [102]. Unlike birefringent phase-matching, which relies on the natural asymmetry of the crystal lattices to satisfy the phase-matching condition, QPM utilises crystals that have undergone process called domain engineering to create a designed poling structure, shown in Fig. 2.5**a**. These crystals are typically made to produce light fields in a collinear manner, where the pump, signal and idler

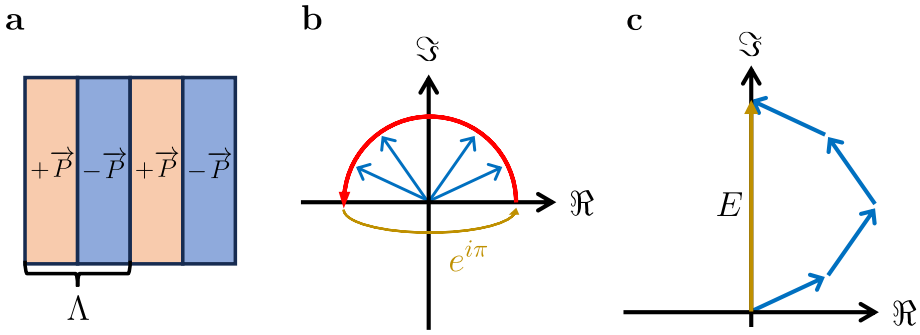

Figure 2.5: **a** Poling structure of a periodically polled crystal. Here each domain (red and blue) is prepared in such a way that the positive and negative charges swap periodically. As a result a polarisation vector $\overrightarrow{P}$ flips as well, which leads to an effective π phase shift between the electric fields. **b** Effect of QPM on the phase experienced by the electric field E propagating through the crystal. Thanks to the occurrence of a π phase shift, the phase is reset every poling period Λ. **c** Effect of the QPM on the electric field.

are all travelling along the same direction. This has the advantage of easier collection of photon pairs since the placement of collection optics at opposite angles on cones, as used in some other methods, can be challenging.

The key principle behind QPM is the introduction of a periodic poling structure inside the crystal. This structure involves swapping the positive and negative charges in the crystal lattice with a certain period Λ, resulting in a change in the crystal's polarisation. The periodic flipping of the crystal structure introduces a π phase shift between the crystal's polarisation and the electromagnetic waves each time the structure changes from one domain to another.

By introducing a π phase shift at the precise point where the collective phase mismatch reaches π, the overall phase shift is reset to 0. This allows the field to grow throughout the crystal, as the destructive interference resulting from different phases is overcome. This process is shown in Fig. 2.5**b-c**. The technique of periodically poling the crystal structure is referred to as domain engineering, and each section of one polarisation within the poling period is

called a domain [104]. Thus, one poling period contains two domains with opposite polarisation's.

Because the poling crystal structure can introduce a phase shift of exactly π, the most effective scheme to build up the field while the light is propagating through the crystal is to introduce this phase shift whenever the fields have just collected a π phase mismatch. With this information, calculating the poling period becomes straightforward. The length within which the electromagnetic waves, with phase mismatch κ, have collected π in phase shift is $l = \frac{\pi}{\kappa}$. As, such the poling period, comprised of two domains, equals

$$\Lambda = \frac{2\pi}{\kappa}, \tag{2.13}$$

if we inject this into Eq. 2.12

$$k_p = k_i + k_s + \frac{2\pi}{\Lambda}, \tag{2.14}$$

This new phase-matching condition depends on the poling period Λ. If we now rewrite the Eq. 2.14 in terms of the wavelength

$$\frac{n_p}{\lambda_p} = \frac{n_s}{\lambda_s} + \frac{n_i}{\lambda_i} + \frac{1}{\Lambda}, \tag{2.15}$$

where n_j represents the temperature dependant index of refraction for the pump, signal and idler. From Eq. 2.9 expressed in terms of wavelength we have $\lambda_s = (1/\lambda_p - 1/\lambda_i)^{-1}$, this allows to reduce the phase-matching problem to

$$\frac{n_p}{\lambda_p} = n_i \left(\frac{1}{\lambda_p} - \frac{1}{\lambda_i} \right) + \frac{n_i}{\lambda_i} + \frac{1}{\Lambda}. \tag{2.16}$$

Now the only thing left is to include the temperature T dependence which for ppKTP crystal used in Chapters 5 & 6 can be extracted from [105] and

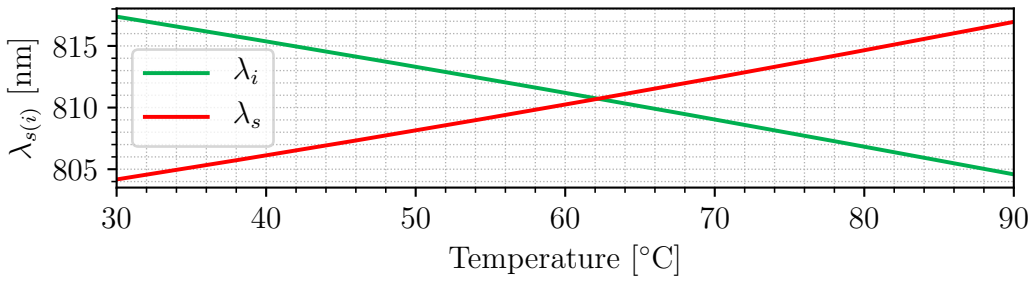

Figure 2.6: Resulting theoretical signal (λ_s) and idler (λ_i) wavelengths generated in a ppKTP crystal with poling period of $\Lambda = 10$ μm pumped with $\lambda_p = 405.36$ nm as a function of crystal temperature.

its impact on the length of the poling period Λ is given by

$$\Lambda = \Lambda_0 \left(1 + \alpha(T - 25°\text{C}) + \beta(T - 25°\mathbf{C})^2\right), \tag{2.17}$$

where $\alpha = 6.7 \times 10^{-6}$ °C and $\beta = 11 \times 10^{-9}$ °C [105]. In addition to the poling period, the crystal temperature influences the refractive indices. In the ppKTP crystal used in the experiments described in Chapters 5 & 6 the pump and signal are both polarised in the y direction, while the idler is polarised along the z. The room temperature values of the corresponding refractive indices are given by the following Sellmeier equations [106]

$$n_y^2 = 3.45018 + \frac{0.04341}{\lambda^2 - 0.04597} + \frac{16.98825}{\lambda^2 - 39.43799}, \tag{2.18a}$$

$$n_z^2 = 4.59423 + \frac{0.06206}{\lambda^2 - 0.04763} + \frac{110.80672}{\lambda^2 - 86.12171}. \tag{2.18b}$$

The variation of the refractive index with temperature can be expressed as

$$\Delta n(\lambda, T) = n_1(\lambda)(T - 25°\text{C}) + n_2(\lambda)(T - 25°\text{C})^2, \tag{2.19}$$

where coefficients $n_{1,2}$ are written as a third order polynomial

$$n_{1,2}(\lambda) = \sum_{m=0}^{3} a_m \lambda^{-m}, \tag{2.20}$$

and values of a_m can be found in Table 2.1. Together if we substitute all of these values into Eq. 2.16 together with the chosen poling period of the ppKTP crystal $\Lambda = 10$ μm and solve for the measured pump wavelength $\lambda_p = 405.36$ nm (See Chapters 5 & 6), we can obtain the resulting signal and idler pair wavelengths as a function of the crystal temperature in Fig. 2.6. This shows that the target temperature for generating degenerate and collinear photon pairs is 63°C.

It is worth mentioning that the situation presented in this Section assumes a perfectly monochromatic pump. However, in practice, the pump has a spectral bandwidth that broadens the spectra of the signal and idler photons [107].

	y polarisation		z polarisation	
	n_1 [10^{-6}]	n_2 [10^{-8}]	n_1 [10^{-6}]	n_2 [10^{-8}]
a_0	6.2897	-0.14445	9.9587	-1.1882
a_1	6.3061	2.2244	9.9228	10.459
a_2	-6.0629	-3.5770	-8.9603	-9.8136
a_3	2.6486	1.3470	4.1010	3.1481

Table 2.1: Coefficients for KTP refractive index dependence on temperature

2.5.2 Photon statistics

The strong temporal correlation between the signal and idler arms manifests as a high probability of detecting a signal photon and an idler photon simultaneously [108].

Let us consider a situation in which the third party (an observer), does not have access to idler stream, and can only detect the signal photons. In such case, the photon statistics of the signal mode P_n^s appear to follow a thermal distribution [80, 81]

$$P_n^s = \sum_{n=0}^{\infty} \frac{\nu^n}{(\nu+1)^{(n+1)}}, \tag{2.21}$$

where $\nu = \sinh^2|r|$ and r is a parameter proportional to the pump amplitude and $r << 1$ [100]. This distribution resembles a thermal distribution with pump power as a parameter controlling the average photon number. From [80] we know that the photon statistics of the signal mode are indistinguishable from the photon statistics of a thermal source with temperature

$$T_s = \frac{\hbar \frac{c}{\lambda_s}}{2k_B \ln(\coth|r|)}, \tag{2.22}$$

where $\hbar$ is reduced Planck's constant, k_B is Boltzmann's constant and c is speed of light in the vacuum. Using the Equation 2.22 we can calculate that to match the temperature on the surface of the Sun (6000 K) for a wavelength of 810 nm the r parameter would have to be above 1.

The lack of access to the idler stream and the resulting thermal-like photon statistics in the signal mode offer a remarkable advantage in applications such as covert LIDAR. However, this advantage is maximised when the mean signal rate is small compared to the environmental background level. In such scenarios, the observer can not distinguish the signal photons from the general thermal background. This covert operation capability allows for enhanced security and confidentiality, as the signal photons remain indistinguishable from the thermal background. Nonetheless, a sudden surge in thermal background at specific wavelengths, could potentially raise suspicions, thereby highlighting the importance of maintaining a balanced signal rate.

2.5.3 Optimal focusing parameter

Coincidence detection plays a pivotal role in quantum-enhanced LIDAR, as discussed in Section 1.1.2.1, enabling the rejection of background level and

enhancing the sensitivity of measurements. To perform coincidence detection efficiently, it is imperative to detect photons generated in the process of colinear SPDC with high efficiency. As our LIDAR system relies on fiber-coupled single-photon detectors, it becomes crucial to maximise the fiber-coupling efficiency of these single photons.

The efficiency of fiber coupling is significantly influenced by the focusing parameter ϑ involved in the colinear SPDC process [109]. Optimising this focusing parameter is of paramount importance to maximise the probability of both photons of a pair being efficiently coupled into single-mode fibers.

The focusing parameter can be expressed as [109]

$$\vartheta = \frac{L}{z_R}, \tag{2.23}$$

where L represents the length of the crystal used in the SPDC process, and z_R denotes the Rayleigh range

$$z_R = \frac{\pi w_0^2}{\lambda}, \tag{2.24}$$

where w_0 is the beam waist and λ is the wavelength of the pump beam used in the SPDC process.

Previous theoretical and experimental studies have shown that the optimal focusing parameter of the pump and resulting pair beams should fall within the range of $1 < \vartheta < 3$ [109]. Staying within this range ensures efficient coupling of the generated photon pairs into single-mode fibres. Deviating from this range may result in a reduced coupling efficiency, negatively impacting the performance of the quantum-enhanced LIDAR.

Numerical calculations were performed to determine the optimal focusing parameter. The wavelength of the pump is 405 nm, and for the resulting pair, it is 810 nm. The crystal length is predetermined at 10 mm. This leaves the beam waist of the pump/pair as the only variable. Using Eq. 2.23, we

have calculated that for optimal fibre coupling of the photon pairs resulting from the SPDC process, the pump/pair beam has to have a waist of 30 μm $< w_0 <$ 35 μm.

2.6 Spontaneous Four Wave Mixing in birefringent fibers

Spontaneous four-wave mixing is a third-order $\left(\chi^{(3)}\right)$ non-linear optical process, which occurs in all-optical materials - including optical fibers [92, 93]. In this process, two strong optical fields (ω_{p1} and ω_{p2}) are converted to two distinct light fields at other wavelengths (typically called *signal* at higher angular frequency ω_s and the *idler* at the lower angular frequency ω_i). Generation of photon pairs in an optical fibre has the advantages of well defined spatial mode which is beneficial for the purpose of quantum-enhanced LIDAR as it simplifies the detection process. The process of SFWM is shown in Fig. 2.7. Commonly, the two pump fields are chosen to be degenerate in the frequency domain (ω_p), so that the process can be sustained using a single high-power laser. If a beam of light, at either signal or idler frequency, will be launched into the fibre together with the pump beam - it will be amplified. When both signal and idler modes are initially empty, a spontaneous four-wave mixing process is seeded by quantum vacuum noise - signal and idler modes appear in the spectrum as sidebands, equidistantly spaced in frequency about the degenerate pump peak [92].

At the quantum level, this process can be seen as the virtual absorption of two pump photons (p), polarised along one of the principal axes of a birefringent fibre (slow or fast), and creation of a photon pair - signal (s) and idler (i), polarised along the opposite fiber axis. Because of the nearly instant response of $\chi^{(3)}$ Kerr non-linearity in an optical fiber, detection of one photon from the newly created pair (usually lower energy idler), heralds generation of the

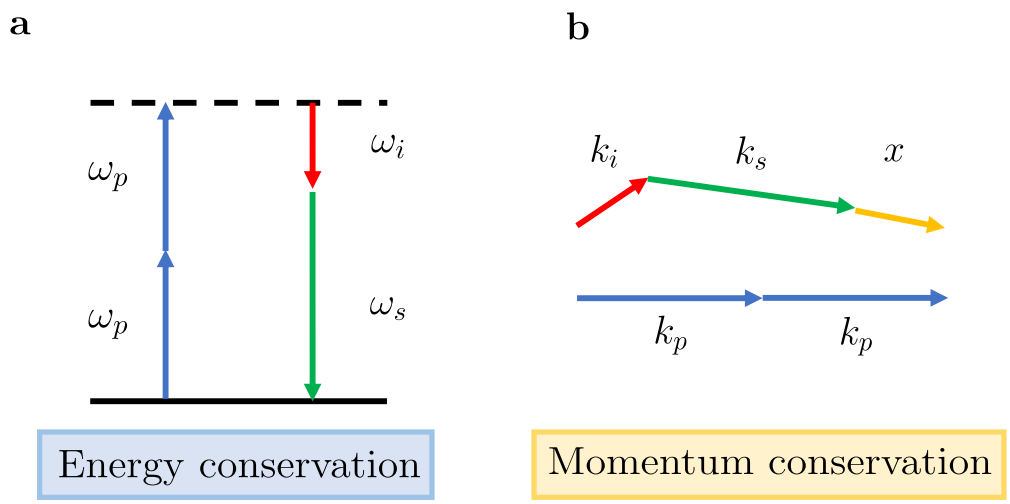

Figure 2.7: Diagram depicting the principles of **a** energy conservation and **b** momentum conservation. In **b** $x = \frac{2}{3}\gamma P_p$ and represents the correction to the phase mismatch from Eq. 2.26

signal photon [92].

Frequencies of the signal and idler photons that result from the SFWM process are determined by energy conservation

$$2\omega_p = \omega_s + \omega_i, \tag{2.25}$$

and phase-matching contour

$$\kappa = k_s + k_i - 2k_p + \frac{2}{3}\gamma P_p, \tag{2.26}$$

where, κ is the phase mismatch between the propagation constants of the signal, idler and two pump waves - caused by the chromatic dispersion in the fibre, with $k_j = \frac{n_j \omega_j}{c}$ $(j = s, i, p)$ for a light wave with angular frequency ω_j propagating in the medium with refractive index n_j. Only when κ is near zero, the average probability of generated photon pair will increase along the entire length of the fibre [92]. The $\frac{2}{3}\gamma P_p$ term in Eq. 2.26 is a correction to the phase mismatch resulting from self-phase and cross-phase modulations

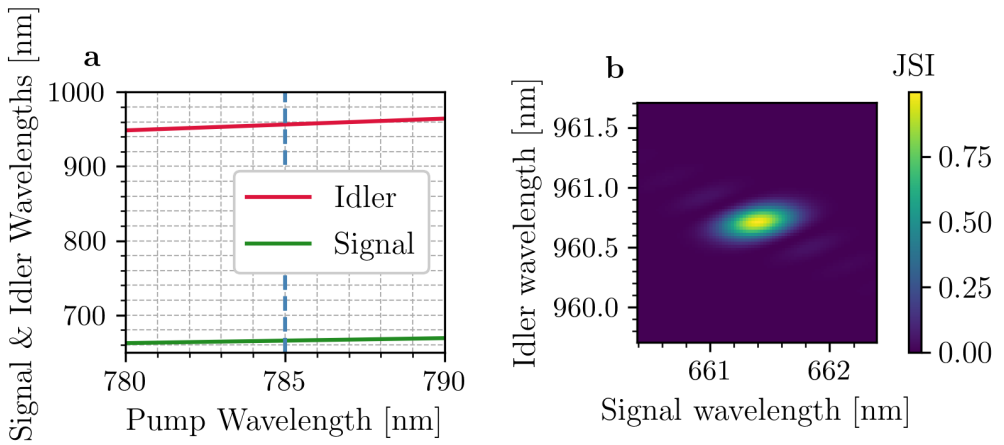

Figure 2.8: **a** Theoretical birefringent phase-matching contour as a function of the pump central wavelength λ_p. Signal wavelengths are marked in green, and idler wavelengths are marked in red with a blue dotted line marking the central frequency of the pump used in Chapter 4. Values for the Fibercore HB800G optical fibre, operating in normal regime $\Delta n = 4.3 \times 10^{-4}$ [49]. **b** Resulting joint spectral intensity of the generated signal & idler pair, with purity of 71%, fibre is assumed to be $L = 10$ cm long and the pump is assumed to be the output of the OFCG described in Section 3.9.

of the intense pump pulse, here P_p is the peak power of the pump and γ is the non-linear coefficient of the fibre [92]

$$\gamma = \frac{2\pi n_2}{\lambda_p A_{\text{eff}}}, \tag{2.27}$$

where λ_p is the pump central wavelength, A_{eff} is the effective cross-sectional area of the fiber mode, and n_2 is the non-linear refractive index of the material.

In order to generate photon pairs compatible with Si-SPADs, we have chosen the centre wavelength of the pump to be $\lambda_0 = 785$ nm. For that pump wavelength, the fiber exhibits normal dispersion, where longer wavelength components of the laser pulse travel faster than shorter wavelength components (this situation is reversed for longer wavelengths operating in an anomalous dispersion regime). While operating in a normal dispersion regime, where

$2k_p < k_s + k_i$, the non-linear term increases the phase mismatch. Because of that, higher order dispersion terms become relevant, and phase-matching can be realised close to the zero dispersion for large separation of the signal and idler wavelengths.

The contribution of the dispersion, both material and waveguide, and the birefringence of the optical fibre to the phase-matching condition can be seen, if we write Eq. 2.26 as [110]

$$\kappa = 2k_p - k_s - k_i + 2\Delta n\frac{\omega_p}{c} + \frac{2}{3}\gamma P_p, \tag{2.28}$$

where Δn is the difference between the effective refractive indices along the fast and slow axis of the fibre. Wavelengths simultaneously satisfying Eq. 2.25 and Eq. 2.26 are plotted in Fig. 2.8**a** The quantum state of generated signal & idler photon pairs, can be expressed as [92]

$$|\Phi\rangle = \int\int d\omega_s d\omega_i f(\omega_s, \omega_i)\hat{a}_s^\dagger(\omega_s)\hat{a}_i^\dagger(\omega_i)\,|0,0\rangle\,, \tag{2.29}$$

where $\hat{a}_j^\dagger$ $(j = s, i)$ is the creation operator for signal and idler modes respectively, and $f(\omega_s, \omega_i)$ is the joint spectral amplitude of the photon pair, approximately equal to [110]

$$f(\omega_s, \omega_i) \approx \alpha(\omega_s + \omega_i) \cdot \phi(\omega_s, \omega_i), \tag{2.30}$$

where $\alpha(\omega_s + \omega_i)$ is the pump envelope function,

$$\alpha(\omega_s + \omega_i) = \exp\left[-\frac{(\omega_s + \omega_i - 2\omega_p)^2}{4\sigma_p^2}\right], \tag{2.31}$$

and $\phi(\omega_s, \omega_i)$ is phase-matching function,

$$\phi(\omega_s, \omega_i) = \mathrm{sinc}\left(\frac{\kappa L}{2}\right)\exp\left(\frac{i\kappa L}{2}\right). \tag{2.32}$$

To understand the state of generated photon pair, evaluation of the joint spectral intensity (JSI) is essential. The JSI, $|f(\omega_s, \omega_i)|^2$, represents a two-dimensional probability distribution associated with signal and idler emission frequencies, and allows us to characterise spectral and temporal characteristics of the output bi-photons. The shape of the JSI can be controlled by carefully choosing pump bandwidth σ_p, length of the fibre L and the angle θ_{si} phase-matching function $\phi(\omega_s, \omega_i)$ makes with the ω_s axis - this angle is dependant on higher order dispersion properties of the fiber (group velocities of pump, signal and idler photons). Simulation of the FWM process is shown in Fig.2.8**b**. In addition, it can be shown (using a truncated Taylor expansion) that the full-width half-maximum (FWHM) bandwidth of the signal and idler fields, is given by [92]

$$\Delta\omega_{s(i)} = \frac{2\pi c}{\left|\mathcal{N}_{s(i)} - \mathcal{N}_{i(s)}\right| L} + 2\left|\frac{\mathcal{N}_{i(s)} - \mathcal{N}_p}{\mathcal{N}_{s(i)} - \mathcal{N}i(s)}\right| \Delta\omega_p, \tag{2.33}$$

where $\mathcal{N}_j (j = s, i, p)$ are the group indices for signal, idler and the pump, given by $\mathcal{N}_j = (\omega_j \frac{\delta n_j}{\delta \omega}\Big|_{\omega_j} + n_j)$. The first term in Eq. 2.33 shows that a finite bandwidth exists even for the perfectly monochromatic pump, due to the finite length of the optical fibre L. If L were to be increased, as a result, the phase mismatch would reduce - which would lead to a decrease in the bandwidth over which signal & idler photons are generated. The number of idler photons generated scales quadratically as a function of the pump power P_p, and fibre length, i.e. $N_i \propto L^2 P_p^2$ [111].

2.6.1 Spectral Purity

In the ideal case of pure state generation, the joint spectral amplitude (JSA) of the output signal and idler photon pair, should be separable - $f(\omega_s, \omega_i) = S(\omega_s)I(\omega_i)$. Here functions $S(\omega_s)$ and $I(\omega_i)$ represent spectral amplitudes of the signal and idler separately.

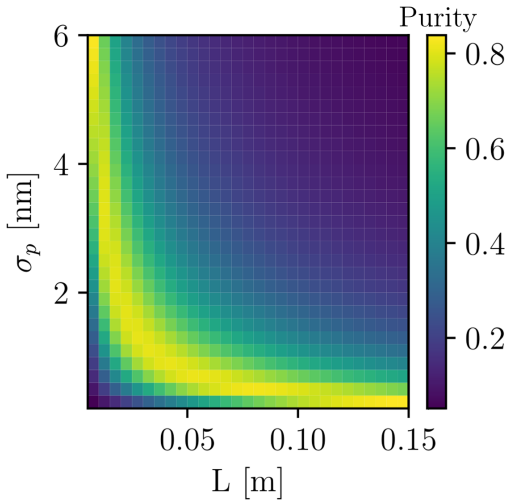

Figure 2.9: Theoretical purity as a function of pump bandwidth σ_p and fiber length L.

To quantify the degree of inseparability - the degree of correlation between signal and idler modes; Schmidt decomposition of the JSA can be utilised [112]. The resulting cooperativity parameter K represents the number of modes excited by SWFM. An ideal pure state has the cooperativity parameter $K = 1$. Purity of the state can be expressed by inversion of the cooperativity parameter $\mathcal{P} = 1/K$ [112]. The purity in our case is mainly dependent on σ_p and L choice. The theoretical purity of a state generated in process of SFWM described in the previous section was plotted in Fig. 2.9.

2.7 Optimisation of an OFCG Heralded Photon Source

As was mentioned in section 2.4, to obtain photon pairs for quantum illumination in the process of SFWM in a birefringent fiber, a pulsed light source is preferred. Pulsed sources offer distinct advantages over continuous-wave sources, as they provide temporal confinement of energy, facilitating efficient SFWM interactions.

To enable the successful operation of quantum-enhanced LIDAR, it is essential for the pair detection rate to surpass the dark count rate of the SPADs utilised in Chapters 5 and 6, which typically hovers around 250 Hz [113]. Consequently, a minimum pair detection rate of 1 kHz was chosen to ensure efficient detection and reliable performance.

The rate of photon pair production in SFWM is dependent on the fibre length (L) and peak power per pulse (P_{pk}). The relationship between the pair production rate (N) and these parameters can be described as follows [110]

$$N \propto L^2 \cdot P_{\text{pk}}^2. \tag{2.34}$$

This scaling law demonstrates that longer fibres and higher peak powers per pulse result in increased pair production rates.

OFCG offer unique advantages over conventional mode-locked lasers, such as Ti:Sapphire lasers, for SFWM applications. The coupled cavity OFCGs provide flexibility in choosing the central wavelength of the pulse, allowing tailored generation of photons at desired wavelengths. Additionally, OFCGs enable the generation of high repetition rates of pulses, which are challenging to achieve with traditional mode-locked lasers. By producing ∼GHz trains of pulses with lower peak power per pulse, OFCGs enable covert operation by spreading the photon generation probability over a broader temporal range.

To estimate our expected pair detection rate we scale experimental data from [49], featuring a commercial pulsed Ti:Sapphire laser generating bandwidth-limited pulses with $\Delta\lambda = 3$ nm centred at 704 nm, with a repetition rate $R_r = 80$ MHz. For an $L_c = 10$ cm fibre, pair rates of $N_{\text{exp}} = 23000$ pairs/s are obtained from an average power of 15 mW. Assuming sech^2 pulse shape (expected from this type of a mode-locked system), this corresponds to a pulse width of 0.17 ps with a peak pulse power of $P_{\text{pk,ref}} = 1.1$ kW. The pair detection rate per pulse (α) can be determined as N_{exp}/R_r. Thus, the

predicted pair detection rate using an OFCG can be expressed as

$$N = \left(\frac{P_{\text{pk}}}{P_{\text{pk,ref}}} \right)^2 \cdot \alpha \cdot 2f_m, \tag{2.35}$$

where P_{pk} represents the peak power per pulse estimated from our model, and $2f_m$ denotes the repetition rate of our system.

From the above, it is apparent that to effectively utilise the OFCG source for efficient heralded photon generation in the process of SFWM, it is essential to optimise the peak power per pulse. In Chapter 3, we will employ a numerical model to estimate the output power, repetition rate and pulse width from the OFCG. This information will then be used to calculate the peak power per pulse, and subsequently, the expected pair production rate. Optimising these parameters is crucial for enhancing the capabilities of our quantum-enhanced LIDAR system.

Part II

High-efficiency optical frequency comb generation

Chapter 3

Modelling of a single and coupled-cavity OFCG

3.1 Introduction

This chapter signifies the commencement of my original research contributions; the content and discussions presented herein are a direct result of my independent work.

Optical frequency comb technology serves as the foundation for a wide array of applications in sensing and meteorology [45–47]. In addition to enabling precise measurements, frequency combs also offer a valuable resource for generating numerous frequency modes, facilitating the realisation of scalable quantum systems [48]. Typically, these experiments involve the use of pulsed lasers derived from bulky, high-power, and optically pumped mode-locked laser systems, producing temporal pulses with durations ranging from a few femtoseconds to hundreds of picoseconds and operating at a typical repetition rate of approximately 1 to 100 MHz. Furthermore, these mode-locked laser systems find applications in quantum LIDAR, where they efficiently generate pairs of single photons, such as those in a birefringent single-mode optical

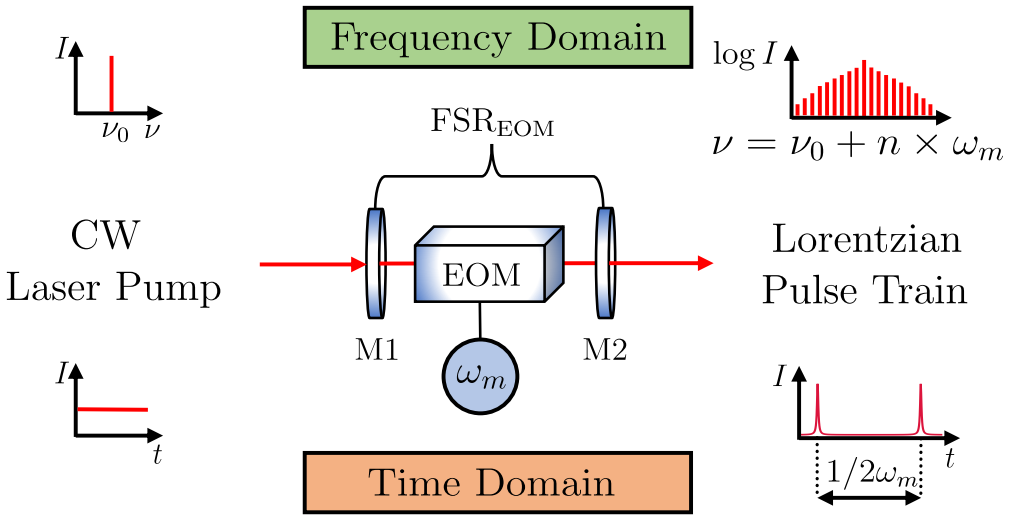

Figure 3.1: OFCG formed from a CW pump laser injected into an optical cavity containing the EOM formed by mirrors M1 & M2 with free spectral range FSR$_{\mathrm{EOM}}$ chosen to be integer multiple of a modulation frequency of an EOM ω_m. This configuration converts the input CW signal into a frequency comb, resulting in the generation of short temporal pulses at a repetition rate of $2\omega_m$.

fiber [49, 50].

One route towards compact, efficient frequency combs has been enabled by recent advances in cavity-based electro-optic frequency combs in thin-film lithium niobate [114], utilising the general critical coupling scheme proposed in [115]. While these devices offer very large free spectral ranges and a compact footprint [116, 117], the inherent material losses in waveguide technologies present certain challenges. These losses limit the wavelengths over which these devices can operate. Additionally, losses in output coupling from chips further impact the efficiency and dynamic tuning capabilities of the devices. As a result, there is a constraint on the maximum theoretical efficiency achievable, and the devices can not be dynamically tuned.

An alternative method for generating a frequency comb is to use an electro-optical modulator (EOM) embedded in an optical cavity to convert a continuous wave (CW) laser into a coherent pulse train using an optical fre-

quency comb generator (OFCG). By employing an intra-cavity EOM, an OFCG can convert a CW pump into a train of mode-locked pulses [51–54], as shown in Fig. 3.1. This approach allows for the generation of optical pulses with extremely high repetition rates of up to 20 GHz while achieving pulse widths ranging from hundreds of picoseconds down to a few hundred femtoseconds [54]. The benefits of this approach include the flexibility to operate at arbitrary pump wavelengths through the use of appropriate optics, dynamic adjustment of pulse width by modifying the EOM modulation depth, and minimal timing jitter, making it suitable for precise timing signal distribution [55]. Using a single cavity the output efficiency of the OFCG is fundamentally limited to a few percent [51, 53–55], preventing high-power comb generation. However, this can be overcome using coupled-cavity setup [57].

This Chapter describes how to design an efficient and compact source of optical pulses using the OFCG. The primary purpose of the OFCG is to act as a pump source for the process of spontaneous four-wave mixing (SFWM) described in Section 2.6. Our ultimate goal is to generate a minimum of 1.5 kHz photon pairs to operate well above the ∼300 Hz dark-count rate of single photon avalanche diodes (SPADs) used for building quantum-enhanced LIDAR, as discussed in Section 2.7. In this Chapter, we will discuss the theoretical models of both single and coupled-cavity OFCGs [57]. The Chapter will investigate the optimisation of OFCG parameters and explore the limitations of the design, providing valuable insights for subsequent experimental realisation in Chapter 4.

3.2 Generation of the short optical pulses from the OFCG

In Section 2.3, the effect of the EOM on a light passing through it was described. Light propagating through an EOM modulated with a sine wave

at the frequency ω_m experiences instantaneous phase change [54, 55]. As a result of that phase modulation the power from the input laser frequency ν_0 is coupled into sidebands with frequencies $\nu_0 \pm k\omega_m$, where k is an integer. The amount of power coupled into these sidebands depends on the modulation depth δ, which scales with the magnitude of the electric field applied to the crystal (See Eq. 2.5). The power relation between sidebands can be described using Bessel function identities (See Eq. 2.6).

In Fig. 3.1, we consider the EOM placed in an optical cavity with a free spectral range (FSR) FSR_{EOM} chosen to match the integer multiple of the EOM frequency of modulation ω_m. Under these conditions, the sidebands generated when the single-frequency input light passes through the EOM will resonate the neighbouring longitudinal modes of the optical cavity, leading to a cascade effect where sidebands generated from the input frequency ν_0 give rise to new sidebands. This cascade effect results in the output of the OFCG, forming a frequency comb centred at the input frequency ν_0 with a double-sided exponential decay in comb amplitude (or power), where the spacing between adjacent modes is equal to the modulation frequency ω_m [52–55, 57].

The Fourier transform of the resulting frequency spectrum reveals that the temporal output is a train of Lorentzian shaped pulses with a repetition rate of $2\omega_m$ [52–55, 57]. The full-width at half-maximum (FWHM) pulse width τ_p of the OFCG can be approximated as [51]

$$\tau_p = \frac{1}{2F\delta\omega_m}, \tag{3.1}$$

where F is the finesse of the resonant cavity, and δ is the modulation depth in radians. The finesse of the optical cavity is related to the intensity reflectivity of the mirrors constituting the cavity and determines the number of round-trips the light within the cavity undergoes. It can be expressed as [118]

$$F = \frac{\pi\sqrt{R}}{1-R}, \tag{3.2a}$$

$$R = \sqrt{R_1 R_2}, \tag{3.2b}$$

where R_i is the intensity reflectivity of mirror Mi in Fig. 3.1.

From Eq. 3.1, we see that achieving a short pulse τ_p requires maximising the finesse F, modulation depth δ and frequency of modulation ω_m. From Eq. 3.2a, we find that to maximise the finesse high reflectivity mirrors need to be used. The highest reflectivity mirrors available off the shelf typically have intensity reflectivity of $R = 0.99$, resulting in $F = 312$. The modulation frequency ω_m is limited primarily by the relative size of the EOM crystal and the associated power thresholds for higher frequencies. For our application, we have chosen to align with commercially available EOMs with modulation frequencies up to 2.5 GHz. This choice is further elaborated in Section 3.6.2 where we discuss the damage threshold of the EOM crystal in detail. For the chosen centre frequency of 780 nm, among the available free-space EOM devices, the highest achievable modulation depth was 2.1 radians.

Substituting these parameters into Eq. 3.1, results in a FWHM pulse width of $\tau_p = 0.3$ ps. It is essential to note that Eq. 3.1 does not account for the dispersion effects of the crystal discussed in Section 3.4.1, which will broaden the pulse leaving the OFCG. Realistically, the effects of dispersion and limits of efficiency restrict practical operation of OFCG sources to the ps regime, as will be shown in this Chapter.

To maximise the usefulness of the OFCG to generate a train of optical pulses for the generation of heralded photon pairs in the process of SWFM (See Section 2.7), optimising the peak power per pulse emitted from the OFCG

P_{pk} is necessary. The peak power per pulse is

$$P_{pk} = \frac{E_{pk}}{\tau_p}, \tag{3.3}$$

where E_{pk} is energy per pulse and τ_p is the FWHM pulse duration. This shows that in order to maximise the peak power per pulse emitted from the OFCG, we need to maximise the pulse energy and minimise the FWHM pulse width. The energy per pulse generated from the OFCG will depend on its output efficiency η_{SC}, this output efficiency will dictate how much of the input optical power will be converted into a Lorentzian pulse train.

3.3 Output efficiency of the OFCG

In the previous Section, we discussed the importance of optimising both the FWHM pulse width τ_p and the output efficiency of the OFCG to generate high-power pulses. The output efficiency of the single-cavity OFCG is given by the following equation [55]

$$\eta_{SC} = \frac{(1-R)^2}{\pi R(1-RT_c)\delta}, \tag{3.4}$$

where T_c is the intensity transmission through the EOM crystal. From Eq. 3.4 we can observe that increasing the modulation depth δ and power reflectivity of the cavity mirrors (finesse) leads to a decrease in the output efficiency η_{SC}. This effect is related to the impedance matching of the optical cavity.

A cavity is considered impedance-matched when the intensity reflectivity coefficient of the input-coupling mirror balances all the losses within the cavity, excluding the input coupling efficiency [119]. When the cavity is impedance-matched and resonant with the input light, the internal circulating power reaches a maximum as the incident light is optimally coupled into the cavity. The reflection at the input-coupling mirror becomes zero, indicating that

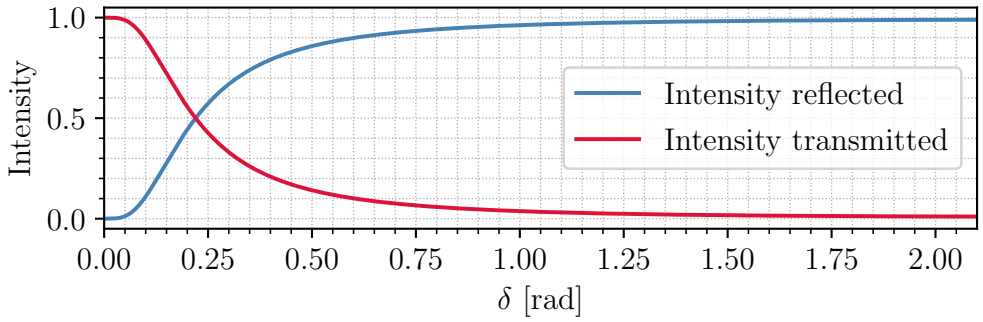

Figure 3.2: Effect of increasing the modulation depth δ on the amount of light reflected - in blue, and transmitted - in red, through the OFCG. The cavity mirrors were chosen to be impedance matched $r_1 = r_2$, and the cavity loss comes from the EOM coupling power from the input mode into sidebands. The input intensity I_0 is normalised to 1. As the modulation depth increases, the reflection from the input mirror increases and the transmission through the OFCG decreases, showing the dependence of cavity performance on the modulation depth.

all incident light is transmitted into the cavity, while the cavity output sees maximum transmission. The intensity of the light reflected from the input mirror I_r of the optical cavity is given by [119]

$$I_r = I_0 \frac{(r_1 - r_{Loss})^2}{(1 - r_1 r_{Loss})^2}, \tag{3.5}$$

where I_0 is the intensity of light incident on the cavity, $r_1 = \sqrt{R_1}$ is the amplitude reflectivity of the input mirror, and r_{Loss} is the fraction of the electric field that remains in the cavity after one round trip, excluding the input coupling loss.

In a situation where there is no loss in the optical cavity, the electric field remaining in the cavity after a round trip is equal to the reflectivity of the output mirror $r_{Loss} = r_2$. For the cavity to be impedance matched, $r_1 = r_2$.

In the case of the OFCG, the coupling of light from the input mode to sideband modes is seen as a loss by the incident light on the cavity. The magnitude of the electric field left in the input mode after one round-trip can be expressed using the Bessel function $|J_0(\delta)|^2$ (Eq. 2.6). The Bessel

function is squared due to light propagating through the EOM twice per round-trip, therefore the magnitude of the electric field left in the input mode is $r_{Loss} = r_2|J_0(\delta)|^2$. Figure 3.2 shows how increasing the modulation depth δ impacts the transmission through the OFCG. In order to impedance match the cavity of the OFCG while operating at high modulation depth, a lower reflectivity input mirror can be used. Unfortunately, this lowers the finesse, which is essential for generating short pulses according to Eq. 3.1.

Equations 3.1 and 3.4 show that it is not possible to generate short optical pulses with high output efficiency from a single-cavity OFCG, as increasing either cavity finesse or modulation depth increases the loss from the input light mode, resulting in an impedance mismatch that inhibits efficient input coupling into the cavity and hence the low output, with $<1\%$ being typical for experiments [53, 55].

To overcome this limitation, a coupled-cavity configuration [57] will be investigated in Section 3.6.

3.4 Theory of an Electro-optic modulator in a cavity

We consider an EOM placed in an appropriate cavity configuration, where the cavity's free spectral range is a sub-harmonic of the modulation frequency. In our model, we employ an approximation: the light passes through the EOM only once per round trip within the cavity, and the crystal responsible for modulation is effectively considered twice as long. This simplifies the analysis and allows for better preservation of accuracy. Additionally we assume the round trip of the cavity is short compared to the modulation period. This ensures that the phase modulation imparted by the EOM is coherent with the cavity resonance conditions. The output electric field can be calculated by considering the situation in Fig. 3.3. We can represent all of the electric

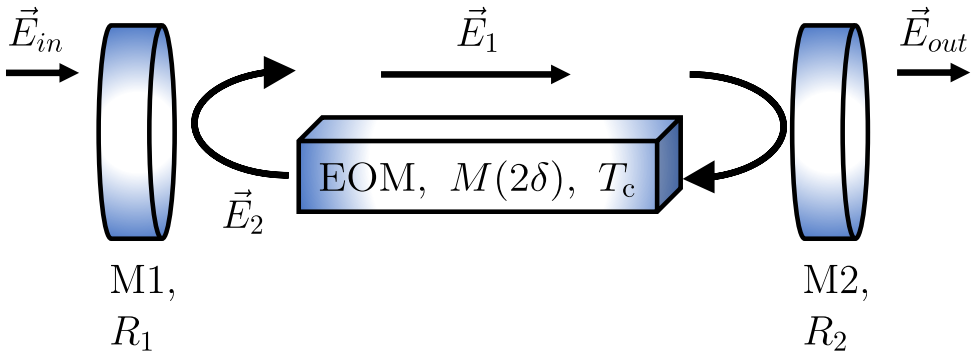

Figure 3.3: Model of a single-cavity OFCG. The electric field incident on the input mirror of the OFCG M1 (with intensity reflectivity R_1) is denoted as $\vec{E}_{\text{in}}$. Electric field $\vec{E}_2$ is the field transmitted through the mirror M1, then reflected by mirror M2 (with intensity reflectivity R_2) after it propagates through the EOM crystal (crystal transmission denoted as t_c), where it undergoes phase modulation ($M(2\delta)$). This electric field is then combined with the electric field transmitted by the M1 and denoted as $\vec{E}_1$. Finally, $\vec{E}_{out}$ is the electric field leaving the cavity. In the model, we assume that the light passes the crystal only once per round-trip and that the crystal is twice as long.

fields involved as follows

$$\vec{E}_1 = t_1\vec{E}_{\text{in}} + r_1\vec{E}_2, \tag{3.6a}$$

$$\vec{E}_2 = t_c^2 r_2 \Phi(\phi_k) M(2\delta)\vec{E}_1, \tag{3.6b}$$

where $\vec{E}_{\text{in}}$ represents the incident field, defined here as a vector of frequency modes, where only the central frequency that is excited and equal to 1. The transmission through the crystal is denoted as t_c. The reflectivity and transmittance of mirrors M1(2) are denoted by $r_{1(2)}$ and $t_{1(2)}$ respectively. The matrix $\Phi(\phi_k)$ represents the full round-trip phase change due to crystal dispersion and can be expressed as

$$\Phi(\phi_k) = \begin{bmatrix} e^{-i\phi_k} & 0 & \dots & \dots & 0 \\ 0 & \ddots & \ddots & & \vdots \\ \vdots & \ddots & e^{-i\phi_0} & \ddots & \vdots \\ \vdots & & \ddots & \ddots & 0 \\ 0 & \dots & \dots & 0 & e^{-i\phi_{-k}} \end{bmatrix}, \tag{3.7}$$

where k is the sideband order and ϕ_k is the phase change due to crystal dispersion per sideband, as discussed in detail in Section 3.4.1. $M(2\delta)$ is the transformation matrix of the EOM, which was obtained using Eq. 2.6. This matrix can be represented as

$$M(2\delta) = \begin{bmatrix} J_0(2\delta) & -J_1(2\delta) & J_2(2\delta) & \dots & J_k(2\delta) \\ J_1(2\delta) & J_0(2\delta) & -J_1(2\delta) & \dots & -J_{k-1}(2\delta) \\ J_2(2\delta) & J_1(2\delta) & J_0(2\delta) & \dots & J_{k-2}(2\delta) \\ \vdots & \vdots & \vdots & \ddots & \vdots \\ J_k(2\delta) & J_{k-1}(2\delta) & J_{k-2}(2\delta) & \dots & J_0(2\delta) \end{bmatrix}, \tag{3.8}$$

where $J_i(\delta)$ is Bessel function identity of order i, and an origin δ. In the model, to accurately represent $\pm k$ sidebands along with the carrier (mode 0), k was constrained to always be even. Here δ is the modulation depth defined in Eq. 2.5. The simplification where light passes the crystal only once per cavity round trip and the crystal is twice as long is grounded in the relationship of the transformation matrix M, where we observe that $M(\delta)^2 = M(2\delta)$. By adopting this assumption, we significantly streamline the complexity of the calculations, ensuring that numerical stability is maintained throughout the analysis. Squaring matrices, especially when represented using a finite size, introduces numerical inaccuracies due to truncation errors. Squaring the truncated matrix during calculations exacerbates this error. In contrast, using a single finite-size matrix better preserves accuracy.

Using Eq. 3.6a and 3.6b we can solve for the field state in $\vec{E_1}$ depending on

incident field $\vec{E}_{\text{in}}$

$$\vec{E}_1 = \left[\mathbb{1} - r_1 r_2 t_c^2 \Phi(\phi_k) M(2\delta)\right]^{-1} t_1 \vec{E}_{\text{in}}. \tag{3.9}$$

It is important to note that because of the continuous nature of the Bessel functions in $M(2\delta)$, there are sporadic instances where the matrix in Eq. 3.9 may become non-invertible. However, as long as the input modulation depth is not a continuous function, it is highly unlikely that values of modulation depth input will result in a non-existent inverse of the matrix. The likelihood of encountering exact values that lead to non-invertibility is extremely low. Therefore, while non-invertibility is a theoretical possibility, it does not pose a significant risk to the overall performance and reliability of the model under typical conditions.

Using the Eq. 3.9, we can calculate the output electric field of the OFCG, denoted as $\vec{E}_{\text{out}}$, to be

$$\vec{E}_{\text{out}} = t_2 t_c \sqrt{\Phi(\phi_k)} M(\delta) \vec{E}_1, \tag{3.10}$$

where $\sqrt{\Phi(\phi_k)}$ and $M(\delta)$ represent half round trip phase change matrix and half round trip coupling matrix, respectively. The calculated output of the electric field represents the values of the electric field modes in the frequency domain. These values can be Fourier transformed to obtain the temporal output of the OFCG.

3.4.1 Dispersion effects

Due to the finite dispersion of the EOM crystal, the phase difference between the central mode and the k^{th} sideband increases with k. Eventually, this phase difference becomes large enough for the sideband to no longer resonate with the optical cavity where the crystal is placed. When one of the sidebands stops being resonant with the optical cavity, its amplitude is

strongly suppressed. This results in the truncation of the frequency comb, which in effect broadens the pulse emitted from the OFCG [51–53]. This dispersion limit produces a sharp cutoff of the comb spectrum, limiting its span to [120]

$$\Delta f = \frac{\left[2\left(-\beta+\delta\right)G\right]^{1/2}}{\pi}, \tag{3.11}$$

where β is the normalised detuning between the input laser frequency ν_o and the nearest cavity resonance v_r, defined as $\beta = \left[\pi\left(\nu_o - v_r\right)\right]/\mathrm{FSR}_{\mathrm{EOM}}$. The $\mathrm{FSR}_{\mathrm{EOM}}$ is the free spectral range of the optical cavity containing the EOM, defined as $\mathrm{FSR}_{\mathrm{EOM}} = c/2(l - L_c n_{\mathrm{crystal}})$, where l is the cavity length, L_c is the crystal length, and n_{crystal} is the refractive index of the EOM crystal at the centre wavelength of the input laser λ_0 in the vacuum. The modulation depth is denoted as δ and coefficient G is related to the EOM material dispersion by $G = 2\pi c/D\lambda_0^2 L_c$. D is the material dispersion defined as

$$D = \frac{\lambda_0}{c}\frac{\partial^2 n}{\partial \lambda^2}_{\lambda=\lambda_0}. \tag{3.12}$$

Equation 3.12 can be related to the group velocity dispersion (GVD) by use of [53]

$$\mathrm{GVD} \cong \frac{D\lambda_0^2}{2\pi c}. \tag{3.13}$$

A second source of dispersion in the system can arise from the dielectric coating of the cavity mirrors. For femtosecond lasers this can play a significant role in the resulting pulse, however for operation in the picosecond pulse regime targeted in this work, this effect is much weaker than crystal dispersion and can be neglected.

The total round trip phase change per sideband is given by [53, 120]

$$\phi_k = \beta + k\frac{\pi\Delta\omega_m}{\mathrm{FSR}_{\mathrm{EOM}}} + \frac{k^2}{2}\mathrm{GVD}\cdot L_c(2\pi\omega_m)^2, \tag{3.14}$$

where the first term β represents the detuning between the centre frequency of the input laser and the nearest cavity resonance. The second term reflects the detuning between the modulation frequency ω_m and the free spectral range of the optical cavity containing the EOM, here $\Delta\omega_m = |\omega_m - \mathrm{FSR}_{\mathrm{EOM}}|$. The last term arises from the dispersion in the EOM crystal.

In a scenario where the cavity length is stabilised to ensure that the resulting free spectral range $\mathrm{FSR}_{\mathrm{EOM}}$ becomes a subharmonic of ω_m, and the laser is simultaneously stabilised to that cavity, the first two terms of Eq. 3.14 vanish. Consequently, this leads to the generation of a wide frequency comb with its span being limited solely by the crystal dispersion, as described by

$$\Delta f = \frac{(2\delta G)^{1/2}}{\pi}. \tag{3.15}$$

3.5 Modelling of a Single Cavity OFCG

The theoretical framework of the single-cavity OFCG provides an expression (Eq. 3.10) that serves as a predictive tool for estimating the system's output. To model the system, we employed the Python programming language, taking into account the considerations of simulation time optimisation and accuracy. To strike an optimal balance between the two, we truncate the size of the transformation matrix $M(2\delta)$ to 2501, which allows us to calculate the amplitude of $\pm$ 1250 sidebands of the frequency comb. Importantly, the fractional power in the extreme modes is sufficiently small to ensure that this truncation does not introduce significant inaccuracies. A single run of the simulation with a matrix size of 2501 takes approximately 40 seconds, whereas increasing the matrix size to 5001 extends the runtime to about 200 seconds. The outcomes of both simulation runs are virtually identical, with differences in simulated efficiencies below $10^{-4}\%$ and no variation in the predicted pulse widths. This comparison underscores our choice's efficiency,

allowing for reliable results within a reasonable timeframe.

The primary objective is to determine the appropriate parameters necessary for generating short and intense pulses of light using single-cavity OFCG. Accordingly, our focus will centre on optimising the FWHM pulse width τ_p, which needs to be minimised to achieve the maximal peak pulse power, as shown in Section 3.2. The second parameter of interest is the efficiency of the OFCG, as it plays a crucial role in converting pump laser power into a high-power Lorentzian pulse train.

Certain parameters are predetermined, including the choice of crystal material, its length, the EOM frequency of modulation ω_m, and the pump central wavelength λ_0. The choice of the pump centre wavelength λ_0 at 785 nm was motivated by its ability to generate photon pairs at ∼660 nm and ∼960 nm through the process of SFWM in a birefringent optical fibre (See Section 2.6). These photon pairs are well-suited for detection using silicon-based single photon avalanche detectors (SPADs). To this end, we use a magnesium-doped lithium tantalate crystal (Mg:$LiTaO_3$) with dimensions of 1.5 mm x 2 mm x 27 mm, based on commercially available EOM devices. This particular crystal was chosen due to its linear GVD of 308 fs^2/mm at the central wavelength of $\lambda_0 = 785$ nm, as reported by Moutzouris et al. [121]. Additionally, the crystal is assumed to have anti-reflective (AR) coatings on both facets, resulting in a high intensity transmission through the crystal ($T_c = 0.9999$) according to the EOM manufacturer's datasheet. The EOM frequency of modulation ω_m was chosen to be equal to 2.39 GHz due to restrictions of the experimental setup, as discussed in Section 3.7.

A typical result of the numerical simulation is shown in Fig. 3.4. The mirror intensity reflectivities were set to $R_1 = R_2 = 0.99$ and the modulation depth was set to $\delta = 2.1$ radians, the choice of those parameters was motivated by the discussions in Section 3.2. Figure 3.4**a** shows the spectral output of the single-cavity OFCG and Fig. 3.4**b** shows the same spectral output on a

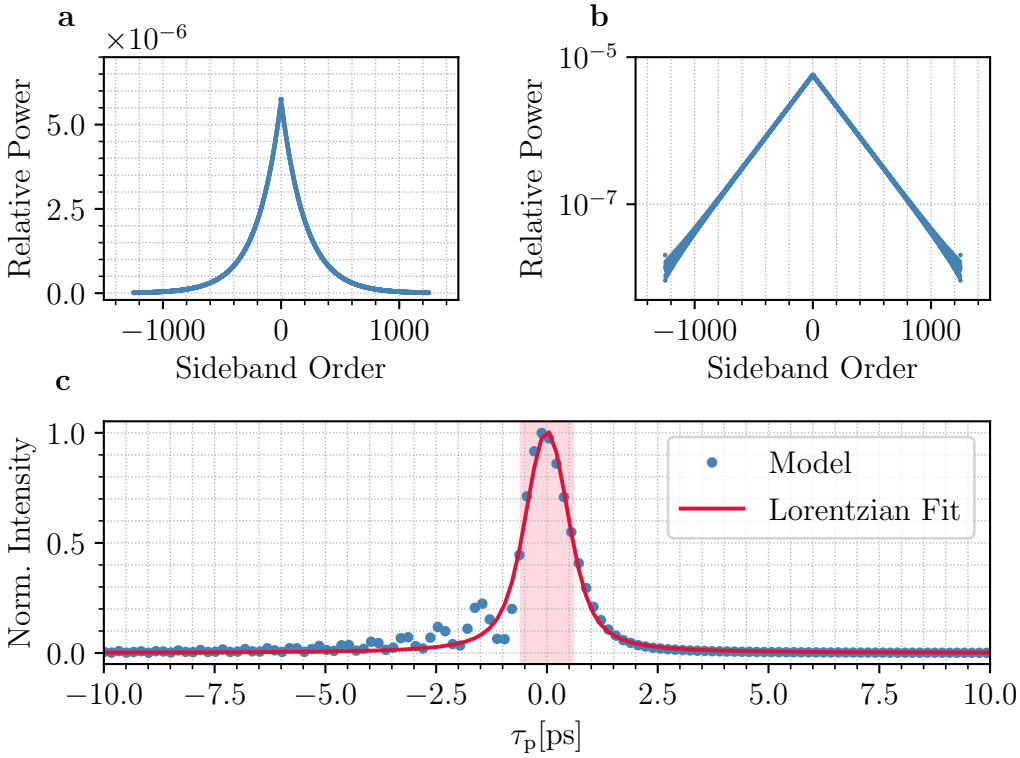

Figure 3.4: A typical result of the numerical model of the single-cavity OFCG. Parameters of the model were $\delta = 2.1$ radians, $R_1 = R_2 = 0.99$ and the remaining parameters as detailed in the Section 3.5. The input electric field was set to 1. The resulting efficiency $\eta_{SC} = 0.235$ % was calculated by summing the squared electric field of each sideband and dividing it by the input intensity of 1. **a** The spectral output of the single-cavity OFCG. **b** The semi-log plot of the spectral output. **c** The temporal output of the single-cavity OFCG obtained by performing the Fourier transform of the spectral output. The model data was fitted with a Lorentzian function to estimate the FWHM pulse width of $\tau_p = 1.17$ ps indicated by the red shaded area.

semi-log scale. The linear relationship of the sidebands on the semi-log plot signifies the exponential relationship between the sidebands, as predicted by other theoretical models [52, 53]. Deviations from this linear relationship as the sideband order increases can be attributed to the truncation effect due to the finite transformation matrix size $M(2\delta)$ and dispersion effects described in Section 3.4.1. Figure 3.4**c** shows the temporal output of the OFCG, this was obtained by performing a Fourier transformation of the spectral output in Fig. 3.4**a**. The red area marks the FWHM pulse width. Notably, due to the linear spectral phase causing a constant time delay for each pulse train, the

OFCG output actually comprises two interleaved pulse trains with a relative time delay determined by the phase slope difference [55]. Figure 3.4**c** shows only one of the pulses. The asymmetry of the pulse is again an effect of the truncation of the transformation matrix $M(2\delta)$ and the crystal dispersion effect.

3.5.1 Temporal output of a Single Cavity OFCG

The aim of this Section is to identify the parameters of the OFCG resulting in the shortest optical pulse τ_p emitted from the OFCG. The temporal output of the OFCG is a Lorentzian pulse train with a repetition rate equal to $2\omega_m$ [52–55, 57]. Due to the linear spectral phase, two pulses are generated per each duty cycle [55].

To extract the temporal output, we performed a Fourier transform of the spectral output from the numerical model described in Section 3.4. The FWHM pulse width τ_p was obtained by fitting the pulse shape with a Lorentzian function.

We conducted two simulations to investigate the impact of the modulation depth δ and the optical finesse F on the pulse width. The results of these simulations are presented in Figure 3.5. In the first simulation (Figure 3.5**a**), we varied the modulation depth δ while keeping the optical finesse F constant at 312. By adjusting the modulation depth, we control how much of the power from the light propagating through the EOM is being coupled into sidebands. The second simulation (Figure 3.5**b**) focused on examining the effect of the optical finesse F on the pulse width while keeping the modulation depth fixed at 2.1 radians. The optical finesse characterizes the number of times light passes through an electro-optic modulator (EOM). Our simulations confirm the prediction of Eq. 3.1 that an increase in optical finesse and modulation depth leads to a decrease in the FWHM pulse width τ_p. It is worth noting, that for the parameters of the OFCG which result in the short-

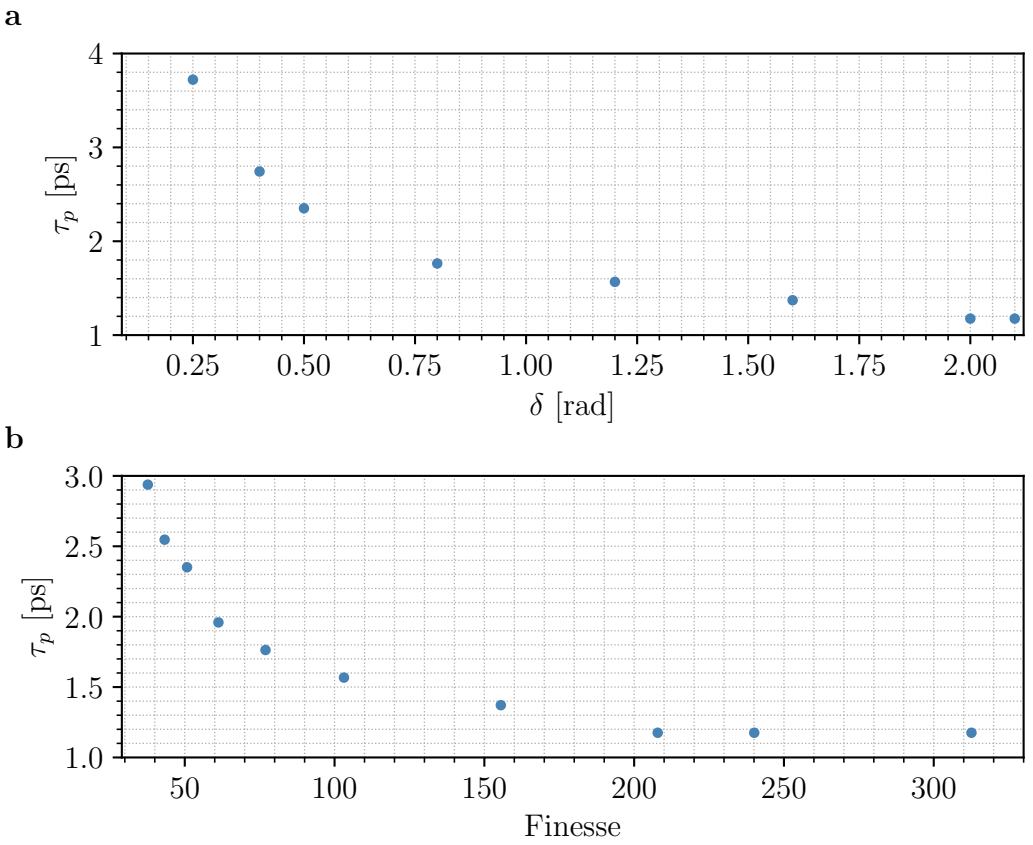

Figure 3.5: The pulse width τ_p as a function of **a** modulation depth, and **b** optical finesse. In **a** F = 312. In **b** the δ = 2.1 radians. The remaining parameters of the model are set to values described in Section 3.5.

est τ_p of 1.17 ps ($\delta = 2.1$ radians and $F = 312$), Eq. 3.1 predicts $\tau_p = 0.35$ ps. This discrepancy is due to the inclusion of dispersion effects in our numerical model, which are not accounted for in Eq. 3.1.

To show the trade-off between minimal FWHM pulse width τ_p and the OFCG output efficiency discussed in Section 3.3, we conducted simulations using our numerical model. These simulations involved obtaining the temporal output of the single cavity OFCG while varying the modulation depth for a fixed finesse value of 312.

Figure 3.6 showcases the results of our simulations, presenting three distinct pulses generated as the value of modulation depth was set to 1, 1.5 and 2 radians. We observe that as the modulation depth δ increases, the FWHM

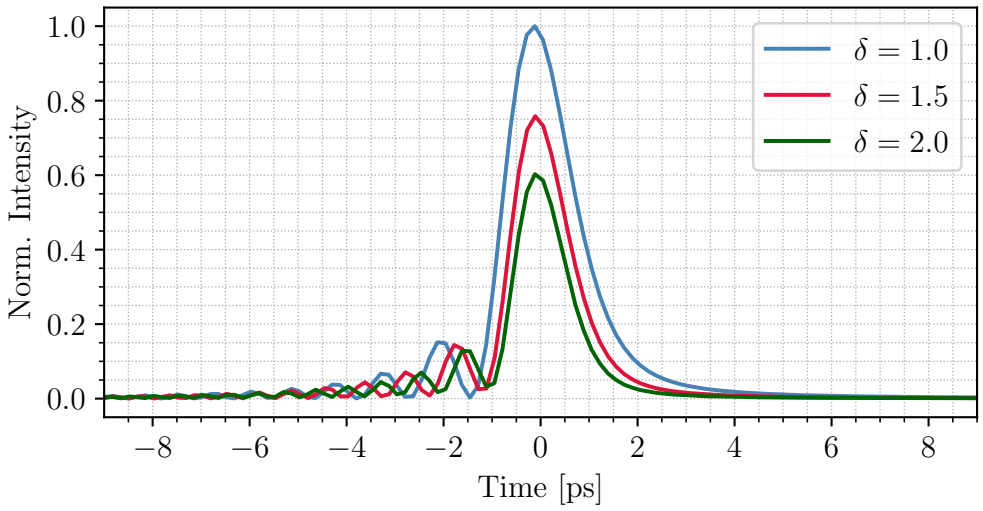

Figure 3.6: The temporal output of the single cavity OFCG for three different modulation depth values $\delta = 1$, 1.5, and 2 radians, corresponding to pulse widths of $\tau_p = 1.77$ ps, 1.37 ps, and 1.17 ps, respectively. The plot illustrates the trade-off between pulse width and energy per pulse in a single cavity OFCG. As the modulation depth increases and the pulse width decreases, the energy per pulse diminishes. The optical finesse of the OFCG cavity is set to 312, while the remaining numerical model parameters are described in Section 3.5.

pulse width decreases, albeit at the expense of diminishing intensity. This reduction in intensity is a direct consequence of the decrease in the output efficiency of the OFCG. The underlying cause is an impedance mismatch due to losses in the input light mode, as elaborated in Section 3.3.

3.5.2 Optimising the efficiency of the Single Cavity OFCG

In the following subsections, we will discuss the impact of the modulation depth δ and optical finesse F on the output efficiency of the OFCG.

Using our numerical OFCG model we can estimate the output efficiency η_{SC} by comparing the total output intensity in all modes excited by the OFCG

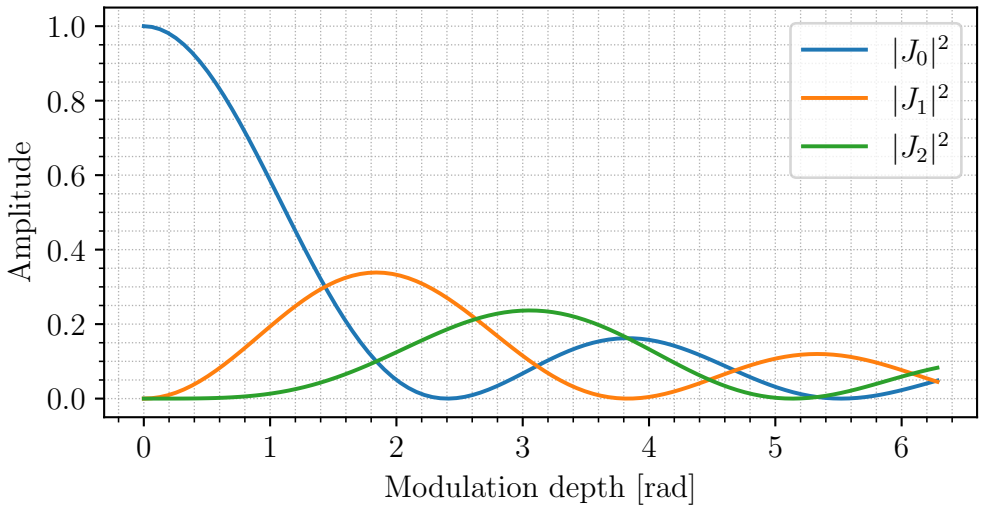

Figure 3.7: Amplitude of the carrier ($|J_0|^2$) and the first two sidebands ($|J_{1,2}|^2$) as a function of the modulation depth δ in radians.

$|E^2_{\text{out}}|$, to the input intensity incident on the input mirror of the OFCG $|E^2_{\text{in}}|$

$$\eta_{\text{SC}} = \frac{|E^2_{\text{out}}|}{|E^2_{\text{in}}|}, \tag{3.16}$$

For ease of comparison in our model, we assume that the incident electric field $\vec{E}_{\text{in}}$ has only central mode excited and equal to 1.

By performing numerical simulations, we calculate the efficiency (η_{SC}) for different values of modulation depth δ and optical finesse F. We present the results and discuss the trends observed, providing an understanding of how these parameters affect the performance of the OFCG.

3.5.2.1 Variation of modulation depth

The modulation depth is a measure of how efficiently the carrier energy is transferred into sidebands. Bessel functions provide the amplitude of these sidebands as a function of the modulation depth, which is proportional to the drive voltage (See Section 2.3). When the EOM is driven harder, higher-order sidebands can be created and the carrier can be completely suppressed.

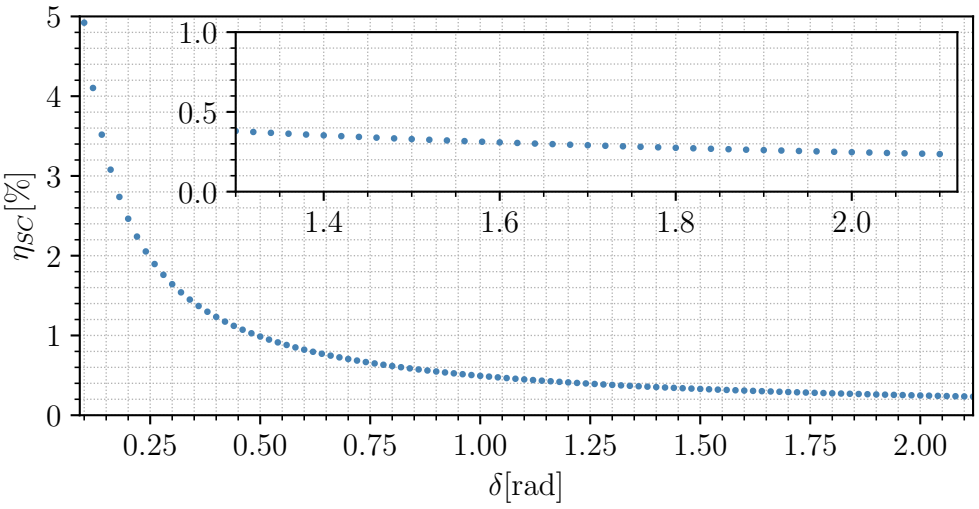

Figure 3.8: Results of the numerical simulation in which the modulation depth has been varied between 0.1 and 2.1. This upper limit of the modulation depth was set in order to match the maximum modulation depth achievable by the EOM used in the experiment described in Chapter 4. Here the finesse of the OFCG cavity is assumed to be 312, and the remaining parameters of the model are assumed to be as described in Section 3.5. The inset shows a close-up of the results for modulation depth between 1.5 and 2.1 radians.

This occurs at a modulation index of roughly 2.4 radians. The relationship between sidebands and carrier amplitude is shown in Fig. 3.7.

In this Section to judge the impact of the modulation depth δ, we assume that the cavity mirrors M1 & M2 have intensity reflectivities equal to $R_1 = R_2 = 0.99$, which results in the finesse of $F = 312$. This is motivated by findings in Section 3.5.1, where it was established that in order to achieve the shortest FWHM pulse width τ_p high finesse is required.

Figure 3.8 shows the impact of varying the modulation depth on the OFCG efficiency. As shown in the figure, the total output power decreases as the modulation index increases. This decline in total output power is attributed to changes in the impedance matching of the cavity. The coupling of light from the central frequency mode to sideband modes is seen as a loss by the incident light on the cavity, which affects the coupling into the cavity as

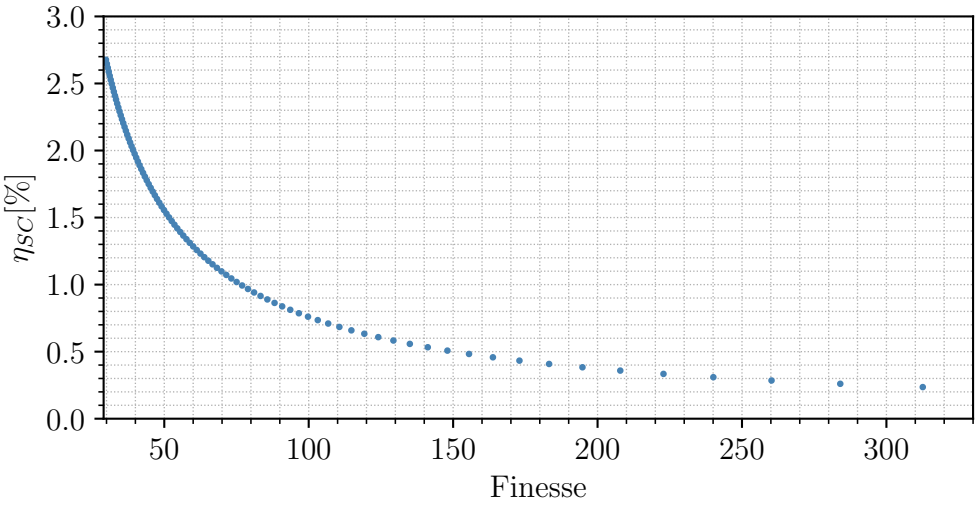

Figure 3.9: Results of the numerical simulation in which the optical finesse has been varied between 30 and 312. which corresponds to varying mirror intensity reflectivity from 0.9 to 0.99. These values were chosen after checking what mirror coatings were available to buy off-shelf. Here the modulation depth of the EOM is assumed to be 2.1, and the remaining parameters of the model are set to values described in Section 3.5.

explained in Section 3.3.

With an increase in modulation depth, the central mode is being more efficiently coupled into outer modes. This impacts the efficiency of the device, resulting in a throughput of only 0.235 % for our system with a modulation depth of 2.1 and finesse of 312.

3.5.2.2 Variation of Optical finesse

The finesse of an optical cavity, which is a measure of its ability to store light, is directly influenced by the reflectivity of its mirrors. Higher mirror reflectivity leads to higher finesse, indicating a greater number of round-trips that light can perform within the cavity before leaking out. This relationship can be described by Eq. 3.2a, which relates finesse and mirror reflectivity.

To assess the impact of the optical finesse F of the OFCG cavity on OFCG efficiency η_{SC}, we set the modulation depth (δ) to 2.1 in this Section. This

choice is motivated by the discussions in Section 2.2 and 3.5.1, where it was established that in order to minimise the FWHM pulse width τ_p modulation depth needs to be maximised.

Figure 3.9 illustrates the influence of varying the optical finesse on the efficiency of the OFCG. As depicted in the figure, the total output power decreases as the optical finesse increases. This decline can be attributed to changes in the impedance matching of the cavity, discussed in Section 3.2. With an increase in optical finesse, light performs more round-trips within the cavity, thereby passing through the electro-optic modulator (EOM) more times. This repeated passage through the EOM negatively impacts the impedance matching of the central mode into the cavity, as the central mode is gradually depleted with each passage. Consequently, the efficiency of the device is affected, resulting in a throughput of only 0.235% for our system with a modulation depth of 2.1 and a finesse of 312.

3.5.3 Optimisation of the parameters

Previous sections have highlighted the trade-off between increasing the modulation depth and the cavity finesse to achieve shorter pulses, and the increased loss from the central cavity mode resulting in an impedance mismatch. This mismatch inhibits efficient mode-matching into the cavity and hence a low output power [53].

As demonstrated in the previous Section, the parameters necessary to achieve a minimal pulse width ($\tau_p = 1.17$ ps) resulted in an output efficiency of the device of only $\eta_{\mathrm{SC}} = 0.235$ % ($<$ 1 % typical for experiments [53, 54]).

For the given efficiency and pulse width, the required input power of the CW pump laser to achieve a pair detection rate of 1.5 kHz is 100 W (See Section 2.7). However, this power requirement is highly impractical.

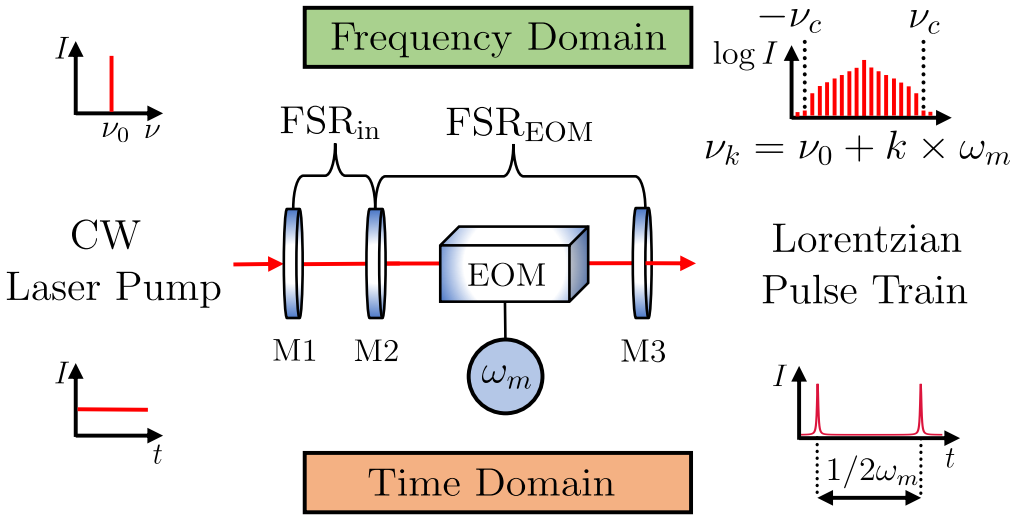

Figure 3.10: Illustration of a coupled-cavity OFCG consisting of a CW pump laser injected into an impedance-matched input cavity (M1 & M2). The input cavity has a free spectral range (FSR) denoted as $\mathrm{FSR_{in}}$, which is used to pump the EOM cavity (M2 & M3). The EOM cavity has a free spectral range denoted as $\mathrm{FSR_{EOM}}$, chosen to be an integer multiple of the EOM modulation frequency (ω_m). This configuration enables the generation of a high-efficiency optical frequency comb, producing short temporal pulses at a repetition rate of $2\omega_m$. The frequency spectrum of the comb exhibits a broad range, with a sharp cut-off at $\pm\nu_c$, representing the characteristic mode resonant with the input cavity.

3.6 Theory of a Coupled Cavity OFCG

The limitation described in the previous Section can be overcome using a coupled-cavity configuration as demonstrated in [57] and shown schematically in Fig. 3.10. Here a planar mirror M2 is placed between the input mirror M1 and the EOM crystal surface - to split the OFCG into two separate cavities - an empty input cavity (M1 + M2), and a second cavity (M2 + M3) containing the EOM, referred to as the EOM cavity. The input cavity is engineered for minimal loss with impedance-matched mirrors $R_1 = R_2$, enabling optimal coupling efficiency by allowing 100% of the optical power to enter the EOM cavity. This configuration effectively bypasses the impedance mismatch challenges between the input light and the EOM cavity, as elabo-

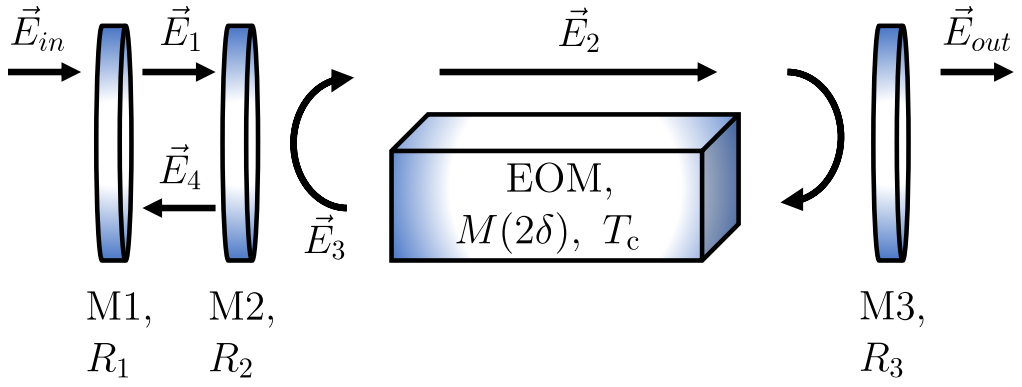

Figure 3.11: Model of a coupled-cavity OFCG. The figure illustrates the optical field propagation within the coupled-cavity OFCG. The incident electric field on the input mirror M1, denoted as $\vec{E}_{\text{in}}$, undergoes reflection with intensity reflectivity R_1. The resulting electric field $\vec{E}_1$ is a combination of the transmitted field $\vec{E}_{\text{in}}$ through M1 and the field $\vec{E}_4$ reflected from M1. Mirror M3 reflects a portion of $\vec{E}_2$ with intensity reflectivity R_3, which then undergoes phase modulation $M(2\delta)$ as it passes through the EOM crystal (with the transmission of the crystal t_c), giving rise to the field $\vec{E}_3$. Another portion of $\vec{E}_1$ is transmitted through M2, resulting in the field $\vec{E}_2$. Finally, $\vec{E}_4$ represents the combination of the transmitted field $\vec{E}_3$ through M2 and the field $\vec{E}_1$ reflected from M1. The electric field $\vec{E}_{out}$ represents the field leaving the EOM cavity. In this model, we assume that the light passes through the crystal only once per round-trip, and the crystal length is doubled.

rated in Section 3.3.

To solve the coupled-cavity OFCG we take situation in Fig. 3.11

$$\vec{E}_1 = \Phi_1 \times \left(t_1 \vec{E}_{\text{in}} + r_1' \vec{E}_4\right), \tag{3.17a}$$

$$\vec{E}_2 = t_2 \vec{E}_1 + r_2' \vec{E}_3, \tag{3.17b}$$

$$\vec{E}_3 = t_c^2 \Phi_2 \times M(2\delta) \times r_3 \vec{E}_2, \tag{3.17c}$$

$$\vec{E}_4 = \Phi_1 \times \left(t_2' \vec{E}_3 + r_2 \vec{E}_1\right), \tag{3.17d}$$

where Φ_1 is a phase matrix, representing half round trip phase change between sidebands, in first cavity, Φ_2 is a phase matrix, representing full round trip phase change between sidebands in the EOM cavity (Eq. 3.7), M(2δ) is full round trip transformation matrix, t_c is the transmission through the EOM crystal, $r(t)_i$ represent mirror M_i reflectivity (transmittance) on left side of

mirrors respectively, while $r'(t')_i$ represent mirror M_i reflectivity (transmittance) on the right side of the mirrors. Relation between those can be represented as

$$r' = r, \tag{3.18a}$$

$$t' = -t, \tag{3.18b}$$

this ensures the transmission phase is preserved. By substituting Eq. 3.17c into Eq. 3.17b we obtain

$$\vec{E}_2 = t_2\vec{E}_1 + r'_2 r_3 t_c^2 \left(\Phi_2 M(2\delta)\vec{E}_2\right), \tag{3.19a}$$

$$\vec{E}_2 = \left[\mathbb{1} - r'_2 r_3 t_c^2 \Phi_2 M(2\delta)\right]^{-1} t_2\vec{E}_1, \tag{3.19b}$$

after that we substitute Eq. 3.17c into Eq. 3.17d to obtain

$$\vec{E}_4 = \Phi_1 \left(t'_2 r_3 t_2 t_c^2 \Phi_2 M(2\delta)\left[\mathbb{1} - r'_2 r_3 t_c^2 \Phi_2 M(2\delta)\right]^{-1}\vec{E}_1 + r_2\vec{E}_1\right), \tag{3.20}$$

finally we substitute Eq. 3.19b and Eq. 3.20 into (3.17a), to solve the steady state of the system

$$\begin{aligned}\vec{E}_1 = \big[\mathbb{1} - \big(&r'_1 t'_2 r_3 t_2 t_c^2 \Phi_1\Phi_1\Phi_2 M(2\delta) \\ &\left\{\mathbb{1} - r'_2 r_3 t_c^2 \Phi_2 M(2\delta)\right\}^{-1} + r'_1 r_2 \Phi_1\Phi_1\,)\big]^{-1} \\ &t_1\Phi_1\vec{E}_{\text{in}},\end{aligned} \tag{3.21}$$

now to obtain the output electric field we substitute Eq. 3.21 into Eq. 3.19b and multiply the result by the transmittance of the third mirror, half round trip phase matrix in the EOM cavity, and half round trip transformation matrix.

$$\vec{E}_{\text{out}} = t_3 t_c \sqrt{\Phi_1} M(\delta)\vec{E}_2. \tag{3.22}$$

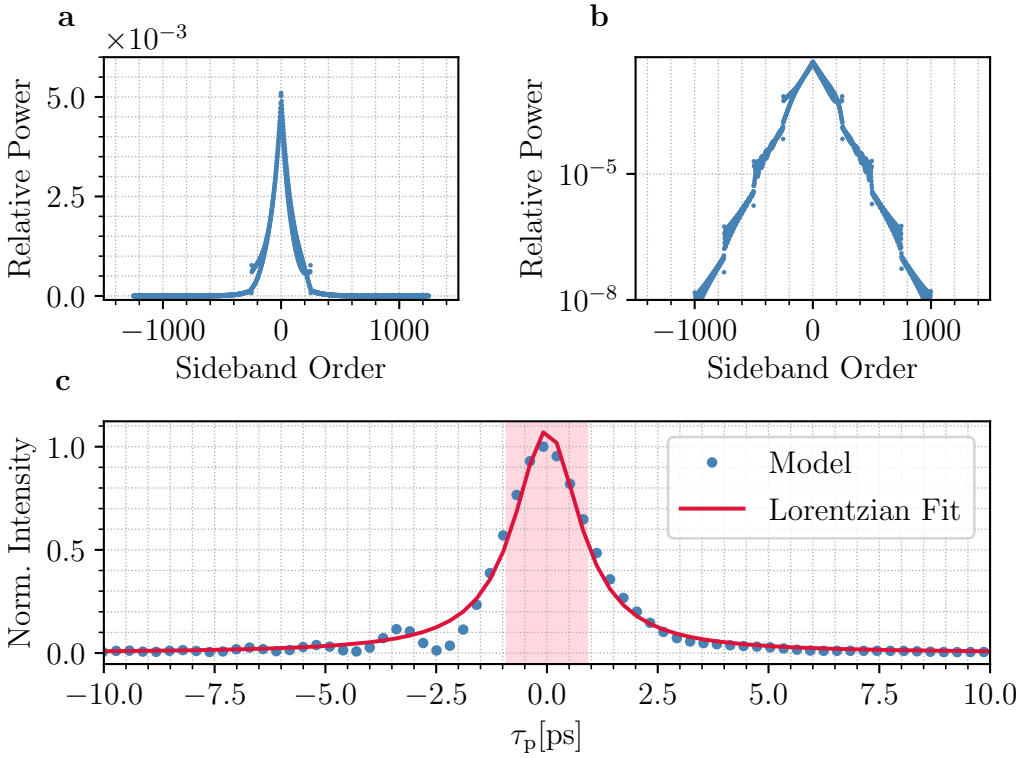

Figure 3.12: The output of the coupled cavity OFCG where FSR of the input cavity was chosen to be resonant with the 250^{th} sideband. **a** The frequency spectrum of the coupled cavity OFCG as a function of sideband order. **b** The semi-log of **a**. The effect of the characteristic mode can be seen as a sharp cut-off in the frequency comb. **c** Temporal output of the coupled cavity OFCG, the red shaded area shows the FWHM pulse width τ_p=1.8 ps.

3.6.1 Characteristic mode

For the coupled-cavity setup, an additional restriction on the frequency width of the generated comb arises when the i^{th} sideband becomes resonant with the j^{th} mode of the input coupling cavity. In this situation, the sideband propagating in the EOM cavity can not be perfectly reflected by mirror M2 and instead is allowed to propagate in the input cavity. The first sideband that is completely resonant with the coupling cavity is called the characteristic mode (ν_c). This resonance has a negative impact on the maximum comb width, which leads to the temporal broadening of the output of the OFCG.

To demonstrate this mechanism, we have modelled two distinct situations. In the first instance, shown in Figure 3.12, we purposely chose the FSR of

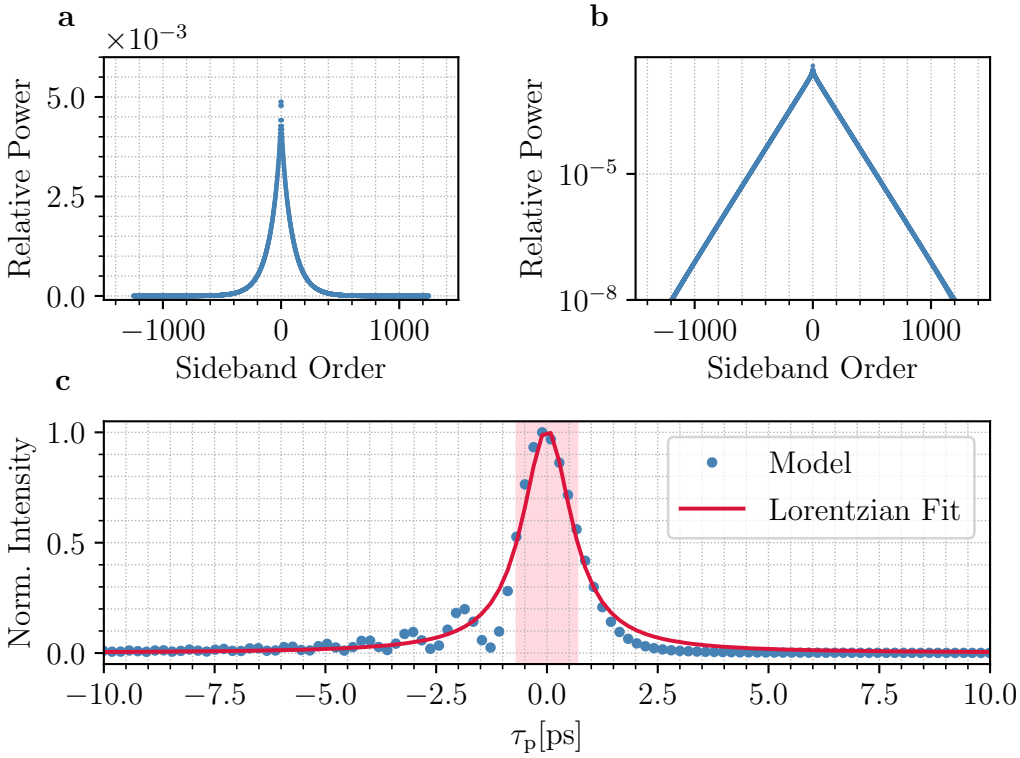

Figure 3.13: The output of the coupled cavity OFCG where FSR of the input cavity was chosen to not be resonant with any of the sidebands. **a** The frequency spectrum of the coupled cavity OFCG as a function of sideband order. **b** The semi-log of **a**. **c** Temporal output of the coupled cavity OFCG, the red shaded area shows the FWHM pulse width τ_p=1.4 ps. This plot was generated using the same parameters of the model as Fig. 3.12.

the input cavity incorrectly, resulting in the 250^{th} sideband generated by the OFCG in the EOM cavity becoming resonant with the input cavity. The frequency spectrum in Figure 3.12**a-b** clearly shows a sharp cut-off due to the characteristic mode. By performing the Fourier transform of the resulting frequency spectrum, we estimate FWHM pulse width $\tau_p = 1.8$ ps. To estimate the impact of the characteristic mode on the pulse width, we performed a second simulation.

Figure 3.13 shows the output of the numerical model using the same parameters as those used to generate Figure 3.12, except for the FSR of the input cavity, which was chosen to not become resonant with the sidebands generated in the EOM cavity. As expected, the frequency output in Figure 3.13**a-b**

exhibits no cut-off. The width of the pulse generated by the coupled cavity OFCG, where the FSR of the input cavity was chosen correctly, is equal to $\tau_p = 1.4$ ps, as shown in Figure 3.13**c**.

Comparing these two results, we observe that the FSR of the input cavity has a significant impact on the FWHM pulse width ($\Delta\tau_p = 0.4$ ps) and needs to be carefully selected.

To minimise the FWHM pulse width, the FSR of the input cavity is chosen with a large minimum common denominator with the FSR of the EOM cavity, and a large finesse to reduce the cavity linewidth. The linewidth requirement prevents the sidebands from partially leaking into the input cavity.

3.6.2 EOM damage threshold

The AR coating of the EOM crystal has a damage threshold of 20 W/mm^2, according to the datasheet provided by the manufacturer. Due to high loss in the EOM cavity, the limitation imposed by the damage threshold can be omitted in the single cavity OFCG Section. However, in the coupled-cavity situation where the efficiency can reach >90%, the damage threshold needs to be taken into consideration.

One way to overcome this limitation is to expand the beam passing through the crystal. This can be achieved by either introducing additional optics that will expand the beam within the EOM cavity or by increasing the length of the EOM cavity. Since each optical element introduces loss in the EOM cavity, reducing its finesse and thereby the width of the generated frequency comb (see Section 3.5.2.2), we have decided to maximise the beam size on the crystal facet by expanding the length of the EOM cavity.

The crystal facet has a size of 1.5 mm $\times$ 2 mm, and it is important to ensure that the beam size does not cause clipping on the crystal, which would introduce loss each time light passes through it. To calculate the maximal

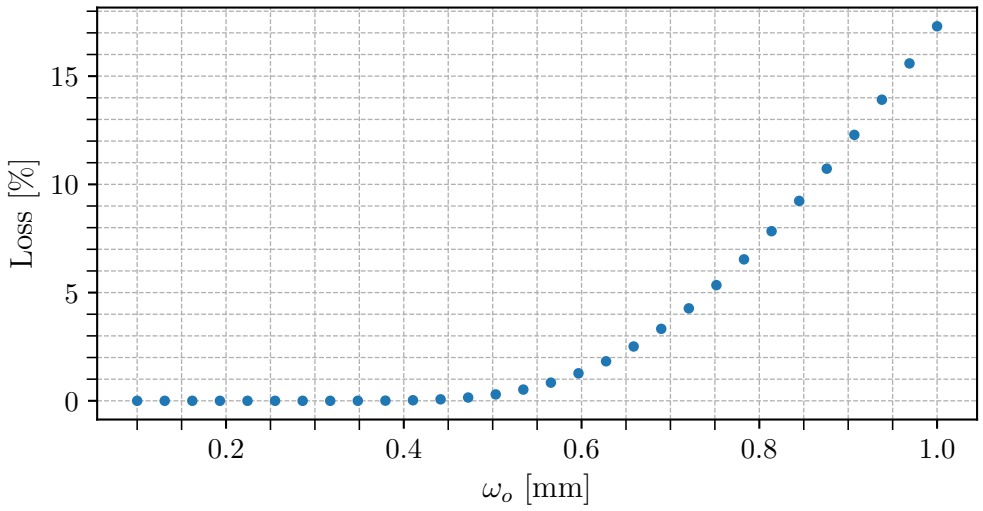

Figure 3.14: Loss on the crystal facet due to clipping of size 1.5 mm × 2 mm as a function of the incident beam waist w_0. The beam is assumed to hit the centre of the 1.5 x 2 mm aperture. The plot shows the variation in loss as the beam waist is scanned. The optimal incident beam waist size of $w_0 = 0.5$ mm, corresponding to a loss of 0.003 %, is selected to ensure near 100 % transmission through the crystal facet.

Gaussian beam size that allows for near 100 % transmission, we can use the expression

$$\text{Power Loss} = 1 - \int_{-x/2}^{x/2} \int_{-y/2}^{y/2} P_0 \exp\left(-2\frac{x^2+y^2}{w_0^2}\right) dy\, dx \tag{3.23}$$

where P_0 is the total power of the beam, x and y are the aperture size in x and y axis, and w_0 is the beam waist. Figure 3.14 shows a situation in which we set the aperture size to 1.5 mm x 2 mm and scanned the beam waist w_0, calculating the amount of loss caused by expanding the beam on the crystal facet. From this, we have picked the optimal value of $w_0 = 0.5$ mm, corresponding to a loss of 0.003 %. This optimal value represents the target beam waist size for minimal intra-cavity loss.

In the following sections, the light intensity incident on the EOM crystal facets will be carefully monitored to ensure that the system operates below the damage threshold of the EOM. The objective is to calculate the maximum

allowable input power for the pump laser, such that the intra-cavity intensity remains below the damage threshold.

The intracavity intensity, represented by the squared electric field $|E_2|^2$ propagating within the EOM cavity (Eq. 3.17b), will be used to determine the maximum input power. Given the design constraints outlined in Section 3.7, the waist size we achieved, $w_A = 0.473$ mm, is the closest to the optimal value of 0.5 mm. Assuming a waist size of $w_A = 0.473$ mm, we calculate the maximum input power of the pump laser ($\mathrm{P_p}$) that complies with the damage threshold limit of 20 W/mm^2

$$\text{Damage Threshold} \geq \mathrm{P_p} \times \frac{|E_2|^2}{|E_{\mathrm{in}}|^2} \times \frac{2}{\pi w_A^2}. \tag{3.24}$$

3.7 Optical cavity design for the coupled-cavity OFCG

The coupled-cavity design for the OFCG is required to fulfil the following criteria:

- The modulation frequency ω_m needs to be less than 2.5 GHz to fall within the bandwidth of the 5 GHz fast photodetector used to lock the cavity.
- The FSR of the EOM cavity $\mathrm{FSR_{EOM}}$ needs to be a subharmonic of the ω_m.
- Flat mirror M2 has a thickness of 6.35 mm and the glass (BK7) it is made of has a refractive index of 1.45. This glass surface is AR-coated and needs to be placed either in the EOM or the input cavity.
- The FSRs of the input cavity (M1 + M2) $\mathrm{FSR_{in}}$ and the EOM $\mathrm{FSR_{EOM}}$ (M2+M3), must be chosen with a large minimum common denomina-

tor. This choice is critical to prevent the broadening of optical pulses generated by the OFCG, as elaborated in Section 3.6.1.

- To achieve good mode matching between the input and EOM cavities, it is essential that mirror M2 be flat, and the waist of light propagating in the system must rest on the surface of mirror M2. This requirement can be optimised by adjusting the radii of curvature of mirrors M1 and M3.

- The beam radius on the crystal facet must be as close to 0.5 mm as possible to minimise the intensity on the EOM crystal and reduce clipping losses on the crystal, as described in Section 3.6.2.

To design the coupled-cavity, we started by evaluating the available off-shelf mirrors with radii of curvature (ROC) ranging from 100 mm to 1000 mm. These values of ROC were used to simulate beam propagation in the coupled-cavity system using reZonator software [122].

In our simulations, we had two main requirements. First, the beam waist w_0 resting on the flat mirror M2 needed to be identical for both cavities to ensure good mode matching between them. This ensured the efficient transfer of light between the input and EOM cavities. Second, the output of the system had to exhibit a beam radius greater than 0.5 mm. This condition was crucial to guarantee that the crystal could be positioned within the cavity in a manner allowing for the beam radius on the crystal facet to closely match the desired 0.5 mm. This alignment was necessary to address the damage threshold limit discussed in Section 3.6.2.

By conducting these simulations, we obtained combinations of radii of curvature (ROC) values for mirrors M1 and M3, along with corresponding cavity lengths that satisfied all the requirements mentioned above. These cavity lengths directly influenced the possible combinations of FSRs, as FSR $= c/2l$, where c is the speed of light in vacuum and l is the cavity length.

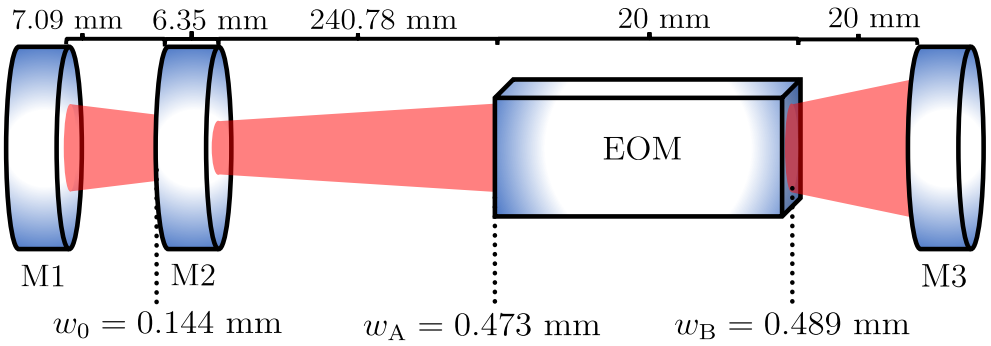

Figure 3.15: Design of the couple-cavity OFCG. Here the input cavity is formed with 1000 mm ROC mirror M1 and flat mirror M2. The distance between mirrors is 7.09 mm leading to $\mathrm{FSR_{in}} = 21.13$ GHz. The EOM cavity is formed with flat mirror M2 and a ROC = 300 mm mirror M3. Length of the EOM cavity is 287.13 mm (physical, not optical path length) setting the $\mathrm{FSR_{EOM}} = 478$ MHz.

The next step involved considering the possible FSRs of the input and EOM cavities and selecting the design with the largest minimum common denominator between the $\mathrm{FSR_{in}}$ and $\mathrm{FSR_{EOM}}$.

The final design, fulfilling all of the requirements described previously is shown in Fig. 3.15. The input cavity is constructed using input mirror M1 with an ROC of 1000 mm and flat mirror M2. The distance between these mirrors is set to 7.09 mm, resulting in an input cavity $\mathrm{FSR_{in}} = 21.13$ GHz. The waist of the input laser rests on the surface of the flat mirror M2 and has a radius of $w_0 = 0.144$ mm.

The EOM cavity consists of flat mirror M2 and mirror M3 with an ROC of 300 mm. The AR-coated side of the flat mirror M2 faces the EOM cavity. The distance between the reflective surface of mirror M2 and mirror M3 is 287.13 mm, resulting in FSR of the EOM cavity $\mathrm{FSR_{EOM}} = 478$ MHz. This length of the EOM cavity requires us to use the frequency of the EOM modulation $\omega_m = 2.39$ GHz to fulfil the requirement of $\mathrm{FSR_{EOM}} = \omega_m/k$ where k is a integer. The waist of the EOM cavity aligns with the reflective surface of flat mirror M2 and has the same radius as the input cavity, $w_0 = 0.144$ mm, ensuring good mode matching between the two cavities. At the

crystal facet closer to the input cavity, the beam radius is $w_{\mathrm{A}} = 0.473$ mm.

For this cavity configuration, the 477^{th} sideband of the EOM cavity will become resonant with the input cavity. This sets the characteristic mode of the coupled-cavity OFCG to $\nu_c = 477$.

3.8 Modelling of a Coupled Cavity OFCG

The theoretical framework of the coupled-cavity OFCG provides an expression (Eq. 3.22) that serves as a predictive tool for estimating the system's output. To model the system, we employed the Python programming language, taking into account the considerations of simulation time optimisation and accuracy. To strike an optimal balance between the two, we set the size of the transformation matrix $M(2\delta)$ to 2501. This choice enables us to obtain efficient and reliable results within a reasonable time frame.

In this Section, we will delve into the practical application of the theoretical data derived from the mathematical solutions presented in Section 3.6. The primary objective is to determine the appropriate parameters necessary for generating short and intense pulses of light using coupled-cavity OFCG. Accordingly, our focus will centre on optimising the efficiency of the coupled-cavity OFCG, as it plays a crucial role in converting pump laser power into a high-power Lorentzian pulse train. The second parameter of interest is the FWHM pulse width τ_p, which needs to be minimised to achieve the maximal peak pulse power, as shown in Section 3.2.

For the optimisation process of the coupled-cavity OFCG, we have selected reflectivities of 0.99 for input cavity mirrors (M1 + M2). This choice is underpinned by the imperative to safeguard the EOM AR-coating against damage stemming from excessively high intra-cavity intensities. Maintaining a critical threshold of intra-cavity intensity is pivotal in preventing such harm.

Furthermore, the pursuit of higher reflectivity mirrors, such as 0.999, results

in an optical cavity with significantly heightened finesse. While increased finesse is advantageous in mitigating sideband leakage from the EOM cavity, it also poses challenges. Requiring narrow linewidth input lasers to lock to a narrow linewidth input cavity, these high-power lasers with narrow linewidths are expensive.

Additionally, adopting a mirror with a reflectivity of 0.999 for the input coupler necessitates an output coupler (M3) with a reflectivity below 0.9 to balance the cavity losses and output coupling efficiently. However, sourcing mirrors that meet both the 300 mm ROC requirement and the desired reflectivity of less than 0.9 proves to be challenging. The difficulty lies in the availability of such mirrors off the shelf. This combination of specifications is not commonly stocked, leading to the need for a custom-made mirror. Opting for a custom solution would significantly increase the cost, presenting a notable constraint in the design and budget of our setup.

In light of these considerations, we made the deliberate decision to set the reflectivities of mirrors M1 and M2 to $R_1 = R_2 = 0.99$ during the optimisation process of the coupled-cavity OFCG.

3.8.1 Results for Coupled Cavity OFCG

A typical result of the numerical simulation is presented in Fig. 3.16. For this simulation, the mirror intensity reflectivities were set to $R_1 = R_2 = 0.99$ and $R_3 = 0.96$, and the modulation depth was set to $\delta = 2.1$ radians.

Figure 3.16**a** shows the spectral output of the single-cavity OFCG and Fig. 3.16**b** shows the same spectral output on a semi-log scale. The linear relationship of the sidebands on the semi-log plot is disrupted by the partial leakage of the 500^{th} sideband to the input cavity.

Figure 3.16**c** shows the temporal output of the OFCG, this was obtained by performing a Fourier transformation of the spectral output in Fig. 3.16**a**.

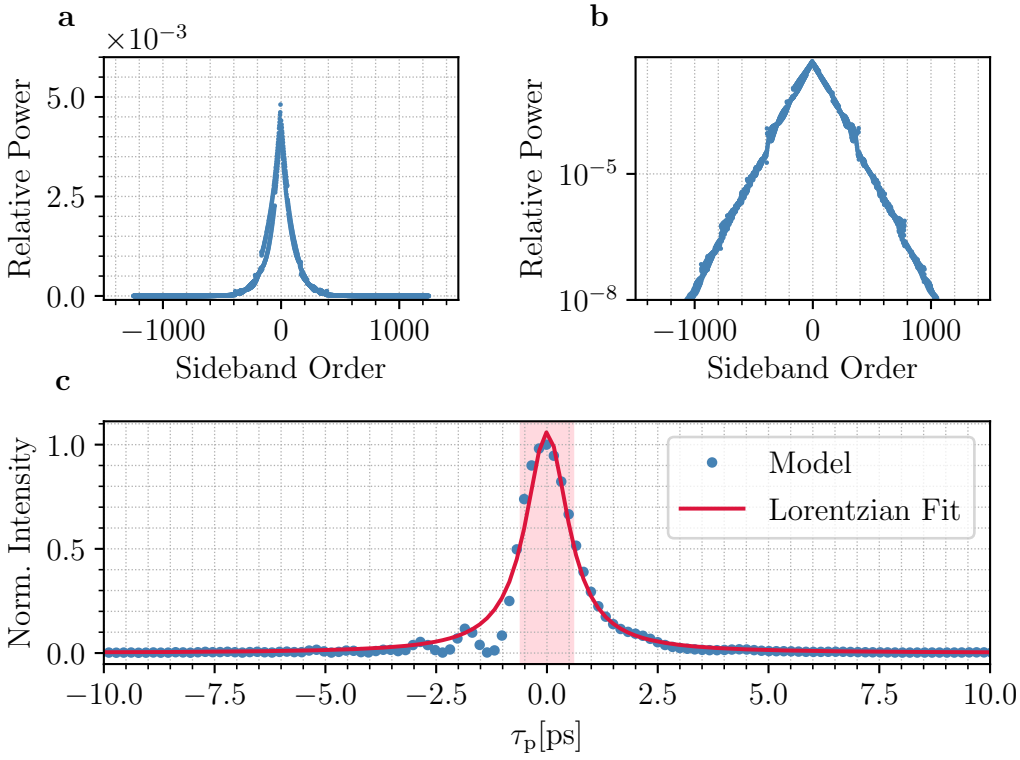

Figure 3.16: A typical result of the numerical model of the coupled-cavity OFCG. Parameters of the model were $\delta = 2.1$ radians, $R_1 = R_2 = 0.99$, $R_3 = 0.96$, $\mathrm{FSR_{in}} = 21.13$ GHz, $\mathrm{FSR_{EOM}} = 478$ MHz and remaining parameters as detailed in the Section 3.5. The input electric field was set to 1. The resulting efficiency $\eta_{\mathrm{SC}} = 81.9$ % was calculated by summing the squared electric field of each sideband and dividing it by the input intensity of 1. **a** The spectral output of the single-cavity OFCG. **b** The semi-log plot of the spectral output. **c** The temporal output of the single-cavity OFCG obtained by performing the Fourier transform of the spectral output. The model data was fitted with a Lorentzian function to estimate the pulse width of $\tau_p = 1.2$ ps indicated by the red shaded area.

The red area marks the FWHM pulse width τ_p=1.2 ps. The asymmetry of the pulse is a combined effect of the truncation of the transformation matrix $M(2\delta)$, the crystal dispersion effect, and the effect of the partial leakage of the 500^{th} sideband to the input cavity.

These results provide insight into the spectral and temporal characteristics of the coupled-cavity OFCG, demonstrating the impact of various factors on the pulse shape and the disruption of the sideband relationship due to characteristic mode.

3.8.2 Optimisation of the coupled-cavity OFCG

The primary objective is to maximise the effective pair detection rate obtained from output pulses from the OFCG. This pair rate scales as a function of P^2/τ_p both of which depend on the OFCG cavity parameters. To achieve this goal, we conducted a series of simulations utilising the numerical model presented in Section 3.6, in order to maximise the pair production rate in the process of SWFM. Throughout these simulations, we will systematically vary two parameters the modulation depth δ and the power reflectivity of the output mirror M3 R_3. The reflectivity of the mirrors M1 and M2 are set to $R_1 = R_2 = 0.99$, as discussed in Section 3.8.

The modulation depth will be varied within a range spanning from 0.1 to 2.1 radians. This range has been selected in order to match the modulation depth of the EOM we have ordered for this experiment. Simultaneously, the power reflectivity of the output mirror M3 will be varied across a spectrum ranging from 0.9 to 0.99. This spectrum has been chosen due to the availability of these mirrors with a desired ROC of 300 mm to buy off-shelf.

The decision to set the input power at 300 mW as the default stems from the availability of single-mode, single-frequency laser diodes operating at the desired wavelength of 785 nm. This input power level ensures compatibility with the diodes while allowing us to comprehensively explore the parameter space. However, it is crucial to emphasize that during each simulation run, we will closely monitor the intra-cavity intensity. As a precautionary measure, we will lower the input power whenever necessary to ensure that the operation remains well below the damage threshold, safeguarding the integrity of the AR-coating of the EOM.

Our investigation will unfold in several stages, focusing on the following key aspects:

1. **Efficiency Data Analysis:** We will initially examine the efficiency

data obtained from our simulations. By systematically varying the modulation depth and reflectivity of the output mirror, we aim to identify optimal combinations that yield superior efficiency in power conversion.

2. **Pulse Width Data Analysis:** Following the efficiency analysis, we will delve into the pulse width data. This step involves evaluating the impact of different modulation depths and mirror reflectivities on the temporal characteristics of the output pulses. This analysis is pivotal in determining the trade-offs between efficiency and pulse duration, aiding in the selection of parameters that align with the desired pulse duration specifications.

3. **Peak Power Per Pulse Estimation:** Combining the efficiency and pulse width data, we will determine the estimated peak power per pulse for various parameter combinations. This estimation will be calculated while considering the maximum input power allowed to maintain safe operation. The resulting peak power per pulse values will serve as crucial benchmarks for the subsequent evaluation of photon pair generation through the process of SFWM.

This Section outlines our comprehensive approach to optimizing the peak power per pulse generated by the coupled-cavity OFCG. Through systematic simulations and parameter variations, we aim to uncover optimal conditions that maximize power extraction while adhering to operational safety limits. The resulting insights will not only enhance our understanding of the OFCG's performance but will also serve as a foundation for estimating the potential photon pair generation via SFWM.

3.8.2.1 Variation of efficiency

In our pursuit of optimizing the peak power per pulse generated by the coupled-cavity OFCG, we begin by analyzing the output efficiency of the system η_{CC} under different parameter settings. This analysis provides insights into the power conversion effectiveness and guides us towards parameter combinations that yield superior efficiency.

To conduct this analysis, we systematically vary the modulation depth δ and the power reflectivity of the output mirror M3 within the prescribed ranges.

The efficiency of the coupled-cavity OFCG is determined by the ratio of the output power to the input power. Mathematically, the efficiency η_{CC} is defined as follows

$$\eta_{\mathrm{CC}} = \frac{|E|^2_{\mathrm{out}}}{|E|^2_{\mathrm{in}}}, \tag{3.25}$$

where $|E|^2_{\mathrm{out}}$ represents the output power and $|E|^2_{\mathrm{in}}$ is the input power. For simplicity, we assume that the input power to the coupled-cavity OFCG is equal to 1.

Through our simulations, we created an efficiency map that illustrates how different combinations of modulation depth and mirror reflectivity impact the efficiency of the OFCG. This map, shown in Fig. 3.17, allows us to identify regions of high efficiency, guiding us towards optimal parameter values.

Preliminary observations suggest that efficiency tends to peak at modulation depth $\delta \sim 1$, and drops slightly as we increase the reflectivity of the mirror M3. The peak output efficiency $\eta_{\mathrm{CC}} = 99\%$ was observed for $\delta = 1$ and $R_3 = 0.9$.

In the following Section, we will delve into the analysis of pulse width data, providing insights into the temporal characteristics of the generated pulses. By combining efficiency and pulse width analyses, we aim to make informed decisions that align with our goal of maximizing peak power per pulse.

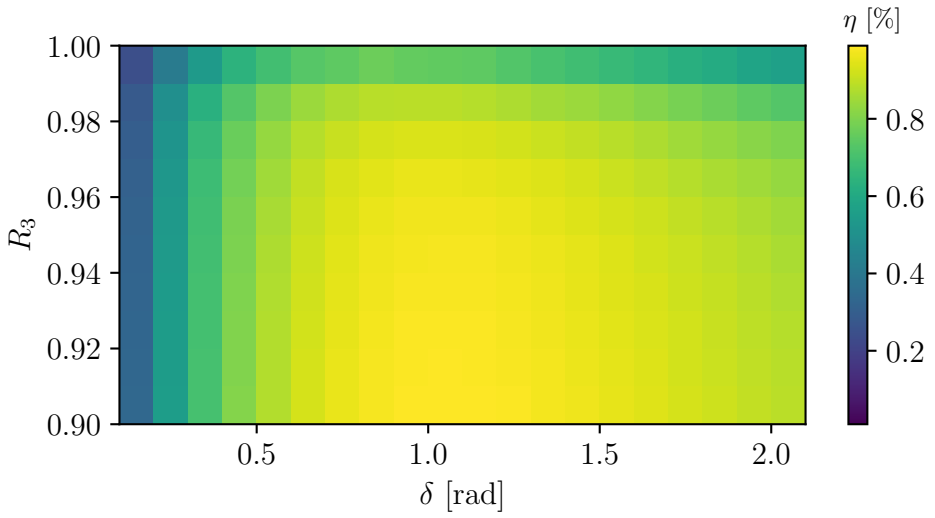

Figure 3.17: Output efficiency optimisation results indicating a maximum efficiency at a modulation depth of 1 rad. For modulation depths greater than 1 rad, a noticeable slight decrease in efficiency is observed, delineating the optimal modulation depth for peak efficiency.

3.8.2.2 Variation of pulse width

Having explored the efficiency landscape, we now turn our attention to the temporal characteristics of the output pulses, which are of paramount importance for our application of the coupled-cavity OFCG.

To investigate the FWHM pulse width τ_p, we systematically examine the impact of different modulation depths δ and mirror M3 reflectivities on the temporal profile of the output pulses. Our simulations, conducted using the numerical model of the coupled-cavity OFCG, enable us to acquire FWHM pulse width data for each parameter combination by performing a Fourier transform of the spectral output of our simulation.

By systematically varying the modulation depth and mirror reflectivity, we construct a $1/\tau_p$ colour map shown in Fig. 3.18, that illustrates how different parameter combinations influence the temporal characteristics of the generated pulses. To make the Fig. 3.18 easier to read, we plotted the $1/\tau_p$ values, this way of presenting the data makes it easy to spot the shortest pulses

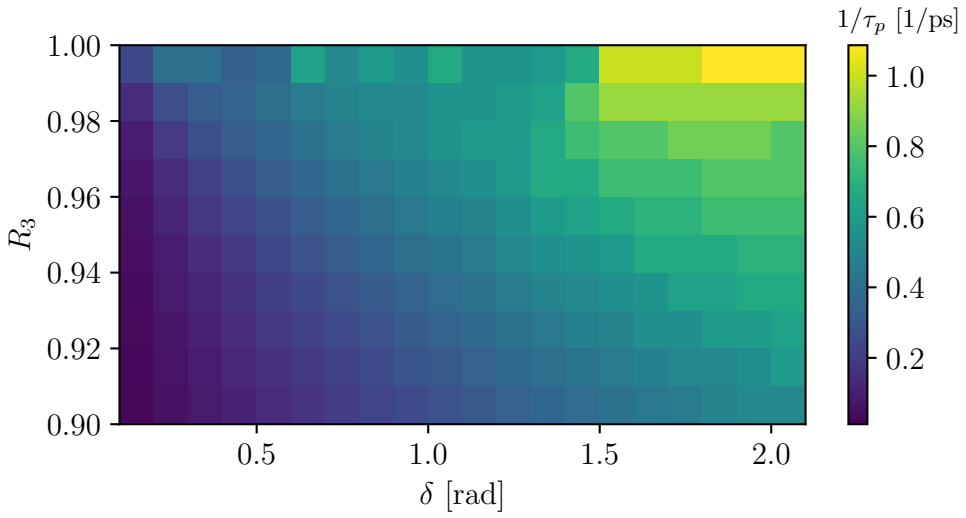

Figure 3.18: The result of FWHM pulse width τ_p optimisation. The values plotted here correspond to $1/\tau_p$, this ensures that the highest value aligns with the shortest FWHM pulse width.

by looking at the highest values. As expected we are observing that as we increase both δ and R_3 values, the pulses become shorter, with the shortest pulse $\tau_p = 0.92$ ps recorded for the $\delta = 2.1$ and $R_3 = 0.99$.

Our analysis aims to strike a balance between efficiency and pulse width. In some cases, higher efficiency may lead to broader pulses, while narrower pulses could be obtained at the expense of efficiency. By combining the insights gained from the efficiency and pulse width analyses, we can make informed decisions regarding the parameter settings that align with our objectives.

The optimal parameter combinations, both in terms of efficiency and pulse width, will be crucial inputs for our subsequent calculations of peak power per pulse. By considering these interrelated aspects, we aim to achieve the desired balance between output efficiency and the FWHM pulse width, ultimately enhancing the performance of the coupled-cavity OFCG.

In the next Section, we will combine the efficiency and pulse width data, along with considerations for maximum input power, to estimate the peak power

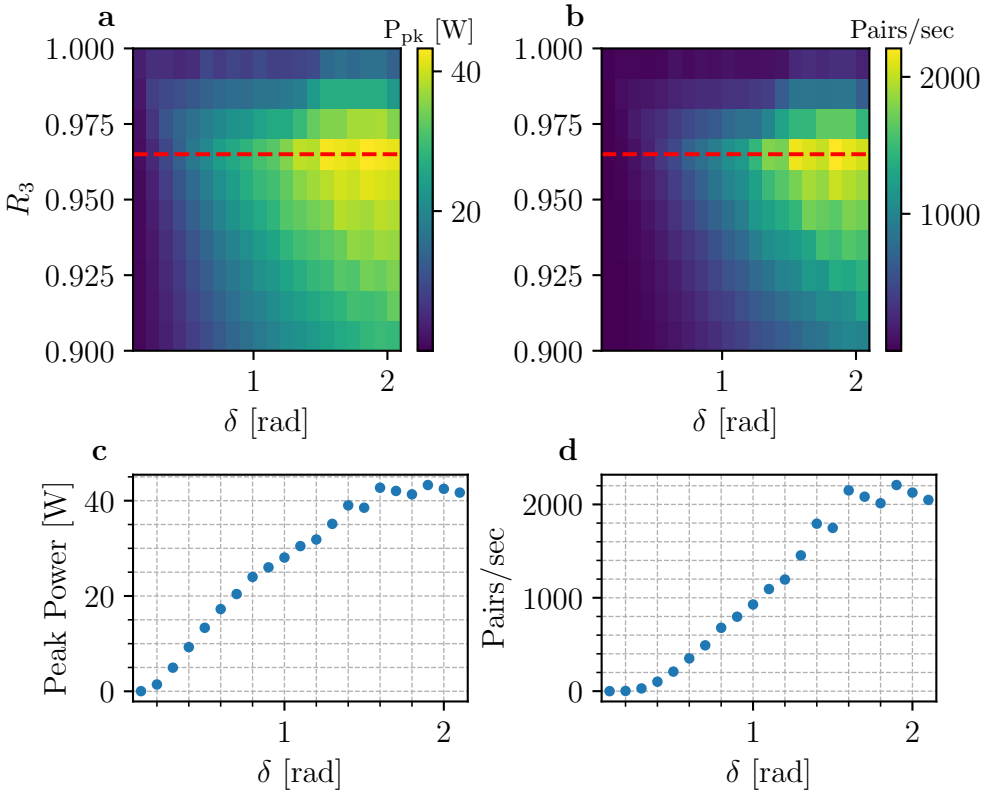

Figure 3.19: **a** The results of peak power per pulse P_{pk} optimisation. **b** The pair detection rate in the process of SFWM is estimated using results shown in **a** and Eq. 2.35 from Section 2.7. **c** Cross-section of P_{pk} at $R_3 = 0.96$ as a function of modulation depth δ. **d** Cross-section of the pair detection rate at $R_3 = 0.96$ as a function of modulation depth δ.

per pulse. This estimated peak power will serve as a foundational metric for evaluating the potential generation of photon pairs through SFWM.

3.8.2.3 Optimisation of the coupled-cavity OFCG parameters

With insights gained from the efficiency and pulse width analyses, we now embark on estimating the peak power per pulse P_{pk} generated by the coupled-cavity OFCG. This metric holds significant importance, as it provides a clear indication of the power available in individual pulses, a critical factor in our application of generating photon pairs via SFWM.

To calculate the estimated peak power per pulse, we integrate the efficiency

data and the pulse width data obtained from our simulations. The efficiency values guide us in selecting parameter combinations that optimize power conversion, while the pulse width data ensures that the generated pulses meet our desired temporal characteristics.

Mathematically, the estimated peak power per pulse P_{pk} can be calculated as

$$P_{pk} = \frac{P_{in}\eta_{CC}}{2\omega_m \tau_p} \tag{3.26}$$

where P_{in} is the input power with maximum value of 300 mW, limited by the damage threshold of the EOM. The results of the simulation can be seen in Fig. 3.19**a**. We record the highest value of $P_{pk} = 43.28$ W for $\delta = 1.8$ and $R_3 = 0.96$.

Additionally, the estimated peak power per pulse serves as a pivotal parameter for evaluating the potential generation of photon pairs through SFWM. The rate of photon pair generation depends on the P_{pk} and properties of the medium. To estimate the amount of photon pairs generated via SFWM in a 10 cm long HB800G fibre we use Eq. 2.35 from Section 2.7. The resulting estimated pair detection rate can be seen in Fig. 3.19**b**. Here for the $\delta = 1.8$ and $R_3 = 0.96$ we observe the highest pair detection rate of 2200 pairs/sec.

To further elucidate the dependency of these parameters, we provide cross-sectional views of the peak power per pulse P_{pk} and the pair detection rate at $R_3 = 0.96$. These cross-sections, shown in Fig. 3.19**c** and Fig. 3.19**d** respectively, offer a detailed look at how modulation depth δ influences these critical metrics.

3.9 Conclusions

In this Chapter, we embarked on a comprehensive journey to optimise the performance of the coupled-cavity OFCG. Our investigation was grounded

in a meticulously developed numerical model of the OFCG, which served as the cornerstone of our optimisation process. Through systematic simulations and analyses, we aimed to enhance the peak power per pulse generated by the system.

After conducting a thorough analysis, we have made a strategic decision regarding the construction of the coupled-cavity OFCG. We have selected mirror reflectivities of 0.99 for M1, 0.99 for M2, and 0.96 for M3, respectively. We plan to employ an electro-optic modulator (EOM) with a modulation depth of 1.8, modulated at a frequency of 2.39 GHz. This combination of parameters is anticipated to achieve an efficiency of 81.9 % and produce pulses with a FWHM of 1.2 ps, leading to an estimated photon pair detection rate of 2200 pairs per second through SFWM.

The culmination of our modelling and optimisation efforts, coupled with the meticulous development of the OFCG model, provides a solid foundation for the subsequent phase of our study - the experimental realization of the coupled-cavity OFCG. The next Chapter will detail the practical implementation, presenting the setup, procedures, and results of our endeavours to bring this device to life.

Chapter 4

Experimental Realisation of a Coupled-Cavity OFCG

4.1 Introduction

This Chapter describes experimental realisation of a coupled-cavity optical frequency comb generator (OFCG). This device, discussed in detail in Chapter 3, employs an intra-cavity electro-optical modulator (EOM) to convert a single-frequency continuous-wave (CW) input light into a Lorentzian train of pulses with a repetition rate twice the modulation frequency of the EOM.

In the previous Chapter, we designed a coupled-cavity OFCG system optimised for generating high-power pulses. This high-power pulsed source is crucial for generating photon pairs through spontaneous four-wave mixing (SFWM), a process detailed in Chapter 2, which in turn can be harnessed for quantum-enhanced LIDAR applications.

The focal point of this Chapter revolves around characterising the efficiency and full-width at half-maximum (FWHM) pulse width of the coupled-cavity OFCG. These two parameters wield substantial influence over the peak power per pulse, a critical factor in the photon pair generation process. The charac-

terisation of these parameters will enable us to critically assess the device's viability as a pump source for photon pair generation. It is important to note that we have set a stringent requirement of 1.5 kHz to ensure operation well above the dark-count rate of silicon-based single-photon avalanche diodes (SPADs), which typically resides around 300 Hz [113].

This chapter provides a comprehensive account of the steps undertaken to attain this objective, representing solely my work. The journey commences with the characterisation of a key element within the OFCG setup – the EOM. Subsequently, the focus shifts towards the realisation and characterisation of the single-cavity OFCG, serving as a preliminary stage to the coupled-cavity configuration. The Chapter concludes with a successful realisation of the coupled-cavity OFCG. We characterise the device and compare the experimental results to those predicted by the numerical model developed in Chapter 3.

4.2 The EOM characterisation

In this study, the characterisation of the EOM played a pivotal role, enabling us to measure two critical parameters. The crystal's intensity transmission (T_c) and its modulation depth (δ) when subjected to varying electrical power ($\mathrm{P_{RF}}$). These parameters hold substantial significance for the performance of the OFCG and play a crucial role in the numerical model introduced in Chapter 3.

To measure the crystal's transmission, we conducted a simple experiment by passing a laser beam through the EOM. By comparing the optical power before and after the device, we measured the intensity transmission $T_c = 0.996 \pm 0.001$, slightly lower than the assumed value of 0.9999 in the model. This difference can be attributed to real-world imperfections in the crystal's transmission, not fully accounted for in the idealised model assumption of

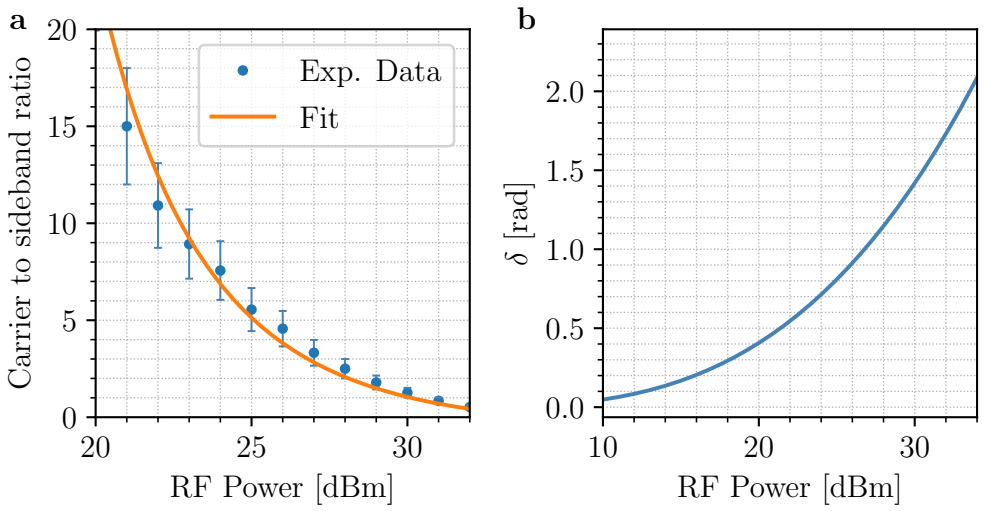

Figure 4.1: Characterisation of the modulation depth of the EOM. **a** Experimental measurement of the intensity ratio between the carrier and the first sideband, along with a fit function $|J_0(P_{RF}/\delta)|^2/|J_1(P_{RF}/\delta)|^2$ using modulation depth as a free parameter. The analysis reveals the dependency between the power of the electric field P_{RF} and the modulation depth δ. The errorbars are the standard error after repeating the measurement 10 times. The errorbar size increases for lower values of RF Power due to low intensity of the first sideband compared to the root mean square noise of the signal read out on the oscilloscope. **b** depicts the relationship between modulation depth and applied electric field power, derived from the fitting process detailed in **a**. It is worth noting that while this estimate is not perfect (in **a** the deviation from the fit can be observed) it gives a good rough estimate of the effective modulation depth in our experiments.

transmission depending solely on anti-reflective (AR) coating.

To map the modulation depth (δ) to the electrical power P_{RF} applied to the EOM, we designed an experimental arrangement that involved placing the EOM in front of a Fabry-Perot cavity scanned using a piezo actuator. We measured the intensities of the carrier and the first sideband as a function of applied RF power, using a photodetector positioned behind the Fabry-Perot cavity. To determine the resulting modulation depth, we utilised the known ratio of intensity between the carrier and the first sideband, expressed as $|J_0(\delta)|^2/|J_1(\delta)|^2$ (see Fig. 3.7). We used a fit function with modulation depth δ as a free parameter to calculate the modulation depth as the function of

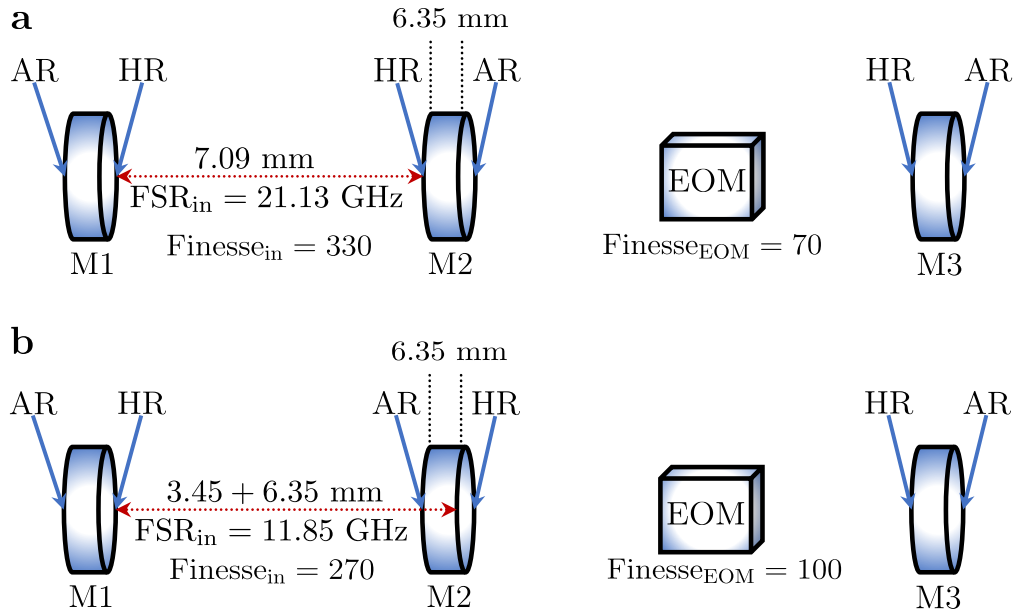

Figure 4.2: Two configurations of the OFCG depend on the placement of the AR-coated side of a flat mirror M2. **a** Original design of the OFCG where the AR-coated side of the flat mirror M2 is placed inside of the EOM cavity (M2 + M3). This configuration allowed for the optimal FSR of the input cavity of $\mathrm{FSR_{in}} = 21.13$ GHz. **b** Revisited design, where the AR-coated side of the mirror M2 is placed inside the input cavity. This change was motivated by the fact that the cavity with AR-coated side of the mirror was experiencing a decrease in the optical finesse. The EOM cavity FSR is set to 478 MHz for both configurations.

power applied to the EOM. The results of this experiment can be seen in Fig. 4.1. This simple experiment allowed us to map the modulation depth of the EOM to the RF power applied from the EOM driver. We have measured an attainable range of δ to be between 0.08 and 2.05 radians.

4.3 Revisiting the optical cavity design

During the assembly of the single-cavity OFCG, we encountered significant experimental challenges related to the placement of the anti-reflective (AR) coating of mirror M2. This can be seen in Fig. 4.2. Initially, we planned to position the AR-coating inside the EOM cavity (M2 + M3). This decision

was motivated by the desire to achieve the optimal free spectral range (FSR) of the input cavity (M1 + M2), to avoid resonance between the input cavity and one of the sidebands. This was discussed in section 3.6.1. The AR-coated side of the mirror has a thickness of 6.35 mm and refractive index of 1.45 which sets the minimal distance between mirrors of the input cavity, preventing us from achieving the optimal value of $\mathrm{FSR_{in}} = 21.13$ GHz.

To provide a context, it is important to note that the EOM cavity, when devoid of the EOM crystal, boasted a finesse of 121. Unfortunately, placing the AR coating inside the EOM cavity resulted in significant losses, reducing the optical finesse to 70. Conversely, with the AR coating outside of the EOM cavity, the finesse increased to 100. The optical finesse of the EOM cavity, as previously discussed in Chapter 3, plays a crucial role in determining the minimal pulse width τ_p generated by the OFCG.

To ensure higher peak power per pulse and avoid pulse broadening, we numerically estimated the full-width at half-maximum (FWHM) pulse width. This is because maintaining a constant modulation depth ensures consistent efficiency across the system. Therefore, the pulse width becomes the primary variable influencing the peak power per pulse. By optimising the pulse width, we directly affect the peak power achievable, with a narrower pulse width leading to higher peak power under the same efficiency conditions. When the input cavity had the optimal FSR (21.13 GHz) and the EOM cavity's finesse was 70, the resulting pulse width was $\tau_p = 2.1$ ps at modulation depth of 2.1. In the case where the input cavity FSR is set to 11.85 GHz but the EOM cavity finesse is 100 the resulting pulse width is $\tau_p = 1.7$ ps.

To maintain narrow pulse widths, we decided to relocate the AR coating to the side of the input cavity, accepting the trade-off of a sub-optimal FSR in the input cavity.

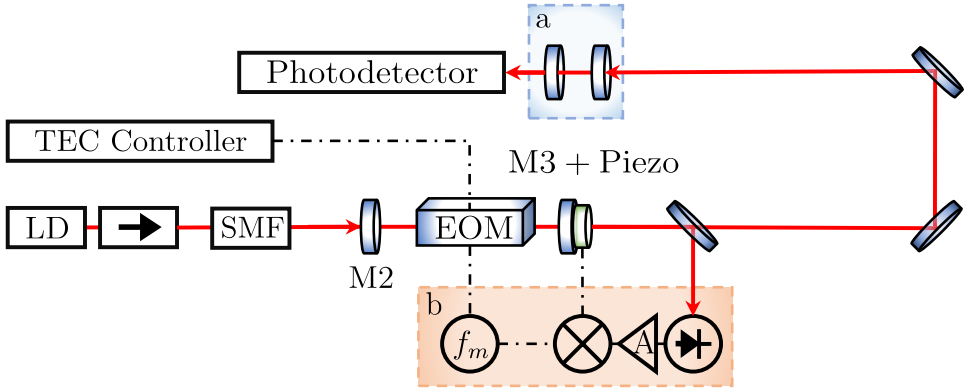

Figure 4.3: Schematic of the experimental setup showing a CW laser diode (LD) with a tandem isolator. Light is then sent into a polarisation maintaing single-mode optical fibre (SMF) to clean-up the spatial mode and launched from said fibre to the EOM cavity in free-space. The EOM cavity length is stabilised using a piezo actuator on M3 locked using an error signal derived from demodulation of a fast-photodiode signal (FPD). a : The frequency domain of the output pulses is analysed in a Fabry-Perot analysis cavity. b : Electronics allowing to stabilise the EOM cavity length. The fraction of the light transmitted through OFCG is detected by a fast photodetector. This signal is amplified and then demodulated at the modulation frequency ω_m and low-pass filtered before being sent to a fast Red-Pitaya-based PID controller which applies the feedback to the piezo actuator. Temperature of the EOM is stabilised using a TEC conbtroller.

4.4 The Single Cavity OFCG

4.4.1 Experimental set-up and Cavity Lock

Moving forward, our examination shifts to the single-cavity OFCG, laying the groundwork before exploring the coupled-cavity configuration. This phase not only serves as a foundational exploration but also enables us to compare the results of the single-cavity numerical model, described in the previous chapter, with experimental data. Such comparison is crucial for validating the model. This approach ensures a logical progression in our study, grounding the advancements in coupled-cavity OFCG within the insights gleaned from both theoretical and experimental analyses of the single-cavity setup.

The experimental setup for our realisation of a single-cavity OFCG is shown

schematically in Fig. 4.3. The pump light for the system was derived from a distributed Bragg reflector laser diode. While an initial plan mentioned the use of a 785 nm wavelength, technical difficulties with the 785 nm laser necessitated a shift to a laser operating at a wavelength of 780 nm. This laser provided a maximum power output of 30 mW for the experiment. To counteract the considerable optical feedback originating from the cavity housing the EOM, we introduced a 60 dB tandem isolator. The laser diode was coupled into a single-mode polarisation-maintaining fibre, ensuring effective spatial mode-matching into the EOM cavity. The beam leaving the fiber had a waist of 144 μm, aligned with the High-Reflectivity (HR) coated side of the input mirror M2. The intra-cavity EOM is chosen to have a resonant frequency of $\omega_m = 2.39$ GHz. The EOM crystal has length $\mathrm{L_c} = 27$ mm, group velocity dispersion GDV = 308 $\mathrm{fs}^2/\mathrm{mm}$ and intensity transmission $T_c = 0.996$. In the experiment we tune the modulation depth δ by adjusting the applied microwave power to give δ in the range of 0.3 to 2.05 rad, actively stabilising the EOM resonance frequency using feedback to a Peltier cooler that controls the crystal temperature.

The EOM cavity is constructed using flat mirror M2 and concave mirror M3 with a radius of curvature 300 mm. The power reflectivity of the mirrors was measured experimentally resulting in $R_2 = 0.99$ and $R_3 = 0.96$ for mirrors M2 and M3 respectively. The AR coating of the mirror M2 was placed outside of the EOM cavity to avoid compromising optical finesse, as discussed in Section 4.4. The finesse of the EOM cavity was restricted to 100 due to the losses caused by the finite crystal transmission and the imperfect AR coating on the crystal facet. Following initial coarse alignment, adjustments to the EOM cavity length were performed to achieve a free spectral range $\mathrm{FSR_{EOM}} = 478$ MHz, corresponding to the fifth subharmonic of the modulation frequency ω_m. Additionally, precise positioning of the EOM crystal was paramount, ensuring its placement at an anti-node of the microwave modulation frequency. This configuration guaranteed the relative phase of successive

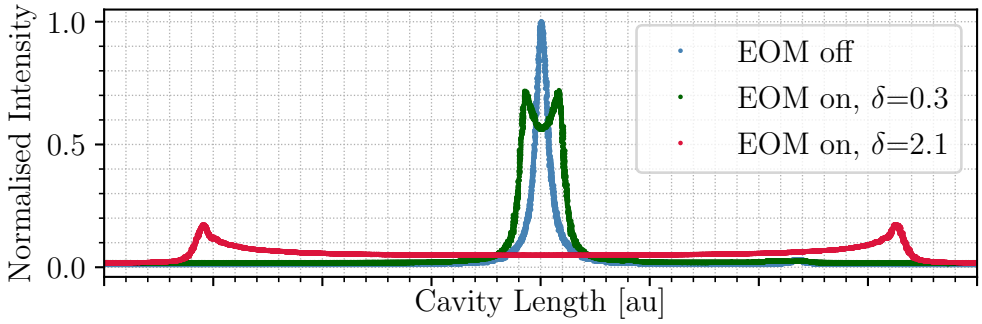

Figure 4.4: The output of the OFCG when the cavity length is scanned. When the modulation is turned off the output has a lineshape of a typical Fabry-Perot etalon with a finesse of 100 shown in blue. Red and green traces, representing modulation depths $\delta = 0.3$ and 2.1 radians respectively, show a frequency modulated double peak shape. The length of the cavity was detuned using piezo actuator with the same voltage applied to it for each scan. This shows the relative width of the features.

cavity round-trips adds constructively [123]. Initial placement of the EOM crystal was approximately in the fifth anti-node of the modulation frequency $\sim \lambda_m = 2.5$ cm from M3, where $\lambda_m = c/(5\omega_m)$. Subsequent refinement was carried out using a translation stage to maximise the suppression of the fundamental mode, thereby optimising the round-trip RF phase matching condition [123]. To optimise the position of the EOM in the cavity we use the fact that the power in the central frequency decreases as the modulation depth increases.

The output intensity from the EOM cavity as a function of the cavity sweep can be seen in Fig. 4.4. This intensity profile distinctly changes when the modulator is on. The output when the modulator is off is equivalent to the response of a typical Fabry-Perot etalon with a finesse of 100. Upon activating the modulator, a distinctive double-peak structure emerges. This characteristic response is a consequence of time averaging of the high-frequency sinusoidal sweep induced by the EOM [124], effectively modulating the cavity length. This output can be used to provide an error signal which can be used to stabilise the length of the cavity to the laser pump frequency.

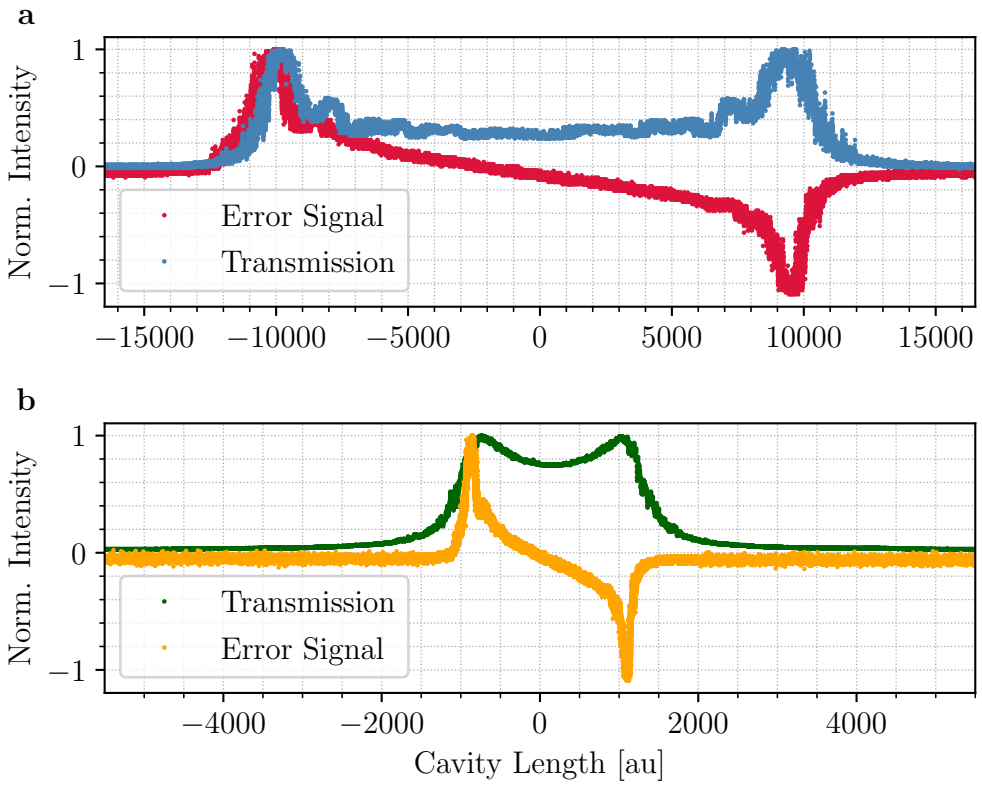

Figure 4.5: The lineshape output of the OFCG when the EOM cavity is scanning and the error signal obtained by demodulation of the output lineshape. **a** Modulation depth $\delta = 2.1$ radians. **b** Modulation depth $\delta = 0.3$ radians. From **a** and **b** we can observe that increasing the modulation depth increases the error signal bandwidth. The length of the cavity was detuned using piezo actuator with the same voltage applied to it for each scan. This shows the relative width of the features.

Additionally, there is another pivotal application for this output. It offers a method to synchronise the cavity FSR with the modulation frequency, ω_m. This is achieved by monitoring the minimal value of the double-peak structure, measured in the centre of the double peak structure. By fine-tuning the length of the cavity until the least value is discerned, it guarantees that the FSR of the EOM cavity aligns with the harmonic of the modulation frequency.

Stabilisation of the EOM cavity is achieved through the incorporation of a piezo actuator employed on mirror M3. To generate a dispersive error

signal, a portion of the light transmitted through mirror M3 is extracted and directed toward a fast-photodiode, as shown in Fig. 4.3. The resultant photodiode signal is subsequently demodulated at the modulation frequency ω_m and then subjected to a low-pass filter. We utilise the fact that at the exact resonance the power of the ω_m harmonic almost vanishes [54]. The error signal - shown in Fig. 4.5 is then amplified and directed to a fast Red-Pitaya-based PID controller [125]. By utilising this error signal in conjunction with the Red-Pitaya-based PID controller and the piezo actuator, we effectively lock the cavity to the pump laser. The control loop bandwidth is limited to 80 kHz due to piezo actuator bandwidth. This stabilisation mechanism guarantees that the performance of the optical frequency comb generator remains consistently aligned and synchronised with the input laser source.

4.4.2 Single Cavity results

To evaluate the performance of the single-cavity OFCG, we measured the output efficiency η_{SC} as a function of modulation depth. The efficiency of the OFCG was obtained by comparing the output optical power transmitted through the mirror M3, to the input optical power incident on mirror M2. Results of this experiment are shown in Fig. 4.6, with error bars representing the standard deviation of 30 measurements at each modulation depth δ. This experimental data was compared to a parameter-free theoretical curve taken from Eq. 3.4. We obtain a good agreement with the theory for the high values of modulation depth $\delta > 1.25$ and observe a slight deviation for $\delta < 1.25$. This can be attributed to the significantly lower bandwidth of the error signal when δ is reduced, as seen in Fig. 4.5.

To monitor the frequency output of the OFCG, an analysis cavity was integrated into the experimental configuration. Analysis cavity is a high-finesse ($F_{\mathrm{A}} = 312$) and high FSR ($\mathrm{FSR_A} = 130$ GHz) Fabry-Perot optical cavity. These attributes enabled the analysis cavity to effectively discern light

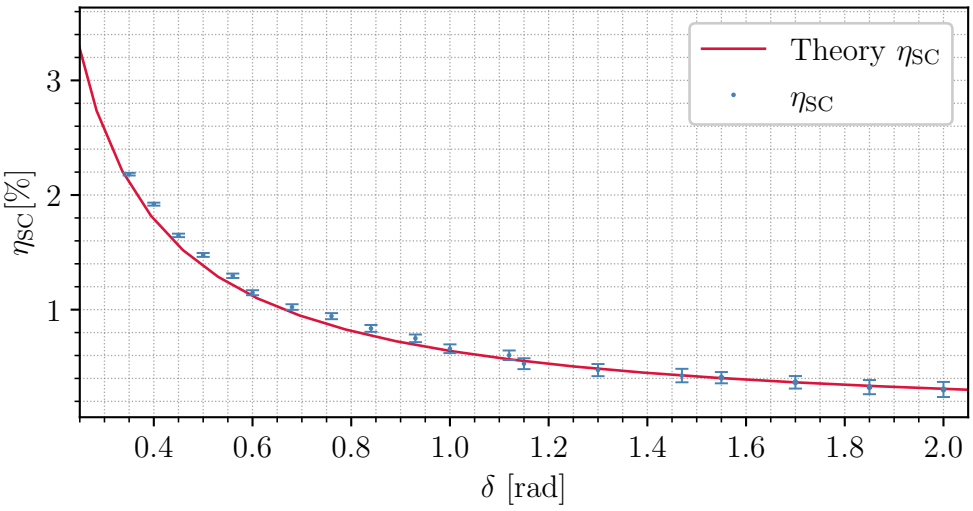

Figure 4.6: The output efficiency of a single-cavity OFCG as a function of modulation depth δ. In red, a theory curve obtained by substituting experimentally measured parameters of the system into Eq. 3.4. The error bars represent a standard deviation of 30 measurement at each modulation depth.

modes with a separation greater than $\frac{\mathrm{FSR_A}}{F_A} = 0.417$ GHz, a resolution capability well-suited for resolving a frequency comb with mode spacing of $\omega_m = 2.39$ GHz.

To align the analysis cavity, we locked the EOM cavity to a resonance while deactivating the EOM modulation. This ensured a single-mode output from the EOM cavity, which was subsequently directed into the analysis cavity. The alignment process continued until transverse modes were adequately suppressed. The frequency spectrum for the single-cavity OFCG operating at modulation depth $\delta = 0.1, 0.3, 1.25$ and 2.05 radians can be seen in Fig. 4.7. As the modulation depth is increased the spectral envelope becomes broader, but starts showing a deviation from the monotonic exponential decay with sideband order expected for the output of an OFCG. This deviation is likely due to residual amplitude modulation, which has been observed in previous experiments [51, 120, 126].

Given the low measured output power ($<$1% efficiency, $\sim$ 0.3 mW), direct

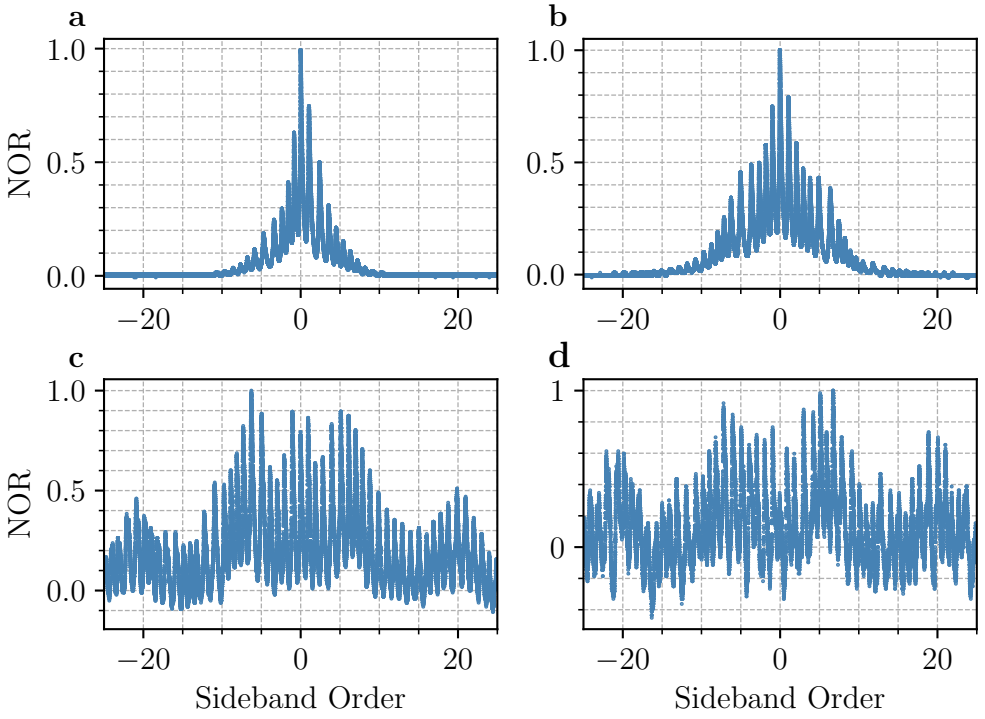

Figure 4.7: The frequency spectrum for the single-cavity OFCG operating at modulation depth **a** $\delta = 0.1$ rad **b** $\delta = 0.15$ rad, **c** $\delta = 1.41$ rad and **d** $\delta = 2.05$ rad. As the modulation depth increases, the comb's width exceeds the FSR of the analysis cavity, leading to an overlap or folding of the sidebands. NOR stands for normalised oscilloscope reading.

assessment of the pulse width proved unfeasible without resorting to advanced techniques, such as second-harmonic generation autocorrelation measurement [127]. As an alternative means to indirectly gain insights into the pulse lineshape, we turned to the frequency comb data displayed in Fig. 4.7. To validate the Lorentzian linewidth of the pulse, we performed a Fourier transform of the frequency comb generated at $\delta = 2.05$, as shown in Fig. 4.8**a**. Importantly, in conducting this Fourier transform, we assumed a phase relationship that was extrapolated from the phase relation in the numerical model of the OFCG. This assumption facilitated the approximation of the pulse shape from the spectral data, a technique necessitated by the challenges in direct time-domain measurement of the pulse width.

With the confirmed Lorentzian nature of the OFCG output, we employed

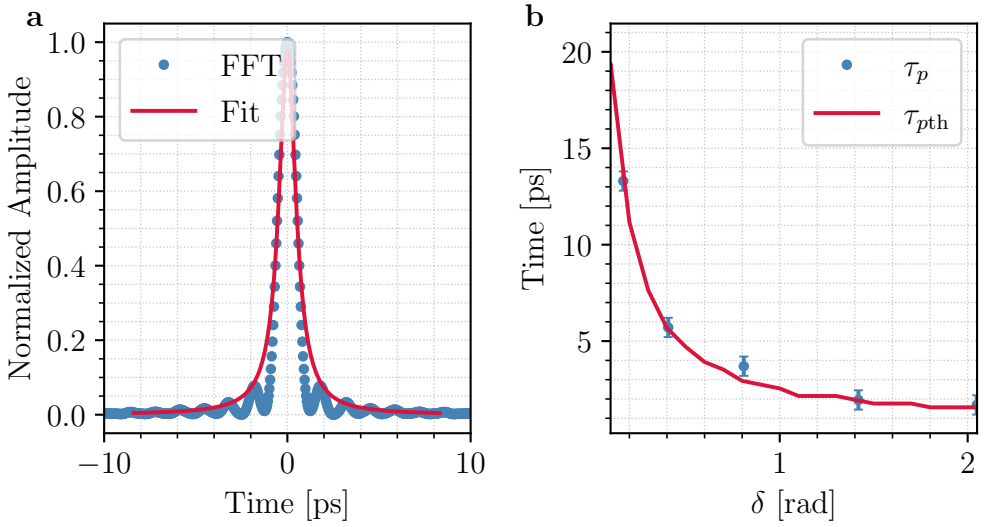

Figure 4.8: The analysis of the single-cavity temporal domain. **a** The Fourier Transform of the single-cavity OFCG frequency spectrum seen in Fig. 4.7**d**. The Fourier transform confirms the Lorentzian pulse shape. The resulting FWHM pulse width is 1.7 ± 0.05 ps. **b** FWHM pulse width τ_p as a function of modulation depth δ. In red, a theory curve obtained by substituting experimentally measured parameters of the system into the numerical model described in Chapter 3. The error bars represent a standard deviation of 30 measurement at each modulation depth.

the time-bandwidth product [128] (TBWP) to estimate the FWHM pulse width, denoted as τ_p

$$\tau_p = \frac{\text{TBWP}}{\Delta f}, \tag{4.1}$$

where TBWP for a Lorentzian is 0.142 [128] and Δf is the recorded FWHM bandwidth of the frequency comb seen in Fig. 4.7. This methodology allowed us to estimate the FWHM pulse width of the OFCG output as a function of modulation depth, as illustrated in Fig. 4.8**b**. We have measured the minimum value of $\tau_p = 1.7 \pm 0.05$ ps at modulation depth $\delta = 2.05$ radians. The experimental data aligns well with the numerically generated theory curve plotted on the experimental data.

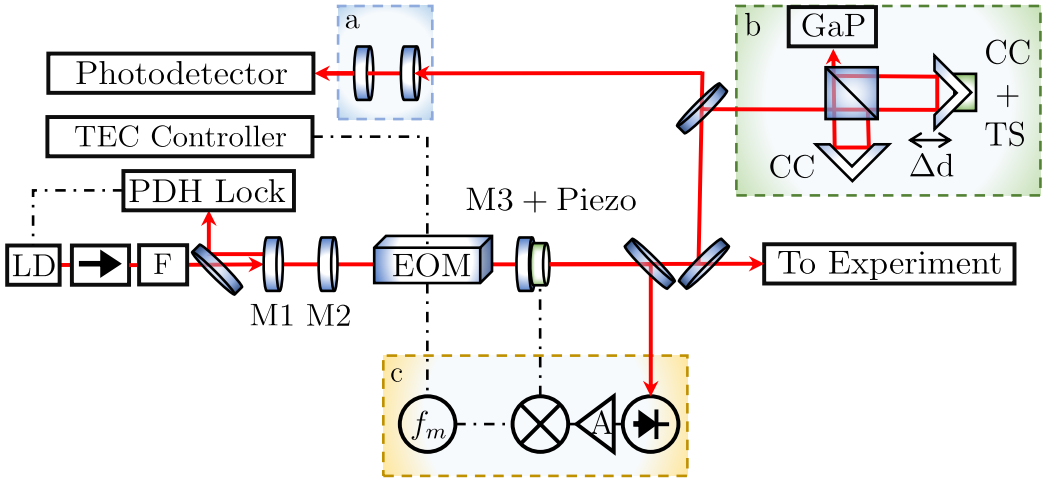

Figure 4.9: Schematic of the experimental setup showing a CW laser diode (LD) with a tandem isolator locked to the input cavity (M1+M2) using a Pound-Drever-Hall lock. Similarly to the situation in single cavity setup (Fig. 4.9) polarisation maintaining single-mode optical fibre (F) is used to clean-up the spatial mode. The EOM cavity length is stabilised using a piezo actuator on M3 locked using an error signal derived from demodulation of a fast-photodiode signal (FPD). a : The frequency domain of the output pulses is analysed in a Fabry-Perot analysis cavity. b : An auto-correlation setup with time variable delay, here CC is a corner-cube, TS is a motorised translation stage used to generate a time delay $2\Delta d/c$ and GaP is a slow GaP photodetector. c : Electronics allowing to stabilise the EOM cavity length. Details about the EOM cavity lock can be found in Section 4.4.1. Temperature of the EOM is stabilised using a TEC controller.

4.5 Coupled Cavity OFCG

4.5.1 Experimental set-up and Cavity Lock

To increase the output efficiency of the OFCG and build upon the insights gained from the single-cavity configuration, a coupled-cavity configuration was adapted from [57].

The experimental setup used to realise the coupled-cavity OFCG is schematically shown in Fig. 4.9. The input cavity (M1+M2) is a plano concave cavity with $R_1 = R_2 = 0.99$ formed using an input mirror M1 (ROC=1000 mm) and a flat mirror M2, with separation of 12.6 mm tuned to obtain a mea-

sured FSR of $\mathrm{FSR_{in}} = 11.85 \pm 0.05$ GHz. The reflectivity values (R_1 and R_2) were determined experimentally. This was accomplished by constructing an optical cavity with the specific mirrors in question and then measuring the cavity's finesse. The cavity was constructed using a monolithic brass mount to minimise the impact of the mechanical vibrations on the optical table. Mirror M2 is oriented with the AR-coated surface located inside the input cavity to suppress losses within the EOM cavity (M2+M3), resulting in a measured finesse of the input cavity $F = 280 \pm 10$. The pump light was derived from a distributed Bragg reflector laser diode operating at a wavelength of 780 nm. The laser diode output was directed into the experiment, with 30 mW measured at the input cavity mirror M1. This measurement takes into account a 25% loss introduced by the fibre coupling into the single-mode polarisation maintaining fibre, effectively quantifying the efficiency of light delivery to the cavity. Due to considerable optical feedback from the input mirror M1, a 60 dB tandem isolator is used, and a diode is fiber coupled into a single-mode polarisation-maintaining fiber to allow efficient mode-matching into the input cavity. The pump light is stabilised to the input cavity using a Pound-Drever-Hall lock [129], using a current modulation to add sidebands to the laser output at $\pm$ 4 MHz. We measured a 95% transmission of input light into the EOM cavity while the laser is stabilised, loss in transmission can be attributed to etalon effects between the HR-coated surface of mirror M1 and the AR-coated surface of mirror M2.

To stabilise the coupled-cavity system we have developed a procedure in which first we bring the input cavity close to a resonance to couple a small portion of light into the EOM cavity. Next, we engage the EOM cavity lock as described in Section 4.4.1. With the EOM cavity stabilised to the length corresponding to the fifth subharmonic of modulation frequency ω_m, we engage the Pound-Drever-Hall lock of the input cavity and lock the system. It is worth noting that due to our choice of material (brass) for building the monolithic input cavity, the slight temperature changes in the lab would

lead to a thermal drift of the cavity length. This would result in the coupled-cavity system being stable only for short periods (up to a few hours). To improve the stability of the system a material with a low thermal expansion coefficient (such as Invar [130]) could be used.

4.5.2 Coupled Cavity results

This section focuses on the characterisation of the coupled-cavity OFCG, with particular attention directed towards two key parameters, the output efficiency (η_{CC}) and the resulting FWHM pulse width (τ_p).

The significance of these parameters lies in their pivotal role in estimating the peak power per pulse, a crucial factor for the successful generation of photon pairs within the context of our quantum-enhanced LIDAR experiment. In particular, the peak power per pulse serves as a determining factor for the achievable pair detection rate through SFWM, an essential requirement for our experiment, where a minimum rate of 1.5 kHz or higher is sought.

The output efficiency (η_{CC}) of the coupled-cavity OFCG directly influences the amount of useful optical power that can be extracted from the system. This parameter is of paramount importance as it directly impacts the overall performance of the photon pair generation process.

The FWHM pulse width (τ_p) characterises the temporal duration of individual pulses within the optical frequency comb. In our case, the pulse width τ_p plays a crucial role in determining the feasibility of achieving the required photon pair detection rate for quantum-enhanced LIDAR.

To facilitate an accurate assessment of the system's performance, the experimental values of both the efficiency (η_{CC}) and the pulse width (τ_p) was compared to the numerical model developed in the Chapter 3.

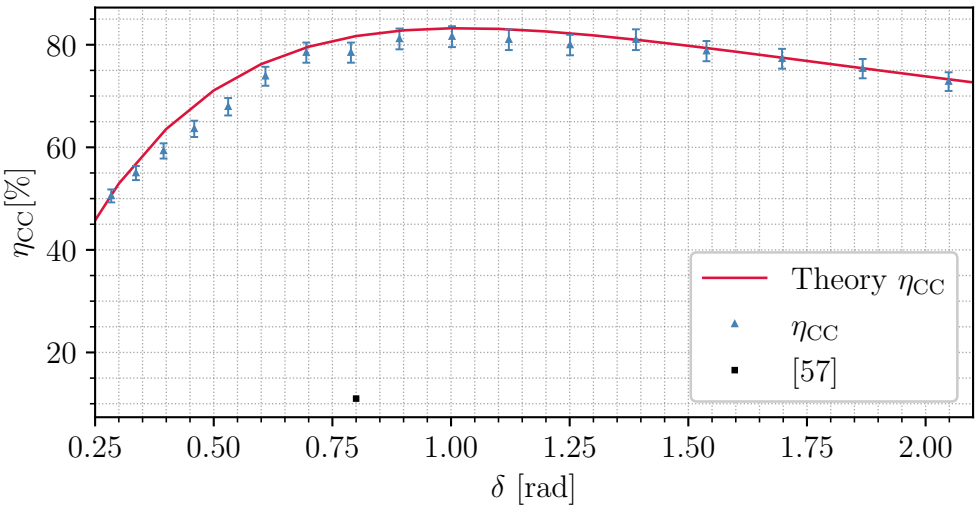

Figure 4.10: The output efficiency of the coupled-cavity OFCG η_{CC} as a function of modulation depth δ. In red, a theory curve obtained by substituting experimentally measured parameters of the system into the numerical model described in the Chapter 3. The black square represents output efficiency measured during the first demonstration of the coupled-cavity OFCG in [57]. The error bars represent a standard deviation of 30 measurement at each modulation depth.

4.5.2.1 Output efficiency characterisation

In line with the methodology used for the single-cavity OFCG case, the output efficiency η_{CC} was measured by comparing the output power transmitted through the mirror M3 to the input optical power incident on the mirror M1, while the modulation depth δ was varied. Results are shown in Fig. 4.10, with error bars representing the standard deviation of 30 measurements at each modulation depth. The maximum output efficiency η_{CC} of $81 \pm 2\%$ was recorded for $\delta = 1$ rad, this is more than two orders of magnitude improvement over the single-cavity OFCG operating at the same modulation depth. Compared to the previous demonstration of a coupled-cavity setup in [57] we recorded a 7-fold increase in the output efficiency.

The experimental data was compared to the results of the numerical simulation using parameters given in Section 4.5.1. Similarly to the single cavity

case, we observe a good agreement with the theoretical efficiency curve, with slight deviations for values of $\delta < 1.25$. This can be explained by a lower bandwidth of the error function, as well as increased leakage of the fundamental mode pump light from the EOM cavity into the input cavity which perturbs the lock, preventing stable operation at low values of modulation depth. Light remaining in the fundamental mode after propagating through the EOM is permitted to propagate in the input cavity, the amount of power remaining in the central mode can be seen in Fig. 3.7 in the previous Chapter.

4.5.2.2 Temporal output of the coupled-cavity OFCG

To characterise the pulse train output from the coupled-cavity OFCG, an analysis of its frequency and temporal output was performed. To this end, some of the output light is picked off and directed to an analysis cavity and an autocorrelation module as shown in Fig. 4.9. The analysis cavity consists of two mirrors with identical power reflectivity $R_A = 0.99$ and an FSR of $FSR_A = 130$ GHz. The autocorrelation module is a scanning Michelson interferometer using travelling corner cubes to adjust the relative pulse delay between the two arms [131]. For detecting the output of the interferometer, a slow GaP photodiode, in conjunction with a high-gain, low-noise current amplifier, was engaged. This arrangement ensured the precise capture and reliable amplification of the interferometer's output signal, aiding in the subsequent analyses.

The frequency spectrum for the dual-cavity OFCG operating at $\delta = 2.05$ rad is shown in 4.11**a**. This spectrum exhibits an FWHM bandwidth of approximately ∼90 GHz. Given the inherent properties of the OFCG output pulses, which should ideally follow a Lorentzian distribution, this bandwidth corresponds to a transform-limited FWHM pulse width of roughly ∼1.75 ps. Here the spectral envelope shows a deviation from the monotonic exponential decay with sideband order expected for a Lorentzian, however calculating

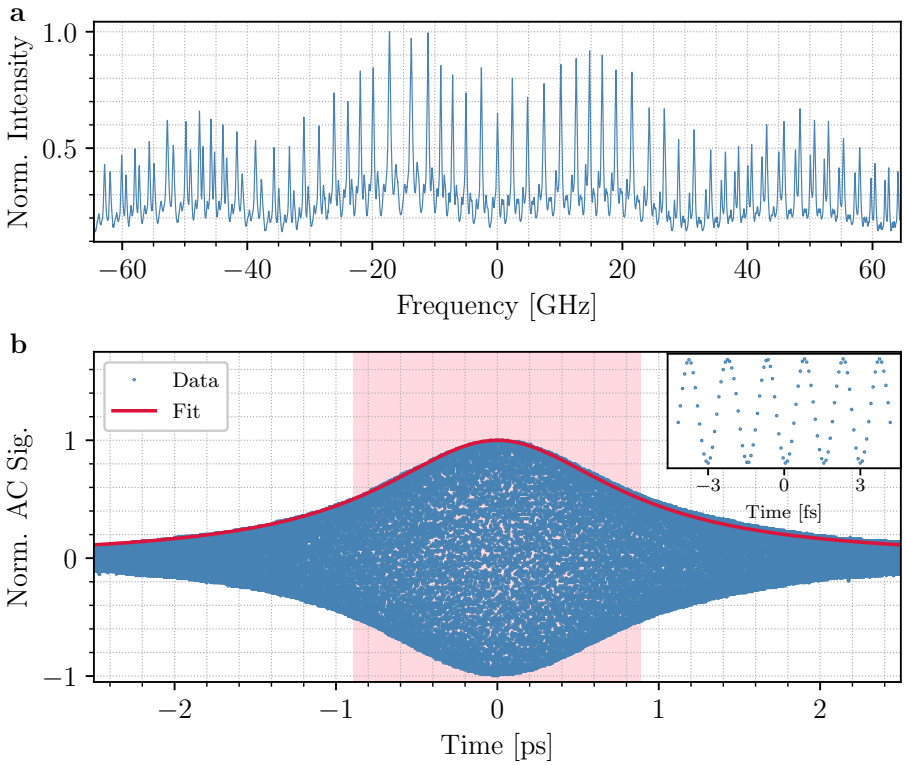

Figure 4.11: **a** The frequency spectrum of the OFCG is shown, measured using an analysis cavity with a free spectral range (FSR_A) of 130 GHz. Additional modes seen on the plot are due to incomplete suppression of transverse modes in the analysis cavity and overlapping frequency combs caused by the narrower FSR_A compared to the produced frequency comb. **b** The normalized field autocorrelation signal obtained using a scanning Michelson interferometer. The solid red line corresponds to a Lorentzian fit function employed to calculate the FWHM pulse width, resulting in $\tau_p = 1.77 \pm 0.04$ ps. The inset plot provides a depiction of the field autocorrelation signal at a femtosecond scale. Both traces were acquired using $\delta = 2.05$ rad.

the Fourier transform of the observed spectrum with the appropriate phase relationship caused by the round-trip phase accumulated in the EOM cavity shows excellent agreement with a Lorentzian pulse shape. This deviation in spectral output is likely due to residual amplitude modulation, which has been observed in previous experiments [51, 120, 126]. Comparing the spectra of the single- (Fig. 4.7) and coupled-cavity (Fig. 4.11) outputs reveals a congruent envelope. This congruence serves as a confirmation that the source of this spectral deviation is indeed rooted in the EOM cavity itself.

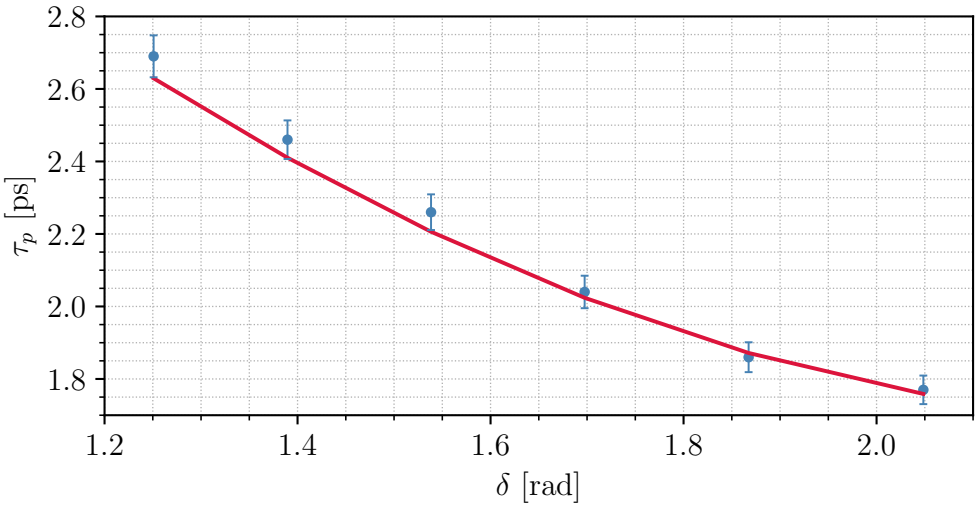

Figure 4.12: FWHM pulse width τ_p as a function of the modulation depth δ. In red, a theory curve obtained by substituting experimentally measured parameters of the system into the numerical model described in the Chapter 3. The deviation from the theory curve for lower values of modulation depth δ can be attributed to cavity lock instabilities and feedback from the EOM cavity into the input cavity for lower values of modulation depth. The error bars represent a standard deviation of 30 measurement at each modulation depth.

In order to measure the pulse width independently we record the field autocorrelation as shown in 4.11**b**, using the observed interference fringes to calibrate pulse delay. Due to the relatively low peak pulse power, we are unable to observe a two-photon absorption feature using the GaP detector, and this data therefore corresponds to the linear field autocorrelation signal [131]. To determine the pulse width, a Lorentzian fit was applied to the temporal envelope. The outcome of this fitting procedure yielded an FWHM pulse width measurement of 1.77 ± 0.04 ps. This measurement closely aligns with the pulse width derived from the spectral characterization conducted utilizing the analysis cavity.

Using the autocorrelation module we have performed measurements of FWHM pulse width τ_p as a function of modulation depth δ. The results of that experiment can be seen in Fig. 4.12. Here, the deviation from the

theory curve for lower values of modulation depth δ can be attributed to cavity lock instabilities and feedback from the EOM cavity into the input cavity for lower values of modulation depth.

4.5.2.3 Variation of the characteristic mode

The OFCG output pulse width depends strongly on the characteristic mode ν_c of the EOM cavity that becomes resonant with a mode of the input cavity, as discussed in Section 3.6.1. This characteristic mode leads to a distinct cutoff in the frequency comb's spectrum, resulting in a reduction in its maximum spectral span and an increase in the temporal width of the output pulse. The behaviour of the characteristic mode is closely tied to the FSRs of both the input and EOM cavities. To prevent the premature onset of the characteristic mode, careful selection of these FSR values is imperative. Consequently, to optimise the generation of short optical pulses, we conducted an experiment. In this experiment, we systematically varied the FSR of one cavity while measuring the FWHM of the resultant optical pulse.

The monolithic design of the input cavity prevents scanning of $\mathrm{FSR_{in}}$. Instead, we scan the FSR of the EOM cavity by adjusting the frequency of modulation ω_m and temperature-tuning the EOM back into resonance, followed by adjusting the physical EOM cavity length to ensure it remains an integer multiple of the modulation frequency. This approach means we can scan $\mathrm{FSR_{EOM}}$ without introducing a relative detuning between the EOM and the cavity, such that changes in pulse width arise only from a change in the ratio of $\mathrm{FSR_{EOM}}$ to $\mathrm{FSR_{in}}$.

Results are shown in Fig.4.13, where the effect of changing the ratio between $\mathrm{FSR_{in}}$ and ω_m on the measured pulse width can be observed corresponding to an increase in pulse width as the characteristic mode number is reduced as the EOM cavity is tuned away from the optimum operating point. We additionally add the predictions of the theoretical model, which shows excellent

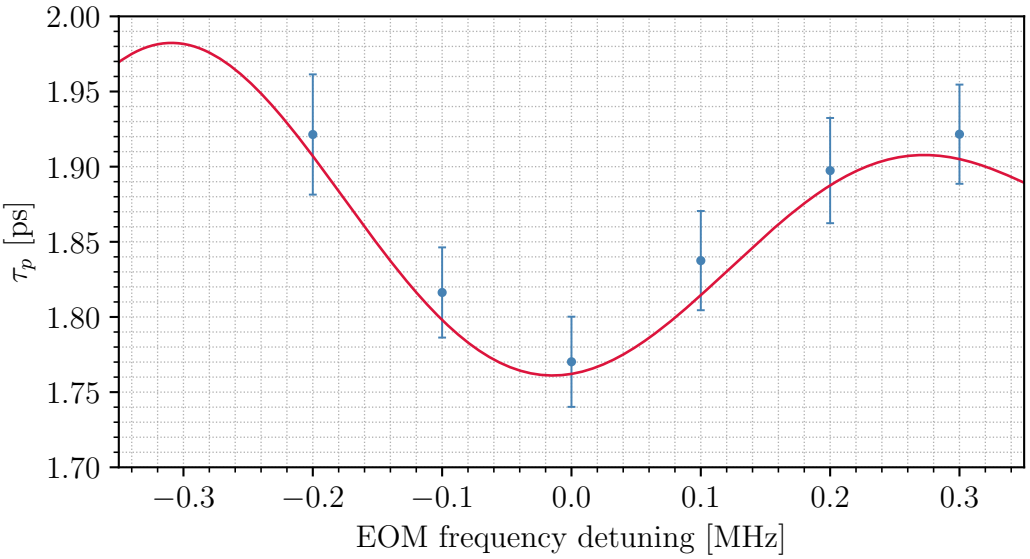

Figure 4.13: The FWHM pulse width as a function of the EOM cavity frequency detuning. For each EOM resonance frequency, the cavity length is adjusted to ensure the cavity FSR is a harmonic of the modulation frequency. The solid line shows a fit to the theoretical model. Data presented here are obtained with a modulation depth of $\delta = 2.05$ rad.

agreement with the observed changes.

4.5.3 Peak power per pulse

Extracting the output efficiency and the FWHM pulse width allows us to calculate the peak power per pulse (P_{pk}) of the coupled-cavity OFCG using

$$P_{pk} = \frac{P_{in}\eta_{CC}}{2\omega_m \tau_p}, \tag{4.2}$$

where the P_{in} is the average optical power going into the coupled-cavity OFCG, η_{CC} is the output efficiency of the device, $2\omega_m$ is the repetition rate of the Lorentzian pulse train and τ_p is the FWHM pulse width.

Using this equation we can extract the peak power per pulse as a function of modulation depth. Results are shown in Fig. 4.14, with the drop in output efficiency for $\delta > 1$ observed in Fig. 4.10 compensated by the reduction in pulse width $\propto 1/\delta$ corresponding to a peak pulse power of 2.6 W. Again we

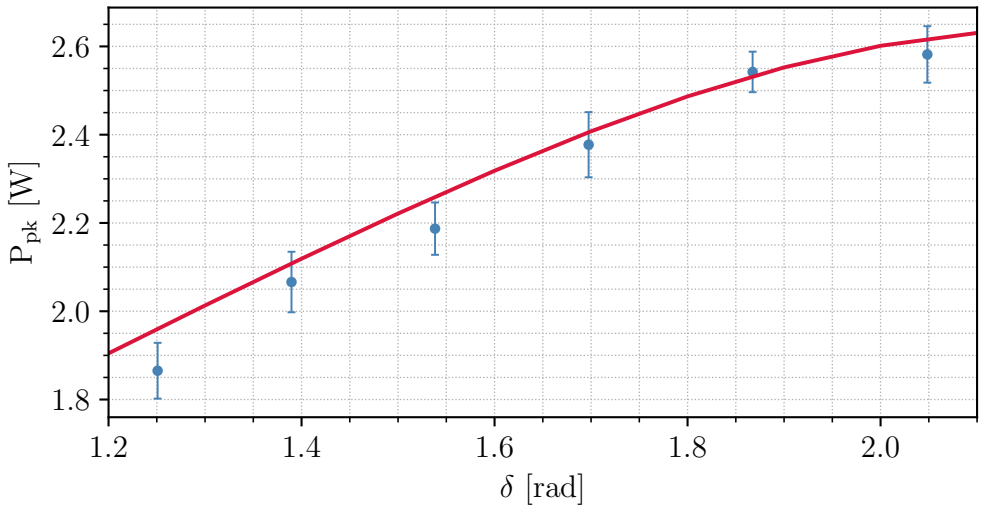

Figure 4.14: The estimated peak power per pulse P_{pk} as a function of modulation depth. In red, a theory curve obtained by substituting experimentally measured parameters of the system into the numerical model described in the Chapter 3. Data presented here were taken using 30 mW input power. The error bars represent a standard deviation of 30 measurement at each modulation depth.

see good agreement with the theoretical model, with a larger deviation in the predicted peak power at lower modulation depths primarily due to the reduction in input cavity lock stability.

4.6 Conclusions

Our research has led to the development of a highly efficient and high repetition rate source of pulsed light. With an input power of 30 mW, peak powers of $\sim$ 2.6 W were observed at a repetition rate of 4.78 GHz, achieving pulse widths down to 1.77 ps constrained by the maximum attainable modulation depth of the EOM. The findings of our study align remarkably well with a parameter-free theoretical model of the OFCG, showcasing its robustness and accuracy.

In our pursuit of obtaining even greater output power, we conducted a com-

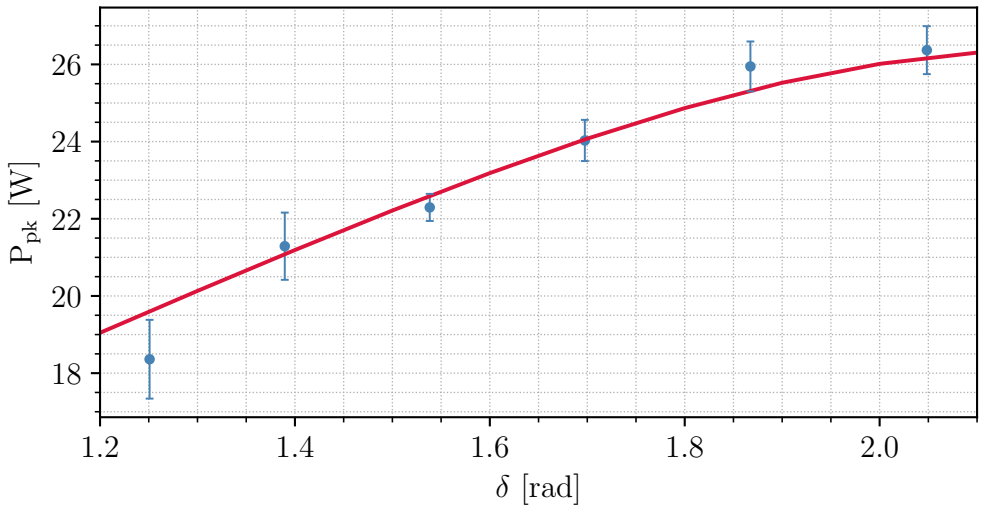

Figure 4.15: The estimated peak power per pulse P_{pk} as a function of modulation depth. Data presented here were taken using 300 mW input power provided by a Ti:Sapphire laser. The error bars represent a standard deviation of 30 measurement at each modulation depth.

prehensive characterisation using a high-power, narrow linewidth Ti:Sapphire laser, operating at a wavelength of 780 nm with a linewidth of less than 1 MHz. This enabled us to channel up to 300 mW of power into the OFCG. Our measurements, as illustrated in Fig. 4.15, affirm that the OFCG retains the same high efficiency and pulse width observed with the low-power laser configuration. The current limitation in operating with higher input powers arises from the damage threshold of the EOM AR coating of 20 W/mm^2. This, combined with the relatively small active crystal aperture of 1.5×2 mm required to maintain a GHz resonance frequency limits us to 300 mW pump.

In future, this can be overcome using alternative coatings or EOM crystal materials, or for example, operating at telecom wavelengths to benefit from higher damage thresholds.

4.6.1 Pair rate estimations

In this Chapter, our foremost objective was to thoroughly evaluate the performance of the coupled-cavity OFCG, particularly with the aim of establishing its suitability as a robust pump source for initiating the process of SFWM. Our primary drive behind this investigation lay in determining whether the generated pulses exhibited the requisite power to serve effectively as a pump source for instigating the SFWM process. Central to this evaluation was the critical criterion of achieving a minimum pair detection rate of 1.5 kHz. This threshold was thoughtfully chosen to operate well above the dark count levels of silicon-based SPADs, ensuring reliable and accurate detection [113].

We examined the coupled-cavity OFCG's output efficiency and pulse width. These parameters served as crucial indicators of the system's capability to generate pulses of the desired power for our intended purpose. Our investigation yielded an output efficiency of $\eta_{\mathrm{CC}} = 72.4$ % and a FWHM pulse width of $\tau_p = 1.77$ ps. These pulses were generated at a repetition rate equal to twice the modulation frequency of the EOM, equating to $2\omega_m = 4.78$ GHz. Leveraging these parameters allowed us to compute a peak power per pulse of $\mathrm{P_{pk}} = 25.5$ W, assuming an input power of 300 mW, constrained by the EOM's damage threshold.

With this peak power value in hand, we could estimate a pair detection rate of 0.75 kHz using the Eq. 2.35 outlined in Section 2.7. Notably, this value fell short of the prediction from the numerical model described in Chapter 3, where we predicted above 2 kHz pairs. This discrepancy could be attributed to various factors, including losses introduced by imperfect crystal transmission in the EOM, resulting in lower EOM cavity optical finesse. Moreover, the etalon effects in the input cavity, due to the position of the AR coating are creating additional losses. Moving the AR coated side of the mirror M2 led to operating at a suboptimal $\mathrm{FSR_{in}}$, leading to an earlier occurrence of the characteristic mode, impacting the minimal obtainable FWHM pulse

width.

While the coupled-cavity OFCG did not precisely meet our initial power requirements, it still holds promise for generating photon pairs, particularly for applications in Quantum LIDAR. Shifting to longer wavelengths (telecom range) would offer a higher damage threshold for the EOM's AR-coating, enabling the use of a more powerful input laser and consequently boosting the peak power per pulse. Moreover, by rethinking the device's design, such as incorporating a longer input cavity and employing a wedged AR-coated mirror (M2), we could potentially mitigate the etalon effect, leading to improved performance and optimised characteristic mode.

In conclusion, though our current photon source might not have met all the desired specifications, the journey does not end here. The potential for generating photon pairs remains bright, with avenues for improvement and optimisation ready to be explored. The photon source may be evolving, but its potential impact endures.

Part III

Quantum-enhanced LIDAR

Chapter 5

Heralded Single Photon Source

5.1 Introduction

Central to the idea of quantum-enhanced LIDAR is the concept of heralding the creation of single photons. When a photon pair is generated near-simultaneously, a local detection of one of the photons can be used to herald the presence of the second photon of the pair. Leveraging this coincidence detection mechanism, we can significantly enhance the signal-to-background ratio (SBR) of our LIDAR system by effectively discriminating against uncorrelated background photons [14]. This Chapter describes the experimental realisation and characterisation of a heralded single photon source which will become the beating heart of the quantum-enhanced LIDAR in Chapter 6.

Initially, our path towards generating photon pairs for the purpose of quantum-enhanced LIDAR involved the development of a coupled-cavity optical frequency comb pulsed source. As detailed in Chapter 3, we had planned to use that source to generate pairs of photons in the process of Spontaneous Four-Wave Mixing. However, rigorous characterisation revealed an inability to meet our stringent power requirements, primarily due to the material limitations. This necessitated a strategic shift, redirecting our focus toward

using Spontaneous Parametric Down-Conversion (SPDC) process as a source of photon pairs. In this scheme, a single pump photon undergoes a transformation into a correlated pair of signal and idler photons, offering compelling prospects with small temporal uncertainty in the photon pair creation process being ideal for coincidence detection.

This chapter describes the creation and characterisation of our photon pair source, we commence with the experimental realisation of the heralded photon source. Subsequently, we transition to the essential apparatus facilitating our investigations into time-correlated single photon counting. This section comprises an exhaustive analysis of Single-Photon Avalanche Diodes (SPADs) and the time tagger, instrumental components responsible for achieving precise timing of photon detection events.

Following this, we delve into the meticulous process of characterising the performance of our heralded single photon source. This pivotal step underpins our research efforts, enabling the fine-tuning and optimisation of the source for quantum-enhanced LIDAR applications.

The findings unveiled within this Chapter, representing solely my work, serve as the foundational bedrock upon which the next Chapter will build. In Chapter 6, we will harness the capabilities of this heralded photon source to conduct target discrimination and time-of-flight rangefinding measurements, thus realising the transformative potential of quantum-enhanced LIDAR in the domain of precision measurements and remote sensing.

5.2 Heralded Photon source

To realise the heralded photon source, shown schematically in Fig. 5.1, we will be utilising the SPDC Type-II process. In this process, described in detail in Section 2.5, a pump photon interacts with the nonlinear medium, where it spontaneously gives rise to a non-classically correlated pair of photons

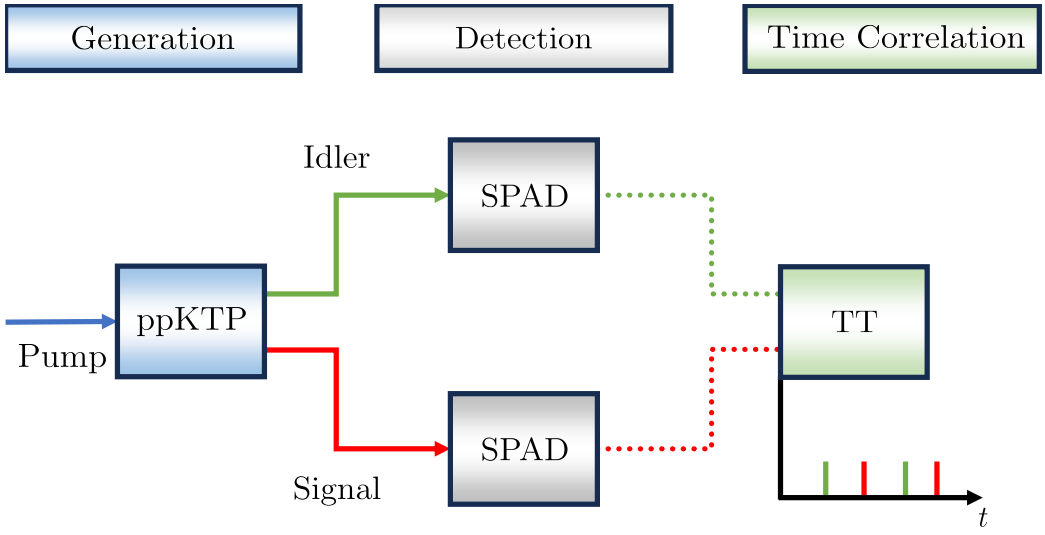

Figure 5.1: Diagram showing the heralded photon source. The 405 nm pump interacts with the ppKTP crystal at the temperature of 62°C, where in the process of Type-II SPDC a wavelength-degenerate photon pair at 810 nm is created. The resulting photon pair is then separated and detected using SPADs. These SPADs generate an electrical signal upon successful detection of the signal/idler photon. This electrical signal is then directed to a time-tagger (TT) which allows us to determine with picosecond resolution the time of arrival of the electrical signal emitted by the SPADs. Time-tagger resolution is however limited by the timing jitter of the SPADs.

typically called the signal and idler photons.

For our realisation of the heralded photon source we have chosen a periodically-poled potassium titanyl phosphate (ppKTP) with a poling period of 10 μm and a pump wavelength $\lambda_p = 405$ nm. This decision was motivated by a couple of factors, the first being the colinear output of the resulting signal and idler fields exiting the ppKTP crystal. This colinearity simplifies the task of coupling these photons into optical fibers and detecting them with SPADs. The ability to efficiently collect and detect photons is of paramount importance in our experiments, as discussed in Section 2.5.3.

Secondly, the signal and idler photons generated through SPDC Type-II possess orthogonal polarisation. This property is instrumental in our experiment as it enables the separation of the photon pair with minimal optical compo-

nents, as each optical element introduces potential loss of photon pairs. In our experiments, we will be utilising a polarising beam splitter to split the signal and idler photons.

Finally, the pump wavelength of 405 nm and the crystal poling period of 10 μm were chosen in order to generate a wavelength-degenerate signal/idler pair at $\lambda_{s/i} = 810$ nm at a reasonable temperature of the crystal of $\sim 62°$C (See Section 2.5.1). Generation of photon pairs at 810 nm allows for the use of silicon-based SPADs, which have high photon detection efficiency (>50%) at that wavelength.

When a photon is incident on the active area of a SPAD, the detector emits an electrical signal with finite probability. These electrical signals are then directed to a device called a time-tagger. This instrument provides us with the ability to determine with $\sim$ picosecond resolution the moment when each SPAD detects a signal/idler photon. However, while the time-tagger offers picosecond resolution, the measurement is limited by the timing jitter of the SPAD detectors, which in our experiment is assumed to be approximately 250 ps (explained in more detail in Section 5.2.2.1).

In the following Sections, we will take a closer look at the steps required to experimentally realise the heralded photon source.

5.2.1 Experimental Setup

The experimental setup for our realisation of the heralded photon source is shown schematically in Fig. 5.2. The pump light for the system was derived from a laser diode operating at a wavelength of 405.36 nm. To prevent the optical feedback originating from reflections on optical elements in the setup, we introduced a 30 dB single-stage isolator. The laser diode was coupled into a single-mode polarisation-maintaining fiber to clean the spatial mode. A 100 mm focusing lens is used to focus the beam to a waist of 11 μm which

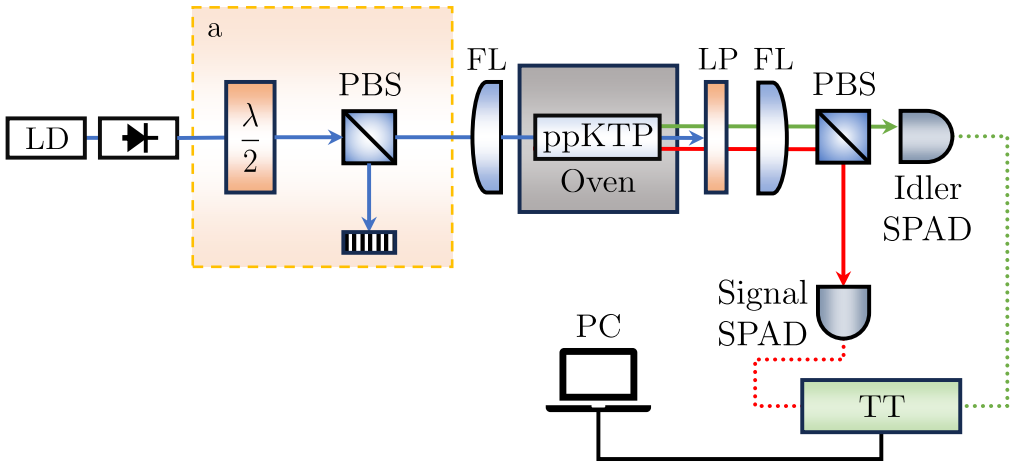

Figure 5.2: The experimental setup used to realise the heralded photon source. A 405.36 nm CW laser diode (LD) with an optical isolator is sent to power control module (a), where a $\lambda/2$ waveplate and a polarising beam-splitter (PBS) is used to control the amount of light sent to the experiment. The focusing lens is used to focus the light to an 11 μm spot in the centre of the 10 mm long ppKTP crystal. The crystal is placed in the oven heated up to 62°C to ensure that the photon pair generated in SPDC Type-II are wavelength-degenerate and ∼810 nm. Long-pass filter (LP) is placed behind the crystal to filter out the pump light, and a focusing lens is used to collimate the pair. Another PBS is used to separate the signal (red) and idler (green), which are then fiber-coupled and detected by SPADs connected to the time-tagger (TT). The time-tagger is connected to a PC which controls the experiment.

was aligned to rest in the centre of the 10 mm long ppKTP crystal placed in a temperature-controlled oven heated to 62°C (value calculated theoretically in Section 2.5.1). The crystal is periodically polled along one of the axes, and the quasi-phase-matching (QPM) can be achieved with a pump input along the same axis (See Section 2.5.1). In our experiment, this means that the pump has to be horizontally polarised in order to achieve the QPM condition. In order to control the amount of optical power directed to the crystal without changing the frequency of the pump light (which changes as we vary the current applied) we use a half-waveplate and a PBS. This allows us to vary the amount of power provided to the experiment between 150 μW and 3.5 mW. The waist size is 11 μm while the optimal value for efficient fibre coupling is 33 μm. This provides a brighter source but with some sacrifice of efficiency.

Figure 5.3: The screenshot of a collimated signal beam output of the Type-II collinear SPDC process seen on a CCD camera. The output is a Gaussian with waist of a 466 μm.

A long-pass filter with a cut-off wavelength of 750 nm was placed behind the crystal to filter out the pump light. The remaining signal and idler beams were collimated using a second focusing lens and the signal/idler photons were separated using a PBS. The collimated signal output can be seen in Fig. 5.3. Signal and idler beams were then fiber-coupled and detected using SPADs (Excelitas SPCM AQRH). A bandpass filter (FBH810-10) centred around 810 nm with a bandwidth of 10 nm was placed before the SPADs to filter out the unwanted background light. The electric signals generated upon successful detection of the photons were directed to the time-tagger (Swabian TimeTagger 20). The time-tagger is connected to a PC, which is used to control the experiment.

In the following Section, we will discuss in detail the single photon counting procedure and equipment used to perform this task.

5.2.2 Time-correlated single photon counting

Time-Correlated Single Photon Counting (TCSPC), is a technique rooted in the fundamental principles of photon detection and precise temporal measurement. At its core, TCSPC involves the detection of individual photons, the recording of their arrival times, and the subsequent analysis of the time-of-arrival data. This technique serves as a powerful tool used for fluorescence lifetime imaging [132], time-resolved spectroscopy [133], anti-bunching experiments [134] and in LIDAR experiments operating in the single photon regime [13–16, 31, 135–137].

In the following sections, we will delve into the essential components and techniques associated with TCSPC. This includes an exploration of SPADs and the intricacies of time-tagging photon detection events. Together, these elements form the bedrock of our experimental setup, facilitating the acquisition and analysis of data used to characterise the heralded photon source, as well as, LIDAR experiments.

5.2.2.1 Single photon avalanche detectors

SPADs are solid-state photodetectors sharing similarities with photodiodes and avalanche photodiodes (APDs) [138, 139]. At their core, SPADs consist of a semiconductor p-n junction that responds to a wide range of ionising radiation and electromagnetic wavelengths, spanning from ultraviolet (UV) to infrared (IR). What sets SPADs apart is their operation under an exceptionally high reverse bias voltage, pushing them into a regime where impact ionisation becomes dominant. When a photon strikes the SPAD, it generates an electron-hole pair, and the electric field within the device accelerates one of these carriers to a kinetic energy sufficient to liberate electrons from atoms through ionisation [139]. This initiates an avalanche of carriers, resulting in a detectable electrical pulse. Thanks to this, even a single photon can trigger this avalanche, enabling SPADs to detect photons at the quantum level [139].

Even in low-light conditions, SPADs may produce false-positive signals, known as dark counts [138, 139]. These occur in the absence of incident photons and arise from thermally-generated carriers within the semiconductor. Dark counts stem from generation-recombination processes within the semiconductor material. The dark counts of SPADs used in our experiments have been measured experimentally, the measured values of each detector fell into the 100-250 Hz range, typical to detectors of this type [113]. It is worth noting that without active temperature control the dark count rates would rise exponentially as the temperature of the device rises. The SPADs used in our experiment are thermoelectrically cooled and temperature controlled, ensuring stabilised performance despite ambient temperature changes.

The performance of SPADs is influenced by the wavelength of incident light, which depends on the material properties of the semiconductor, particularly its energy bandgap. Different semiconductor materials, including silicon [140] and germanium [141], have been employed to fabricate SPADs. Each material exhibits a unique spectral sensitivity based on its energy bandgap. In our experiment, we employed silicon-based SPADs, which thanks to their bandgap of 1.14 eV [142] at room temperature can achieve up to 60% detection efficiency of photons at 810 nm.

In our application of quantum-enhanced LIDAR, SPADs are used not only to detect the arriving photons but also to measure their time of arrival with high precision. The former task is complicated by the detector's timing jitter, arising from both intrinsic photon timing fluctuations and SPAD detection mechanisms. Several factors contribute to timing variability within SPADs [140, 143, 144]:

- Photons may be absorbed at varying depths, affecting the time it takes for carriers to reach the active p-n junction [145].
- Carrier diffusion to the active p-n junction is material-dependent, introducing timing variations [143].

- The avalanche process is probabilistic, leading to variations in avalanche initiation and growth times [140].

The timing jitter of the SPADs used in our experiments is on the level of $\sim$ 250 ps according to the specification provided by the manufacturer, this timing jitter was confirmed experimentally by measuring the minimum rangefinding resolution achievable by the quantum-enhanced LIDAR in Section 6.6.

SPADs may exhibit saturation effects when exposed to high photon fluxes [146]. As photon rates increase, the SPAD may not fully recover between consecutive avalanche events, reducing linearity and dynamic range. At high count rates above 10^6 counts per second the dead time (and heating effects) begins to affect the count rate leading to saturation around 10^7 counts per second. This also broadens the jitter which could affect gating efficiencies.

5.2.2.2 Time-tagging

Time tagging serves as the backbone of TCSPC experiments, enabling researchers to capture temporal information about detected photons down to picosecond or even femtosecond scales. It plays a pivotal role in various applications, including fluorescence lifetime measurement [132], time-resolved spectroscopy [133], and quantum optics experiments [14–16, 31, 135–137]. In the pursuit of characterising our heralded photon source and subsequent LIDAR trials, we harnessed the capabilities of the Swabian Time-Tagger 20, a formidable device recognised for its versatility and advanced functionalities.

The Swabian Time-Tagger 20 boasts exceptional performance characteristics, offering high timing resolution down to $\sim$ 34 ps. Moreover, its ability to run multiple measurements independently using any combination of its 8 input channels and support for high data rates of up to 8.5 million tags per second make it an indispensable tool for our research endeavours.

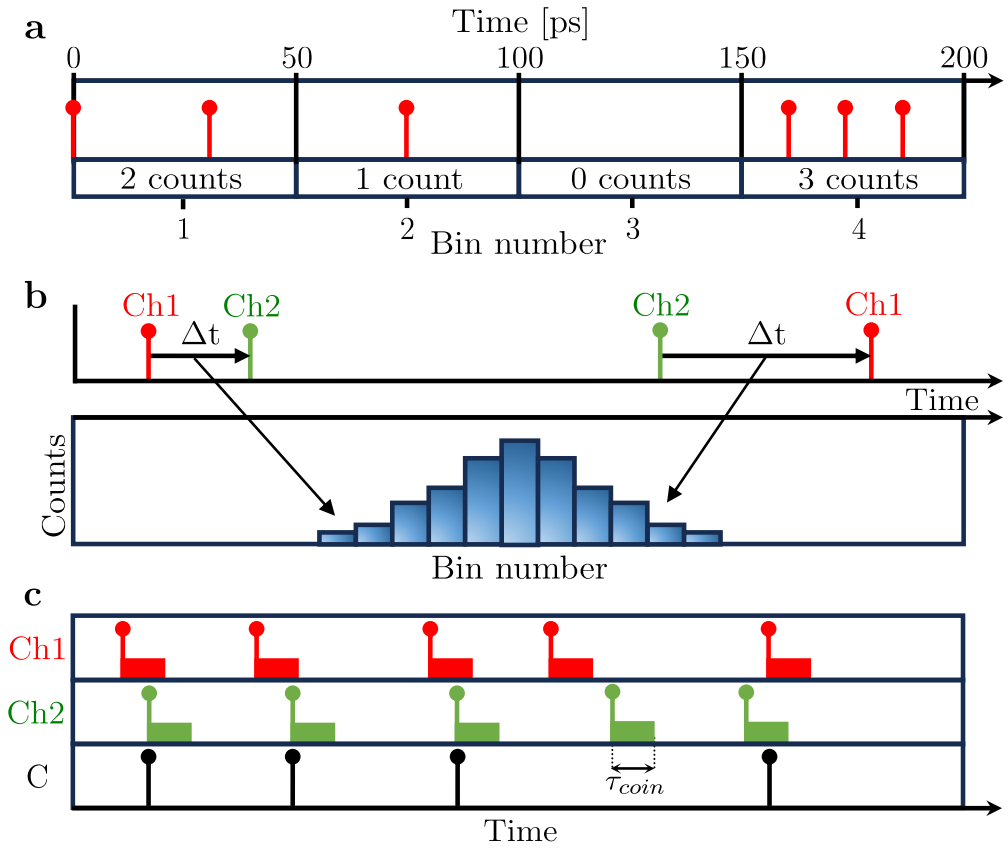

Figure 5.4: Diagram showing different types of measurements possible using Time-Tagger 20. **a** A counts measurement, where tags within a 50 ps bins are counted. The result of this measurement is a two-dimensional array of bins and a number of counts per bin. **b** A correlation measurement, used to create a histogram of time differences between clicks on two channels. **c** A coincidence measurement between channel 1 (red) and channel 2 (green). Here if two click events are registered within user-specified coincidence window τ_{coin}, the virtual coincidence channel C registers a click.

In our forthcoming exploration of experimental methodologies, we will delve into the utilisation of the device, controlled via the Python library provided by Swabian Instruments. Specifically, we will leverage several key functionalities of this instrument to optimise our data acquisition and analysis processes. These functions include:

- **Countrate**: measures the average count rate on one or more channels. More specifically, it determines the counts per second on the specified channel starting from the very first tag arriving after the initialisation

of the measurement.

- **Counter**: provides a time trace of the count rate on one or more channels. This measurement, shown in Fig. 5.4**a**, repeatedly counts tags within a user-specified time interval (binwidth) and stores the result in a two-dimensional array. This can be used to monitor the number of event counts in time without the time averaging.

- **Correlation**: accumulates the time differences between clicks on two channels into a histogram, shown in Fig. 5.4**b**. This is especially useful to determine the time delay between channels.

- **Delay channel**: allows to clone the selected channel and apply a software delay to it. This functionality will be used to synchronise the channels for the purpose of characterising the heralded photon source and to perform the rangefinding measurements where we will be looking at coincidences between locally detected idler and signal probing a target at the distance.

- **Coincidence**: allows to detect coincidence clicks on two or more channels within a given window of time called coincidence window τ_{coin}. This measurement creates a virtual channel which is triggered when all involved channels have received a signal within the given coincidence window. This virtual channel can be analysed using any other functions provided by the time-tagger, for example, the number of coincidences per second can be extracted by applying the countrate measurement to the virtual coincidence channel. In our experiment, we timestamp the coincidence at the time of the last event arriving to complete the coincidence. This type of measurement is shown in Fig. 5.4**c**.

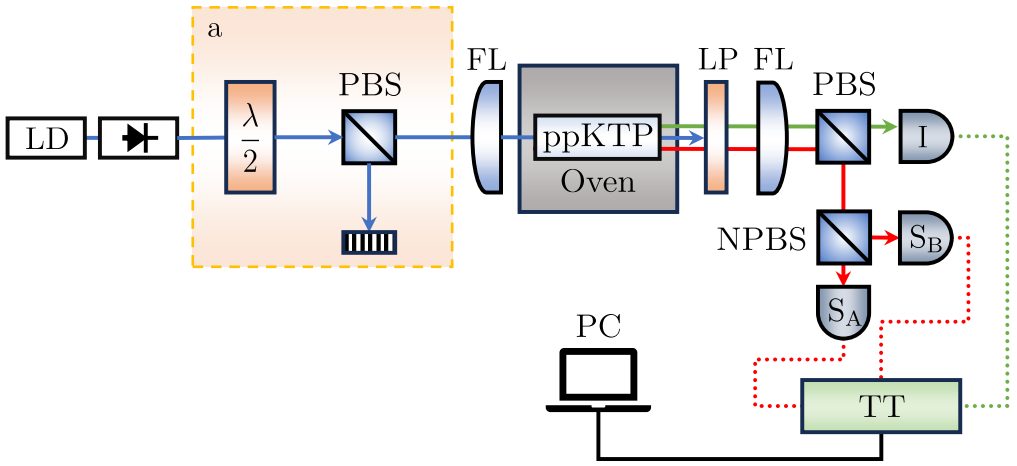

Figure 5.5: The experimental setup used to characterise the heralded photon source. This is a slightly modified version of the setup shown in Fig. 5.2. After the signal and idler modes are split using a PBS, the idler is detected locally using a SPAD (I). Signal mode is split using a 50:50 NPBS, and each half is detected by a separate SPAD (S_A and S_B). Click detection signals from all three detection channels are then directed to the time-tagger (TT) connected to a PC controlling the experiment. The 405.36 nm pump power is controlled using a polarisation-dependent power module in a.

5.2.3 Characterisation of the source

In this Section, we delve into the comprehensive characterisation of the SPDC Type-II single photon source. Our characterisation process is structured into distinct phases, each aimed at revealing different aspects of the source's behaviour. We will first measure the heralding efficiency of the source, a critical parameter signifying the probability of successfully heralding the creation of a photon pair and giving us insight into loss in our system. Next, we will use the result of the heralding efficiency measurement to calculate the source brightness, which will provide insight into the rate at which photon pairs are generated. Finally, we will perform a measurement of idler-conditioned second-order correlation function $g_h^{(2)}(0)$. This final characterisation step will allow us to confirm that the source is indeed generating single photons and allow us to estimate the quality of the source.

To carry out these characterisations, we used an experimental setup shown in

Fig. 5.5. This setup is similar to the one presented in Fig. 5.2, with a slight difference. After separating the signal and idler modes, we introduce a 50:50 non-polarising beam-splitter (NPBS) in the signal path. This NPBS allows for directing half of the signal photons into one SPAD (signal A) and the other half to separate SPAD (signal B). This setup, known as the Hanbury-Brown-Twiss configuration [39], is crucial for measuring the idler-conditioned second-order coherence function. Before setting up this experiment, we carefully evaluated multiple NPBSs to find one that is as close as possible to the 50:50 ratio we need. The NPBS we selected had a measured ratio of 50.1:49.9, which we deemed most suitable for our experiments.

In the following Section, we will focus on the synchronisation of time-tagger channels, a crucial step in ensuring the accuracy and reliability of our experimental data. This synchronisation will enable us to precisely correlate events across different channels, providing us with the temporal information necessary for our analysis. To achieve this, we will employ a method that leverages the time-tagger functionalities described in Section 5.2.2.2.

5.2.3.1 Channel synchronisation

Precise synchronisation of detection channels is required to perform the characterisation of heralded photon sources. The delay between the channels might be introduced by different lengths of the cables connecting the SPADs to the Time-Tagger, the difference between the path length between signal and idler channels, and the delays introduced by the electronics used to process the click data. In this Section, we delve into the crucial process of determining and applying delays between the idler and signal channels of our heralded photon source. The synchronisation achieved through this method forms the foundation for subsequent experiments, including idler-conditioned second-order coherence measurements and distance determination in LIDAR trials.

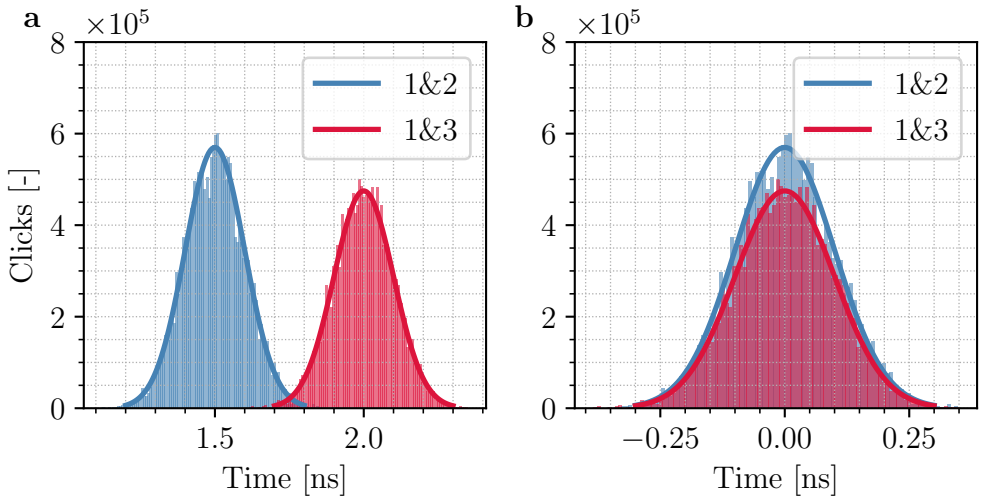

Figure 5.6: Example illustrating the process of synchronising three detection channels. **a** The result of two independent correlation measurements. The blue histogram represents the result of the correlation measurement between the idler detection channel (Channel 1) and signal A (channel 2), while the red histogram shows the same measurement between the idler and signal B (channel 3). After we perform the measurement, each histogram data is fitted using a Cauchy distribution to find its centre, which corresponds to a delay between channel 1 and channel 2/3. **b** After we find the delays between the channels, we apply a delay function to channels 2 and 3 which synchronises all the channels.

Let us consider a situation in Fig. 5.2, here there are three detection channels present, an idler detection channel and a 50:50 split of the signal detection channel (signal A and signal B). To synchronise these channels, we employ a two-step process of correlation measurement. In the first step, we perform a correlation measurement between the idler (channel 1) and the signal A (channel 2). This measurement yields a histogram displaying the relative delay between the clicks of the idler and signal A. Subsequently, we fit this histogram with a Cauchy distribution enabling us to determine the centre of the distribution, which corresponds to the relative delay between these channels. We experimented with different fit functions and decided that the Cauchy distribution provides the best fit to the histogram data.

In the second step, we replicate the process by performing a correlation mea-

surement between the idler and Signal B (channel 3). Like the previous step, this yields a histogram representing the relative delay. We again fit this histogram with a Cauchy distribution to pinpoint the centre, corresponding to the relative delay between the idler and Signal B. The results of the aforementioned steps can be seen in Fig. 5.6**a**.

Armed with the delay information gathered from the correlation measurements, we proceed to synchronize the channels. By applying a software delay to Signal A and Signal B based on the calculated delays, we aim to ensure that all three channels (idler, Signal A, and Signal B) are synchronised in time.

To confirm successful synchronisation, we repeat the correlation measurements between idler and Signal A/B after applying the software delay, which can be seen in Fig. 5.6**b**. The hallmark of successful synchronisation is the simultaneous clicking of all channels, enabling the potential to perform an idler-conditioned second-order coherence measurement. This measurement plays a pivotal role in characterising the properties of our photon source, providing valuable insights into its quantum properties.

The significance of the delay determination and synchronisation process extends to LIDAR trials. Here, the idler will be detected locally and a signal is tasked with probing a target at a specific distance before detection. The delay between these channels corresponds to the distance the signal photons have to travel before they are detected. The accurate determination of this distance relies on the synchronisation achieved through this method, enabling precise coincidence detection between the idler and signal for LIDAR applications.

In summary, the meticulous process of determining and applying delays between the idler and signal channels in our heralded photon source forms the cornerstone of our research. This synchronisation method is instrumental in characterising our photon source and enables the successful execution of

various experiments, from second-order coherence measurements to distance determination in LIDAR trials.

5.2.3.2 Heralding efficiency

The heralding efficiency of a photon source is a crucial parameter in quantum optics and quantum information processing, as it determines the reliability of indicating the presence of exactly one photon in a given mode. The heralding efficiency is given by [147]

$$\eta_{s(i)} = \frac{\mathrm{N_{coin}}}{\mathrm{N}_{s(i)}}, \tag{5.1}$$

where $\eta_{s(i)}$ is the signal (idler) heralding efficiency, $\mathrm{N_{coin}}$ is the number of coincidence events between signal and idler modes within a coincidence window τ_{coin}, and $\mathrm{N}_{s(i)}$ is a number of photon detection events in the signal (idler) mode.

In an ideal scenario, a heralded photon source should provide a heralding signal that unambiguously indicates the existence of a single photon [148], resulting in $\eta_s = \eta_i = 1$. However, in practice, no photon source is truly ideal, and several factors can lead to what is known as a "missing-photon error" [148]. This error occurs when a heralding signal is issued by an idler detection, but no photon is actually present in the signal mode. Several factors contribute to missing photon errors, such as background present in the heralding signal, photon loss due to crystal absorption, and imperfections of optical elements or fibre coupling. The use of imperfect photon detectors (i.e., detectors with detection efficiency $<100\%$) also contributes to a decrease in source heralding efficiency. The heralding efficiency, therefore, provides an estimate of the total loss in the system.

In our experiment, we measured the signal and idler heralding efficiency using

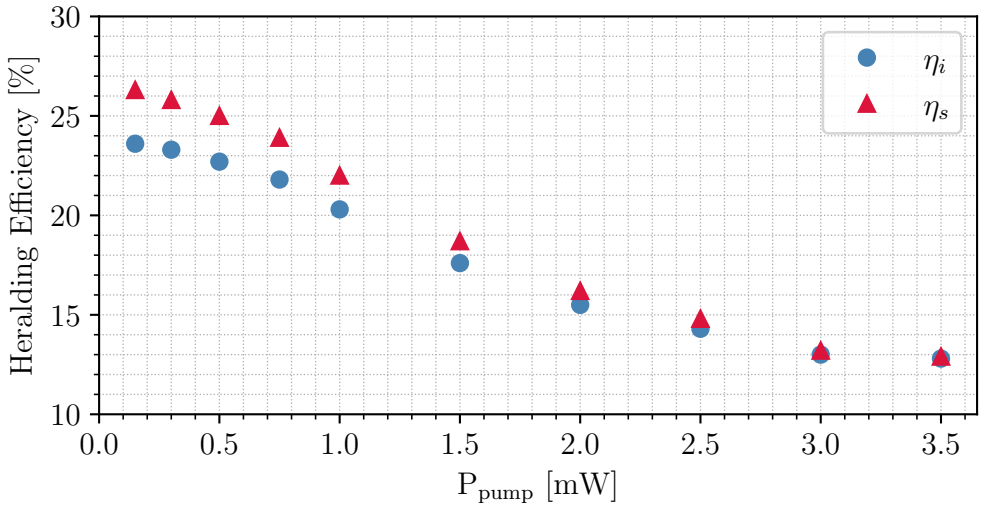

Figure 5.7: The results of heralding efficiency measurement as a function of pump power. During this experiment, the integration time per measurement was set to 1 s and the coincidence window was set to 0.5 ns. The error bars representing the standard error after 3000 measurements are smaller than the data points.

a modified Eq. 5.1, expressed as

$$\eta_s = \frac{(\mathrm{N_{coinA}} + \mathrm{N_{coinB}})}{(\mathrm{N}_{s\mathrm{A}} + \mathrm{N}_{s\mathrm{B}})}, \tag{5.2a}$$

$$\eta_i = \frac{(\mathrm{N_{coinA}} + \mathrm{N_{coinB}})}{N_i}, \tag{5.2b}$$

where the $\mathrm{N_{coinA(B)}}$ is the number of coincident detections between idler and signal A (signal B), and $\mathrm{N}_{s\mathrm{A(B)}}$ is the number of detections of the signal A (signal B) modes.

Results of the heralding efficiency measurement can be seen in Fig. 5.7. The measurement was conducted with integration time per measurement of 1 s, and coincidence window width of $\tau_{\mathrm{coin}} = 0.5$ ns. The choice of these values was motivated by our findings in Section 5.2.3.4. The measurement was repeated 3000 times with integration time per single measurement of 1 s (leading to 3000 s total sampling time). Incorporating shorter sampling interval allows us to gain access to the information about short term drifts. Addi-

tionally we can easily combine the data from each short sampling interval to reconstruct statistics for longer intervals. The heralding value decreases as the input power increases. This observed change in heralding efficiency can be attributed to the saturation of the SPADs used in our experiment. The saturation effect notably impacts the system when the pump power exceeds 1 mW, driving the signal and idler count rates beyond the manufacturer-specified saturation threshold of 1 million counts per second. This condition leads to a diminished effective detection efficiency due to the saturation of the SPADs used in our experiment.

The highest recorded heralding efficiency of 26.3±0.2% for signal and 23.6±0.1% for idler was recorded for the pump power of 150 μW. These values of heralding efficiency are notably lower than the results presented in literature [147, 148], where heralding efficiencies of up to ∼90% were demonstrated. This discrepancy can be attributed to our choice of detectors, with a detection probability of approximately 60% at 810 nm, which significantly reduces the maximal achievable detection efficiency. Additionally, the loss of the signal/idler photons can be attributed to the sub-optimal waist size of the pump mode, which lowers the fibre coupling efficiency of the signal/idler.

5.2.3.3 Brightness

Brightness, in the context of a single photon source, serves as a fundamental metric that influences the source's suitability for a range of quantum applications, including quantum key distribution [149, 150] and quantum LIDAR [13, 15–17, 31]. At its core, brightness quantifies the rate at which photon pairs are generated by the source, making it a critical factor in the design and assessment of quantum systems.

A high brightness source implies the rapid generation of single photons, enabling high data transfer bandwidth and enhancing the efficiency of quantum systems [149, 150]. Conversely, a source with low brightness may impose lim-

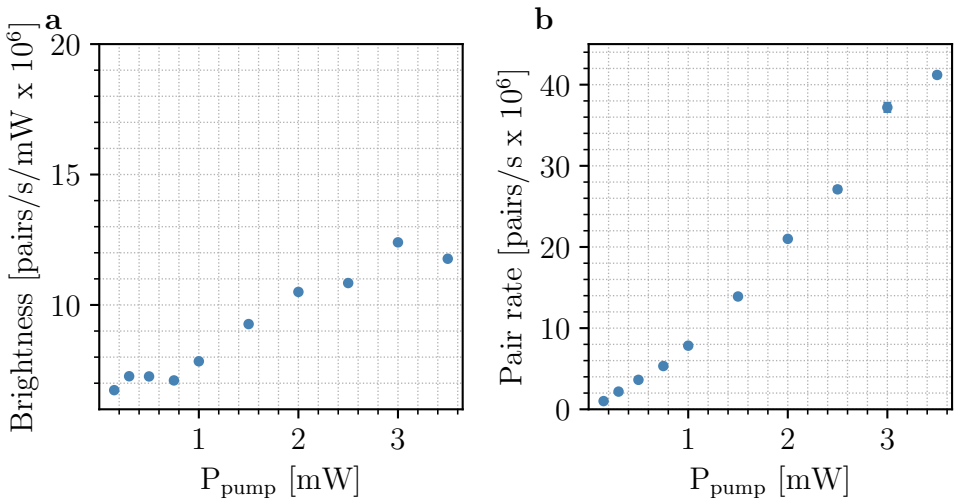

Figure 5.8: The results of brightness characterisation. During this experiment, the integration time per measurement was set to 1 s and the coincidence window was set to 0.5 ns. The error bars representing the standard error after 3000 measurements are smaller than the data points. **a** Shows the measured brightness, while **b** shows the number of photon pairs generated at different pump powers. At low pump power (sub 1 mW) we observe a near-linear relationship between the pump power and the pair production rate, which becomes quadratic as the pump power is increased beyond 1 mW.

itations on the feasibility and performance of quantum technologies, resulting in slower data acquisition rates.

The brightness of our single photon source is calculated using the following expression [147]

$$\text{Brightness} = \frac{\text{N}_i \times (\text{N}_{s\text{A}} + \text{N}_{s\text{B}})}{(\text{N}_{\text{coinA}} + \text{N}_{\text{coinB}}) \times \Delta t \times \text{P}_{\text{pump}}}, \tag{5.3}$$

where Δt represents the integration time of a single measurement, and P_{pump} denotes the average pump power used during the measurement.

In our experiment, shown in Fig. 5.8, we varied the pump power P_{pump} between 0.15 and 3.5 mW, while the integration time was set to $\Delta t = 1$ s. Coincidences were measured with a coincidence window of $\tau_{\text{coin}} = 0.5$ ns. We have observed a near-linear relationship between the pump power and the pair

production rate for pump powers below 1 mW. As the pump power increases beyond this threshold, the relationship becomes quadratic, a behaviour that aligns with observations in the literature [151–154]. This non-linear increase in brightness per milliwatt beyond 1 mW can be partly attributed to distortion in counting results at high rates, likely due to the broadening of the coincidence peak. Such broadening impacts the coincidence rate, which appears in the denominator of Eq. 5.3, thus artificially inflating the calculated brightness.

5.2.3.4 Second-order coherence function

The idler-conditioned second-order coherence function often denoted as $g_h^{(2)}(0)$, provides important information about the quantum properties of a single photon source [39]. The $g_h^{(2)}(0)$ measures the probability of detecting two signal photons conditioned on the idler detection at zero delay, therefore to prepare this measurement we need to synchronise the idler and both signal channels as described in Section 5.2.3.1.

In an ideal single-photon source, $g_h^{(2)}(0) = 0$, meaning that the probability of detecting two signal photons after the idler has been detected is zero. This ideal condition represents a perfectly pure single-photon source where only one photon pair is emitted at a time.

However, in practice, real single photon sources may exhibit some imperfections, such as presence of background or multiphoton emissions. In such cases, $g_h^{(2)}(0)$ may be greater than 0, indicating the presence of unwanted photons or higher-order photon emissions. The higher $g_h^{(2)}(0)$ is above 0, the less ideal the single photon source is considered. When $g_h^{(2)}(0)$ is significantly greater than 0, it implies the potential presence of multiple photons arriving simultaneously in the signal and idler mode, which can reduce the source's suitability for quantum applications requiring strict single photon states.

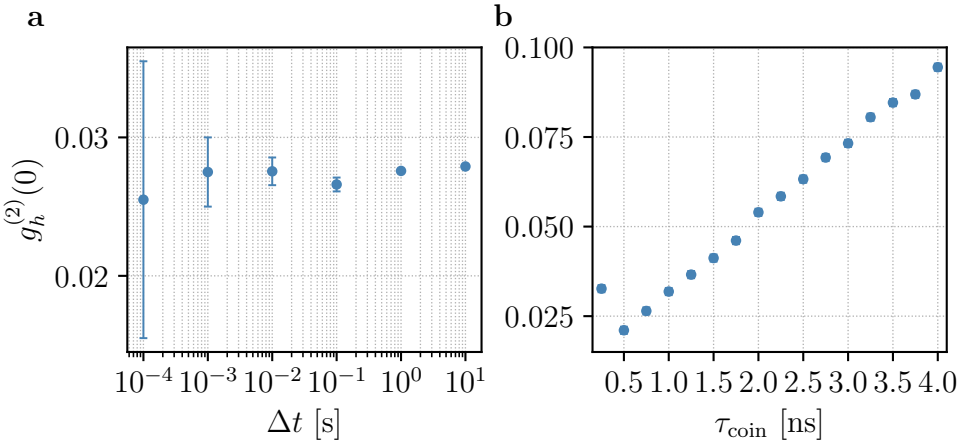

Figure 5.9: Results of the optimisation of integration time Δt and coincidence window width τ_{coin} for performing the heralded photon source characterisation. **a** Result of the $g_h^{(2)}(0)$ measurement of the heralded photon source while the integration time Δt was varied. For each integration time, 100 measurements at a pump power of 1 mW and a coincidence window of 0.5 ns were taken. The error bars represent the standard error after taking 100 measurements. **b** The result of the $g_h^{(2)}(0)$ measurement while the value of coincidence window τ_{coin} was varied. The aim of this measurement was to determine the optimal value of τ_{coin} for which the $g_h^{(2)}(0)$ was minimised. Here the 0.25 ns datapoint is anomalous because the combined time jitter of the signal and idler detectors exceeds the coincidence time and therefore not all coincidences can be captured, leading to inflated $g_h^{(2)}(0)$.

The experimentally determined $g_h^{(2)}(0)$ can be written as [39]

$$g_h^{(2)}(0) = \frac{\mathrm{N_{coinAB}} \times \mathrm{N_i}}{\mathrm{N_{coinA}} \times \mathrm{N_{coinB}}}, \tag{5.4}$$

where $\mathrm{N_{coinAB}}$ is the number of coincidence events between idler, signal A, and signal B.

Before conducting the proper measurement of the $g_h^{(2)}(0)$, we aimed to identify the optimal values for the coincidence window width τ_{coin} and integration time Δt. Our motivation for optimising the integration time per measurement was to strike a balance between measurement accuracy and data acquisition time. Figure 5.9**a** shows a result of $g_h^{(2)}(0)$ measurement performed at varying integration time Δt while maintaining a constant coincidence window

$\tau_{\text{coin}} = 0.5$ ns. The error bars represent the standard error after 100 repeated measurements for each data point. As expected, the standard deviation of measurements significantly decreases as the integration time increases. Diminishing returns are observed when pushing above an integration time of 1 s, with error bars dropping to $\pm 0.0005, 0.0001$ and 0.00008 for integration times of 0.1 s, 1 s, and 10 s (the total sampling times for each Δt were 10 s, 100 s, and 1000 s), respectively. Operating at high repetition rates enables the rapid accumulation of small sample statistics, which can then be aggregated to match the sample size of longer integration times while preserving real-time dynamics. This approach allows for window-averaging to larger sample times with short Δt, in contrast to single long-duration data points that yield the same total sum but with a slower update rate. To balance measurement accuracy and data acquisition time, we selected $\Delta t = 1$ s as the integration time for our measurements.

Figure 5.9**b** presents $g_h^{(2)}(0)$ measurements while varying the coincidence window width τ_{coin} between 0.25 and 10 ns. These measurements were taken at a pump power of $\text{P}_{\text{pump}} = 1$ mW and an optimal integration time of $\Delta t = 1$ s. The error bars represent the standard error after 500 measurements per data point. The minimum value of $g_h^{(2)}(0) = 0.02113 \pm 0.0001$ was recorded for a coincidence window of 0.5 ns, leading us to select this as the optimal value for characterising our heralded photon source.

After determining the optimal values of Δt and τ_{coin}, we proceeded to measure $g_h^{(2)}(0)$ as a function of the pump power P_{pump}. The results of this characterisation are shown in Fig. 5.10, where the pump power ranged from 0.15 to 3.5 mW. The error bars represent the standard error after 500 measurements.

In Fig. 5.10, we observe the relationship between $g_h^{(2)}(0)$ and the pump power. Specifically, we find that this relationship is initially linear, but it becomes increasingly quadratic as the pump power is increased. This behaviour was observed by other experimental groups [151–154].

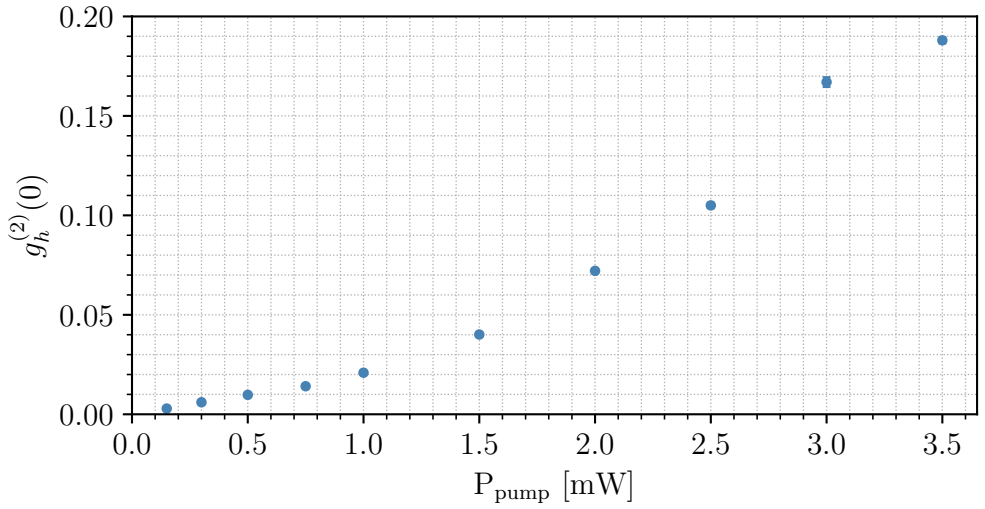

Figure 5.10: Results of idler-conditioned second-order coherence measurement while input power to the crystal was varied between 0.15 and 3.5 mW. To perform this optimised values of integration time $\Delta t = 1$ s and coincidence window $\tau_p = 0.5$ ns were used. It is important to note that there is a slight discrepancy between the x-axis values of this figure and those in Fig. 5.9, attributable to pump power drift over the course of the experiment.

The minimum value of $g_h^{(2)}(0)$ recorded in our experiments is 0.0029 ± 0.0002, this occurred at an input power of 150 μW. It is worth noting that this near-zero value of $g_h^{(2)}(0)$ underscores the exceptional single-photon purity of our source, comparable to other studies reporting similar outcomes [155].

5.3 Conclusion

In this Chapter, our journey has revolved around establishing the fundamental framework for our quantum-enhanced LIDAR experiments, centred on the development and characterisation of a heralded single photon source based on SPDC Type-II. These pivotal steps provide the bedrock for the quantum-enhanced LIDAR research that lies ahead.

Our venture began with the creation of a straightforward yet highly effective SPDC Type-II heralded single photon source. This source harnessed the

power of a continuous-wave (CW) input pump laser at 405 nm, generating wavelength-degenerate photon pairs at 810 nm detected by Si-SPADs. This development was guided by our vision of deploying this practical source in quantum-enhanced LIDAR experiments.

The characterisation of the single-photon source was a crucial endeavour, encompassing a comprehensive assessment of heralding efficiency, brightness, and the idler-conditioned second-order coherence function. Our experimental endeavours unveiled a heralding efficiency of approximately 20% in the low-power regime, thoughtfully tailored to meet the demands of quantum-enhanced LIDAR applications. One of the standout achievements was the attainment of a high source brightness, quantified at around 7.55 pairs/sec/mW within the low pump power regime. Additionally, the low value of $g_h^{(2)}(0)$ indicated that our source consistently yielded single photons with an impressively high degree of purity. It is worth noting that while our heralding efficiency may not quite reach the levels reported in certain other experiments (which have approached 90%), the amalgamation of high brightness and single photon purity solidifies our device's standing as a viable and promising candidate for quantum-enhanced LIDAR applications.

Looking ahead, this Chapter serves as a pivotal juncture in our quest to push the boundaries of LIDAR technology through quantum enhancement. With the solid foundation laid out in this Chapter, we eagerly anticipate the next phase of our research journey. In the upcoming Chapter, we will harness the power of a log-likelihood framework to analyse our experimental data, offering us a deeper understanding and enabling us to fully unlock the immense potential of quantum-enhanced LIDAR technology.

Chapter 6

Quantum-enhanced LIDAR - experimental results

6.1 Introduction

Optical LIDAR is a pivotal technology for achieving precise target detection and rangefinding with high spatial precision [3, 4], utilised in a range of applications from performing ground surveys [5], monitoring sea levels [6], to aiding navigation in autonomous vehicles [7]. Under conditions necessitating low-light levels and a substantial background, arising from low target reflectivity, environmental noise, or deliberate jamming, classical LIDAR techniques fail to discern between signal and background photons leading to diminished signal-to-background ratio and an inability to detect targets confidently.

Significant progress has been made towards exploiting LIDAR at the single photon level [156] enabled by advances in detector technologies and computational analysis to enable 3D imaging using single-pixel detection [157] or single photon cameras [158] suitable for operating in adverse backgrounds [159, 160], however typically these devices operate using strong mod-

ulated classical light sources for target illumination to compensate for low return probability. In contrast, quantum-enhanced illumination [161] offers a compelling alternative approach, whereby the utilisation of non-classical heralded photon sources affords the exploitation of coincidence detection techniques, enabling effective background photon suppression without temporal modulation of the signal source [14–16].

The original framework for quantum illumination proposed by Lloyd [17] demonstrated that by exploiting entanglement it was possible to out-perform classical systems, with an extension to Gaussian state analysis bounding the maximum quantum advantage to 6 dB assuming an unknown optimal measurement [18, 19]. Measurement protocols have been proposed offering up to 3 dB advantage [20, 21], whilst a detection scheme able to exploit the full quantum advantage [22, 23] remains a significant technical challenge. Experimental demonstrations of quantum illumination with phase-sensitive detection have been performed in-fiber with background added at the detectors [21], with recent extensions to operation in the microwave domain compatible with radar applications [24–26].

A much simpler approach is to exploit the temporal correlations arising from photon pairs generated using spontaneous parametric downconversion using either pulsed or continuous (CW) sources [28]. Experimental demonstrations have shown enhancement in the signal-to-background ratio by exploiting these correlations [14, 15, 29, 30], offering robust operation with respect to classical jamming [14, 16] and first demonstrations of rangefinding [13, 15, 31]. Recently, using dispersion compensating fibres a further enhancement in quantum detection was demonstrated by spreading the background across multiple time-bins whilst preserving the temporal correlation of the two-photon coincidence to achieve 43 dB times enhancement in Signal-to-Background Ratio (SBR) at background levels up to three times the signal level [32]. Additionally, detector multiplexing [33] permits multi-mode

range-finding that can enable covert operation using light that is spectrally and statistically indistinguishable from the background [31].

In this chapter, we will first showcase the signal-to-background ratio (SBR) advantage of quantum-enhanced LIDAR over its classical counterpart. Following this, I introduce the experimental implementation of the Log-likelihood value (LLV) framework, a concept theorised by my collaborator Richard Murchie [27, 162]. This collaboration combines the theoretical model developed by Richard with my experimental efforts to illustrate the efficacy of quantum-enhanced LIDAR through empirical data.

6.2 Quantum-enhanced LIDAR - experimental realisation

Our objective is to utilise coincidence detection between locally detected idler photons and the signal probing a target at a known distance [14, 15, 29, 30] to reject the background while maintaining a single photon level of operation.

We will begin by presenting the experimental setup employed for this laboratory demonstration. This setup will serve as the foundation for our investigations into quantum-enhanced LIDAR. We will also explain the methods we used to measure and calibrate loss within the system, as well as how we introduced controlled background into the experiment.

Our preliminary results will provide an initial glimpse into the potential of quantum-enhanced LIDAR. Specifically, we will focus on the SBR improvement achieved through our coincidence detection method when compared to classical detection protocols. These results will lay the groundwork for a more comprehensive analysis of the capabilities and limitations of our quantum-enhanced LIDAR system using the log-likelihood framework.

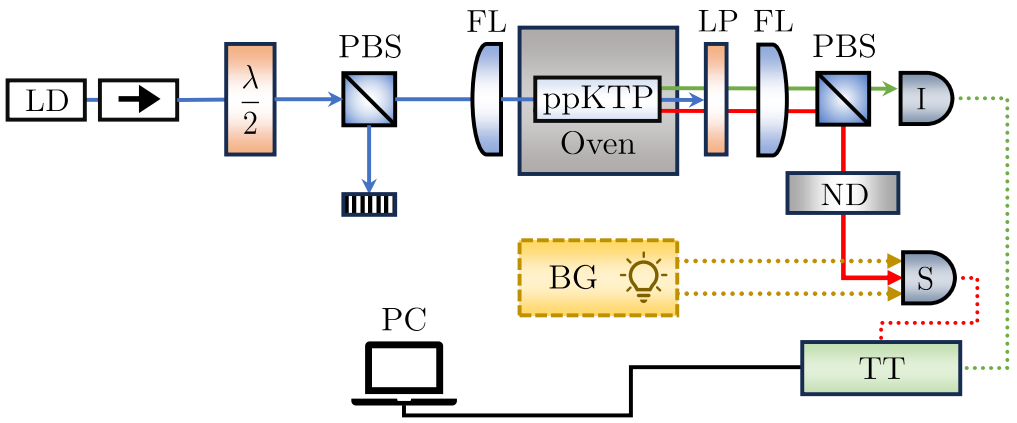

Figure 6.1: The experimental setup used to characterise the heralded photon source. This is a slightly modified version of the setup shown in Fig. 5.2. After the signal and idler modes are split using a PBS, the idler is detected locally using a SPAD (I). An ND filter (ND) is introduced in front of the signal SPAD (S), to simulate the loss in the system. The background (BG) was simulated using a 810 nm LED, and the LED is placed in such a way that the background is coupled exclusively into the signal SPAD. Click detection signals from signal (S) and idler (I) detection channels are then directed to the time-tagger (TT) connected to a PC controlling the experiment.

6.2.1 Experimental setup

The experimental setup for the laboratory demonstration of the quantum-enhanced LIDAR is shown schematically in Fig. 6.1. This setup is a slightly modified version of the setup presented in Section 5.2.1 (Fig. 5.2). The 405.36 nm pump light derived from a CW laser diode is pumped into a ppKTP crystal, where in the process of SPDC Type-II a pair of photons at ∼810 nm is generated. Due to the nature of the SPDC Type-II process, described in detail in Section 2.5, the idler and signal photons are orthogonal in polarisation. This allows us to separate the pair using a polarising beam splitter (PBS). After the photon pair is separated, we introduce an ND filter in the signal detection path to simulate the loss and the target reflectivity in our system. In addition to simulating different levels of loss and finite target reflectivity with ND filters, we introduce ambient background in the system using an LED with a central wavelength of 810 nm. To prevent the

background from affecting the idler detection we have introduced shielding around both idler and signal fibre coupling optics. In order to make sure that the background is not contaminating the idler path we have performed a series of experiments in which we measured the photon count rate on idler and signal channels with and without the background source engaged. We have not observed any significant difference between the amount of photon counts on the idler channel. In the experiments, the absence of a target was simulated by placing a beam block in the signal path. The beam block was placed at the angle in such a way that it did not change the level of background.

In order to accommodate for the ND filter, beam block and background source, the signal mode path had to be significantly longer than the idler mode path. To perform the coincidence measurements we had to calibrate the relative delay between the signal and idler detection channels, the process of this calibration was described in detail in Section 5.2.3.1.

6.2.1.1 Loss & target reflectivity

The accurate identification of target objects probed with LIDAR systems is challenged by loss. Loss encompasses attenuation due to absorption, scattering, reflection, and transmission, leading to weakened signal return. Addressing these challenges often requires advanced signal processing, sensor design, and calibration techniques [163].

In the context of LIDAR measurements, the target reflectivity refers to the ability of an object or surface to reflect light back to the LIDAR sensor. Target reflectivity is a critical factor in LIDAR technology because it directly affects the quality and accuracy of the measurements taken by the LIDAR system.

In our system, the loss and the finite target reflectivity are simulated using a set of ND filters with different levels of attenuation. To calibrate how

	Signal Return	**Loss [dB]**	**Target reflectivity**
No Filter	1160000 ± 10000	-8.1 ± 0.1	1
ND10	244000 ± 3000	-14.9 ± 0.1	0.16 ± 0.01
ND12	142000 ± 2000	-17.3 ± 0.1	0.091 ± 0.001
ND20	73000 ± 1000	-20.2 ± 0.1	0.047 ± 0.001
ND30	13400 ± 200	-27.5 ± 0.1	0.0087 ± 0.0001
ND40	2760 ± 40	-33.5 ± 0.1	0.0017 ± 0.0001
ND60	648 ± 9	-40.7 ± 0.1	0.00042 ± 0.00001
ND80	48 ± 1	-52.0 ± 0.1	0.000031 ± 0.000001

Table 6.1: Signal return, loss (propagation loss + reflectivity + detector efficiency) and target reflectivity for different levels of attenuation. The experiment was performed for a pump power of 1 mW.

much loss each filter introduces, we first need to establish the number of photons generated at the ppKTP crystal for a given amount of power. We estimate this using the results of the source brightness calibration presented in Section 5.2.3.3.

Next, we must measure how many of the detection events registered by the single photon avalanche detectors (SPADs) come from the detector's dark counts. To prepare for this measurement, we close the doors to the optical table where the experimental setup is placed and turn off ambient light in the laboratory. We also ensure that the pump light is blocked before it reaches the non-linear crystal to ensure no photon pairs are generated. After completing these steps, we perform a series of photon counting measurements with an integration time of 1 second per measurement to experimentally measure the dark counts of the signal and idler SPAD detectors, which are $N_{darkS} = 213 \pm 1$ counts per second and $N_{darkI} = 117 \pm 1$ counts per second, respectively.

For the loss calibration, here defined as combination of propagation loss, detector efficiency and loss resulting from imperfect target reflectivity, we

set the pump power to 1 mW, which corresponds to a pair production rate of 7.55 ± 0.01 million pairs per second. We calculate the loss using the following formula

$$\text{Loss} = 10 \log_{10} \left(\frac{\text{N}_{\text{return}} - \text{N}_{\text{darkS}}}{7.55 \times 10^6} \right), \tag{6.1}$$

We also estimate the reduction in target reflectivity which will be used as one of the parameters allowing us to model the LIDAR system in Section 6.4. Target reflectivity is calculated using the following formula

$$\text{Target reflectivity} = \frac{\text{N}_{\text{return}} - \text{N}_{\text{darkS}}}{\text{N}_{\text{return}'}}, \tag{6.2}$$

where $\text{N}_{\text{return}'} = 1160000$ is the number of signal photons detected with no additional attenuation. Using the known Brightness of the source (7.55 million pairs per second), detector efficiency ($\eta = 60\%$) and number of photons detected when no additional sources of attenuation are present ($\text{N}_{\text{return}'} = 1160000$) we can calculate the collection efficiency of the system to be 25.6%. The results of the calibration are shown in Table 6.1, which provides a clear overview of the measured loss and reduction in target reflectivity for each filter used in the experiment.

6.2.1.2 Background source

LIDAR systems face a formidable challenge in accurately identifying target objects due to the presence of background. Ambeint background encompasses any unwanted signals or fluctuations that interfere with the intended measurements.

In the context of LIDAR, we identify several potential sources of background:

- **Detector Dark Counts:** Dark counts represent unintended signals detected by photodetectors even in the absence of incident photons. Potential causes of dark counts in SPADs were described in detail in

Section 5.2.2.1, and the results of the dark-count characterisation of our detectors can be found in Section 6.2.1.1.

- **Environmental Factors:** LIDAR systems often operate in environments where thermal background radiation is present. These effects are especially important when operating in the infrared regime of detection, where the background radiation is especially strong.

- **Intentional Jamming:** In specific scenarios, particularly security or military applications, intentional jamming can serve as a deliberate source of background.

- **System Imperfections:** No LIDAR system is entirely immune to imperfections. Optical aberrations, electronic noise in data acquisition systems, and calibration errors can all introduce background counts.

The presence of background within LIDAR systems has far-reaching consequences on the accuracy of target object identification. For example, background can lead to inaccuracies in determining the precise distance between the LIDAR sensor and target objects, affecting the reliability of distance measurements. The presence of background can also result in false positives, where non-existent objects are identified, and false negatives, where actual objects are missed. Such errors can have critical implications for applications like autonomous driving and robotics [164–166].

To simulate the presence of background in our system, we have used an LED with a central wavelength of 810 nm. The LED was powered by a low-noise laser driver (Koheron DRV300). The choice of such a sophisticated driver for controlling our background level was motivated by the requirement of a steady output. To further reduce the fluctuations of the background intensity, we decided to place an attenuation filter in front of the LED, reducing its intensity output by a factor of 10. This allows us to drive the background-generating LED at higher current levels, and because the current noise (25

nA) of the driver is independent of the current applied to the diode, this leads to a decrease in background fluctuations. Driving the LED at higher current levels might lead to additional drift resulting from changes in the temperature of the LED, but the impact of that effect was negligible and unobservable in the laboratory. A steady level of background is required to make the comparison between classical (CI) and quantum-enhanced (QI) detection protocols, as CI is extremely susceptible to any drift in background level. This is especially true when the loss in the system is high (<-40 dB). Under these conditions, signal return rates approaching single counts per second can be expected and drifts in background levels can lead to CI interpreting changes in the background as a sign of an object appearing when there is none. The background drift does not impact the coincidence-based QI detection to the same degree, which will be demonstrated in Section 6.5.

6.2.2 Signal-to-Background measurement

In the context of LIDAR, the SBR is a fundamental metric that quantifies the quality and reliability of the acquired data. SBR is a measure of the strength of the desired signal, relative to the background and unwanted interference within the LIDAR system.

To investigate the SBR advantage of QI over CI, we consider the simplified case of a target at a known distance. The source is operated at $P_{\text{pump}} = 0.2\,\text{mW}$ pump power, with a background level for the signal detector set to $N_{\text{background}} \approx 2.5 \times 10^6$ counts per second, approximately five times stronger than the average emitted signal power. The idler detector has a background level of $N_{\text{I:background}} \approx 7 \times 10^3$ counts per second. To compare the CI and QI protocols, we introduce the signal-to-background ratio

$$\text{SBR} = \frac{N_{\text{in}} - N_{\text{out}}}{N_{\text{out}}}, \tag{6.3}$$

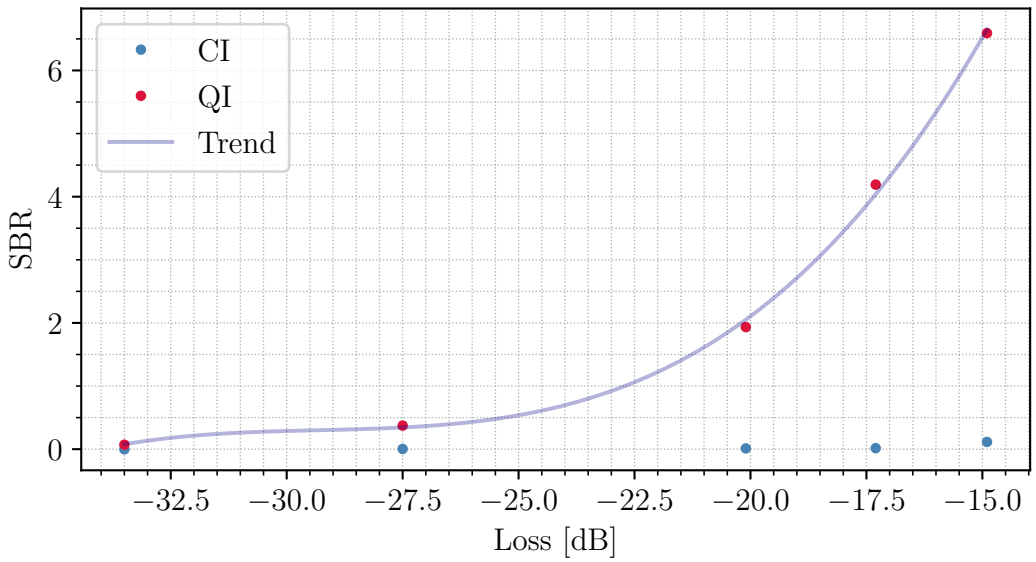

Figure 6.2: Demonstration of enhanced SBR for QI vs CI when comparing signal with (without) target based on signal counts (CI) and coincidence measurements (QI) as a function of loss. All measurements were performed with a signal count rate of $N_S = 388 \times 10^3$ counts per second, $N_{background} = 2.5 \times 10^6$ counts per second and the idler detector background is 7×10^3 counts per second. Polynomial fit has been added to this plot to serve as a 'line to guide the eye'.

where N_{in} is the number of detection events when the target is present, and N_{out} is the number of detection events when the target is absent. For the target-absent case, a beam-block is placed in the signal path such that only the background signal reaches the detector.

The definition of a detection event changes depending on whether we are analysing the CI or QI protocol. In the case of CI, the detection event is simply the total number of signal detector clicks within a 1 s window, while for QI, we define the detection as the total number of coincidence events between idler and signal detector clicks in a 1 s window, measured using a 1 ns coincidence window.

A comparison of CI and QI SBR as a function of loss in the system is shown in Fig. 6.2. This demonstrates a clear advantage of the QI approach in enhancing the SBR for detection at all times, which can be understood from the enhanced rejection of background level in the QI regime when conditioning

signal detection events using the heralded idler. In the following Sections, we will utilise this advantage and combine the coincidence-based detection with a new analysis framework [27, 162].

6.3 LLV analysis framework

In both target detection and range finding the aim is to evaluate, based on a finite set of measurements, whether or not a target is present. This reduces to a state discrimination problem of deciding whether the measured statistics correspond to the target being present (hypothesis 1 - H1) or absent (hypothesis 0 - H0). Prior analysis of this problem has focused on the fundamental bounds given an unknown optimal measurement scheme [17, 18] or formulated this as a probe transmission estimation problem whereby the uncertainty of the transmission estimation is described by the Cramér–Rao bound [15, 16]. In either approach, a fundamental issue lies in defining the threshold at which to consider a target present or absent.

In this work, we use an alternative analysis protocol based on the log-likelihood value (LLV) Λ defined as [27, 162]

$$\Lambda(x,k) = \ln\left(\frac{P_{\mathrm{H1}}(x,k)}{P_{\mathrm{H0}}(x,k)}\right), \tag{6.4}$$

where x represents the measured detector count data, k is the number of trials and $P_{\mathrm{H1,0}}(x,k)$ represents the probability that the target is there (or not) given x events after k trials. When calculating Λ in the case of quantum illumination (QI) x is the number of detected coincidence events in a measurement time T for a given coincidence window τ_{coin}, and k is the number of idler clicks, whilst for classical illumination (CI) x is the number of signal detection events and $k = T/\tau_{\mathrm{coin}}$.

An advantage of using the log-likelihood ratio is that it gives a natural thresh-

old value of $\Lambda = 0$ that is independent of the system parameters, providing a degree of self-calibration in the system. If $\Lambda < 0$ it is more likely that the target is absent, whilst for $\Lambda > 0$ it is more likely that a target is present. To evaluate the error associated with making a decision on whether a target is present using this threshold, we introduce the distinguishability $\phi = 1 - [(1 - P_{\mathrm{D}}(0) + P_{\mathrm{FA}}(0)]$ where P_{D} is the probability of correctly detecting a target that is there and P_{FA} is the false alarm probability caused by incorrectly detecting a target when there is not one present. Numerically these probabilities are evaluated by integrating over the underlying LLV probability distributions associated with H1 ($P_{\mathrm{H1}:\Lambda}$) and H0 ($P_{\mathrm{H0}:\Lambda}$) respectively [162]

$$P_{\mathrm{D}}(d_{\mathrm{LLV}}) = \sum_{z=d_{\mathrm{LLV}}}^{\infty} P_{\mathrm{H1}:\Lambda}[z], \tag{6.5a}$$

$$P_{\mathrm{FA}}(d_{\mathrm{LLV}}) = \sum_{z=d_{\mathrm{LLV}}}^{\infty} P_{\mathrm{H0}:\Lambda}[z]. \tag{6.5b}$$

This can be easily understood as evaluating distinguishability by calculating the fraction of data points with $\Lambda > 0$ when the object is present or absent.

To determine the error bars for distinguishability, we first calculate the mean and standard deviation for the respective LLV distributions when the target is present and when it is absent. Then, we integrate these distributions to ascertain the probabilities of detection and false alarms. From these probabilities, we compute the distinguishability metric, ϕ.

In the limit where the underlying Poisson count distributions can be modelled as Gaussian [162] (valid for the data shown in the thesis), the LLV distributions for H1 and H0 also become Gaussian, with mean value $\mu_{Hi:\Lambda} = M\bar{x}_{Hi} + Ck$, where $C = \log((1 - p_{\mathrm{H1}})/(1 - p_{\mathrm{H0}}))$ and a standard deviation equal to $\sigma_{Hi:\Lambda} = M\sigma_{Hi}/\sqrt{N_{\mathrm{av}}}$, where N_{av} corresponds to the average window length being considered.

For the case of CI, as above $k = T/\tau_c$, with mean signal levels given by

$\bar{x}_{Hi}^{\mathrm{CI}} = kp_{Hi}^{\mathrm{CI}}$ and standard deviation $\sigma_{Hi}^{\mathrm{CI}} = \sqrt{kp_{Hi}^{\mathrm{CI}}(1-p_{Hi}^{\mathrm{CI}})}$. For the QI case, we use $k = (T/\tau_c)p_I^{\mathrm{QI}}$ corresponding to the average number of times the idler fires. The mean coincidence rate is then $\bar{x}_{Hi}^{\mathrm{QI}} = kp_{Hi}^{\mathrm{QI}}$ with standard deviation $\sigma_{Hi}^{\mathrm{QI}} = \sqrt{kp_{Hi}^{\mathrm{QI}}(1-p_{Hi}^{\mathrm{QI}})}$.

Defining a threshold LLV value Λ_c, the probabilities of detection and false alarm can then be evaluated as

$$P_{\mathrm{D}} = \int_{\Lambda_c}^{\infty} \exp\left(-\frac{(x-\mu_{\mathrm{H1:}\Lambda})^2}{2\sigma_{\mathrm{H1:}\Lambda}^2}\right) dx, \tag{6.6a}$$

$$P_{\mathrm{FA}} = \int_{\Lambda_c}^{\infty} \exp\left(-\frac{(x-\mu_{\mathrm{H0:}\Lambda})^2}{2\sigma_{\mathrm{H0:}\Lambda}^2}\right) dx. \tag{6.6b}$$

For the distinguishabilities quoted above we use threshold $\Lambda_c = 0$ throughout the thesis.

To effectively apply the LLV framework for target discrimination, certain a priori knowledge about the system under investigation is required. Specifically, this framework necessitates an understanding of the mean photon number attributable to the background ($\bar{n}_{\mathrm{bg}}$), the mean photon number generated in the process of SPDC ($\bar{n}$), and the reflectivity of the target (ξ) to calculate the H1 distribution. The first two parameters can be accurately estimated through a brief calibration measurement, the procedure for which is elucidated in detail in Section 6.3.3. While in our experiments the target reflectivity is established and detailed in Section 6.2.1.1, there might be scenarios where it is not precisely known. In such situations, we can set the reflectivity to an arbitrary value, ξ, to ascertain whether any targets in the observed area possess at least this minimum reflectivity. This adjustment influences the sensitivity of the LLV analysis to slight variations in signal return. Essentially, the experiment can be framed as inquiring, "Is there a target with a minimum reflectivity of ξ?" Moreover, it is feasible to conduct several LLV analyses concurrently, each with a different target reflectivity assumption, to identify targets of various reflectivities.

6.3.1 Single-shot detection probabilities

In order to evaluate the log-likelihood ratio, it is necessary to calculate the underlying probabilities of detection and coincidence events that occur within a single coincidence window τ_{coin}. These probabilities depend on the average photon number generated in the process of SPDC $\bar{n}$, target reflectivity ξ, the average background on the signal ($\bar{n}_{\text{bg}}$) and idler ($\bar{n}_{\text{bg,I}}$) detectors, detection efficiency of the signal (η_{S}) and idler detectors (η_{I}). The detection efficiencies account for all system loss and finite quantum efficiency in the limit of a perfect target reflectivity. Below we extend the analysis framework presented in [162] to the regime of detection in the presence of a Poissonian background source, as used in this experiment setup.

To model the CI case, the probabilities of signal detector firing with the target present $p_{\text{H1}}^{\text{CI}}$ (or absent $p_{\text{H0}}^{\text{CI}}$) are given by

$$p_{\text{H0}}^{\text{CI}} = 1 - \exp\left(-\bar{n}_{\text{bg}}\eta_{\text{S}}\right), \tag{6.7a}$$

$$p_{\text{H1}}^{\text{CI}} = 1 - \frac{1}{1+\gamma\eta_{\text{S}}\xi\bar{n}} \exp\left(-\frac{\bar{n}_{\text{bg}}\eta_{\text{S}}}{(1+\eta_{\text{S}}\gamma\xi\bar{n})}\right). \tag{6.7b}$$

In the QI case, the single shot probabilities reflect the probability of a signal event within the coincidence time τ_{coin} conditioned on the idler firing. When the object is absent, the detector only fires due to background and the probability of a signal event is equivalent to the CI case with no target. With the target present, it is necessary to derive the click probability by considering the idler-conditioned signal state as a thermal-difference state. The thermal difference state [167] is defined as a weighted difference of two thermal states, where the second state has a mean photon number that is lower or equal to that of the first state. In this context, one state is unconditioned and the other is conditioned on the absence of a click, fulfilling the necessary

requirements. This approach results in the QI click probabilities given by

$$p_{\mathrm{H0}}^{\mathrm{QI}} = p_{\mathrm{H0}}^{\mathrm{CI}}, \tag{6.8a}$$

$$p_{\mathrm{H1}}^{\mathrm{QI}} = 1 - \frac{1}{p_{\mathrm{I}}^{\mathrm{QI}}}\Bigg(\frac{1}{1+\bar{n}\xi\eta_{\mathrm{S}}\beta}\exp\big(\eta_{\mathrm{S}}\bar{n}_{\mathrm{bg}}(\frac{\bar{n}\xi\eta_{\mathrm{S}}\beta}{1+\bar{n}\xi\eta_{\mathrm{S}}\beta}-1)\big) - \frac{(1-p_{\mathrm{I}}^{\mathrm{QI}})}{1+\bar{n}_{\mathrm{I:X}}\xi\eta_{\mathrm{S}}\beta}\exp\big(\eta_{\mathrm{S}}\bar{n}_{\mathrm{bg}}(\frac{\bar{n}_{\mathrm{I:X}}\xi\eta_{\mathrm{S}}\beta}{1+\bar{n}_{\mathrm{I:X}}\xi\eta_{\mathrm{S}}\beta}-1)\big)\Bigg), \tag{6.8b}$$

where $\bar{n}_{\mathrm{I:X}} = \bar{n}(1+\eta_I\bar{n}_{\mathrm{bg,I}}-\eta_{\mathrm{I}})/(1+\eta_{\mathrm{I}}\bar{n}_{\mathrm{bg,I}}+\bar{n}\eta_{\mathrm{I}})$ is the signal state mean photon number after conditioning from a no click event at the idler and $p_{\mathrm{I}}^{\mathrm{QI}}$ is the idler firing probability equal to

$$p_{\mathrm{I}}^{\mathrm{QI}} = 1 - \frac{1}{1+\eta_{\mathrm{I}}\bar{n}+\eta_{\mathrm{I}}\bar{n}_{\mathrm{bg,I}}} \tag{6.9}$$

Furthermore, in these equations, we introduce two additional parameters, γ and β. These parameters allow for adjustments to match the data obtained for CI and QI respectively, to account for detector non-linearities and variations in the heralding efficiency due to changes in pump power and coincidence window duration.

6.3.2 Log-likelihood ratio

In the limit of k trials it is possible to express the LLV defined in Eq. 6.4 in a linear form [162] dependent only upon the single-shot probabilities p_{H0} and p_{H1} using $\Lambda(x,k) = Mx+Ck$, where $M = \log((p_{\mathrm{H1}}*(1-p_{\mathrm{H0}}))/(p_{\mathrm{H0}}(1-p_{\mathrm{H1}})))$ and $C = \log((1-p_{\mathrm{H1}})/(1-p_{\mathrm{H0}}))$.

For data acquired over an integration time T, the CI LLV is calculated using x as the number of detected signal events and $k = T/\tau_{\mathrm{coin}}$ corresponding to the number of trials of duration τ_{coin} within the integration window. For the QI LLV, x is the number of measured coincidence counts and k is the number of idler firing events.

6.3.3 Experimental procedure

To perform the LLV analysis of the experimental data we have developed a three-step procedure, the goal of this procedure is to estimate the system parameters and the click probability distributions for scenarios when the target is present and when the target is absent. After the three measurements are completed we can proceed to apply the LLV framework to the experimental data and compare the target present (H1) and target absent (H0) cases. Prior to taking the measurements we have used a technique described in Section 5.2.3.1 to calculate the relative delay between the signal and idler detection channels. The experimental procedure requires performing three measurements:

1. **Calibration of the system**: We start the experimental procedure with the calibration of the environment. We identify two potential sources of background within the system, deliberate background injected via an LED (only signal detector) and dark counts of SPADs (both detectors). To calibrate this background, we execute a calibration procedure involving the acquisition of 300 measurements. Each measurement corresponding to counts accumulated in one integration time T. Throughout this process, we ensure that the pump light is obstructed from reaching the ppKTP crystal. We record click counts on both the signal and idler detectors, as well as coincidences between the signal and idler detectors.

2. **Target absent**: We enable the pump light to enter the ppKTP crystal. In this phase of data collection, we introduce a beam block into the signal photons path, effectively preventing them from reaching the SPAD. We consider all the signal detector counts to come from the LED simulating the background level. This measurement scenario simulates a condition where no target is present for us to probe. During this

stage, we extract a small portion of the acquired data for the purpose of calibrating the click probabilities associated with the absence of a target (H0).

3. **Target present**: In the last phase of our measurement procedure, we remove the beam block from the signal path, enabling the signal photons and background photons coming from the LED to interact with the SPAD. Once again, we set aside a small portion of the data gathered for the purpose of estimating the click probability distribution when the target is present (H1).

After all measurements are completed, we use the data gathered in step 1 to estimate the average background ($\bar{n}_{\mathrm{bg}}$) and ($\bar{n}_{\mathrm{bg,I}}$) from the signal and idler detector counts respectively. Next, we estimate the mean photon number generated in the process of SPDC ($\bar{n}$) from a small portion of the data taken in step 3 (typically first 50 measurements), we use the idler click data due to no additional attenuation present in the idler photon path. To perform the estimation of the mean photon number we use the heralding efficiency values measured in Section 5.1. Using the estimated values of background and mean photon number we calculate the theoretical probabilities of signal and idler detectors firing with an assumption of finite target reflectivity measured in Section 6.2.1.1.

6.4 Target discrimination

The accurate identification of target objects probed with LIDAR systems is challenged by loss and background. Loss encompasses attenuation due to absorption, scattering, reflection, and transmission, leading to weakened signal return. Background involves unwanted signals from detectors (dark counts), environmental factors (thermal background, jamming), and system imperfections, introducing inaccuracies and distortions. Addressing these

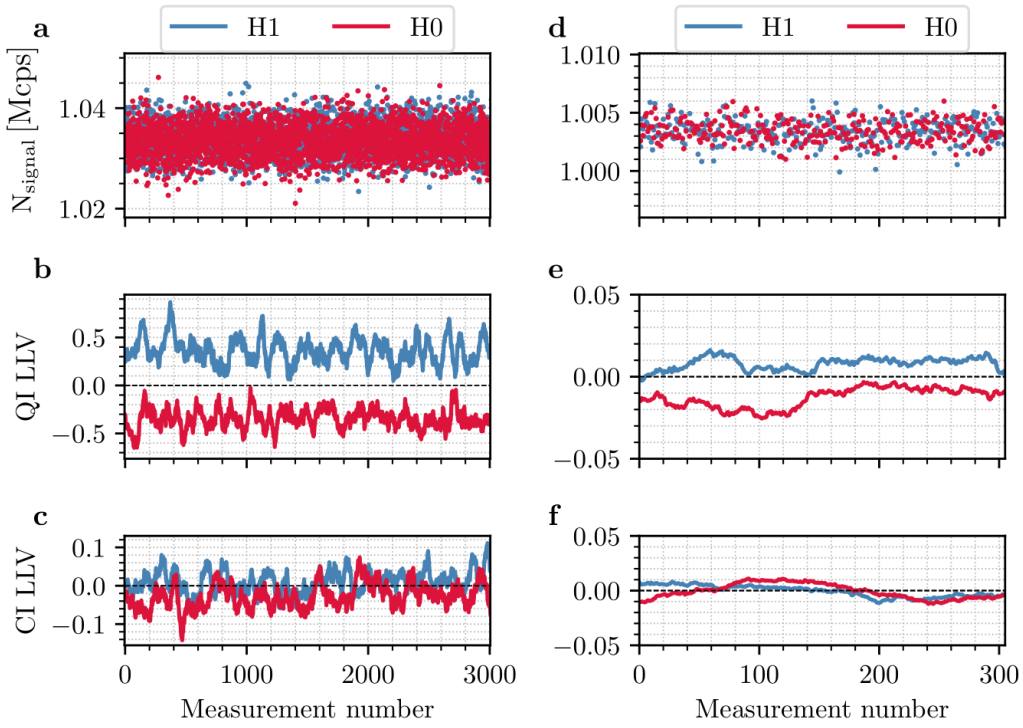

Figure 6.3: **a-c** Measurement in which signal is experiencing 33.5 dB loss in the presence of 10^6 background counts per second corresponding to SBR_{CI} of -37.9 dB. In **a** detection events registered by the signal detector are shown, while **b** and **c** show LLV analysis with 50 measurement moving average, applied to coincidence detection and classical detection respectively. In **d-f** we repeat the measurement after increasing the loss to 52 dB and reducing the SBR_{CI} to -51.5 dB, here to compensate for the low signal return of 7.1 $\pm$ 0.9 counts per second we increase the integration time per measurement to 1 s. Following the established convention we show signal detector count-rate in **d**, LLV analysis with 150 measurement moving average applied to quantum-enhanced **e** and classical **f** data.

challenges often requires advanced signal processing, sensor design, and calibration techniques [163]. Here we demonstrate the performance of our simple LIDAR system using single photon counting modules based on SPADs for detection.

Fig. 6.3 shows the performance of the LIDAR system for detecting a stationary target operating under two distinct loss regimes of 33.5 and 52 dB, approaching values typically encountered in real LIDAR systems ($\leq$ - 50 dB) [31]. In both cases, the system operates in a regime with an average back-

ground count rate of 10^6 counts per second, and using a coincidence window of $\tau_{\text{coin}} = 1$ ns.

For the data shown in Fig. 6.3**a-c** with a loss of 33.5 dB, the crystal is pumped at 50 μW giving a pair production rate of 377 $\pm$ 5 thousand counts per second. For the object present case, this gives an effective signal return rate of 167 $\pm$ 1 counts per second, corresponding to a classical signal to background of $\text{SBR}_{\text{CI}} = -37.9 \pm 0.1$ dB. To evaluate the quantum SBR ratio, we take the ratio of the measured coincidence rate with target present and background source turned off, against the number of accidental coincidences recorded with the background source enabled and target absent. For this data we find values of 39.1 $\pm$ 0.4 and 200.2 $\pm$ 0.5 counts per second respectively giving $\text{SBR}_{\text{QI}} = -7.1 \pm 0.1$ dB. We acquire 3050 consecutive measurements using an integration time of $T = 0.1$ s for both target-present and target-absent scenarios. Figure 6.3**a** shows the raw signal counts measured in each case, showing that the additional signal counts with the target present are indistinguishable compared to the $\sim$ 1000 count standard deviation of the background counts.

To apply the LLV analysis to the data, the single shot probability distributions $p_{\text{H}_{1,0}}$ are estimated using the first 50 measurements of each case, as described in Section 6.3.3. From this, the LLV $\Lambda(x, k)$ for each data point can be calculated, resulting in single-shot distinguishabilities of $\phi_{\text{QI}} = 0.31 \pm 0.01$ and $\phi_{\text{CI}} = 0.086 \pm 0.003$ respectively, demonstrating the enhancement in detection performance using QI. To enhance further the distinguishability we perform a rolling window average with $N_{\text{av}} = 50$ to smooth the data. Figure 6.3**b-c** shows the corresponding averaged LLV data for QI and CI, which clearly reveals that despite the relatively small change in signal level on the detector the QI enhanced LIDAR is able to discriminate between target present and target absent robustly, with the corresponding averaged Λ values never crossing zero. The classical LLV however is significantly nois-

ier, with both cases frequently crossing the detection threshold leading to significant error if using this for discrimination.

In Fig. 6.3**d-f** the loss is increased to -52 dB, with the pump power increased to 150 μW to increase the outgoing pair rate to 1.13 ± 0.02 million counts per second whilst maintaining the same level of background. In this regime the effective signal return rate in the object present case reduces to 7.1 ± 0.9 counts per second, corresponding to a classical signal to background of $\mathrm{SBR_{CI}} = -51.5 \pm 0.6$ dB. The coincidence counts rates with target present and background source disabled equal to 1.8 ± 0.1 counts per second and for target-absent with background engaged equal to 577 ± 1 counts per second respectively, leading $\mathrm{SBR_{QI}} = -25.1 \pm 0.2$. As the system is now operating with a signal over 5 orders of magnitude smaller than the background level, the integration time is increased to $T = 1$ s for these measurements. As before, Fig. 6.3**d** shows that the raw signal counts are indistinguishable, however using a rolling window of $N_{\mathrm{av}} = 150$ from Fig. 6.3**e-f** it is clear that the QI LLV is able to discriminate between target present and absent cases despite these challenging operating parameters whilst the CI LLV is entirely unreliable, with distinguisbabilities of $\phi_{\mathrm{QI}} = 0.67 \pm 0.22$ and $\phi_{\mathrm{CI}} = 0.33 \pm 0.02$ for the window-averaged data.

6.5 Jamming

Classical jamming of LIDAR systems refers to intentional interference aimed at disrupting the operation of LIDAR technology, as well as operation in an environment where the level of background fluctuates. Intentional jamming techniques involve emitting strong modulated light or laser signals or deploying countermeasures to confuse or overwhelm the LIDAR sensor. The objective of intentional jamming of LIDAR systems is to hinder accurate data gathering, compromise situational awareness, or impede target detection and

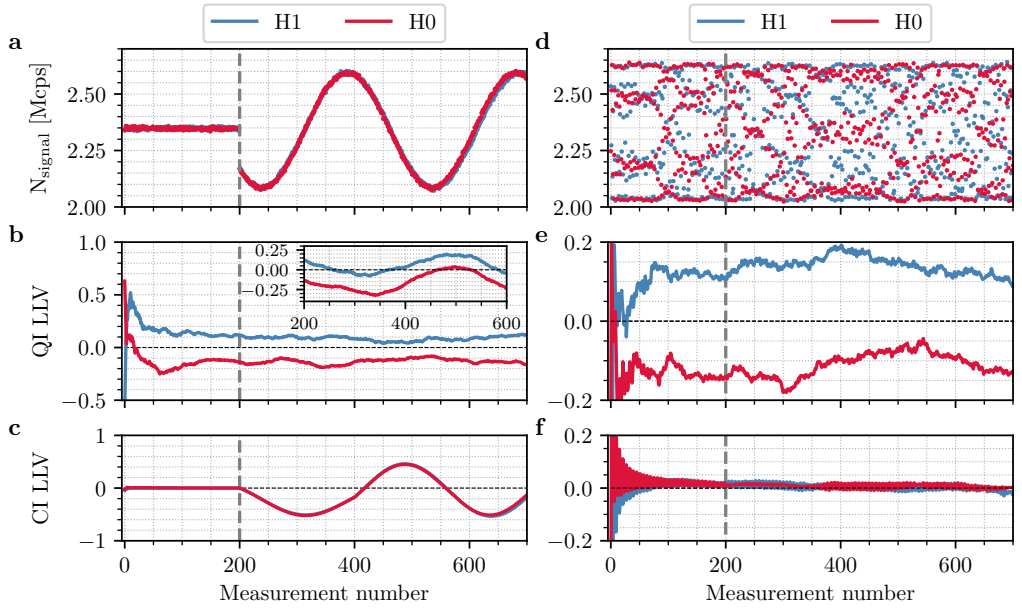

Figure 6.4: Two jamming experiments, in **a-c** we apply slow modulation after estimating the H1 & H0 probabilities with a static background for 200 measurements (grey vertical dashed line) and in **d-f** we apply fast modulation of the background and estimate the probabilities with dynamic background (grey vertical dashed line). Both experiments were performed under identical conditions of 33.5 dB loss, 2.3×10^6 average background counts per second, 0.3×10^6 modulation amplitude and integration time of 0.1 s. Here in **a** and **d** signal detector count rates are plotted. In **b** and **e** LLV analysis applied to our quantum-enhanced experimental data is shown, here on plot **b** the inset shows the LLV analysis without dynamic background tracking, and the main plot shows the results with us dynamically tracking the background. In **c** and **f** results of classical LLV analysis were plotted.

classification. Such jamming activities can lead to impaired perception and navigation capabilities in autonomous vehicles and other LIDAR-dependent applications, potentially resulting in hazardous scenarios. In the following, we demonstrate the resilience of quantum-enhanced LIDAR to dynamic jamming using both slow and fast modulation of the background level. For both of these experiments, the target loss was set to 33.5 dB, pump power to 50 μW, $T = 0.1$ s, with an average background of 2.3×10^6 counts per second modulated with an amplitude of 0.3×10^6 counts per second.

Figure 6.4**a-c** shows the effect of applying a slow sinusoidal background mod-

ulation after an initial period of constant background which is used to estimate the single shot probabilities $p_{\mathrm{H}_{1,0}}$. In the inset of Fig. 6.4**b** we show the QI LLV evaluated assuming the initial constant background data, which shows that whilst we maintain a clear separation between the QI LLV for object present and absent case, the modulation is visible in the data.

To mitigate this effect we implement dynamic background tracking by using the raw-signal data to estimate the average background level associated with each measurement (valid in this regime where $\bar{n}_{\mathrm{bg}} \gg \bar{n}_{\mathrm{sig}}$). Using our model (See Section 6.5.1), we create a look-up table (LUT) of probabilities $P_{\mathrm{H}_{1,0}}$ for different background levels $\bar{n}_{\mathrm{bg}}$ whilst keeping all other parameters constant. For each measurement, we then use the raw signal counts to assign the appropriate probability distribution when calculating the single-shot LLV. This pre-calculated LUT approach can be used to enable real-time implementation in future experiments using the signal count-rate to track the background. The resulting QI LLV is shown in the main plot of Fig. 6.4**b**, which has now eliminated the modulation and shows the QI LIDAR can be made immune to slow jamming with a single shot distinguishability of $\phi_{\mathrm{QI}} = 0.15 \pm 0.03$ despite the 26 % background modulation. For comparison, Fig. 6.4**c** shows the classical LLV (for which no background correction is possible) is completely unable to distinguish between the two regimes and has been spoofed by the jamming signal.

In Fig. 6.4**d-f** we perform a second experiment where a fast white background source is now added to the slow classical modulation, resulting in a pseudo-random background level seen from the signal on the number of signal counts in **d**. As with the slow modulation, the QI LLV is immune to the fast background changes whilst the classical LLV data is entirely washed out with the fast background changes causing the CI LLV to average to zero making it unable to distinguish if a target is present. These data highlight the advantage of QI not only in performing the target discrimination better

but also in providing a system robust to jamming.

6.5.1 Dynamic Background Tracking

For the slow classical jamming data shown in Fig. 6.4**a** the system parameters are initially obtained by performing analysis of the first 200 measurements with static background $\bar{n}_{\mathrm{bg,S}}$. We then define 25 discrete background levels in the range 2.1-2.7$\times 10^6$ counts per second, and for each value recalculate the single shot click probabilities in Eqs. 6.7 and 6.8 using a re-scaled value of $\bar{n}'_{\mathrm{bg,S}}$. Subsequently, the experimental data obtained with jamming engaged was analysed by calculating the LLV for each point in time by using the relevant click probabilities associated with the level that closest matches the instantaneous signal counts to dynamically track slow changes in the background.

6.6 Rangefinding

The main application of LIDAR-based systems involves the use of time-of-flight detection to estimate the distance to targets. In this Section, we extend our quantum-enhanced LIDAR to demonstrate active rangefinding even in the presence of classical background.

The modified experimental setup used for rangefinding is shown in Fig. 6.5. It is worth noting that for this scheme to work, the reflective target must preserve the polarisation of the signal photons. This is not a realistic assumption unless the target is a dielectric mirror, as used in our setup. This experiment could have been realised without the requirement of preserving polarisation if two mirrors placed at a 45-degree angle were mounted on the translation stage, displacing the signal beam upon reflection. In order to simulate variations in target position, a mirror serving as the target was positioned on a motorized translation stage enabling the target to be moved a

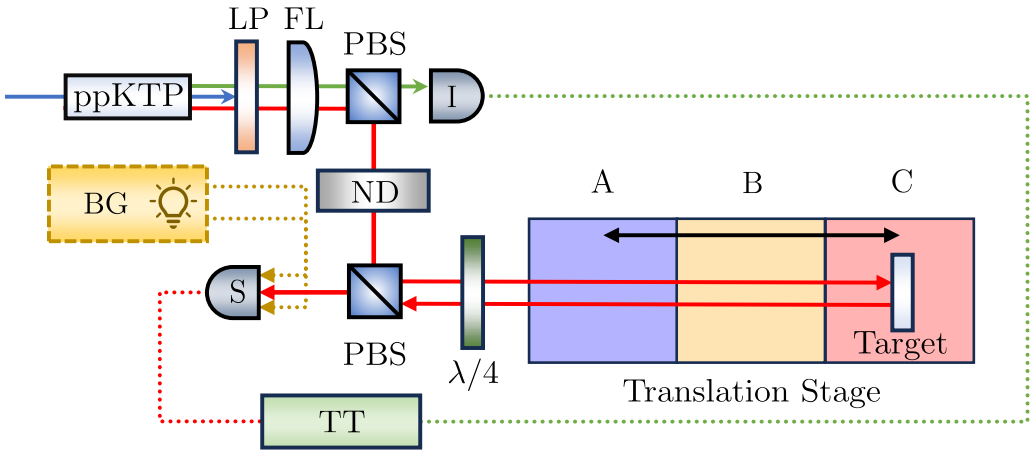

Figure 6.5: The experimental setup used for performing the rangefinding experiment. The photon pair generated in a ppKTP crystal pumped with a 405.35 nm CW laser diode. The idler and the signal are separated using a PBS and the idler is detected locally, signal undergoes attenuation passing through the ND filter and is reflected from a PBS, passes through the $\lambda/4$ waveplate which turns the vertical polarisation into a right-handed circular polarisation, which reflected from a flat mirror serving as a target, becomes left-handed circular polarisation. Upon passing through the $\lambda/4$ again the left-handed circular polarisation becomes horizontally polarised, passes through the PBS and is detected by a signal detector S. Mirror serving as a target is placed on a motorised translation stage which moves between three positions A, B and C separated by 11 cm.

total range of 22 cm. We define three locations separated by 11 cm intervals, denoted as A, B, and C, and assign three parallel coincidence detection channels with delays of $\tau_{x_A} = 1.77$ ns, $\tau_{x_B} = 2.52$ ns, and $\tau_{x_C} = 3.27$ ns corresponding to the round-trip time to each location. As above, the experiment was performed with a loss of 33.5 dB and 50 μW pump power, but with an average background of 0.1 $\times 10^6$ background counts and a jamming amplitude of 10^3 counts per second. To achieve better resolution and mitigate the cross-talk between target positions due to the 250 ps jitter of our detectors, the coincidence window τ_{coin} was set to 0.2 ns.

During the experiment, we acquire data for each coincidence channel in parallel, with the target moved from an initial position of x_A to x_B after 1000 measurements and finally to x_C after 1500 measurements. The results are

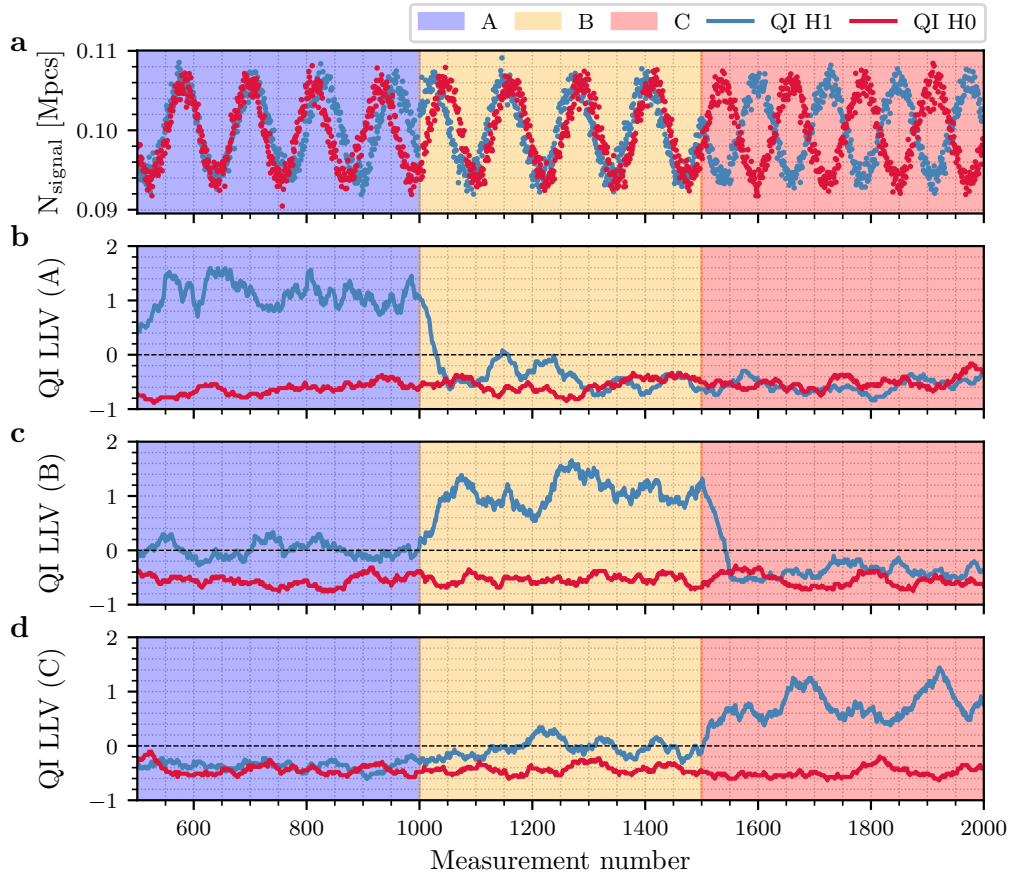

Figure 6.6: We apply a modulated background level and translate the target from an initial location of A = 0 to B = 11 cm after 1000 measurements, moving to C = 22 cm after 1500 measurements. **a** Raw signal counts showing background modulation is constant and independent of the target location. **b-d** QI LLV with coincidence channel delays set to probe targets at A, B, C respectively. These results show the QI can perform confident range finding even in the presence of a significant background.

shown in Fig. 6.6**a-d**, whereas before the raw signal counts are indistinguishable for both target presence and position whilst the corresponding QI LLV channels calculated for $N_{\text{av}} = 50$ clearly reveal the quantum-enhanced LIDAR is able to resolve robustly the location of and hence track the target as it moves between the three distinct locations, despite there being no active modulation of the source, and in the presence of intentional classical background.

Note that since the time reference for range finding comes exclusively from the

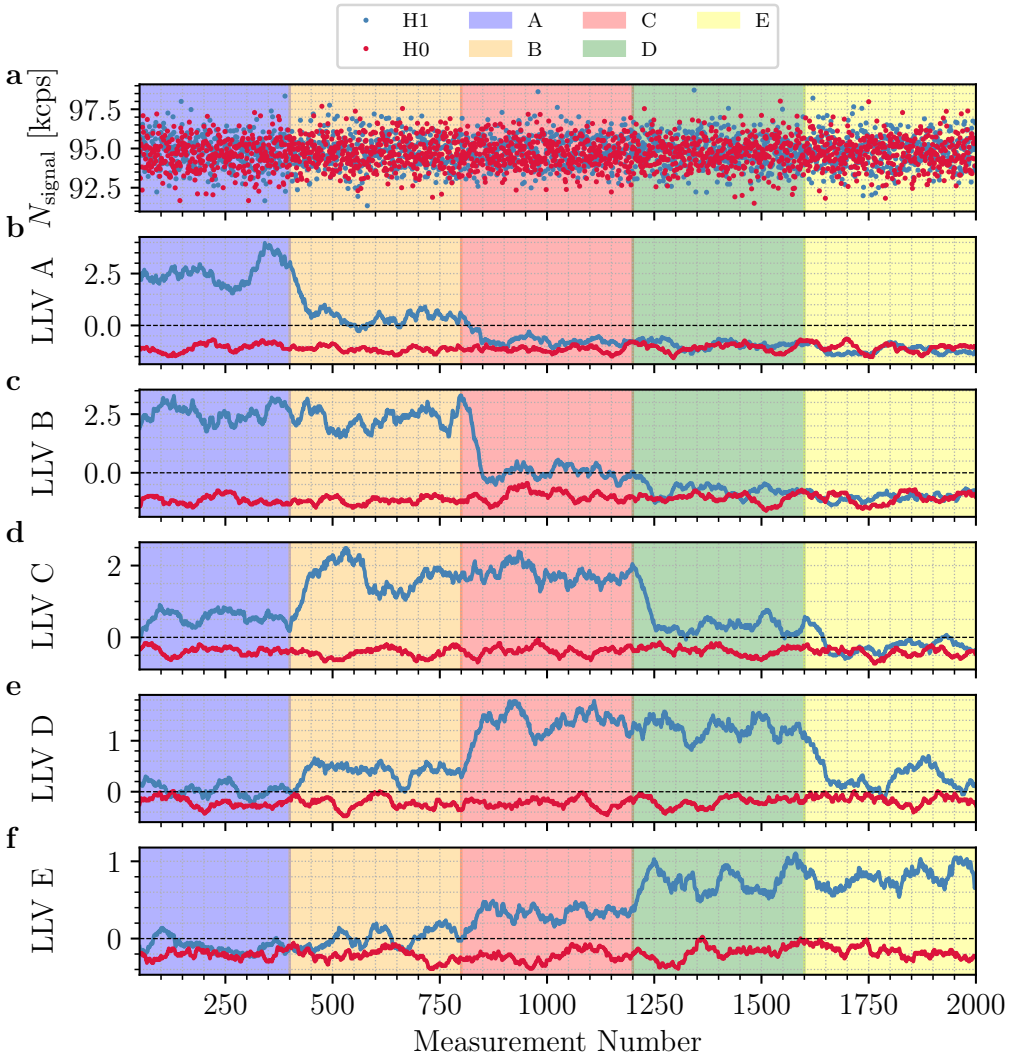

Figure 6.7: Rangefinding experiment using five sequential target positions under static background. The target moves from A = 0 to E = 22 cm, with 400 measurements at each position. **a** shows stable background levels across target locations. **b-f** present QI LLV data for each position, demonstrating the system's incapability to distinguish closely spaced targets due to detector jitter effects.

heralding of the idler photon, the CI detection method is unable to provide any rangefinding information. Further, the SPDC generation of photon pairs from a CW pump provides robustness against spoofing due to the covertness of illumination, which appears to the target as a weak thermal source within the environmental background.

To confirm the spatial resolution of the device and investigate the effects of detector jitter on the system's ability to accurately resolve target positions, an additional experiment was conducted under identical conditions to those described above. However, instead of probing three target positions, five distinct positions were used, designated as A, B, C, D, and E. These positions were separated by increments of 5.5 cm, which is half of the previously used separation, resulting in the following arrangement: position A at 0 cm, B at 5.5 cm, C at 11 cm, D at 16.5 cm, and E at 22 cm. The corresponding delays for these positions were $\tau_{x_A} = 1.77$ ns, $\tau_{x_B} = 2.142$ ns, $\tau_{x_C} = 2.52$ ns, $\tau_{x_D} = 2.90$ ns, and $\tau_{x_E} = 3.27$ ns.

The experiment was performed with just static background, as illustrated in Fig. 6.7. It was observed that when the target was probed at five positions instead of three, the ability of the device to discern the exact position of the target was somewhat impeded, which was evidenced by increased cross talk between adjacent target positions. This cross talk can be attributed to the SPAD timing jitter, which was approximately 0.25 ns.

6.7 Realistic Imaging System

In the previous section, we presented the capabilities of our quantum-enhanced LIDAR system, focusing on target discrimination and rangefinding. Our initial tests used a mirror as a target, along with an ND filter to simulate target reflectivity and an LED to inject background, mimicking background interference. While these results were promising, it is essential to assess the system's performance in more realistic scenarios to evaluate its practical utility. In this section, we modify our experimental setup accordingly to simulate real-world conditions.

To better replicate real-life conditions, we used a white paper target, akin to the variable-reflectivity surfaces like paper, signage, or road markings that

LIDAR systems frequently encounter. This shift from the mirror's high reflectivity to paper's diffuse characteristics introduces new challenges for our quantum-enhanced LIDAR to overcome.

To accommodate the change in target and simulate real-world scenarios, we made several modifications to our experimental setup. The most notable adjustment was the incorporation of a collection optics in the form of a zoom lens. This lens allowed us to collect reflected light from the white paper over an extended range, providing a more comprehensive assessment of the system's performance in practical settings.

6.7.1 Experiment Design & Setup

The experimental setup used to conduct the realistic target detection experiment is shown schematically in Fig. 6.8. To perform the experiment we launch a collimated signal beam to probe a target (a white piece of paper), across the optical table. To collect the light reflected from the target we use a zoom lens imaging system consisting of a variable focal length zoom lens (Navitar MVL7000), a Galilean telescope with a ratio of 2:1 and a collimation lens. The zoom lens is focused on the target prior to taking a measurement and the telescope is used to reduce the beam waist to match the aperture size of the collimation lens. The collimation lens focuses the beam into a multi-mode optical fibre connected to the signal SPAD. Before the target discrimination measurement is performed, we measure the relative delay between the idler detector and the signal detector using a technique described in Section 5.2.3.1. Due to the limited space on the optical table, the distance between the target and the collection optics was limited to $\sim$86 cm. To simulate the case in which the target is absent we simply block the signal beam.

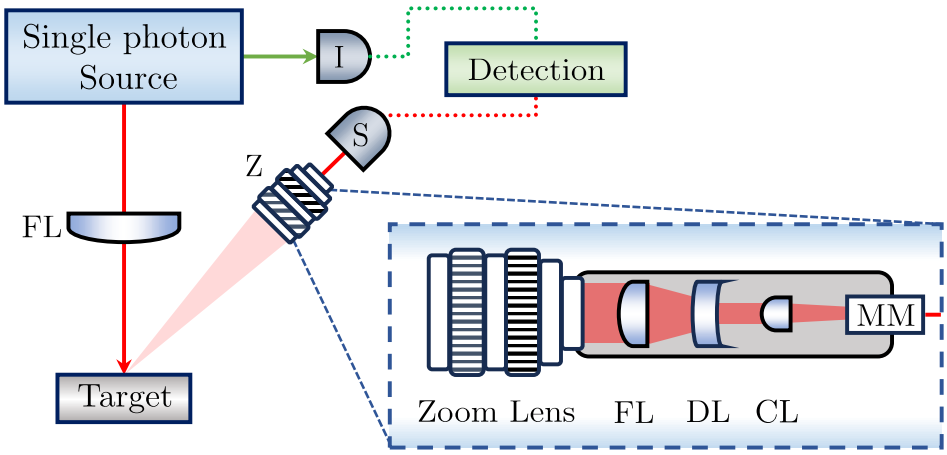

Figure 6.8: The experimental setup used to conduct the realistic detection experiment. Here the idler photon is detected locally, while a collimated beam of signal photons is launched at a target (a white piece of paper). We have used a focusing lens, placed in front of the target to reduce the spot size of the signal beam in order to enhance the collection efficiency. Light reflected from the target is collected using a zoom lens imaging system (Z) focused on the target. The inset shows the system used to collect the reflected light in detail, here the variable focal length zoom lens is used to collect the light from the target. Next, a Galilean telescope consisting of a focusing (FL, f = 100 mm) and diverging (DL, f = -50 mm) lens is used to reduce the beam size to match the size of the collimation lens (CL) which is used to couple the collected light into a multi-mode optical fibre (MM). The imaging system is encased in a lens tube to prevent the background light from leaking into the system.

6.7.2 Results

Figure 6.9 shows the performance of the LIDAR system for detecting a stationary target at two distances of 36 cm and 86 cm. In both experiments, the system operates in a regime with an average background count rate of around 6×10^3 counts per second, and using a coincidence window of $\tau_{\text{coin}} = 1$ ns. The background in the system comes from the ambient light in the laboratory. In both experiments, the crystal is pumped at 3.5 mW giving a pair production rate of 41×10^6 counts per second.

Using the formula

$$\eta = \frac{r^2}{4d^2} \tag{6.10}$$

we can estimate the collection efficiency η for a point source at a working distance d and lens radius r. In the limit of a plane surface scatter, lower bound on efficiency is twice η [168]. This means that at the distance $d =$ 86 cm and for the lens used in the experiment $r = 2.5$ cm we should expect -33 dB loss introduced by the collection efficiency of the zoom lens in our experiment. The transmission through the zoom lens was measured to be $\sim 40\%$ and the efficiency of the SPADs is $\sim 60\%$. This results in expected loss in the system to equal -39.94 dB. In the experiment we measure ∼300 counts per second of the return signal photons (equivalent to -51 dB loss) at a distance of 86 cm. This discrepancy can be attributed to a sub-optimal fibre coupling into the signal detector.

For the data shown in Fig. 6.9**a-c**, the distance between the collection optics and the target is 36 cm and the relative delay between the signal and the idler channels was measured to be 10.6 ns. For the object present case we measured the signal return rate of 380 $\pm$ 1 counts per second corresponding to the classical signal-to-background ratio of $\mathrm{SBR_{CI}} = -12.01 \pm 0.01$ dB. To evaluate the quantum SBR ratio, we take the ratio of the measured coincidence rate with target present minus the coincidence rate with target absent against the coincidence rate when the target is absent. For this data we find values of 55.1 $\pm$ 0.1 and 72.3 $\pm$ 0.1 counts per second respectively giving $\mathrm{SBR_{QI}} = -1.16 \pm 0.01$ dB. We acquire 1000 consecutive measurement using an integration time of $T = 0.1$ s for both target present and absent scenarios.

To apply the LLV analysis to the data, we use the same approach as described in Section 6.4. To enhance the distinguishibility further we perform a rolling window average with $N_{\mathrm{av}} = 15$ to smooth the data. We measured distinguishibilities of $\phi_{\mathrm{QI}} = 0.592 \pm 0.006$ and $\phi_{\mathrm{CI}} = 0.303 \pm 0.004$ respectively for the window averaged data, demonstrating the enhancement in detection performance using QI. Figure 6.9**b-c** shows the corresponding

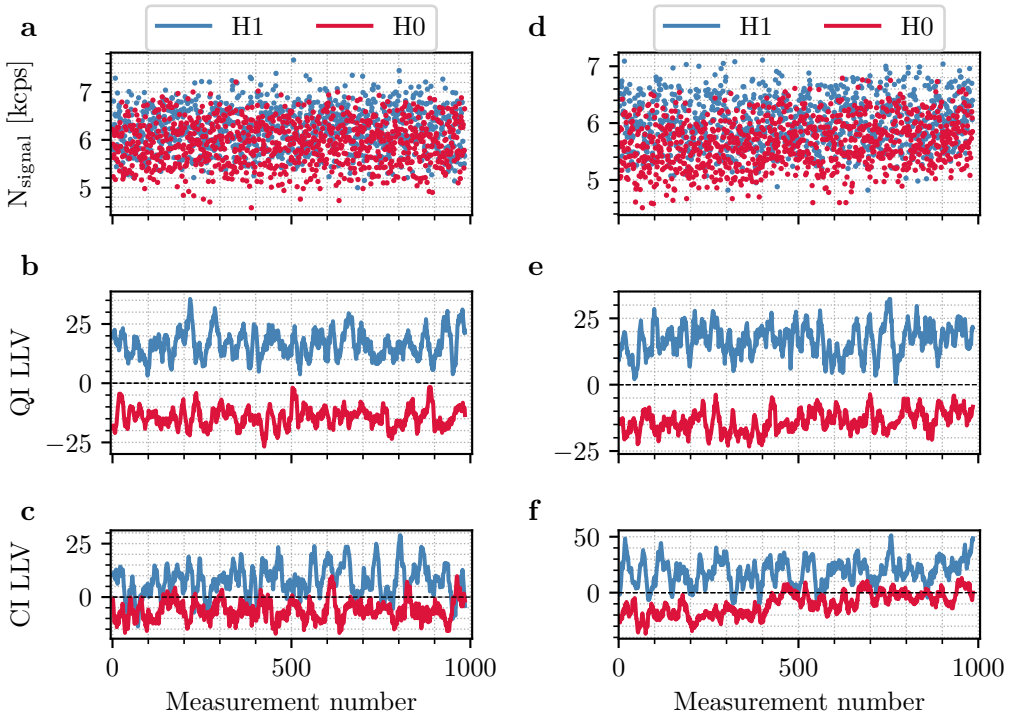

Figure 6.9: **a-c** Measurement in which we are detecting a target 36 cm away from the zoom lens. In **b** detection events registered by the signal detector are shown, while **c** and **d** show LLV analysis applied to coincidence detection and classical detection respectively. In **d-f** we repeat the measurement after increasing the distance between the target and the collection optics to 86 cm. Following the established convention we show signal detector count rate in **d**, LLV analysis with 15 measurements moving average applied to quantum-enhanced **e** and classical **f** data.

averaged LLV data for QI and CI, which reveals that the QI enhanced LIDAR is able to discriminate between target present between target present and target absent robustly, with the corresponding averaged Λ values never crossing zero. The classical LLV however is significantly noisier, with both cases frequently crossing the detection threshold leading to significant error if using this for target discrimination.

In Fig. 6.9**d-f** the distance between the target and the collection optics is increased to 86 cm, corresponding to 14.1 ns delay between the signal and idler detection channels. In this regime the effective signal return rate in the object present case reduces to 294.4 $\pm$ 1 counts per second, corresponding

to a classical signal-to-background ratio of $\mathrm{SBR_{CI}} = -13.05 \pm 0.01$ dB. To evaluate the quantum SBR ratio, we take the ratio of the measured coincidence rate with target present minus the coincidence rate with target absent against the coincidence rate when the target is absent. For this data we find values of 56.1 ± 0.1 and 77.3 ± 0.1 counts per second respectively giving $\mathrm{SBR_{QI}} = -1.21 \pm 0.01$ dB. As previously, we have applied the LLV analysis to the experimental data and using a rolling window of $N_{\mathrm{av}} = 15$ allows us to clearly distinguish between the presence and absence of the target in the QI case, while the CI remains unreliable, with distinguishibilities of $\phi_{\mathrm{QI}} = 0.581 \pm 0.007$ and $\phi_{\mathrm{CI}} = 0.215 \pm 0.005$ for the window averaged data.

6.7.3 Discussion

In conclusion, we have presented an experimental demonstration of a quantum-enhanced LIDAR system utilising a log-likelihood analysis framework for target detection and rangefinding, robust to classical jamming and dynamic background changes in challenging regimes of high background and low signal rates. This work significantly expands beyond prior research on quantum LIDAR based on correlated photon sources [13–16, 31, 32], specifically by operating in the regime of both large environmental backgrounds (SBR < -50 dB) and low signal returns (> 50 dB attenuation), compatible with realistic LIDAR [31]. Our observations reveal a significant improvement in the signal-to-background ratio of up to 30 dB when comparing classical and quantum LIDAR, with the ultimate limitation in quantum gain related to the second-order correlation of the pair source $g^2_{s,i}(0)$ [14]. This improvement represents an approximate 13 dB increase in SBR compared to the findings in [14], and is comparable to the results reported in [15].

Our quantum-enhanced LIDAR approach is resilient against both sinusoidal and white-background modulated classical jamming, and we present a new protocol for active background tracking to reduce sensitivity to slow drifts

or intentional spoofing attempts while remaining immune to high-frequency fluctuations. Specifically, this technique works optimally in the regime of high background where the instantaneous count rate measured on the signal detector provides a real-time probe of the background rate which can then be used to improve the resilience against background when analysing small changes in the measured coincidence rate.

Applying these techniques in a range-finding modality, we demonstrate the ability not only to perform target detection but also to determine the location of the target in the presence of active jamming. Currently, we demonstrate a resolution of 11 cm, limited only by the timing jitter of the Si-SPADs motivated by the ability to incorporate these into a low-power, portable device. Enhanced performance is possible using either better performing Si-SPADs (timing jitter $\sim$35 ps [169] or superconducting nanowire detectors offering significantly reduced timing uncertainty achieving sub-10 ps [170–173] at the cost of requiring a cryogenic cooling system.

While the ability to achieve centimetre-level resolutions with non-cryogenically cooled SPADs is promising for practical applications, it is important to acknowledge the fundamental limitation that long-range or low-reflectivity targets require a sufficient photon flux for at least one return photon within the experiment window. This makes the detection of uncooperative targets at distance challenging, with the demonstrated -52 dB loss comparable to that expected from a Lambertian scatterer at 15 m using a 10 cm diameter telescope. Nonetheless, our results demonstrate that quantum-enhanced LIDAR offers a practical speedup in time to detection, allowing for operation at lower light levels, while presenting a low-intensity random thermal signal to observers. We also note that the detection of cooperative targets could, even with the results presented here, be accomplished at significant distances.

In contrast to other groups [31] that often utilise histogramming approaches to analyse rangefinding data — where click data is averaged to identify the

centre of the coincidence peak and thereby determine the distance to the target — such methods were impractical for our system under the challenging conditions of high background level and low signal returns. Specifically, in scenarios with a -52 dB loss (Fig. 6.3**d-f**), the difference between coincidence counts with and without a target present was approximately 1 coincidence count, with 500 accidental coincidences coming from background. Employing histogramming in these conditions would necessitate significantly increased integration times to accumulate enough data for meaningful analysis, which is not feasible for our operational requirements. This limitation underscores one of the strengths of the LLV framework, which provides robust target detection and rangefinding capabilities even under extreme conditions.

Compared to classical LIDAR methods that rely on amplitude-modulated pulses for rangefinding, our use of continuous-wave sources mitigates the risk of being spotted and spoofed by observers as peak pulse intensity increases. These results emphasise the advantages of exploiting quantum correlations for LIDAR applications and provide a clear pathway towards the realistic deployment of this system in scenarios comparable to real-world operations.

Our investigation into the quantum-enhanced LIDAR system under conditions that closely mimic the real world has produced encouraging outcomes. Adjustments to the experimental setup were essential, with the integration of a zoom lens being a key enhancement for capturing light from non-ideal reflective surfaces at increased ranges.

The system's ability to accurately detect a stationary target at distances of 36 cm and 86 cm—despite the background introduced by ambient laboratory light—demonstrates its resilience and advanced discrimination capabilities over classical LIDAR systems.

These results validate the quantum-enhanced LIDAR's performance advantage in noisy and challenging conditions. The technology shows significant promise for precision-critical applications such as autonomous navigation,

remote sensing, and object recognition in adverse settings [164–166].

The superior performance observed positions quantum-enhanced LIDAR as a transformative prospect for sectors including aerospace, robotics, and environmental monitoring. As the research progresses, we anticipate a broader realisation of quantum-enhanced imaging system's capabilities, paving the way for their extensive adoption and normative integration [164–166].

Part IV

Conclusions and Outlook

Chapter 7

Conclusions and Outlook

This chapter encapsulates the central achievements of this research and delineates the potential trajectories for future advancements in the domain of quantum-enhanced LIDAR.

7.1 Conclusions

The primary aim of this thesis was to explore the development and experimental realisation of quantum-enhanced LIDAR systems, which involved intricate theoretical models and hands-on implementations to achieve significant advancements in quantum sensing technology.

In Chapter 3, a robust numerical model for the coupled-cavity Optical Frequency Comb Generator (OFCG) was crafted. This model was essential for simulating the dynamics within the OFCG and optimising its performance. Through comprehensive simulations, the thesis established optimal parameters for generating a high-power, GHz train of pulses. These parameters included the tuning of cavity lengths, modulation frequencies, and pump power levels, which were crucial for maximising the output power and ensuring stability of the frequency combs produced.

Chapter 4 marked a critical transition from theoretical constructs to practical implementation. The coupled-cavity OFCG was successfully realised and tested under laboratory conditions. With a modest 300 mW input power, the system demonstrated extraordinary efficiency, achieving observed peak powers near 26W at a 4.78 GHz repetition rate. This significant amplification from input to output showcased the potential of the OFCG design to serve as a powerful backbone for advanced photonic systems, including quantum-enhanced LIDAR.

The advancement of heralded single photon sources was explored in Chapter 5. Utilising a continuous-wave input pump laser at 405 nm, the thesis detailed the development of a source with an impressive brightness metric of 7.55 Mcps/mW. Furthermore, a heralding efficiency of around 20% was achieved, a critical metric ensuring the source's compatibility with quantum-enhanced LIDAR systems. These developments are pivotal for quantum communications and sensing applications, where efficient and reliable single photon sources are essential.

The culmination of these efforts was presented in Chapter 6, where a quantum-enhanced LIDAR system was fully implemented and tested. Despite the challenging conditions of significant background (million counts per second) and very low signal rates (few counts per second), the system demonstrated a remarkable enhancement in the signal-to-background ratio. The integration of novel strategies for active background tracking and the application of a log-likelihood analysis framework enabled the system to accurately discern targets even under conditions of active jamming. The system achieved an impressive spatial resolution of 11 cm, although this was limited by the timing jitter of the Si-SPADs used in the experiments.

7.2 Outlook

7.2.1 Improving Pulse Width and Efficiency of a Coupled - Cavity OFCG

The ability of the OFCG to generate pulses with the power levels suitable for generation of single photons through spontaneous four-wave mixing hinges on its output efficiency and pulse width. Currently, the primary limitation in harnessing higher input powers is the damage threshold of the EOM AR coating. The dimensions of the active crystal aperture add to this restriction, capping our pump at 300 mW. Potential avenues for circumventing these challenges include the exploration of alternative coatings or EOM crystal materials. Furthermore, transitioning to telecom wavelengths could confer advantages in terms of heightened damage thresholds.

In our experiments, we achieved an output efficiency of $\eta_{\mathrm{CC}} = 72.4$ % and a FWHM pulse width of $\tau_p = 1.77$ ps. This translated to a peak power per pulse of $\mathrm{P_{pk}} = 25.5$ W. However, our numerical model projected achievable peak powers of $\mathrm{P_{pk_{th}}} = 43.3$ W and pulse widths below a picosecond for the same input power. The disparity between observed and expected outcomes can be attributed to several factors. Chief among them are the imperfections in the EOM's crystal transmission and the etalon effects in the input cavity, which arise due to the positioning of the AR coating. Addressing these issues—perhaps by investigating materials with superior coatings or fine-tuning the input cavity's length in conjunction with a wedged AR coating on mirror M2—might pave the way for enhanced system performance.

7.2.2 Quantum-Enhanced LIDAR - Outlook

The foundation established throughout this thesis delineates several avenues for refining the quantum-enhanced LIDAR system. Real-time processing

of experimental data emerges as an indispensable component for future quantum-enhanced LIDAR systems targeting broader applications. The intrinsic simplicity of the LLV theoretical framework, revolving predominantly around linear operations, is indicative of the potential for real-time processing. Such a real-time system would consistently update log-likelihood values, substantially improving the system's capability in target discrimination and rangefinding. This is paramount for scenarios that demand swift data analysis and decisions, ranging from defence operations to autonomous navigation.

Future improvements in target detection can be achieved by revamping the imaging system. Utilising machine learning algorithms [174], in synergy with an advanced optical array of imaging optics and detectors, might significantly elevate our ability to scan, track, and create 3D maps of targets.

Lastly, while the incorporation of superconducting nanowire detectors [16] could significantly boost the heralding efficiency and curtail time jitter, it is vital to address the trade-offs associated with such detectors. A critical challenge arises from their dependency on intricate cryogenic cooling systems. This requirement substantially escalates the Size, Weight, and Power (SWAP) of the quantum-enhanced LIDAR apparatus, potentially hampering its practicability in real-world scenarios. Currently, we demonstrate a resolution of 11 cm, limited only by the timing jitter of the Si-SPADs, motivated by the ability to incorporate these into a low-power, portable device. Enhanced performance is possible using better performing Si-SPADs (timing jitter $\sim$35 ps) [169].

In essence, the trajectories mapped out here not only present immediate action points but also sketch a broader horizon for the evolution of quantum-enhanced LIDAR in the coming years.

Bibliography

[1] M. I. Skolnik, "Introduction to radar," *Radar handbook*, vol. 2, p. 21, 1962.

[2] D. Atlas, R. Srivastava, and R. S. Sekhon, "Doppler radar characteristics of precipitation at vertical incidence," *Reviews of Geophysics*, vol. 11, no. 1, pp. 1–35, 1973. [Online]. Available: https://doi.org/10.1029/RG011i001p00001

[3] P. McManamon, "Review of ladar: a historic, yet emerging, sensor technology with rich phenomenology," *Opt. Eng.*, vol. 51, p. 060901, 2012. [Online]. Available: https://doi.org/10.1117/1.OE.51.6.060901

[4] N. Li, C. P. Ho, J. Xue, L. W. Lim, G. Chen, Y. H. Fu, and L. Y. T. Lee, "A Progress Review on Solid-State LiDAR and Nanophotonics-Based LiDAR Sensors," *Laser Photonics Rev.*, vol. 16, p. 2100511, 2022. [Online]. Available: https://doi.org/10.1002/lpor.202100511

[5] M.-C. Amann, T. M. Bosch, M. Lescure, R. A. Myllylae, and M. Rioux, "Laser ranging: a critical review of unusual techniques for distance measurement," *Opt. Eng.*, vol. 40, no. 1, p. 10, 2001. [Online]. Available: https://doi.org/10.1117/1.1330700

[6] A. Hooijer and R. Vernimmen, "Global LiDAR land elevation data reveal greatest sea-level rise vulnerability in the tropics,"

Nature Comm., vol. 12, no. 1, p. 3592, 2021. [Online]. Available: https://doi.org/10.1038/s41467-021-23810-9

[7] S. Royo and M. Ballesta-Garcia, "An Overview of Lidar Imaging Systems for Autonomous Vehicles," *Appl. Sci.*, vol. 9, no. 19, p. 4093, 2019. [Online]. Available: https://doi.org/10.3390/app9194093

[8] M.-C. Amann, T. M. Bosch, M. Lescure, R. A. Myllylae, and M. Rioux, "Laser ranging: a critical review of unusual techniques for distance measurement," *Opt. Eng.*, vol. 40, no. 1, pp. 10 – 19, 2001. [Online]. Available: https://doi.org/10.1117/1.1330700

[9] D. Bronzi, F. Villa, S. Tisa, A. Tosi, and F. Zappa, "SPAD Figures of Merit for Photon-Counting, Photon-Timing, and Imaging Applications: A Review," *IEEE Sens. J.*, vol. 16, no. 1, pp. 3–12, 2016. [Online]. Available: https://doi.org/10.1109/JSEN.2015.2483565

[10] G. Chen, C. Wiede, and R. Kokozinski, "Data Processing Approaches on SPAD-Based d-TOF LiDAR Systems: A Review," *IEEE Sens. J.*, vol. 21, no. 5, pp. 5656–5667, 2021. [Online]. Available: https://doi.org/10.1109/JSEN.2020.3038487

[11] C. Niclass, M. Soga, H. Matsubara, M. Ogawa, and M. Kagami, "A 0.18µm CMOS SoC for a 100m-range 10fps 200×96-pixel time-of-flight depth sensor," in *2013 IEEE International Solid-State Circuits Conference Digest of Technical Papers*, 2013, pp. 488–489. [Online]. Available: https://doi.org/10.1109/ISSCC.2013.6487827

[12] J. Walker, S. Seward, J. Rarity, and P. Tapster, "Range measurement photon by photon," *Quant. Opt. J. Eur. Opt. Soc. B*, vol. 1, no. 1, p. 75, 1989. [Online]. Available: https://doi.org/10.1088/0954-8998/1/1/008

[13] J. G. Rarity, P. R. Tapster, J. G. Walker, and S. Seward, "Experimental demonstration of single photon rangefinding using

parametric downconversion," *Appl. Opt.*, vol. 29, no. 19, p. 2939, 1990. [Online]. Available: https://doi.org/10.1364/AO.29.002939

[14] D. G. England, B. Balaji, and B. J. Sussman, "Quantum-enhanced standoff detection using correlated photon pairs," *Phys. Rev. A*, vol. 99, p. 023828, 2019. [Online]. Available: https://doi.org/10.1103/PhysRevA.99.023828

[15] H. Liu, D. Giovannini, H. He, D. England, B. J. Sussman, B. Balaji, and A. S. Helmy, "Enhancing LIDAR performance metrics using continuous-wave photon-pair sources," *Optica*, vol. 6, p. 1349, 2019. [Online]. Available: https://doi.org/10.1364/OPTICA.6.001349

[16] H. Liu, B. Balaji, and A. S. Helmy, "Target Detection Aided by Quantum Temporal Correlations: Theoretical Analysis and Experimental Validation," *IEEE Trans. Aerosp. Electron Syst.*, vol. 56, no. 5, p. 3529, 2020. [Online]. Available: https://doi.org/10.1109/TAES.2020.2974054

[17] S. Lloyd, "Enhanced Sensitivity of Photodetection via Quantum Illumination," *Science*, vol. 321, no. 5895, p. 1463, 2008. [Online]. Available: https://doi.org/10.1126/science.1160627

[18] S.-H. Tan, B. I. Erkmen, V. Giovannetti, S. Guha, S. Lloyd, L. Maccone, S. Pirandola, and J. H. Shapiro, "Quantum Illumination with Gaussian States," *Phys. Rev. Lett.*, vol. 101, p. 253601, 2008. [Online]. Available: https://doi.org/10.1103/PhysRevLett.101.253601

[19] J. H. Shapiro, "The Quantum Illumination Story," *IEEE Aerosp. Electron. Syst. Mag.*, vol. 35, no. 4, p. 8, 2020. [Online]. Available: https://doi.org/10.1109/MAES.2019.2957870

[20] S. Guha and B. I. Erkmen, "Gaussian-state quantum-illumination

receivers for target detection," *Phys. Rev. A*, vol. 80, p. 052310, 2009. [Online]. Available: https://doi.org/10.1103/PhysRevA.80.052310

[21] Z. Zhang, S. Mouradian, F. N. C. Wong, and J. H. Shapiro, "Entanglement-Enhanced Sensing in a Lossy and Noisy Environment," *Phys. Rev. Lett.*, vol. 114, p. 110506, 2015. [Online]. Available: https://doi.org/10.1103/PhysRevLett.114.110506

[22] Q. Zhuang, Z. Zhang, and J. H. Shapiro, "Optimum Mixed-State Discrimination for Noisy Entanglement-Enhanced Sensing," *Phys. Rev. Lett.*, vol. 118, p. 040801, 2017. [Online]. Available: https://doi.org/10.1103/PhysRevLett.118.040801

[23] ——, "Quantum illumination for enhanced detection of Rayleigh-fading targets," *Phys. Rev. A*, vol. 96, p. 020302, 2017. [Online]. Available: https://doi.org/10.1103/PhysRevA.96.020302

[24] D. Luong, C. W. S. Chang, A. M. Vadiraj, A. Damini, C. M. Wilson, and B. Balaji, "Receiver Operating Characteristics for a Prototype Quantum Two-Mode Squeezing Radar," *IEEE Trans. Aerosp. Electron. Syst.*, vol. 56, no. 3, p. 2041, 2020. [Online]. Available: https://doi.org/10.1109/TAES.2019.2951213

[25] C. W. S. Chang, A. M. Vadiraj, J. Bourassa, B. Balaji, and C. M. Wilson, "Quantum-enhanced noise radar," *Appl. Phys. Lett.*, vol. 114, no. 11, 2019. [Online]. Available: https://doi.org/10.1063/1.5085002

[26] S. Barzanjeh, S. Pirandola, D. Vitali, and J. M. Fink, "Microwave quantum illumination using a digital receiver," *Science Adv.*, vol. 6, no. 19, p. eabb0451, 2020. [Online]. Available: https://doi.org/10.1126/sciadv.abb0451

[27] R. J. Murchie, J. D. Pritchard, and J. Jeffers, "Theoretical comparison of quantum and classical illumination for simple detection-based

LIDAR," in *Quantum Communications and Quantum Imaging XIX*, K. S. Deacon and R. E. Meyers, Eds., vol. 11835, International Society for Optics and Photonics. SPIE, 2021, p. 118350G. [Online]. Available: https://doi.org/10.1117/12.2597042

[28] H. Yang, W. Roga, J. D. Pritchard, and J. Jeffers, "Gaussian state-based quantum illumination with simple photodetection," *Opt. Express*, vol. 29, no. 6, p. 8199, 2021. [Online]. Available: https://doi.org/10.1364/OE.416151

[29] E. D. Lopaeva, I. Ruo Berchera, I. P. Degiovanni, S. Olivares, G. Brida, and M. Genovese, "Experimental Realization of Quantum Illumination," *Phys. Rev. Lett.*, vol. 110, p. 153603, 2013. [Online]. Available: https://doi.org/10.1103/PhysRevLett.110.153603

[30] B. Balaji and D. England, "Quantum Illumination: A Laboratory Investigation," in *2018 International Carnahan Conference on Security Technology (ICCST)*, 2018, pp. 1–4. [Online]. Available: https://doi.org/10.1109/CCST.2018.8585557

[31] S. Frick, A. McMillan, and J. Rarity, "Quantum rangefinding," *Opt. Express*, vol. 28, no. 25, p. 37118, 2020. [Online]. Available: https://doi.org/10.1364/OE.399902

[32] P. S. Blakey, H. Liu, G. Papangelakis, Y. Zhang, Z. M. Léger, M. L. Iu, and A. S. Helmy, "Quantum and non-local effects offer over 40 dB noise resilience advantage towards quantum lidar," *Nature Comms.*, vol. 13, no. 1, p. 5633, 2022. [Online]. Available: https://doi.org/10.1038/s41467-022-33376-9

[33] H. Yang, N. Samantaray, and J. Jeffers, "Quantum Illumination with Multiplexed Photodetection," *Phys. Rev. Appl.*, vol. 18, p. 034021, 2022. [Online]. Available: https://doi.org/10.1103/PhysRevApplied.18.034021

[34] R. Loudon, *The Quantum Theory of Light*, ser. Oxford science publications. Clarendon Press, 2000, ch. 3.7.

[35] M. Fox, *Quantum Optics: An Introduction*, ser. Oxford Master Series in Physics. OUP Oxford, 2006.

[36] J. L. Habif, A. Jagannathan, S. Gartenstein, P. Amory, and S. Guha, "Quantum-limited discrimination of laser light and thermal light," *Opt. Express*, vol. 29, no. 5, pp. 7418–7427, Mar 2021. [Online]. Available: https://doi.org/10.1364/OE.417989

[37] J. Liu, Y. Zhou, W. Wang, F. li Li, and Z. Xu, "Experimental study of the second-order coherence of partially polarized thermal light," *Optics Communications*, vol. 317, pp. 18–23, 2014. [Online]. Available: https://doi.org/10.1016/j.optcom.2013.12.023

[38] R. Loudon, *The Quantum Theory of Light*, ser. Oxford science publications. Clarendon Press, 2000, ch. 5.

[39] M. Beck, "Comparing measurements of g(2)(0) performed with different coincidence detection techniques," *J. Opt. Soc. Am. B*, vol. 24, no. 12, p. 2972, 2007. [Online]. Available: https://doi.org/10.1364/JOSAB.24.002972

[40] National Renewable Energy Laboratory, "Astm g173-03 reference spectra derived from smarts v. 2.9.5," https://www.nrel.gov/grid/solar-resource/spectra-am1.5.html, 2024, accessed: 2024-04-22.

[41] M. V. Jabir and G. K. Samanta, "Robust, high brightness, degenerate entangled photon source at room temperature," *Sci. Rep.*, vol. 7, p. 12613, 2017. [Online]. Available: https://doi.org/10.1038/s41598-017-12709-5

[42] M. Scholz, L. Koch, R. Ullmann, and O. Benson, "Single-mode operation of a high-brightness narrow-band single-photon source,"

Appl. Phys. Lett., vol. 94, no. 20, p. 201105, 2009. [Online]. Available: https://doi.org/10.1063/1.3139768

[43] A. Jechow, A. Heuer, and R. Menzel, "High brightness, tunable biphoton source at 976 nm for quantum spectroscopy," *Opt. Express*, vol. 16, no. 17, pp. 13 439–13 449, 2008. [Online]. Available: https://doi.org/10.1364/OE.16.013439

[44] C. Pang, Q. Zhang, Z. Li, and G. Wu, "Portable pulsed coherent lidar for noncooperation targets at the few-photon level," *Sensors*, vol. 21, no. 7, 2021. [Online]. Available: https://doi.org/10.3390/s21072341

[45] T. Udem, J. Reichert, R. Holzwarth, and T. W. Hänsch, "Accurate measurement of large optical frequency differences with a mode-locked laser," *Opt. Lett.*, vol. 24, no. 13, pp. 881–883, 1999. [Online]. Available: https://doi.org/10.1364/OL.24.000881

[46] H. R. Telle and U. Sterr, *Generation and Metrological Application of Optical Frequency Combs*. Berlin, Heidelberg: Springer Berlin Heidelberg, 2001, pp. 295–313. [Online]. Available: https://doi.org/10.1007/3-540-44991-4_12

[47] T. Fortier and E. Baumann, "20 years of developments in optical frequency comb technology and applications," *Commun. Phys.*, vol. 2, 2019. [Online]. Available: https://doi.org/10.1038/s42005-019-0249-y

[48] M. Kues, C. Reimer, J. M. Lukens, W. J. Munro, A. M. Weiner, D. J. Moss, and R. Morandotti, "Quantum optical microcombs," *Nat. Photonics*, vol. 13, p. 170–179, 2019. [Online]. Available: https://doi.org/10.1038/s41566-019-0363-0

[49] B. J. Smith, P. Mahou, O. Cohen, J. S. Lundeen, and I. A. Walmsley, "Photon pair generation in birefringent optical fibers," *Opt.*

Express, vol. 17, no. 26, pp. 23 589–23 602, 2009. [Online]. Available: https://doi.org/10.1364/OE.17.023589

[50] D. G. England, B. Balaji, and B. J. Sussman, "Quantum-enhanced standoff detection using correlated photon pairs," *Phys. Rev. A*, vol. 99, p. 023828, 2019. [Online]. Available: https://doi.org/10.1103/PhysRevA.99.023828

[51] T. Kobayashi, T. Sueta, Y. Cho, and Y. Matsuo, "High-repetition-rate optical pulse generator using a Fabry-Perot electro-optic modulator," *Appl. Phys. Lett.*, vol. 21, no. 8, pp. 341–343, 2003. [Online]. Available: https://doi.org/10.1063/1.1654403

[52] M. Kourogi, K. Nakagawa, and M. Ohtsu, "Wide-span optical frequency comb generator for accurate optical frequency difference measurement," *IEEE J. Quantum Electron.*, vol. 29, no. 10, pp. 2693–2701, 1993. [Online]. Available: https://doi.org/10.1109/3.250392

[53] R. P. Kovacich, U. Sterr, and H. R. Telle, "Short-pulse properties of optical frequency comb generators," *Appl. Opt.*, vol. 39, no. 24, pp. 4372–4376, 2000. [Online]. Available: https://doi.org/10.1364/AO.39.004372

[54] S. Xiao, L. Hollberg, and S. A. Diddams, "Generation of a 20 GHz train of subpicosecond pulses with a stabilized optical-frequency-comb generator," *Opt. Lett.*, vol. 34, no. 1, pp. 85–87, 2009. [Online]. Available: https://doi.org/10.1364/OL.34.000085

[55] S. Xiao, L. Hollberg, N. R. Newbury, and S. A. Diddams, "Toward a low-jitter 10 GHz pulsed source with an optical frequency comb generator," *Opt. Express*, vol. 16, no. 12, pp. 8498–8508, 2008. [Online]. Available: https://doi.org/10.1364/OE.16.008498

[56] Z. Jiang, D. E. Leaird, C.-B. Huang, H. Miao, M. Kourogi, K. Imai, and A. M. Weiner, "Spectral Line-by-Line Pulse Shaping on an Optical Frequency Comb Generator," *IEEE J. Quantum Electron.*, vol. 43, no. 12, pp. 1163–1174, 2007. [Online]. Available: https://doi.org/10.1109/JQE.2007.907033

[57] G. M. Macfarlane, A. S. Bell, E. Riis, and A. I. Ferguson, "Optical comb generator as an efficient short-pulse source," *Opt. Lett.*, vol. 21, no. 7, pp. 534–536, 1996. [Online]. Available: https://doi.org/10.1364/OL.21.000534

[58] J. Kerr, "XL. A new relation between electricity and light: Dielectrified media birefringent ," *London, Edinburgh Dublin Philos. Mag. J. Sci.*, vol. 50, no. 332, pp. 337–348, 1875. [Online]. Available: https://doi.org/10.1080/14786447508641302

[59] ——, "LIV. A new relation between electricity and light: Dielectrified media birefringent (Second paper)," *London, Edinburgh Dublin Philos. Mag. J. Sci.*, vol. 50, no. 333, pp. 446–458, 1875. [Online]. Available: https://doi.org/10.1080/14786447508641319

[60] C. Monroe, "Quantum information processing with atoms and photons," *Nature*, vol. 416, no. 6877, pp. 238–246, 2002. [Online]. Available: https://doi.org/10.1038/416238a

[61] H. P. Yuen and J. H. Shapiro, "Generation and detection of two-photon coherent states in degenerate four-wave mixing," *Opt. Lett.*, vol. 4, no. 10, pp. 334–336, 1979. [Online]. Available: https://doi.org/10.1364/OL.4.000334

[62] F. Steinlechner, S. Ramelow, M. Jofre, M. Gilaberte, T. Jennewein, J. P. Torres, M. W. Mitchell, and V. Pruneri, "Phase-stable source of polarization-entangled photons in a linear double-pass configuration,"

Opt. Express, vol. 21, no. 10, pp. 11 943–11 951, 2013. [Online]. Available: https://doi.org/10.1364/OE.21.011943

[63] H. Takesue and K. Inoue, "Generation of polarization-entangled photon pairs and violation of Bell's inequality using spontaneous four-wave mixing in a fiber loop," *Phys. Rev. A*, vol. 70, p. 031802, 2004. [Online]. Available: https://doi.org/10.1103/PhysRevA.70.031802

[64] L. A. Ngah, O. Alibart, L. Labonté, V. D'Auria, and S. Tanzilli, "Ultra-fast heralded single photon source based on telecom technology," *Laser Photonics Rev.*, vol. 9, no. 2, pp. L1–L5, 2015. [Online]. Available: https://doi.org/10.1002/lpor.201400404

[65] F. Kaneda, K. Garay-Palmett, A. B. U'Ren, and P. G. Kwiat, "Heralded single-photon source utilizing highly nondegenerate, spectrally factorable spontaneous parametric downconversion," *Opt. Express*, vol. 24, no. 10, pp. 10 733–10 747, 2016. [Online]. Available: https://doi.org/10.1364/OE.24.010733

[66] X.-s. Ma, S. Zotter, J. Kofler, T. Jennewein, and A. Zeilinger, "Experimental generation of single photons via active multiplexing," *Phys. Rev. A*, vol. 83, p. 043814, 2011. [Online]. Available: https://doi.org/10.1103/PhysRevA.83.043814

[67] X. Cao, M. Zopf, and F. Ding, "Telecom wavelength single photon sources," *J. Semicond.*, vol. 40, no. 7, p. 071901, 2019. [Online]. Available: https://doi.org/10.1088/1674-4926/40/7/071901

[68] R. W. Boyd, *Nonlinear Optics, Third Edition*, 3rd ed. USA: Academic Press, Inc., 2008, ch. 1.

[69] L. Misoguti, S. Backus, C. G. Durfee, R. Bartels, M. M. Murnane, and H. C. Kapteyn, "Generation of Broadband VUV Light Using Third-

Order Cascaded Processes," *Phys. Rev. Lett.*, vol. 87, p. 013601, 2001. [Online]. Available: https://doi.org/10.1103/PhysRevLett.87.013601

[70] X. Shi, J. Zhang, X. Zeng, X. Lü, K. Liu, J. Xi, Y. Ye, and Z. Lu, "Suppression of residual amplitude modulation effects in Pound–Drever–Hall locking," *Appl, Phys. B*, vol. 124, no. 8, p. 153, 2018. [Online]. Available: https://doi.org/10.1007/s00340-018-7021-y

[71] S. Juan, J. Mingxing, and J. Fei, "Pound–Drever–Hall laser frequency locking technique based on orthogonal demodulation," *Optik*, vol. 168, pp. 348–354, 2018. [Online]. Available: https://doi.org/10.1016/j.ijleo.2018.04.098

[72] Z. Tai, L. Yan, Y. Zhang, X. Zhang, W. Guo, S. Zhang, and H. Jiang, "Electro-optic modulator with ultra-low residual amplitude modulation for frequency modulation and laser stabilization," *Opt. Lett.*, vol. 41, no. 23, pp. 5584–5587, 2016. [Online]. Available: https://doi.org/10.1364/OL.41.005584

[73] P. Chang, H. Shi, J. Miao, T. Shi, D. Pan, B. Luo, H. Guo, and J. Chen, "Frequency-stabilized Faraday laser with 10^{-14} short-term instability for atomic clocks," *Appl. Phys. Lett.*, vol. 120, no. 14, p. 141102, 2022. [Online]. Available: https://doi.org/10.1063/5.0083390

[74] J. Li, X. Yi, H. Lee, S. A. Diddams, and K. J. Vahala, "Electro-optical frequency division and stable microwave synthesis," *Science*, vol. 345, no. 6194, pp. 309–313, 2014. [Online]. Available: https://doi.org/10.1126/science.1252909

[75] R. W. Boyd, *Nonlinear Optics, Third Edition*, 3rd ed. USA: Academic Press, Inc., 2008, ch. 11.

[76] A. Yariv, *Optical Electronics*, ser. Oxford series in electrical and computer engineering. Oxford University Press, 1991, ch. 9.

[77] F. Flamini, N. Spagnolo, and F. Sciarrino, "Photonic quantum information processing: a review," *Reports on Progress in Physics*, vol. 82, no. 1, p. 016001, 2018. [Online]. Available: https://doi.org/10.1088/1361-6633/aad5b2

[78] J.-W. Pan, Z.-B. Chen, C.-Y. Lu, H. Weinfurter, A. Zeilinger, and M. Żukowski, "Multiphoton entanglement and interferometry," *Rev. Mod. Phys.*, vol. 84, pp. 777–838, 2012. [Online]. Available: https://doi.org/10.1103/RevModPhys.84.777

[79] H. J. Kimble, "The quantum internet," *Nature*, vol. 453, no. 7198, pp. 1023–1030, 2008. [Online]. Available: https://doi.org/10.1038/nature07127

[80] B. Yurke and M. Potasek, "Obtainment of thermal noise from a pure quantum state," *Phys. Rev. A*, vol. 36, pp. 3464–3466, 1987. [Online]. Available: https://doi.org/10.1103/PhysRevA.36.3464

[81] B. Blauensteiner, I. Herbauts, S. Bettelli, A. Poppe, and H. Hübel, "Photon bunching in parametric down-conversion with continuous-wave excitation," *Phys. Rev. A*, vol. 79, p. 063846, 2009. [Online]. Available: https://doi.org/10.1103/PhysRevA.79.063846

[82] R. H. Haitz, "Studies on optical coupling between silicon p-n junctions," *Solid-State Electronics*, vol. 8, no. 4, pp. 417–425, 1965. [Online]. Available: https://doi.org/10.1016/0038-1101(65)90119-X

[83] A. Valencia, G. Scarcelli, and Y. Shih, "Distant clock synchronization using entangled photon pairs," *Appl. Phys. Lett.*, vol. 85, no. 13, pp. 2655–2657, 2004. [Online]. Available: https://doi.org/10.1063/1.1797561

[84] S. Magnitskiy, D. Frolovtsev, V. Firsov, P. Gostev, I. Protsenko, and M. Saygin, "A SPDC-Based Source of Entangled Photons and its

Characterization," *J. Russ. Laser Res.*, vol. 36, no. 6, pp. 618–629, 2015. [Online]. Available: https://doi.org/10.1007/s10946-015-9540-x

[85] I. Kim, D. Lee, and K. J. Lee, "Study of Type II SPDC in Lithium Niobate for High Spectral Purity Photon Pair Generation," *Crystals*, vol. 11, no. 4, 2021. [Online]. Available: https://doi.org/10.3390/cryst11040406

[86] A. Vanselow, P. Kaufmann, H. M. Chrzanowski, and S. Ramelow, "Ultra-broadband SPDC for spectrally far separated photon pairs," *Opt. Lett.*, vol. 44, no. 19, pp. 4638–4641, 2019. [Online]. Available: https://doi.org/10.1364/OL.44.004638

[87] R. Kumar and J. Ghosh, "SPDC photon pairs using a spatially anti-symmetric pump beam in a ppLN ridge waveguide," *Appl. Phys. B*, vol. 126, no. 11, p. 186, 2020. [Online]. Available: https://doi.org/10.1007/s00340-020-07537-x

[88] L. J. Wang, C. K. Hong, and S. R. Friberg, "Generation of correlated photons via four-wave mixing in optical fibres," *J. opt., B Quantum semiclass. opt.*, vol. 3, no. 5, p. 346, 2001. [Online]. Available: https://doi.org/10.1088/1464-4266/3/5/311

[89] J. R. Ong, M. L. Cooper, G. Gupta, W. M. J. Green, S. Assefa, F. Xia, and S. Mookherjea, "Low-power continuous-wave four-wave mixing in silicon coupled-resonator optical waveguides," *Opt. Lett.*, vol. 36, no. 15, pp. 2964–2966, Aug 2011. [Online]. Available: https://doi.org/10.1364/OL.36.002964

[90] T. Jeong, J. Park, and H. S. Moon, "Stimulated measurement of spontaneous four-wave mixing from a warm atomic ensemble," *Phys. Rev. A*, vol. 100, p. 033818, 2019. [Online]. Available: https://doi.org/10.1103/PhysRevA.100.033818

[91] L. Xiao-Song, C. Qun-Feng, S. Bao-Sen, and G. Guang-Can, "Generation of a non-classical correlated photon pair via spontaneous four-wave mixing in a cold atomic ensemble," *Chinese Phys. Lett.*, vol. 26, no. 6, p. 064204, 2009. [Online]. Available: https://doi.org/10.1088/0256-307X/26/6/064204

[92] A. McMillan, Y. Huang, B. Bell, A. Clark, P. Kumar, and J. Rarity, "Chapter 12 - four-wave mixing in single-mode optical fibers," in *Single-Photon Generation and Detection*, ser. Experimental Methods in the Physical Sciences, A. Migdall, S. V. Polyakov, J. Fan, and J. C. Bienfang, Eds. Academic Press, 2013, vol. 45, pp. 411 – 465. [Online]. Available: https://doi.org/10.1016/B978-0-12-387695-9.00012-3

[93] K. Garay-Palmett, D. Cruz-Delgado, F. Dominguez-Serna, E. Ortiz-Ricardo, J. Monroy-Ruz, H. Cruz-Ramirez, R. Ramirez-Alarcon, and A. B. U'Ren, "Photon-pair generation by intermodal spontaneous four-wave mixing in birefringent, weakly guiding optical fibers," *Phys. Rev. A*, vol. 93, p. 033810, 2016. [Online]. Available: https://doi.org/10.1103/PhysRevA.93.033810

[94] K. Garay-Palmett, H. J. McGuinness, O. Cohen, J. S. Lundeen, R. Rangel-Rojo, A. B. U'Ren, M. G. Raymer, C. J. McKinstrie, S. Radic, and I. A. Walmsley, "Photon pair-state preparation with tailored spectral properties by spontaneous four-wave mixing in photonic-crystal fiber," *Opt. Express*, vol. 15, no. 22, pp. 14 870–14 886, 2007. [Online]. Available: https://doi.org/10.1364/OE.15.014870

[95] L. Cui, X. Li, and N. Zhao, "Spectral properties of photon pairs generated by spontaneous four-wave mixing in inhomogeneous photonic crystal fibers," *Phys. Rev. A*, vol. 85, p. 023825, 2012. [Online]. Available: https://doi.org/10.1103/PhysRevA.85.023825

[96] S. Azzini, D. Grassani, M. Galli, D. Gerace, M. Patrini, M. Liscidini,

P. Velha, and D. Bajoni, "Stimulated and spontaneous four-wave mixing in silicon-on-insulator coupled photonic wire nano-cavities," *Appl. Phys. Lett.*, vol. 103, no. 3, p. 031117, 2013. [Online]. Available: https://doi.org/10.1063/1.4812640

[97] L. Olislager, J. Safioui, S. Clemmen, K. P. Huy, W. Bogaerts, R. Baets, P. Emplit, and S. Massar, "Silicon-on-insulator integrated source of polarization-entangled photons," *Opt. Lett.*, vol. 38, no. 11, pp. 1960–1962, 2013. [Online]. Available: https://doi.org/10.1364/OL.38.001960

[98] P. Sharma, A. Agrawal, V. Bhatia, S. Prakash, and A. K. Mishra, "Quantum key distribution secured optical networks: A survey," *IEEE Open J. Commun. Soc.*, vol. 2, pp. 2049–2083, 2021. [Online]. Available: https://doi.org/10.1109/OJCOMS.2021.3106659

[99] L. J. Stephenson, D. P. Nadlinger, B. C. Nichol, S. An, P. Drmota, T. G. Ballance, K. Thirumalai, J. F. Goodwin, D. M. Lucas, and C. J. Ballance, "High-rate, high-fidelity entanglement of qubits across an elementary quantum network," *Phys. Rev. Lett.*, vol. 124, p. 110501, 2020. [Online]. Available: https://doi.org/10.1103/PhysRevLett.124.110501

[100] S. Barnett and P. M. Radmore, *Methods in theoretical quantum optics*. Oxford University Press, 2002, vol. 15.

[101] R. W. Boyd, *Nonlinear Optics, Third Edition*, 3rd ed. USA: Academic Press, Inc., 2008, ch. 2.

[102] D. S. Hum and M. M. Fejer, "Quasi-phasematching," *C. R. Phys.*, vol. 8, no. 2, pp. 180–198, 2007, recent advances in crystal optics. [Online]. Available: https://doi.org/10.1016/j.crhy.2006.10.022

[103] C. Zhang, Y.-F. Huang, B.-H. Liu, C.-F. Li, and G.-C. Guo, "Spontaneous Parametric Down-Conversion Sources for Multiphoton

Experiments," *Adv. Quantum Technol.*, vol. 4, no. 5, p. 2000132, 2021. [Online]. Available: https://doi.org/10.1002/qute.202000132

[104] A. R. A. V. Ya. Shur, E. V. Pelegova and I. S. Baturin, "Periodically poled crystals of KTP family: a review," *Ferroelectrics*, vol. 496, no. 1, pp. 49–69, 2016. [Online]. Available: https://doi.org/10.1080/00150193.2016.1157437

[105] S. Emanueli and A. Arie, "Temperature-dependent dispersion equations for KTiOPO4 and KTiOAsO4," *Appl. Opt.*, vol. 42, no. 33, pp. 6661–6665, 2003. [Online]. Available: https://doi.org/10.1364/AO.42.006661

[106] K. Kato and E. Takaoka, "Sellmeier and thermo-optic dispersion formulas for KTP," *Appl. Opt.*, vol. 41, no. 24, pp. 5040–5044, 2002. [Online]. Available: https://doi.org/10.1364/AO.41.005040

[107] H.-T. Lim, K.-H. Hong, and Y.-H. Kim, "Effects of polarization mode dispersion on polarization-entangled photons generated via broadband pumped spontaneous parametric down-conversion," *Scientific Reports*, vol. 6, no. 1, p. 25846, 2016. [Online]. Available: https://doi.org/10.1038/srep25846

[108] D. Andrews, *Photonics, Volume 1: Fundamentals of Photonics and Physics*, ser. A Wiley-Science Wise Co-Publication. Wiley, 2015, ch. 5.

[109] D. Ljunggren and M. Tengner, "Optimal focusing for maximal collection of entangled narrow-band photon pairs into single-mode fibers," *Phys. Rev. A*, vol. 72, p. 062301, 2005. [Online]. Available: https://doi.org/10.1103/PhysRevA.72.062301

[110] J. Lugani, R. J. A. Francis-Jones, J. Boutari, and I. A. Walmsley, "Spectrally pure single photons at telecommunications wavelengths using commercial birefringent optical fiber," *Opt.*

Express, vol. 28, no. 4, pp. 5147–5163, 2020. [Online]. Available: https://doi.org/10.1364/OE.383704

[111] Q. Lin, F. Yaman, and G. P. Agrawal, "Photon-pair generation in optical fibers through four-wave mixing: Role of Raman scattering and pump polarization," *Phys. Rev. A*, vol. 75, p. 023803, 2007. [Online]. Available: https://doi.org/10.1103/PhysRevA.75.023803

[112] K. Zielnicki, K. Garay-Palmett, D. Cruz-Delgado, H. Cruz-Ramirez, M. F. O'Boyle, B. Fang, V. O. Lorenz, A. B. U'Ren, and P. G. Kwiat, "Joint spectral characterization of photon-pair sources," *Journal of Modern Optics*, vol. 65, no. 10, pp. 1141–1160, 2018. [Online]. Available: https://doi.org/10.1080/09500340.2018.1437228

[113] A. Giudice, M. Ghioni, R. Biasi, F. Zappa, S. Cova, P. Maccagnani, and A. Gulinatti, "High-rate photon counting and picosecond timing with silicon-spad based compact detector modules," *J. Mod. Opt.*, vol. 54, no. 2-3, pp. 225–237, 2007. [Online]. Available: https://doi.org/10.1080/09500340600763698

[114] Y. Hu, M. Yu, B. Buscaino, N. Sinclair, D. Zhu, R. Cheng, A. Shams-Ansari, L. Shao, M. Zhang, J. M. Kahn, and M. Lončar, "High-efficiency and broadband on-chip electro-optic frequency comb generators," *Nat. Photonics*, vol. 16, no. 10, pp. 679–685, 2022. [Online]. Available: https://doi.org/10.1038/s41566-022-01059-y

[115] Y. Hu, M. Yu, D. Zhu, N. Sinclair, A. Shams-Ansari, L. Shao, J. Holzgrafe, E. Puma, M. Zhang, and M. Lončar, "On-chip electro-optic frequency shifters and beam splitters," *Nature*, vol. 599, no. 7886, pp. 587–593, 2021. [Online]. Available: https://doi.org/10.1038/s41586-021-03999-x

[116] A. Pasquazi, M. Peccianti, L. Razzari, D. J. Moss, S. Coen, M. Erkintalo, Y. K. Chembo, T. Hansson, S. Wabnitz, P. Del'Haye,

X. Xue, A. M. Weiner, and R. Morandotti, "Micro-combs: A novel generation of optical sources," *Phys. Rep.*, vol. 729, pp. 1–81, 2018, micro-combs: A novel generation of optical sources. [Online]. Available: https://doi.org/10.1016/j.physrep.2017.08.004

[117] T. J. Kippenberg, A. L. Gaeta, M. Lipson, and M. L. Gorodetsky, "Dissipative kerr solitons in optical microresonators," *Science*, vol. 361, no. 6402, p. eaan8083, 2018. [Online]. Available: https://doi.org/10.1126/science.aan8083

[118] H.-A. Bachor and T. C. Ralph, Eds., *Basic Optical Components*. John Wiley & Sons, Ltd, 2008, ch. 5, pp. 99–146. [Online]. Available: https://doi.org/10.1002/9783527619238.ch5

[119] W. Nagourney, "Energy relations in optical cavities," in *Quantum Electronics for Atomic Physics and Telecommunication*. Oxford University Press, 2014, ch. 3.5, pp. 40–43. [Online]. Available: https://doi.org/10.1093/acprof:oso/9780199665488.003.0003

[120] M. Kourogi, B. Widiyatomoko, Y. Takeuchi, and M. Ohtsu, "Limit of optical-frequency comb generation due to material dispersion," *IEEE J. Quantum Electron.*, vol. 31, no. 12, pp. 2120–2126, 1995. [Online]. Available: https://doi.org/10.1109/3.477736

[121] K. Moutzouris, G. Hloupis, I. Stavrakas, D. Triantis, and M.-H. Chou, "Temperature-dependent visible to near-infrared optical properties of 8 mol% Mg-doped lithium tantalate," *Opt. Mater. Express*, vol. 1, no. 3, pp. 458–465, 2011. [Online]. Available: https://doi.org/10.1364/OME.1.000458

[122] N. I. Chunosov, "rezonator," http://rezonator.orion-project.org/, 2023.

[123] A. S. Bell, G. M. Mcfarlane, E. Riis, and A. I. Ferguson, "Efficient

optical frequency-comb generator," *Opt. Lett.*, vol. 20, no. 12, pp. 1435–1437, 1995. [Online]. Available: https://doi.org/10.1364/OL.20.001435

[124] L. R. Brothers, D. Lee, and N. C. Wong, "Terahertz optical frequency comb generation and phase locking of an optical parametric oscillator at 665 GHz," *Optics Letters*, vol. 19, p. 245, 1994. [Online]. Available: https://doi.org/10.1364/OL.19.000245

[125] M. A. Luda, M. Drechsler, C. T. Schmiegelow, and J. Codnia, "Compact embedded device for lock-in measurements and experiment active control," *Rev. Sci. Instrum.*, vol. 90, no. 2, p. 023106, 2019. [Online]. Available: https://doi.org/10.1063/1.5080345

[126] L. R. Brothers and N. C. Wong, "Dispersion compensation for terahertz optical frequency comb generation," *Opt. Lett.*, vol. 22, no. 13, pp. 1015–1017, 1997. [Online]. Available: https://doi.org/10.1364/OL.22.001015

[127] J. AuYeung, "Picosecond optical pulse generation at gigahertz rates by direct modulation of a semiconductor laser," *Appl. Phys. Lett.*, vol. 38, no. 5, pp. 308–310, 1981. [Online]. Available: https://doi.org/10.1063/1.92351

[128] J. Diels, W. Rudolph, P. Liao, and P. Kelley, *Ultrashort Laser Pulse Phenomena*, ser. Optics and photonics. Elsevier Science, 2006, ch. Chapter 1.1.3.

[129] E. D. Black, "An introduction to Pound–Drever–Hall laser frequency stabilization," *Am. J. Phys.*, vol. 69, no. 1, pp. 79–87, 2001. [Online]. Available: https://doi.org/10.1119/1.1286663

[130] M. Matsui and S. Chikazumi, "Analysis of Anomalous Thermal Expansion Coefficient of Fe–Ni Invar Alloys," *J. Phys. Soc.*

Japan, vol. 45, no. 2, pp. 458–465, 1978. [Online]. Available: https://doi.org/10.1143/JPSJ.45.458

[131] V. Wong and I. A. Walmsley, "Analysis of ultrashort pulse-shape measurement using linear interferometers," *Opt. Lett.*, vol. 19, no. 4, pp. 287–289, 1994. [Online]. Available: https://doi.org/10.1364/OL.19.000287

[132] W. Becker, A. Bergmann, M. Hink, K. König, K. Benndorf, and C. Biskup, "Fluorescence lifetime imaging by time-correlated single-photon counting," *Microsc. Res. Tech.*, vol. 63, no. 1, pp. 58–66, 2004. [Online]. Available: https://doi.org/10.1002/jemt.10421

[133] W. Becker, A. Bergmann, G. L. Biscotti, and A. Rueck, "Advanced time-correlated single photon counting techniques for spectroscopy and imaging in biomedical systems," in *Commercial and Biomedical Applications of Ultrafast Lasers IV*, J. Neev, C. B. Schaffer, and A. Ostendorf, Eds., vol. 5340, International Society for Optics and Photonics. SPIE, 2004, pp. 104 – 112. [Online]. Available: https://doi.org/10.1117/12.529143

[134] W. Becker, *Advanced time-correlated single photon counting applications*. Springer, 2015, vol. 111.

[135] G. Buller and A. Wallace, "Ranging and three-dimensional imaging using time-correlated single-photon counting and point-by-point acquisition," *IEEE J. Sel. Top. Quantum Electron.*, vol. 13, no. 4, pp. 1006–1015, 2007. [Online]. Available: https://doi.org/10.1109/JSTQE.2007.902850

[136] S. Pellegrini, G. S. Buller, J. M. Smith, A. M. Wallace, and S. Cova, "Laser-based distance measurement using picosecond resolution time-correlated single-photon counting," *Meas. Sci. Technol.*, vol. 11, no. 6,

p. 712, 2000. [Online]. Available: https://doi.org/10.1088/0957-0233/11/6/314

[137] X. Ai, R. Nock, J. G. Rarity, and N. Dahnoun, "High-resolution random-modulation cw lidar," *Appl. Opt.*, vol. 50, no. 22, pp. 4478–4488, 2011. [Online]. Available: https://doi.org/10.1364/AO.50.004478

[138] S. Cova, M. Ghioni, A. Lacaita, C. Samori, and F. Zappa, "Avalanche photodiodes and quenching circuits for single-photon detection," *Appl. Opt.*, vol. 35, p. 1956, 1996. [Online]. Available: https://doi.org/10.1364/AO.35.001956

[139] F. Zappa, S. Tisa, A. Tosi, and S. Cova, "Principles and features of single-photon avalanche diode arrays," *Sens. Actuator A Phys.*, vol. 140, pp. 103–112, 2007. [Online]. Available: https://doi.org/10.1016/j.sna.2007.06.021

[140] F. Acerbi, A. Ferri, A. Gola, M. Cazzanelli, L. Pavesi, N. Zorzi, and C. Piemonte, "Characterization of Single-Photon Time Resolution: From Single SPAD to Silicon Photomultiplier," *IEEE Trans. Nucl. Sci.*, vol. 61, no. 5, pp. 2678–2686, 2014. [Online]. Available: https://doi.org/10.1109/TNS.2014.2347131

[141] A. Tosi, A. D. Mora, F. Zappa, and S. Cova, "Germanium and InGaAs/InP SPADs for single-photon detection in the near-infrared," in *Advanced Photon Counting Techniques II*, W. Becker, Ed., vol. 6771, International Society for Optics and Photonics. SPIE, 2007, p. 67710P. [Online]. Available: https://doi.org/10.1117/12.734961

[142] B. Streetman and S. Banerjee, *Solid State Electronic Devices*, ser. Prentice-Hall series in solid state physical electronics. Prentice Hall, 2000. [Online]. Available: https://books.google.co.uk/books?id=TymhQgAACAAJ

[143] F. Sun, Y. Xu, Z. Wu, and J. Zhang, "A simple analytic modeling method for spad timing jitter prediction," *IEEE J. Electron Devices Soc.*, vol. 7, pp. 261–267, 2019. [Online]. Available: https://doi.org/10.1109/JEDS.2019.2895151

[144] M. Assanelli, A. Ingargiola, I. Rech, A. Gulinatti, and M. Ghioni, "Photon-timing jitter dependence on injection position in single-photon avalanche diodes," *IEEE J. Quantum Electron.*, vol. 47, no. 2, pp. 151–159, 2011. [Online]. Available: https://doi.org/10.1109/JQE.2010.2068038

[145] K. Ito, Y. Otake, Y. Kitano, A. Matsumoto, J. Yamamoto, T. Ogasahara, H. Hiyama, R. Naito, K. Takeuchi, T. Tada, K. Takabayashi, H. Nakayama, K. Tatani, T. Hirano, and T. Wakano, "A back illuminated 10μm spad pixel array comprising full trench isolation and cu-cu bonding with over 14% pde at 940nm," in *2020 IEEE International Electron Devices Meeting (IEDM)*, 2020, pp. 16.6.1–16.6.4. [Online]. Available: https://doi.org/10.1109/IEDM13553.2020.9371944

[146] F. Guerrieri, S. Tisa, A. Tosi, and F. Zappa, "Two-dimensional spad imaging camera for photon counting," *IEEE Photonics J.*, vol. 2, no. 5, pp. 759–774, 2010. [Online]. Available: https://doi.org/10.1109/JPHOT.2010.2066554

[147] N. Montaut, L. Sansoni, E. Meyer-Scott, R. Ricken, V. Quiring, H. Herrmann, and C. Silberhorn, "High-efficiency plug-and-play source of heralded single photons," *Phys. Rev. Appl.*, vol. 8, p. 024021, 2017. [Online]. Available: https://doi.org/10.1103/PhysRevApplied.8.024021

[148] S. Ramelow, A. Mech, M. Giustina, S. Gröblacher, W. Wieczorek, J. Beyer, A. Lita, B. Calkins, T. Gerrits, S. W. Nam, A. Zeilinger,

and R. Ursin, "Highly efficient heralding of entangled single photons," *Opt. Express*, vol. 21, no. 6, pp. 6707–6717, 2013. [Online]. Available: https://doi.org/10.1364/OE.21.006707

[149] Q. Liu, Y. Huang, Y. Du, Z. Zhao, M. Geng, Z. Zhang, and K. Wei, "Advances in chip-based quantum key distribution," *Entropy*, vol. 24, no. 10, 2022. [Online]. Available: https://doi.org/10.3390/e24101334

[150] H. Z. J. Zeng, M. A. P. Ngyuen, X. Ai, A. Bennet, A. S. Solntsev, A. Laucht, A. Al-Juboori, M. Toth, R. P. Mildren, R. Malaney, and I. Aharonovich, "Integrated room temperature single-photon source for quantum key distribution," *Opt. Lett.*, vol. 47, no. 7, pp. 1673–1676, 2022. [Online]. Available: https://doi.org/10.1364/OL.454450

[151] A. Ling, J. Fan, and A. Migdall, "Towards improved end-to-end system efficiency of photon pair systems," in *Quantum Communications and Quantum Imaging VIII*, R. E. Meyers, Y. Shih, and K. S. Deacon, Eds., vol. 7815, International Society for Optics and Photonics. SPIE, 2010, p. 78150J. [Online]. Available: https://doi.org/10.1117/12.860562

[152] S. Krapick, H. Herrmann, V. Quiring, B. Brecht, H. Suche, and C. Silberhorn, "An efficient integrated two-color source for heralded single photons," *New J. Phys.*, vol. 15, p. 033010, 2013. [Online]. Available: https://doi.org/10.1088/1367-2630/15/3/033010

[153] Z. Ma, J.-Y. Chen, Z. Li, C. Tang, Y. M. Sua, H. Fan, and Y.-P. Huang, "Ultrabright quantum photon sources on chip," *Phys. Rev. Lett.*, vol. 125, p. 263602, 2020. [Online]. Available: https://doi.org/10.1103/PhysRevLett.125.263602

[154] S. Prabhakar, T. Shields, A. C. Dada, M. Ebrahim, G. G. Taylor, D. Morozov, K. Erotokritou, S. Miki, M. Yabuno, H. Terai, C. Gawith, M. Kues, L. Caspani, R. H. Hadfield, and M. Clerici,

"Two-photon quantum interference and entanglement at 2.1 μm," *Science Advances*, vol. 6, no. 13, p. eaay5195, 2020. [Online]. Available: https://doi.org/10.1126/sciadv.aay5195

[155] N. Somaschi, V. Giesz, L. D. Santis, J. C. Loredo, M. P. Almeida, G. Hornecker, S. L. Portalupi, T. Grange, C. Antón, J. Demory, C. Gómez, I. Sagnes, N. D. Lanzillotti-Kimura, A. Lemaítre, A. Auffeves, A. G. White, L. Lanco, and P. Senellart, "Near-optimal single-photon sources in the solid state," *Nature Photonics*, vol. 10, no. 5, pp. 340–345, 2016. [Online]. Available: https://doi.org/10.1038/nphoton.2016.23

[156] J. S. Massa, G. S. Buller, A. C. Walker, S. Cova, M. Umasuthan, and A. M. Wallace, "Time-of-flight optical ranging system based on time-correlated single-photon counting," *Appl. Opt.*, vol. 37, no. 31, p. 7298, 1998. [Online]. Available: https://doi.org/10.1364/AO.37.007298

[157] M.-J. Sun, M. P. Edgar, G. M. Gibson, B. Sun, N. Radwell, R. Lamb, and M. J. Padgett, "Single-pixel three-dimensional imaging with time-based depth resolution," *Nature Comm.*, vol. 7, no. 1, p. 12010, 2016. [Online]. Available: https://doi.org/10.1038/ncomms12010

[158] J. Tachella, Y. Altmann, N. Mellado, A. McCarthy, R. Tobin, G. S. Buller, J.-Y. Tourneret, and S. McLaughlin, "Real-time 3D reconstruction from single-photon lidar data using plug-and-play point cloud denoisers," *Nature Comm.*, vol. 10, no. 1, p. 4984, 2019. [Online]. Available: https://doi.org/10.1038/s41467-019-12943-7

[159] A. M. Wallace, A. Halimi, and G. S. Buller, "Full waveform lidar for adverse weather conditions," *IEEE Trans. Veh. Technol.*, vol. 69, no. 7, pp. 7064–7077, 2020. [Online]. Available: https://doi.org/10.1109/TVT.2020.2989148

[160] R. Tobin, A. Halimi, A. McCarthy, P. J. Soan, and G. S. Buller, "Robust real-time 3D imaging of moving scenes through atmospheric obscurant using single-photon LiDAR," *Sci. Rep.*, vol. 11, no. 1, p. 11236, 2021. [Online]. Available: https://doi.org/10.1038/s41598-021-90587-8

[161] S. Pirandola, B. R. Bardhan, T. Gehring, C. Weedbrook, and S. Lloyd, "Advances in photonic quantum sensing," *Nat. Photonics*, vol. 12, p. 724, 2018. [Online]. Available: https://doi.org/10.1038/s41566-018-0301-6

[162] R. J. Murchie, J. D. Pritchard, and J. Jeffers, "Object detection and rangefinding with quantum states using simple-detection," 2023. [Online]. Available: https://doi.org/10.48550/arXiv.2307.10785

[163] J. Rapp, J. Tachella, Y. Altmann, S. McLaughlin, and V. K. Goyal, "Advances in single-photon lidar for autonomous vehicles: Working principles, challenges, and recent advances," *IEEE Signal Process. Mag.*, vol. 37, no. 4, pp. 62–71, 2020. [Online]. Available: https://doi.org/10.1109/MSP.2020.2983772

[164] M. M. Islam, A. A. R. Newaz, and A. Karimoddini, "A pedestrian detection and tracking framework for autonomous cars: Efficient fusion of camera and lidar data," in *2021 IEEE International Conference on Systems, Man, and Cybernetics (SMC)*, 2021, pp. 1287–1292. [Online]. Available: https://doi.org/10.1109/SMC52423.2021.9658639

[165] S. Singh and B. S. Saini, "Autonomous cars: Recent developments, challenges, and possible solutions," *IOP Conference Series: Materials Science and Engineering*, vol. 1022, no. 1, p. 012028, 2021. [Online]. Available: https://doi.org/10.1088/1757-899X/1022/1/012028

[166] H. Su, R. Wang, K. Chen, and Y. Chen, "A simulation method for lidar of autonomous cars," *IOP Conference Series: Earth and*

Environmental Science, vol. 234, no. 1, p. 012055, feb 2019. [Online]. Available: https://doi.org/10.1088/1755-1315/234/1/012055

[167] D. B. Horoshko, S. De Bièvre, G. Patera, and M. I. Kolobov, "Thermal-difference states of light: Quantum states of heralded photons," *Phys. Rev. A*, vol. 100, p. 053831, 2019. [Online]. Available: https://doi.org/10.1103/PhysRevA.100.053831

[168] Q. Baudenon, B. Hopkins, and C. Pulikkaseril, "Free-space loss model of lambertian reflection for guided-mode lidar," 2024. [Online]. Available: https://arxiv.org/abs/2311.04156

[169] A. Gulinatti, P. Maccagnani, I. Rech, M. Ghioni, and S. Cova, "35 ps time resolution at room temperature with large area single photon avalanche diodes," *Electronics Letters*, vol. 41, no. 5, pp. 272–274, March 2005. [Online]. Available: https://doi.org/10.1049/el:20047445

[170] M. Colangelo, B. Korzh, J. P. Allmaras, A. D. Beyer, A. S. Mueller, R. M. Briggs, B. Bumble, M. Runyan, M. J. Stevens, A. N. McCaughan, D. Zhu, S. Smith, W. Becker, L. Narváez, J. C. Bienfang, S. Frasca, A. E. Velasco, E. E. Ramirez, A. B. Walter, E. Schmidt, E. E. Wollman, M. Spiropulu, R. Mirin, S. W. Nam, K. K. Berggren, and M. D. Shaw, "Impedance-matched differential superconducting nanowire detectors," *Phys. Rev. Appl.*, vol. 19, p. 044093, Apr 2023. [Online]. Available: https://doi.org/10.1103/PhysRevApplied.19.044093

[171] G. G. Taylor, A. McCarthy, B. Korzh, A. D. Beyer, D. Morozov, R. M. Briggs, J. P. Allmaras, B. Bumble, M. D. Shaw, R. H. Hadfield, and G. S. Buller, "Long-range depth imaging with 13ps temporal resolution using a superconducting nanowire singlephoton detector," in *Conference on Lasers and Electro-Optics*.

Optica Publishing Group, 2020, p. SM2M.6. [Online]. Available: https://doi.org/10.1364/CLEO_SI.2020.SM2M.6

[172] A. McCarthy, N. J. Krichel, N. R. Gemmell, X. Ren, M. G. Tanner, S. N. Dorenbos, V. Zwiller, R. H. Hadfield, and G. S. Buller, "Kilometer-range, high resolution depth imaging via 1560 nm wavelength single-photon detection," *Opt. Express*, vol. 21, no. 7, pp. 8904–8915, 2013. [Online]. Available: https://doi.org/10.1364/OE.21.008904

[173] G. S. Buller, N. J. Krichel, A. McCarthy, N. R. Gemmell, M. G. Tanner, C. M. Natarajan, X. Ren, and R. H. Hadfield, "Kilometer range depth imaging using time-correlated single-photon counting," in *Infrared Sensors, Devices, and Applications; and Single Photon Imaging II*, M. Razeghi, P. D. LeVan, A. K. Sood, and P. S. Wijewarnasuriya, Eds., vol. 8155, International Society for Optics and Photonics. SPIE, 2011, p. 81551I. [Online]. Available: https://doi.org/10.1117/12.899377

[174] J. García-Gutiérrez, F. Martínez-Álvarez, A. Troncoso, and J. Riquelme, "A comparison of machine learning regression techniques for lidar-derived estimation of forest variables," *Neurocomputing*, vol. 167, pp. 24–31, 2015. [Online]. Available: https://doi.org/10.1016/j.neucom.2014.09.091